University of Sheffield

School of Biosciences

Pathological Aggregation of Cystatin C and α-Synuclein in Neurodegenerative Disease

Xander Arscott-Barber

A thesis submitted for the degree of Doctor of Philosophy

February 2025

Abstract

Neurodegenerative diseases are chronic conditions that progressive dysfunction in cognition, muscle control, and speech, driven by neuronal death and malfunction due to protein misfolding and aggregation. Current treatments are limited, and understanding the aggregation pathways involved is key to developing more effective therapies. This thesis investigates two such aggregation systems with strong associations to disease.

The first part focuses on cystatin C aggregation in Bunina bodies, observed in amyotrophic lateral sclerosis (ALS). Extensive attempts at optimising expression and purification of recombinant cystatin C from *E. coli* are shown, followed by in vitro aggregation assays. Cystatin C aggregation is induced in conditions similar to cytosol, where Bunina bodies form, by disrupting two structurally critical disulfide bonds. Kinetic analysis suggests a proline-isomerisation step during the aggregation process, as seen in other cystatins. Additionally, preliminary nuclear magnetic resonance (NMR) data hints at a potentially unreported binding interaction between cystatin C dimers and RNA. In vivo overexpression of fluorescently-tagged cystatin C in mammalian cells produces Bunina body-like inclusions, which appear to be actively transported toward the nucleus via the microtubule network.

The second part explores α-synuclein aggregation on POPG lipid membranes, modelling Lewy body formation in Parkinson's disease. This system has previously informed Parkinson's drug development, including an ongoing phase II clinical trial, which heavily supports its disease relevance. This study shows that fully helical α-synuclein remodels POPG membranes into long cylindrical micelles, which form an inter-connected network, spaced 10-20 nm apart, consistent with a double-anchoring mechanism for α-synuclein reported in the literature. After prolonged incubation, a rapid structural transition from α-helix to β-sheet occurs, supporting a hypothesis of amyloid structural propagation along the micelle surface, providing a mechanism for accelerated aggregation and lipid sequestration by α-synuclein amyloids in Parkinson's disease.

Contents

List of Tables

List of Figures

List of Abbreviations

AD = Alzheimer's Disease

AF4 = Asymmetric-Flow Field-Flow Fractionation

AFM = Atomic Force Microscopy

ALS = Amyotrophic Lateral Sclerosis

ApoE = Apolipoprotein E

APP = Amyloid-β Precursor Protein

ATR = Attenuated Total Reflection

Aβ = Amyloid-β

CD = Circular Dichroism

CFE = Cell Free Extract

Cryo-EM = Cryo-Electron Microscopy

CSF = Cerebrospinal Fluid

DIC = Differential Interference Contrast (Microscopy)

DMPS = 1,2-dimyristoyl-sn-glycero-3-phospho-L-serine

DOPC = 1,2-dioleoyl-sn-glycero-3-phosphocholine

DOPS = 1,2-dioleoyl-sn-glycero-3-phospho-L-serine

DTT = Dithiothreitol

FTIR = Fourier-Transform Infra-red (Spectroscopy)

GFP = Green Fluorescent Protein

GWAS = Genome-Wide Association Study

HA = Hemagglutinin

hCC = human cystatin C

IDRs = Intrinsically Disordered Regions

IPTG = Isopropyl-β-D-galactosidase

L:P = Lipid:Protein ratio

LB = Luria-Bertani Growth Media

LC-MS = Liquid Chromatography Mass Spectrometry

LLPS = Liquid-Liquid Phase-Separation

MALS = Multi-Angle Light Scattering

MWCO = Molecular Weight Cut-Off

NACP = Non-Aβ component precursor

NMR = Nuclear Magnetic Resonance (Spectroscopy)

PD = Parkinson's Disease

PDB = Protein Data Bank

PEG = Polyethylene Glycol

POPC = 1-palmitoyl-2-oleoyl-glycero-3-phosphocholine

POPG = 1-palmitoyl-2-oleoyl-glycero-3-phospho-(1'-rac-glycerol)

PrLDs = Prion-like Domains

R_g = Radius of Gyration

SANS = Small-Angle Neutron Scattering

SAXS = Small-Angle X-Ray Scattering

SDS = Sodium Dodecyl Sulphate

SDS-PAGE = Sodium Dodecyl Sulphate Polyacrylamide Gel Electrophoresis

SLD = Scattering Length Density

SUVs = Small Unilamellar Vesicles

TEM = Transmission Electron Microscopy

TIC = Total Ion Chromatogram

Trx = Thioredoxin

TSP = Trimethylsilylpropanoic acid

UV = Ultra-Violet

Acknowledgements

First and foremost, I would like to express my deepest gratitude to my primary supervisor, Rosie Staniforth, for their unwavering support, guidance and kindness throughout my PhD. Your door was always open, whether to talk about science, office drama or share cat-related crises, that openness and availability made a world of difference. Thank you for trusting me with to follow my own research path, whilst always being there to nudge me in the right direction when I felt lost or uncertain. Your balance of encouragement and autonomy has helped shape this thesis as well as my growth and confidence as an independent researcher.

I am also immensely grateful to my secondary supervisors, Robin Highley, for their expert insights into ALS pathology, and Andy Parnell, who greatly assisted in the acquisition and data interpretation of AFM, SAXS and SANS techniques. I deeply appreciate the time and knowledge you both shared.

I would like to especially thank Jon Waltho and Giulia Bigotti, who reviewed this thesis and shared their thoughtful and insightful feedback, as well as Oliver Durrant, for the amazing opportunity to work in collaboration with the UCB Biopharma team.

Many people contributed their time, patience and technical expertise to this work, helping to teach, perform or interpret the various techniques employed throughout this thesis. Of the many involved in this work, I would most like to highlight the contributions of Svet Tzokov and Indrajit Lahiri for their help with electron microscopy; Tatyana Shelkovnikova, Sarah Granger and Rachel Hodgson, who performed the mammalian cell work on my behalf; and Pete Davis, Alex Taylor and F. Aaron Cruz-Navarrete, who welcomed me into the lab and each spent considerable time teaching and advising me on most of the skills and techniques I used day-to-day throughout the project.

I also had the pleasure of working with several brilliant Master's students: Hannah Wiggett, Jessica Stone, Jonny Light and Theo Enache, whose work directly contributed to this thesis. Thank you for your energy, curiosity and hard-working commitment. My collaborations with each of you was a significant highlight of my project.

Outside the lab, I'm endlessly thankful for the love and support of my friends, especially Alvin, Josh, Harry, Tom, Joel, Chel, Senna and Leif. You are always there to keep me company and distract me from feeling stressed or overworked. You help me to laugh and enjoy every day and I genuinely don't know I would have done this without you.

Finally, to Mum and Dad: Your love, encouragement and unwavering belief in me have driven me to the place I am now. Your support is the foundation of everything I've accomplished. Thank you for always being in my corner and for giving me the confidence to pursue a career that I truly enjoy.

Chapter 1: Introduction

1.1 Neurodegenerative Disease: Cause and Impact

The symptoms of neurodegeneration are diverse, ranging from cognitive decline in Alzheimer's disease (AD), problems with muscular control, affecting movement, balance, speech and eventually breathing in Parkinson's disease (PD) and amyotrophic lateral sclerosis (ALS). These symptoms will deteriorate as the disease progresses and are ultimately fatal. Currently, there are no cures for neurodegenerative diseases and treatment is focused on slowing down the progression of symptoms and palliative care.

In the UK, approximately 982,000 individuals are currently living with dementia, an estimated 60-80% of which are due to Alzheimer's Disease [1]. While Alzheimer's disease is the most common neurodegenerative disease, it is closely followed by Parkinson's disease and motor neuron disease. Parkinson's disease currently affects roughly 153,000 [2] people in the UK, while ALS has an incidence rate affecting roughly 3,900 [3] people per year. These figures represent the enormous impact of neurodegenerative diseases and the need to combat them via a thorough understanding of the molecular mechanisms involved in their cause and progression.

The factors that influence an individual's likelihood of developing one of these diseases are fairly consistent. Primary risk factors for these diseases include: age; genetics; poor diet, specifically high blood pressure, obesity and diabetes; smoking, alcohol and drug usage; and traumatic brain or spinal cord injuries [4-6]. Parkinson's and ALS have correlative links to chemical exposure, such as heavy metals, herbicides and pesticides [5, 6], and even the presence of certain gut bacteria has been shown to influence Parkinson's disease in mouse models [7]. Out of all of these, excluding inherited disease forms, age is by far the biggest factor influencing development of these neurodegenerative disease.

One effect of age is the reduced efficiency of cellular proteostasis over time, which includes mechanisms responsible for the removal of misfolded and aggregated protein [8]. Similarly, outside of neurons, protein turnover rates in cerebral spinal fluid have been shown to drastically reduce with age [9]. This would allow proteins more opportunity to aggregate and cause disease.

Other effects include the increasing amounts of reactive oxygen species in aging cells, which leads to long-term oxidative stress and can damage existing biomolecules, potentially inducing aggregation [10, 11]. In the brain, low levels of neuroinflammation start to occur with age [12]. Neuroinflammation in general is linked to neurodegenerative disease and the aggregates formed during these diseases will cause further neuroinflammation, exacerbating the problem [13, 14].

1.2 Evidence for Aggregation Being the Causative Agent of Disease

The dominant theory regarding the causation of neurodegeneration is the misfolding and aggregation of proteins in the brain and central nervous system. These diseases are characterised by the presence of large deposits found in deceased patient nervous tissue, which are primarily comprised of one or a few proteins [15].

1.2.1 Histopathology

The relevance of protein aggregation to neurodegeneration became apparent after their discovery within the brain tissue of patients [16-19]. Alzheimer described seeing two types of fibrillar species within the neuronal cells of his dementia patients [16, 20]; extracellular plaques and intracellular neurofibrillary tangles. Lewy observed dense protein inclusion bodies within the neurons of those who had Parkinson's disease [18], which were later named after him (Lewy bodies).

A more diverse number of inclusions are associated with ALS, with the 4 main distinct populations: Bunina bodies [21]; ubiquitinated inclusions, subdivided into Skein-like and Lewy body-like [22-25]; hyaline conglomerate inclusions [26, 27]; and axonal spheroids [28, 29].

1.2.2 Identification of Aggregate Proteins

Following the histological stains of patient tissue, it was shown that each disease involved various forms of aggregate, which would eventually be characterised to relate specific proteins each disease. Generally, this involved isolation of aggregates by laser microdissection, followed by protein purification and mass-spectrometry. Once the mass-spec data had been cross-referenced with human protein databases, the relevant antibodies for each protein could then be used to immunostain patient tissue and confirm their presence within aggregates.

Using these methods, the plaques observed by Alzheimer were determined to be formed by the peptide fragment amyloid-β (Aβ) [30, 31], while neurofibrillary tangles contained tau protein [32-35]. Lewy bodies present in Parkinson's disease neurons were found to be aggregates of α-synuclein [36-39].

ALS proved more complicated to study, due to the wide variety of different aggregate types, with the prevalence of each varying on a case-by-case basis. The involvement of the nuclear RNA processing protein TDP-43, found within cytoplasmic ubiquitinated inclusions, was discovered through mass-spectrometry of peptide fragments co-purified from brain tissue with ubiquitin antibodies [40]. The

proteins FUS [41], C9ORF72 [42] and SOD1 [43], were each immunostained in neuronal aggregates based on genetic involvement in familial cases of ALS. Meanwhile, cystatin C was detected as a component of Bunina bodies by immunostaining, presumably by happy coincidence, as the authors do not go into much detail on why they chose to use anti-hCC antibody [44].

1.2.3 Protein Expression Levels

One key feature, that appears common to neurodegenerative diseases, are proteins which are "supersaturated". Supersaturation in this sense describes proteins that are predicted to be aggregation-prone, but are also expressed at relatively high concentrations within the cell. Many proteins involved in the aggregation pathways of AD, PD and ALS have been identified as highly supersaturated in healthy neurons compared to other proteins [45, 46].

These proteins are likely maintained in a metastable state, close to their critical concentration, and only require slight perturbations in concentration or aggregation propensity to initiate widespread aggregation. Previously discussed age-related effects, such as disruptions in proteostasis or oxidative stress, could easily provide the impetus needed for such changes to occur.

Many related proteins and mechanisms in these diseases have also been identified by transcriptomic analyses from affected neuronal cells. Some examples include down-regulation of proteins involved in myelin sheath formation in Alzheimer's disease [47], or mRNA splicing dysregulation following TDP-43 depletion in ALS motor neurons [48]. These types of studies also provide databases of potential research targets for further investigation.

1.2.4 Animal Models

Use of animal models has also played a role in verifying the links between aggregation and disease. Treatment of rat and mice neuronal cell cultures with Aβ has been shown to generate intracellular Tau protein aggregates and cause cell death [49, 50]. In transgenic mice, overexpression of Tau or mutant forms of amyloid precursor protein (APP), from which Aβ is cleaved, leads to neuronal aggregate formation and an Alzheimer's-like phenotype. This effect is substantially more severe when both proteins are overexpressed together [51].

Studies involving Parkinson's disease have developed models using rats and fruit flies (*Drosophila*), which have also shown neurodegeneration and motor impairment phenotypes in response to expression of aggregation-prone mutants of α-synuclein [52-54]. The reverse is also true, as model

Drosophila with alternative Parkinson's disease mutations are saved from this phenotype when expressing a mutant of α-synuclein that is unable to aggregate *in vitro* [54].

Various rodent and *Drosophila* models have also been created to help tackle the wide range of familial mutations and protein aggregates seen in ALS. Among these are mouse models of familial TDP-43 mutants [55], as well as modified TDP-43 to remove its nuclear localisation signal [56]; both leading to insoluble cytoplasmic TDP-43 inclusions in neuronal cells, cell death, and ALS-like symptoms in the mice. Other models show ALS symptoms arise from dipeptide repeat inclusions, caused by DNA repeat expansions in C9ORF72 [57, 58], or from various SOD1 familial mutations [59, 60].

1.2.5 Familial Disease Mutations

Inherited forms of neurodegenerative diseases have helped provide concrete associations between specific genes and disease. The strongest examples of this are familial mutations found in APP, which lead to early-onset Alzheimer's disease. Such mutations typically occur nearby, the cleavage sites of APP that form Aβ peptide, and are thought to enhance Aβ production [61-64]. Similar genetic studies of familial AD mutations also revealed the involvement of apolipoprotein E (ApoE) [65], a cholesterol transport protein, that was later shown to bind hydrophobic peptides like Aβ and is present in Aβ and tau aggregates [66, 67].

The involvement of α-synuclein in Parkinson's disease was also discovered by analysing autosomal dominant forms of PD and finding mutations within its gene [68, 69, 70]. *In vitro* experiments using these hereditary mutant forms of α-synuclein then showed they had considerably accelerated aggregation rates [71], which helped to provide further links between aggregation and disease.

Genetics studies for hereditary ALS were understandably more complex, due to the large number of different genes involved. A table reviewing the range of mutations involved in ALS can be found in Taylor et. al. [72]. This shows that the majority of familial mutations causing ALS occur in genes shown to directly aggregate *in vivo*, namely SOD1, TDP-43, FUS and C9ORF72. This once again provides strong evidence that aggregation is a primary causative component of ALS and other neurodegenerative diseases.

1.2.6 Genome-wide Association Studies

Genome-wide association studies (GWAS) compare genetic data from thousands of patients with sporadic forms a disease, to those of healthy individuals, and seek to identify genetic variations that exist between them. In the case of neurodegeneration, such studies often highlight disease-associated genes with functions closely related to the primary aggregating proteins involved.

GWAS of sporadic Alzheimer's disease strongly correlates genes involved in the processing of APP into Aβ and in binding Tau protein, as well as lipid metabolism, which includes previously mentioned ApoE [73]. Parkinson's disease GWAS shows expected links to α-synuclein and genes involved in hereditary forms of PD, but also involved in proteostasis and autophagy mechanisms [74-76], which makes sense as these systems are required to help combat protein aggregation.

Unfortunately, ALS has a more complex genetic background. Excluding familial cases with high-impact single mutations, sporadic ALS is still estimated to have a heritability of around 50% [77]. However, GWAS struggles to account for a large proportion of this proposed heritability, indicating many related genes with minor impacts are involved [78-80]. Despite this, general trends emerged, which once again included disruption in misfolded protein clearance mechanisms, as well as cytoskeletal maintenance [80].

One recent study, using machine learning, combined previous GWAS data with the genomic profile of motor neurons in order to weight genes by their relative expression levels [81]. This approach was very successful in locating additional ALS-associated genes and also demonstrated the neurotoxic effect of some of these mutations in cell culture, though many of these mutations are yet to be investigated.

It's important to note that of the many genes implicated in neurodegenerative diseases by GWAS studies, the vast majority of genes identified can be directly linked to pathways involving the proteins seen in disease aggregates. Meanwhile, the strongest links are still the genes encoding the aggregating proteins themselves. This, coupled with the lack of alternative genetic links, provides a clear indication of the importance of aggregation in these diseases, both familial and sporadic.

1.3 Aggregation and Neurodegenerative Disease

Protein aggregation is caused by the accumulation of misfolded or partially folded proteins into a large thermodynamically stable structure [82, 83]. Typically, this accumulation is driven by interactions between solvent-exposed hydrophobic regions of these proteins, which are then able to bury themselves within the larger aggregate structure [84, 85]. Protein aggregates are often categorised into three groups: oligomeric, amorphous and amyloid.

The term oligomer refers to a, relatively small, discrete number of individual proteins forming an overall quaternary structure [86]. Oligomers of increasing size can be viewed as steps along the aggregation pathway towards the higher order structures, as viewed using an energy landscape model (Figure 1.1).

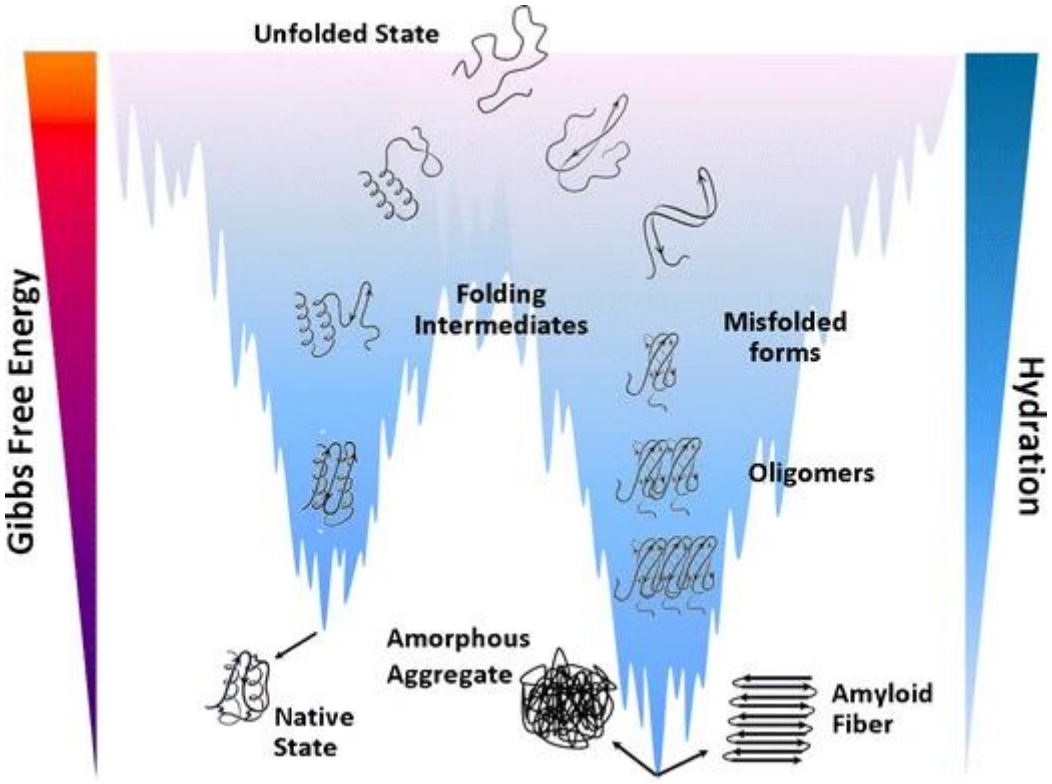

Figure 1.1: The free energy landscape of protein folding and aggregation.
Unfolded protein states with a high free energy are found near the top of the landscape, with generally low energy barriers for conversion towards lower free energy states. During folding, proteins spontaneously travel "downhill" towards the native folded state at a local free energy minimum. Early misfolding events can divert the pathway travelled by the protein, leading towards a different local free energy minimum, which involves nucleation of oligomeric states and eventually amorphous or amyloid aggregation. Figure taken from Corderio et. al. 2014 [87].

Initially misfolded proteins can interact and nucleate the formation of small oligomers, which are shown as one of the many local minima on the energy landscape "funnel" towards aggregation. These oligomer states are often short-lived, and quickly interconvert between states across small energy barriers, represented by the depth of each local minima, growing larger, smaller or structurally converting to another state. Large local energy minima, which have a higher barrier to further conversion, represent populations of more stable, long-lived oligomers. Over time, these molecules tend towards the lowest energy, most stable state, represented by the lowest minima on the landscape. These low energy states are large amorphous or amyloid aggregates and are the final stage of aggregation.

Amorphous aggregates appear as solid 'blobs' of proteins that lack an overall higher-order structure [85]. These aggregates are often thought to be comprised of disordered proteins, driven together by hydrophobic interactions. However, many amorphous aggregates have been shown to contain high proportions of β-sheet structure, indicating the presence of more specific intermolecular interactions stabilising them [88, 89].

Another highly stable aggregate type is amyloid, where individual proteins are aligned into a long fibre. Each subunit contributes β-strands to a parallel cross-β sheet that spans the entire length of the fibre, stabilised by in-register hydrogen bonds between β-strands and a packed hydrophobic core [90]. Despite almost all fibrillar aggregates consisting of a parallel β-sheet structure, packing and ordering of amyloid fibres can vary significantly (Figure 1.2) [91-93]. Aggregation of any particular protein can often yield many different amyloid structures, depending on the assembly conditions. While the majority of fibrillar aggregates exhibit cross-β amyloid structures, there are also rare examples of non-amyloid protein fibres that form as cross-α helical structures instead (Figure 1.3) [94].

The first step of any protein towards aggregation is through a partially unfolded intermediate state [82]. This misfolding can occur due to various environmental conditions, including: pH, temperature, oxidation of side chains by reactive oxygen species, exposure to catalysing surfaces, protein mutations and improper processing of the unfolded protein, for example due to mis-translation or a lack of appropriate chaperones [83, 85, 95]. Exposed hydrophobic regions on these intermediates can then act as binding sites for other similarly misfolded proteins or may even induce the misfolded state in other proteins. These small oligomers will then grow in size by incorporating more monomers, eventually becoming much larger amorphous or fibrillar assemblies.

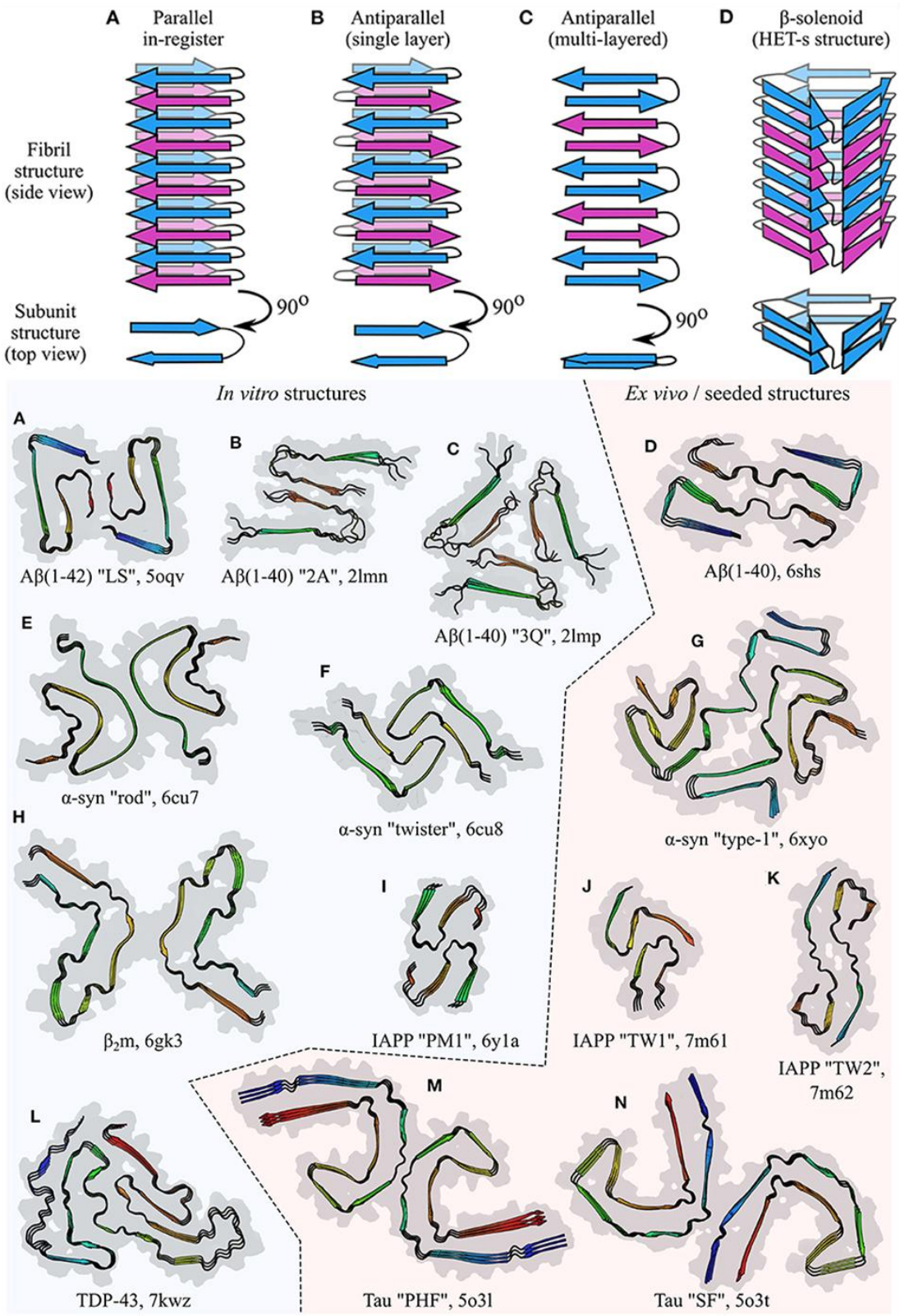

Figure 1.2: The structural diversity of β-sheet amyloids.
(top) Side and top views of general arrangements of β-strands (represented by arrows) in amyloid structures. Individual polypeptide chains are alternately coloured blue or pink. (bottom) Top views of a range of amyloid structures from different sources, cited in Taylor and Staniforth 2022 [92]. Subunit backbones are coloured in a gradient from N-terminus (blue) to C-terminus (red), with surfaces shaded in grey. Figures from Taylor and Staniforth 2022 [92].

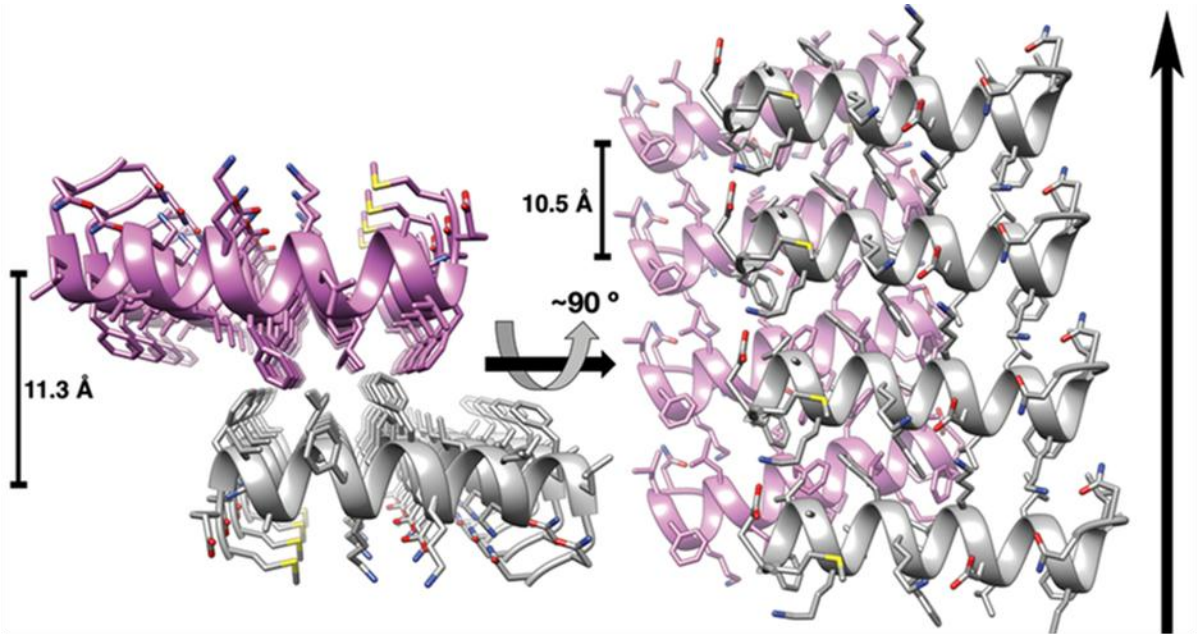

Figure 1.3: The structure of cross-α helical protein fibres.
Shown is an X-ray crystallography structure of *S. aureus* PSMα3 fibrils, that display cross-α structure. The arrow on the right side denotes the fibril axis. Figure from Tayeb-Figelman et. al. 2017 [94].

A variety of different models exist to try and explain aggregation kinetics. The simplest models treat nucleation as slow process, which is limited either by a conformational transition between the normally folded and misfolded states, or by the association of two or more misfolded proteins together to form an initial oligomer (Figure 1.4) [96, 97]. Once the nucleus oligomer has been formed, further aggregation becomes energetically favourable through templating interactions, where additional monomeric protein can become misfolded by association with existing aggregates.

In many cases, this type of model can only explain some of the observed kinetics in *in vitro* aggregation studies. Additional mechanisms, which expand upon the original model, have been suggested to address this disparity, such as surface-catalysed oligomer nucleation [98, 99], fibril fragmentation [100] and liquid-liquid phase-separation [101, 102].

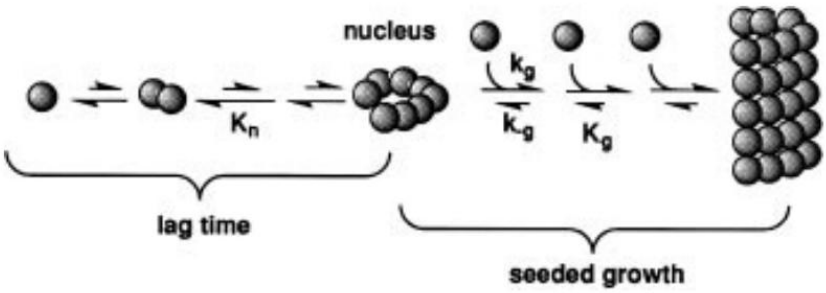

Figure 1.4: Simple model of protein aggregation kinetics.
The lag time is characterised by unfavourable conformational changes and molecular interactions until the aggregate reaches a certain threshold state, the nucleus. Once the nucleus has formed, it templates the misfolding of interacting monomers, which then become part of the oligomer (seeded growth), eventually leading to the formation of large aggregates, such as amyloid fibres. Figure taken from Harper and Lansbury (1997) [97].

Attempting to develop effective therapeutics against aggregation diseases requires identifying which of the wide range of different aggregates is most relevant to disease pathology [103]. There is a general observation that the total amount of aggregates in post-mortem brain tissue does not correlate well with disease severity [104, 105], indicating that end-stage protein deposits are not the main driving force of disease pathology. Coinciding with this are toxicity assays performed on neuronal cell cultures, which have shown that early-stage oligomeric protein mixtures are considerably more neurotoxic than either monomer or fibrillar aggregates [106].

The pathway from monomer to final aggregation states progresses through many different oligomeric states, including off-pathway intermediates [86, 107, 108]. The relative populations and types of oligomers that exist at any one time depends on their individual stability and can change dramatically based on solution conditions. Given the vast heterogeneity of oligomers present in these pathways, and their highly dynamic nature, it is understandably challenging to identify which species are most disease-relevant and to provide targets for therapeutic intervention.

This thesis examines the aggregation of cystatin C in ALS and α-synuclein in Parkinson's disease. Cystatin C has not received much attention for its role in Bunina body formation. Here we focus on the potential impacts of the intracellular environment on cystatin C's aggregation. Meanwhile, a recent Parkinson's clinical drug trial has highlighted the importance of membrane-mediated aggregation in the Parkinson's pathway [109, 110]. We attempt to characterise the structural changes α-synuclein undergoes in this pathway, which are prevented by the drug candidate.

1.4 Amyotrophic Lateral Sclerosis

Amyotrophic lateral sclerosis (ALS) is the most common form of motor neuron disease. It describes the progressive neurodegeneration of both upper and lower motor neurons, causing symptoms of muscle weakness, cramping and stiffness, followed by movement and speech difficulties and ultimately death [111, 112]. The disease progresses rapidly, with an average lifespan following diagnosis of 3-5 years. There are few treatments for ALS, which currently only have very limited effect.

ALS motor neurons contain an unusually wide variety of different protein inclusions, compared to other aggregation diseases. These involve: Bunina bodies, which contain primarily cystatin C and transferrin [21, 44, 113]; ubiquitinated inclusions, usually containing TDP-43, but can instead contain FUS, SOD1, p62 or dipeptide repeats generated from C9ORF72, depending on familial mutations [22-25, 46, 114]; and hyaline conglomerate inclusions and axonal spheroids, both shown to consist of neurofilament proteins [26, 27, 29].

1.4.1 Pathobiology of ALS

It is difficult to determine what common factors link each of these protein inclusions together. It has been suggested that disruption of RNA metabolism may be a core pathogenic feature of ALS, as many of the proteins involved, such as TDP-43 and FUS, are themselves RNA binding proteins [115, 116]. Additionally, other related proteins, including SOD1, have been shown to gain RNA binding capabilities in their familial mutant forms [117]. There is some evidence to suggest that cytoplasmic mRNA stability is affected as a result of these proteins aggregating and that RNA may also be sequestered within these aggregates [42, 118-120].

Another potential link is the breakdown of the autophagy pathway, which regulates the destruction and recycling of damaged organelles [121]. This is of particular concern in neuronal cells, which are not dividing cells and must actively maintain themselves for an entire human lifespan. As such, autophagy is a highly important process in neurons and it has been shown that defects related to autophagy lead to neurodegeneration in both mice and humans [122]. Both ubiquitin and p62 are found associated with most ALS aggregates, which are targeting markers for autophagy [123, 124]. It has been suggested and shown that in early stages of the disease, misfolded aggregates are destroyed via autophagy [125-127]. However, over time this pathway becomes overwhelmed by aggregate formation and is thus unable to perform its normal neuroprotective functions [128-130].

1.4.2 Protein Aggregation in ALS

An interesting observation is the mechanism by which these aggregates form. There is growing evidence that the majority of ALS aggregates form via an initially liquid-liquid phase-separated state. Studies involving TDP-43 have shown that it can spontaneously form phase-separated droplets and that these droplets enhance its aggregation rate [131, 132]. Importantly, ALS-associated mutants of TDP-43 in these studies have a higher propensity to phase-separate. Similar studies have revealed phase-separation is associated with ALS inclusions of SOD1 [133, 134], FUS [135], Ubiquilin-2 [136] and C9ORF72 dipeptide repeats [137-139]. A table of various ALS-related phase-separation and the proteins involved can be found in Pakravan et. al. [140].

Liquid-liquid phase-separation (LLPS) occurs when a liquid is able to partially de-mix into chemical distinct phases, each enriched or depleted in certain subsets of molecules. If a group of molecules (Group A) in a mixed liquid share preferential interactions with each other, there is a decrease in free energy when these molecules associate with each other, compared to with other molecules in the bulk liquid (Group B). Phase-separation will occur spontaneously when the decrease in free energy caused by allowing Group A molecules to stay together outweighs the increase in free energy due to entropy by de-mixing the liquid. Under the right conditions, this can result in LLPS, forming liquid droplets with a higher concentration of Group A molecules and a lower concentration of Group B molecules than the surrounding solution [141, 142].

The relative proportions of Group A and Group B inside the droplet are maintained at an equilibrium, which is dependent on the balance between interaction strength and entropy. Entropy is directly affected by temperature, while interaction strength can be modified by both temperature and solution conditions, such as concentration or ionic strength. Unbalancing this system in either direction will lead to either re-mixing, when entropy becomes the driving force, or a further phase transition to a gel or solid, which occurs when interaction strength increasingly dominates entropy [141, 142].

In cells, LLPS allows for the formation of discrete membraneless compartments, containing high local concentrations of specific macromolecules, which are involved in compartmentalising cell metabolism or signalling [141, 143, 144]. In the literature, these compartments are commonly referred to as biomolecular condensates. Biomolecular condensates can also provide the conditions necessary for aggregation to occur, by increasing the local concentration of aggregation-prone macromolecules above the threshold required to initiate nucleation events [145].

A key element of biomolecular condensate formation is the presence of multivalent intermolecular interactions that drive the entropically unfavourable de-mixing [146-149]. Proteins can achieve this multivalency through a number of different structural properties. LLPS due to multivalent protein-protein interactions has been demonstrated between artificially generated tandem repeats of the SH3 domain, which readily phase-separates with proteins containing proline-rich motifs [150]. However, *in vivo*, LLPS via protein-protein interactions is more often driven by intrinsically disordered regions (IDRs), rather than fully folded domains.

One common class of IDRs are prion-like domains (PrLDs), which are present in a large number of phase-separating proteins, including FUS and TDP-43 [151, 152]. PrLDs are relatively unstructured, highly polar chains and are thought to phase-separate through promiscuous electrostatic interactions or by interactions with arginine and glycine-rich RGG domains, which are also often found in PrLD proteins [146, 147, 153, 154].

Protein RNA-binding capacity is also implicated in phase-separated droplets [147-149]. Nucleic acids are perfect scaffolding molecules, which can easily interact with many binding proteins at once leading to phase-separation. Additionally, the length of RNA or binding affinity to specific sequences are levers that cells can manipulate to regulate a phase-separated state [147]. RNA-binding motifs are present in most ALS aggregating proteins and are another reason why these proteins may undergo LLPS [115-117].

Some proteins also contain specific oligomerisation domains, which define another form of multivalency for interactions between identical proteins. TDP-43 contains an N-terminal oligomerisation domain, which has also been shown to increase its ability to phase-separation *in vitro* [155].

1.4.3 Cystatin C – A Missing Link?

One element of ALS aggregation which is, so far, largely unstudied is the role of cystatin C in Bunina bodies. These cytoplasmic inclusions appear in lower motor neurons in the vast majority of sporadic ALS cases and some familial cases [21, 114, 156]. They have been successfully immunostained for cystatin C and transferrin, and occasionally peripherin [44, 113, 157, 158]. However, not much is known about their formation or biological impact on ALS, aside from observations of Bunina body co-localisation with TDP-43 inclusions [159].

Despite being the only inclusion that is specific to ALS pathology [44], the lack of focus on Bunina bodies is perhaps unsurprising due to the absence of any associated familial mutations [72]. Cystatin

C, the main component of Bunina bodies, is a ubiquitously expressed protease inhibitor that regulates a wide range of protease activity in both lysosomes and is secreted extracellularly throughout the body [160]. So far, there are only two known pathological mutations of cystatin C.

Hereditary cystatin C amyloid angiopathy is caused by the autosomal dominant mutation L68Q, which is only maintained in a small number of Icelandic families [161-163]. This mutation does not appear to affect cystatin C's localisation or inhibitory activity, but instead reduces its stability and increases its propensity to form amyloid aggregates, which are observed extracellularly around blood vessels in the disease [162-166].

The A25T mutation, found at cystatin C's secretory signal cleavage site, is genetically linked to late-onset Alzheimer's disease and age-related macular degeneration [167, 168]. This mutation has been shown to alter the cleavage site during secretion to an upstream position, adding additional N-terminal residues to the final secreted protein [169]. There is conflicting evidence on whether this affects the secretion rate or protease inhibition activity of cystatin C [169, 170], though the exact impact of this mutation on disease is still largely unstudied.

The lack of additional pathogenic mutants of cystatin C may simply show they have yet to be discovered. However, based on the ubiquitous role cystatin C plays in extracellular protease regulation, this could also point towards it being a critical gene whose mutations are largely non-viable. Both L68Q and A25T mutations are likely to reduce extracellular cystatin C concentration or activity, but allow it to carry out its functions enough, at least in early life, to permit these variants.

Regardless of the lack of genetic evidence, cystatin C is still clearly involved in ALS via Bunina body aggregation. The specificity of these aggregates to ALS and their potential interaction with other well-studied aggregates should provide ample justification to further examine these understudied inclusions.

1.5 Cystatin C – Structure, Function and Disease Relevance

1.5.1 Structure and Function of Cystatin C

Human cystatin C (hCC) is a 13.3 kDa cysteine protease inhibitor [171, 172], which is expressed ubiquitously throughout the human body and found secreted in all bodily fluids [171, 173, 174]. It is maintained at high concentrations extracellularly (0.5 µM in CSF and 0.1 µM in serum) and is the most abundant cysteine protease inhibitor [171, 173]. hCC is part of the type 2 cystatin family, which additionally contains other, tissue-specific, small secreted protease inhibitors [175, 176].

Similar to other type 2 cystatins, hCC's structure includes a large antiparallel β-sheet, with a long α-helix laying perpendicular to the β-strands [175-177], affectionately referred to as the "hot-dog" fold (Figure 1.5). This structure is stabilised by the presence of two disulphide bonds, which form in the oxidising environment of the endoplasmic reticulum and are stable in the extracellular matrix [177, 178]. Cystatin C is expressed with a 26 amino acid N-terminal secretory sequence, which is cleaved upon secretion, resulting in a 120-residue folded protein [179, 180].

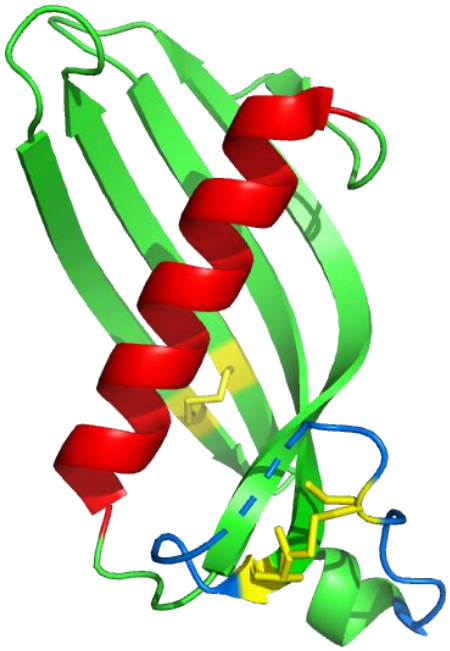

Figure 1.5: The structure of human cystatin C.
A cartoon representation of human cystatin C secondary structural elements and tertiary structural fold is shown. The characteristic "hot-dog" fold is highlighted by the antiparallel β-sheet (green) wrapped around a large α-helix (red). The two disulphide bonds are shown by yellow sticks. hCC also contains a short, disordered loop (blue), which is stabilised by one of the disulphide bonds. Figure created using a deposited x-ray crystal structure (PDB: 3GAX) [177].

The primary targets of type 2 cystatins are members of the cathepsin family of papain-like cysteine proteases [171, 172, 175, 176]. Cathepsins are found primarily in lysosomes, but some have extracellular functions and can escape into extracellular fluids through lysosomal exocytosis [181, 182]. Cystatins competitively inhibit these enzymes to limit their effects and prevent widespread proteolysis [171, 172, 175, 176].

Although present in all fluids, the inhibitory effects of cystatin C is most important in cerebrospinal fluid, where it makes up more than 90% of the total cysteine protease inhibitor concentration [171]. hCC has also been shown to have various other neuroprotective effects, including: signalling cell growth [183-186], moderating inflammatory responses [187-189], regulating autophagy [186, 190-192] and anti-microbial properties [189, 192, 193]. While these are mostly extracellular functions, cystatin C is also known to be internalised [194-196] and have intracellular functions regulating lysosomal proteolysis [172, 174, 176, 194] and even inhibiting viral replication [197, 198]. It is therefore no surprise that changes in the level of hCC in the brain can have wide-reaching effects.

Excessive levels of cystatin C have already been implicated in Alzheimer's disease progression. Cathepsin B, which is primarily localised to the endolysosomal system, but can also be found extracellularly, has been found to associate with amyloid-β plaques [181]. Cathepsin B was then shown, through mice models, to reduce amyloid-β peptide and associated AD pathology, an activity which is subsequently inhibited by the overexpression of cystatin C [199]. In this way, research has shown that high levels of hCC may play an active role in exacerbating AD pathology.

1.5.2 Cystatin C Aggregation

Cystatin C has also been shown to be amyloidogenic itself, via a 3D domain-swapped dimer intermediate (Figure 1.6) [200-202]. 3D domain-swapping involves a dimerisation or multimerization mechanism, in which monomers partially, or completely, unfold and refold to form two identical monomer fold units, where each unit is composed of secondary structure elements contributed by two different polypeptide chains. The topology of cystatin monomers is $\beta_1\alpha\beta_2\beta_3\beta_4\beta_5$. In the dimer form, $\beta_1\alpha\beta_2$ is contributed by one polypeptide chain, while $\beta_3\beta_4\beta_5$ is contributed by the other chain [200-202].

This dimer form is also believed to be an endogenous mechanism of inactivating intracellular hCC until protease levels grow too high [196, 203]. Aggregation of the dimer has been studied in relation to the hereditary cystatin C amyloid angiopathy L68Q mutant [202, 204]. However, dimerisation of the wild-type form and subsequent aggregation has so far only been established *in vitro* at relatively non-

physiological conditions, including: high temperatures [204], low pHs [205], and via synchrotron radiation [206].

Cystatin C can also form long, straight amyloid fibrils with various morphologies and can be decorated with spherical or annular oligomeric structures. Although tetrameric intermediates of cystatin C have not been characterised, they have been generated and characterised *in vitro* by thermal destabilisation or refolding in urea for both wild-type chicken cystatin [207] and mutant cystatin B [208], type 2 and type 1 family cystatins respectively. In these cases, tetramerisation and downstream aggregation depends on a trans- to cis- isomerisation step of a conserved proline residue. Studies examining aggregation of these proteins show a relatively shallow protein concentration dependence, due to the limiting rate of proline isomerisation [209, 210].

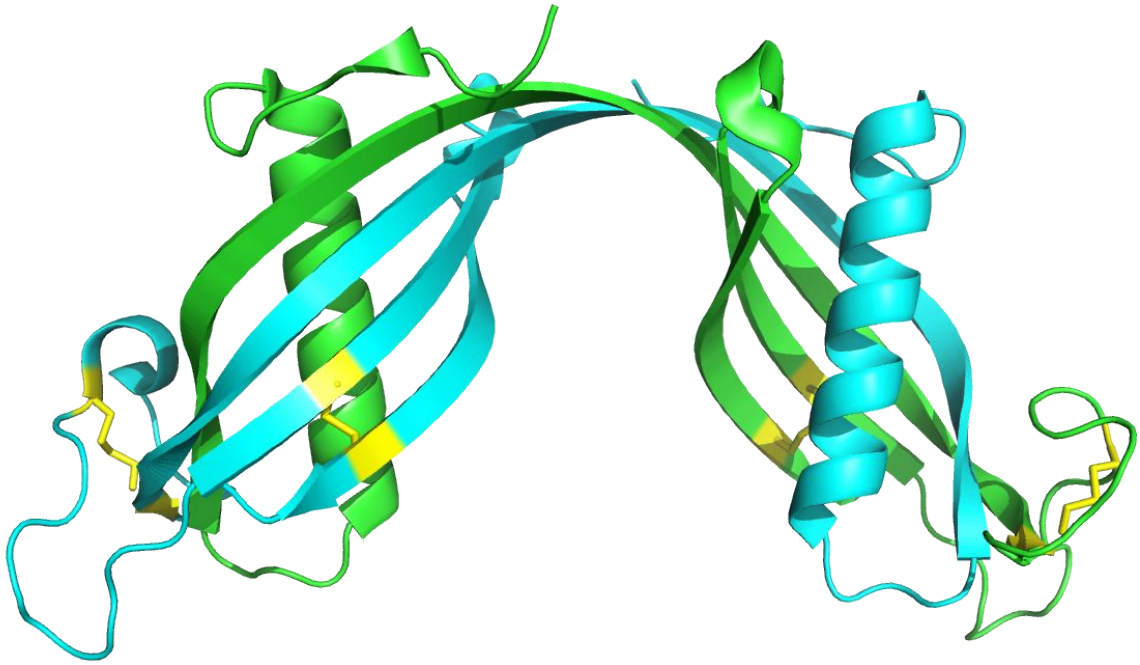

Figure 1.6: Cystatin C domain-swapped dimer.
The dimer structure of cystatin C is shown with individual monomers differently coloured (Green or Cyan). The disulphide bonds for each monomer are shown in yellow. Figure created using a deposited x-ray crystal structure (PDB: 1R4C) [202].

1.5.3 Cystatin C in ALS

In the case of ALS, the levels of cystatin C in cerebrospinal fluid (CSF) have been shown to be significantly reduced [211, 212]. This is likely the result of intracellular aggregation into Bunina bodies, which has also been shown to deplete background levels of hCC inside of motor neurons as well [213]. This global reduction in cystatin C is likely to upregulate autophagy and inflammation in the brain, as well as unbalance intracellular proteostasis, leading to rampant proteolysis.

One potentially interesting feature of cystatin C in ALS, is its connection with TDP-43 cleavage. Another pathological hallmark of most forms of ALS is the formation of aggregated deposits of TDP-43 peptide fragments [214-216]. These fragments are cleaved from full-length TDP-43 by caspase 3 or caspase 7 enzymes [217, 218], which are part of another family of cysteine proteases. Cystatin C is already known to influence caspase 3 activity and has been shown to both upregulate and downregulate its activity in mice and cell culture models [186, 191, 219]. However, *in vitro* assays have also confirmed that this is not via a direct binding interaction of caspase 3 and cystatin C [220]. Therefore, there is a potentially unexplored link between hCC depletion and TDP-43 cleavage and subsequent aggregation. This is particularly intriguing as Bunina bodies and small skein-like TDP-43 inclusions are often the earliest inclusions to be visualised during disease progression [221, 222].

Cystatin C clearly has a wide range of influences on extracellular signalling, including regulating inflammation, as well as neuroprotective roles, such as anti-microbial and anti-viral effects, and the regulation of both intracellular and extracellular proteostasis, autophagy, and apoptosis. In ALS, hCC depletion, via the formation of Bunina bodies, could cause disruptions in all of these processes. It also has a potential role in the initiation of TDP-43 aggregation, leading to further downstream consequences. The currently lack of study on this clearly pathognomonic feature of ALS provides an opportunity to reveal important underlying processes contributing to ALS pathology, which could eventually be exploited by future therapeutic interventions to mitigate or even reverse disease progression.

1.6 Bunina bodies in ALS

Bunina bodies are large, approximately 1-5 µm diameter, round inclusions that are found in the lower motor neurons of patients with ALS [21, 44, 213, 223]. They have been found to be immunopositive for cystatin C [44] and the iron transport protein transferrin [113], with occasional staining observed for the neurofilament protein peripherin [157]. Bunina bodies do not appear to contain other common aggregating proteins or markers of degradation, which includes: α-synuclein [224], p62 [225], APP or amyloid-β [226], tau or microtubule related proteins [44], and ubiquitin [44].

These inclusions have been shown to be highly prevalent, as one study of 102 individuals detected Bunina bodies in 86% of sporadic ALS cases [223]. Staining of Bunina bodies with cystatin C antibodies has shown the appearance of both large individual puncta (Figure 1.7b-d) and small granular bodies (Figure 1.7e-f) [213, 227]. Formation of these bodies also appears to cause intracellular depletion of cystatin C when compared to healthy neurons (Figure 1.7a).

It was previously discussed that cystatin C depletion may have an indirect effect on TDP-43 cleavage and subsequent aggregation. Strengthening this hypothesis, Bunina bodies have occasionally been shown to co-localise with TDP-43 ubiquitinated inclusions [159], which could suggest a common disease pathway. It is also important to note that Bunina bodies are present in C9ORF72 familial ALS mutants, which also involve TDP-43 inclusions [228, 229]. However, Bunina bodies are notably absent when TDP-43 pathology is not featured, namely in ALS involving FUS or SOD1 familial mutants [230-232]. Furthermore, the occurrence of Bunina bodies has been described to increase overall TDP-43 aggregation [233] and potentially even occurs prior to any initial TDP-43 aggregation in some cases [221, 222].

Electron microscopy of Bunina bodies from tissue autopsies has characterised these inclusions as dense, amorphous aggregates with no surrounding membrane (Figure 1.8). They are often found with small amounts of tubular and vesicular structures lining their periphery, as well as hollow regions inside the bodies, containing bundles of filamentous material [44, 227, 234, 235]. Some studies have described apparent similarities between Bunina bodies and laminated cytoplasmic bodies, which originate from the rough endoplasmic reticulum [234, 236], whilst others suggest a link to the Golgi and lysosomes [44, 227].

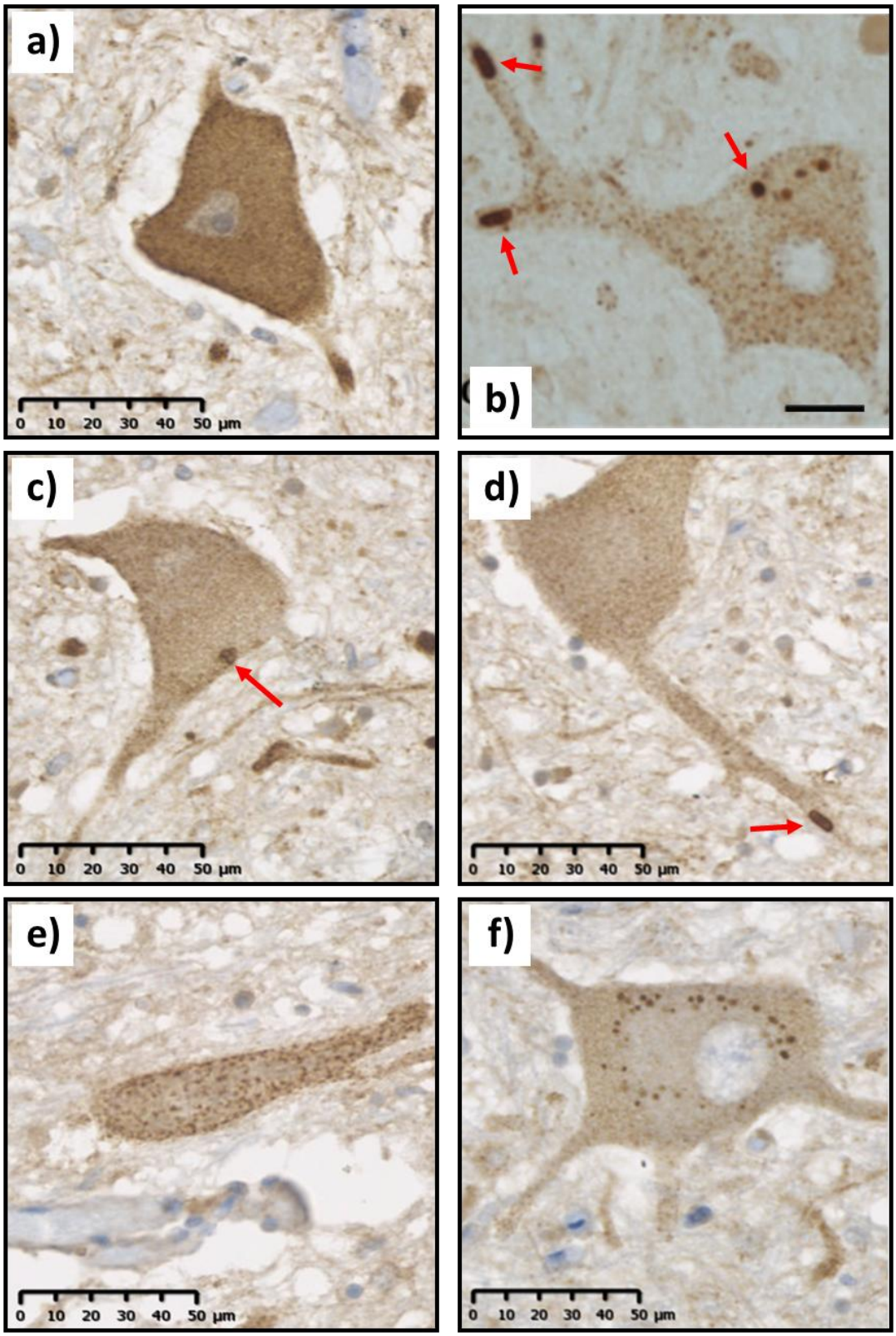

Figure 1.7: Immunostaining of Bunina bodies in ALS motor neurons.
Tissue sections of lower motor neurons stained for the presence of Bunina bodies with cystatin C antibody. a) A healthy neuron showing a background cytoplasmic staining for hCC. b-d) Examples of large hCC-positive puncta, marked with red arrows. e-f) Examples of small granular Bunina bodies. Image in b) from Okamoto et. al. 2008 [227] (scale bar = 20 µm). Images in a) and c-f) from Granger and Highley 2020 [213].

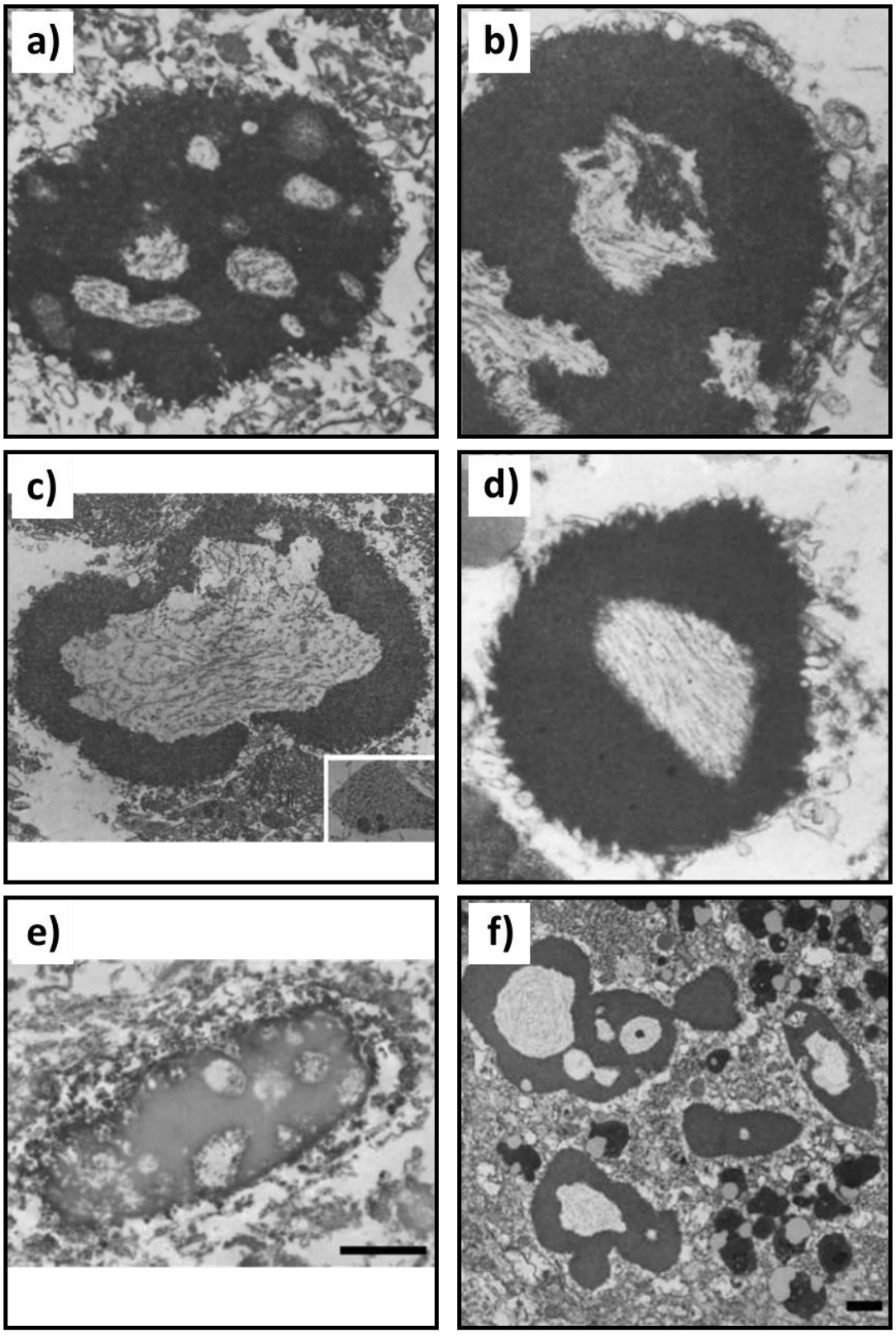

Figure 1.8: Electron Microscopy of Bunina bodies.
Examples of published electron microscopy of Bunina bodies showing they are dense, amorphous aggregates with hollow regions containing fibrillar aggregates. Vesicular and tubular membrane-like structures can be seen lining the edges of the Bunina bodies. a) and c) are 6570x magnification, b) is 15750x magnification, a-c) Figures from Tomonaga et. al. 1978 [234]. d) 19000x magnification, figure from Sasaki and Maruyama 1993 [235]. e-f) Scale bars = 2 µm, figures from Okamoto et. al. 2008 [227].

Given the limited information currently available on Bunina bodies, we can only speculate as to the mechanisms that lead to their formation. Though not typically discussed in an intracellular context, cystatin C does still appear to occupy the cytoplasm at significant levels in motor neurons (Figure 1.7a) [213]. Bunina bodies often have membrane components in close proximity [44, 227, 234, 235], which could suggest they originate from within secretory bodies, though this has yet to be observed. Alternatively, negatively-charged membranes may simply colocalise with Bunina bodies due to the unusually positive charge of cystatin C, from which they are made.

Aggregation of cystatin C in Bunina bodies appears to be initially amorphous [44, 227, 234, 235], potentially through a liquid-liquid phase-separated intermediate state similar to many other ALS inclusions. Indeed, one could imagine the hollow spaces that exist within these inclusions to be akin to bubbles trapped in a solidifying jelly, which form as the concentrated liquid droplet solidifies into a Bunina body.

Due to the lack of contrary evidence, it seems likely that cystatin C aggregation into Bunina bodies occurs entirely within the cytoplasm. So far, there has not been much exploration of cystatin C's ability to phase-separate or aggregate in cytosolic conditions, and this subject will be a key element of this thesis. Some important factors that are considered here are the impact of an intracellular reducing environment on cystatin C, particularly on its disulphide bonds, as well as the effects of RNA, ionic strength and macromolecular crowding on the aggregation propensity of this protein.

1.7 Lewy bodies in Parkinson's Disease

Parkinson's disease (PD) is primarily characterised by symptoms of tremor, stiffness and dysregulation of motor functions [237]. This is due to a lack of dopamine, caused by the progressive degeneration of dopaminergic neurons in the substantia nigra, a region of the brain that controls movement [238, 239]. PD pathology follows the formation of large intraneuronal inclusions known as Lewy bodies [18], which primarily consist of fibrillar α-synuclein [38, 240, 241].

Lewy bodies can form both within neurites, thin protrusions that extend from the main neuronal cell body (the soma) to form axons or dendrites, and within the soma itself [111, 112]. In neurites, Lewy bodies are restricted by the surrounding membrane and fill the space, forming elongated inclusions that block passage through the neurite (Figure 1.9d-f) [240, 241]. Meanwhile, somatic Lewy bodies appear as very large spherical inclusions that stain strongly for α-synuclein (Figure 1.9a-d) [240, 241].

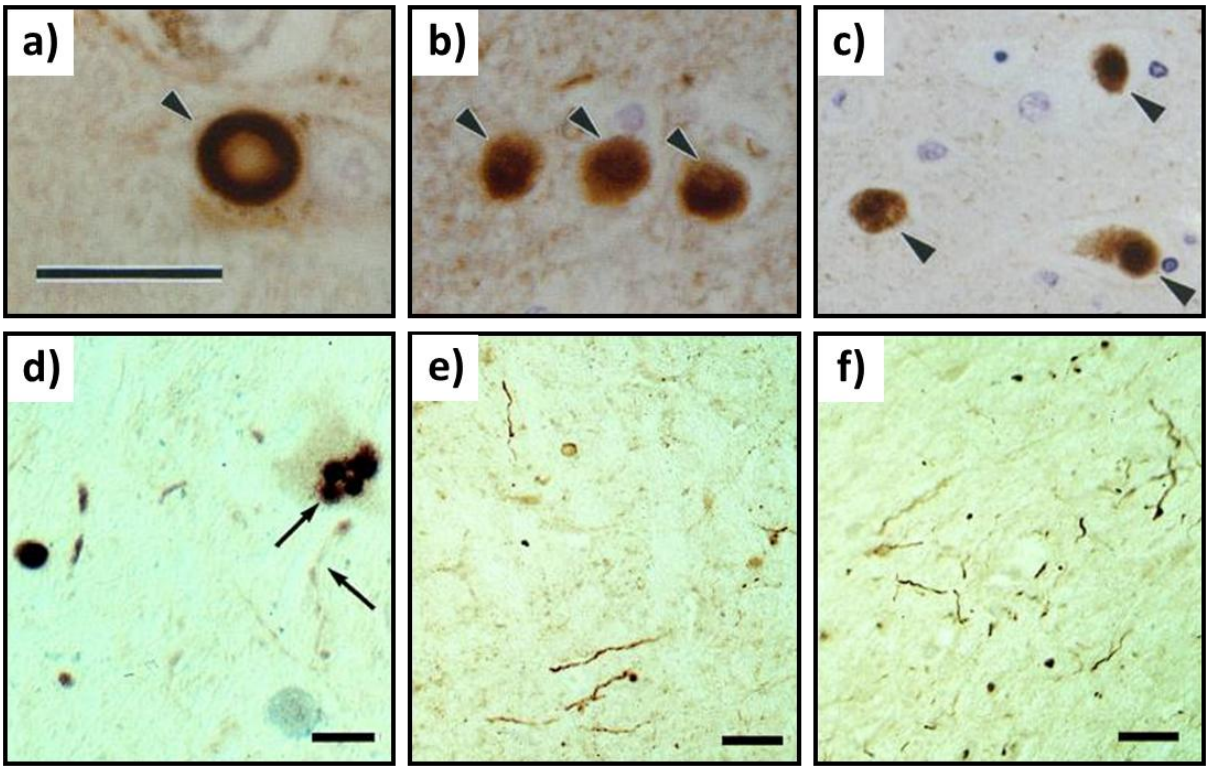

Figure 1.9: Immunostaining of Lewy bodies in Parkinson's disease neurons.
PD patient neuronal tissue from the substantia nigra (a, d-f) or cingulate cortex (b-c), immunostained for α-synuclein. a-c) Large somatic Lewy bodies can be seen highlighted by arrows. d) Arrows point towards both a cluster of large Lewy bodies and a Lewy neurite. e-f) Thin Lewy bodies can be seen inside neurites. a-c) From Baba et. al. 1998 [241], scale bar in a) equivalent to 30µm in a) and b), and 60 µm in c). d-f) From Spillantini et. al. 1998 [240], d) scale bar is 30 µm, e-f) scale bars are 100 µm.

Microscopy of Lewy bodies from patient tissue shows them to contain a highly dense core of aggregated material, with radiating fibrillar structures extending from the centre (Figure 1.10) [242-245]. Immunostaining, first for neurofilaments and then later for α-synuclein, showed that, while some of these fibrils were neurofilaments, the majority were α-synuclein fibrillar aggregates [38, 240, 243]. Many Lewy bodies also appear to contain substantial amounts of disrupted membrane vesicles and even mitochondria, which are found around the Lewy body periphery or trapped inside, surrounded by α-synuclein fibres (Figure 1.10b-d) [242, 244, 245].

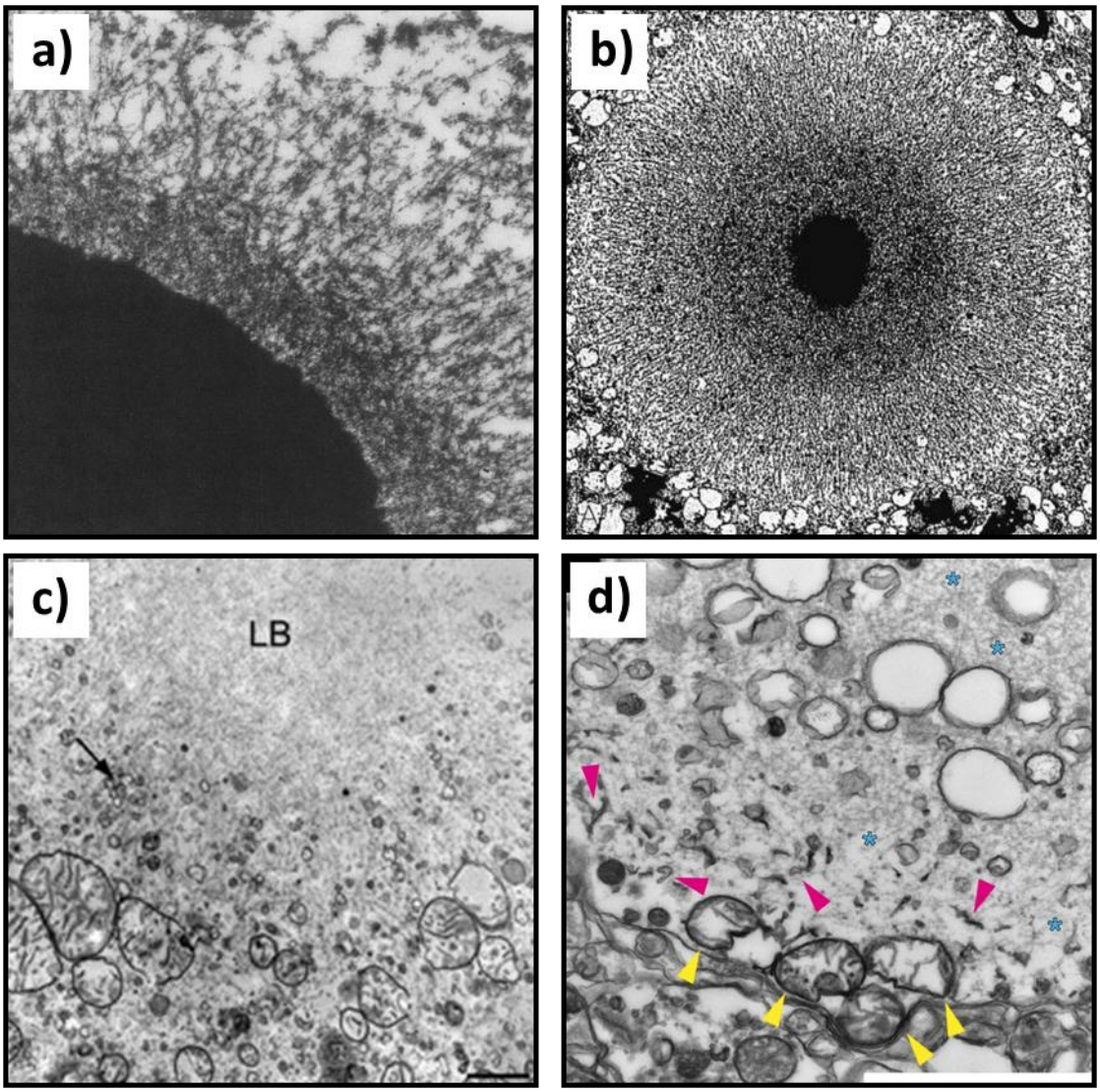

Figure 1.10: Electron microscopy of Lewy bodies.
Shown are differently scaled micrographs of Lewy bodies in PD patient neurons. a-c) Transmission electron microscopy showing a dense, aggregated core with radiating fibrils. Many small vesicles and mitochondria can be seen around the periphery of b) and c). d) Correlative light-electron microscopy showing a network of fibrils (blue asterisks) and large vesicular structures near the centre of the Lewy body. Small tubular vesicles (red arrowheads) and damaged mitochondria (yellow arrowheads) can be seen near the edges. a) Figure from Galloway et. al. 1992 [243], 23000x magnification. b) Figure from Forno 1996 [244], 6000x magnification. c) Figure from Soper et. al. 2008 [245], scale bar = 500 nm. d) Figure from Shahmoradian et. al. 2019 [242], scale bar = 2 µm.

Over time, small aggregates of α-synuclein are capable of escaping damaged neurons and pass into neighbouring healthy neurons to seed further aggregation [111, 246]. This transmission of α-synuclein eventually leads to more widespread Lewy body formation and neurodegeneration outside the substantia nigra, leading to symptoms of cognitive decline in the later stages as the pathology progresses into cortical regions of the brain [247]. At present, therapeutic intervention primarily

consists of using dopamine agonists to treat movement-related symptoms. However, these do not affect disease progression or cognitive impairment later in life.

In addition to α-synuclein, the composition of Lewy bodies has been shown to include: neurofilaments [248], fragmented membrane and vesicle lipids [242], ubiquitin ligases (parkin, dorfin and SIAH) [249-251], a de-ubiquitinase (UCH-L1) [252], and synphilin-1 [253, 254], a protein of unknown endogenous function shown to bind α-synuclein and also plays a role in inhibiting the ubiquitin ligases, thus disrupting Lewy body proteolysis [255, 256].

Lewy body-like pathology, and the associated PD symptoms of motor dysfunction, have been recapitulated by targeted expression of α-synuclein in the neurons of both rat [53] and fruit fly [52] animal models. Strengthening this association is the fact that many familial forms of PD are a direct result of point mutations within the gene encoding α-synuclein [68-70]. Gene duplication or triplication, increasing wild-type α-synuclein expression, also leads to late- or early-onset PD respectively [257, 258, 259]. This genetic link is further reinforced for sporadic PD by GWAS studies that identify high risk polymorphisms within the α-synuclein gene [74-76].

Despite the obvious involvement of ubiquitin-mediated proteolysis enzymes, which is a common occurrence for most protein inclusions, α-synuclein remains the primary component of Lewy bodies and its strongest genetic link. Therefore, the study of α-synuclein aggregation is a key element in understanding Lewy body formation, the effects of toxic aggregation products and Parkinson's disease progression as a whole.

1.8 α-Synuclein – Structure, Function and Disease Relevance

Small hydrophobic fragments of α-synuclein were originally discovered alongside amyloid-β (Aβ) in Alzheimer's disease plaques, where they were hypothesised to help seed Aβ aggregation. These "non-Aβ components" were sequenced and found to share the same precursor protein, termed the "non-Aβ component precursor" (NACP) [37]. Purification of NACP from human brain tissue led to the discovery of a second, homologous protein and the two were named α-synuclein and β-synuclein respectively [36].

Although discovered through its relation to Alzheimer's disease, α-synuclein would quickly be implicated in Parkinson's disease through genetic studies of inherited forms of the disease, identifying a dominant mutant alleles and duplications of the α-synuclein gene that correlated with early-onset forms of Parkinson's [68-70, 257-259]. Based on this finding, Lewy bodies from sporadic cases

of Parkinson's disease were stained positive with antibodies for α-synuclein, confirming it to be a major factor in the disease pathology [38, 240, 241].

α-synuclein is a 140 amino acid protein that is part of the synuclein family of small, highly charged proteins which are abundant in the central nervous system [36, 37]. It has been reported that as much as 1% of neuronal cytosolic protein is α-synuclein, the majority of which is localised to presynaptic termini [260]. The soluble structure of α-synuclein is mostly a disordered monomer [261, 262]. However, α-synuclein does fold in the presence of lipid membranes, forming an N-terminal broken amphipathic α-helix that lays across the membrane surface to facilitate binding (Figure 1.11) [245, 263-266].

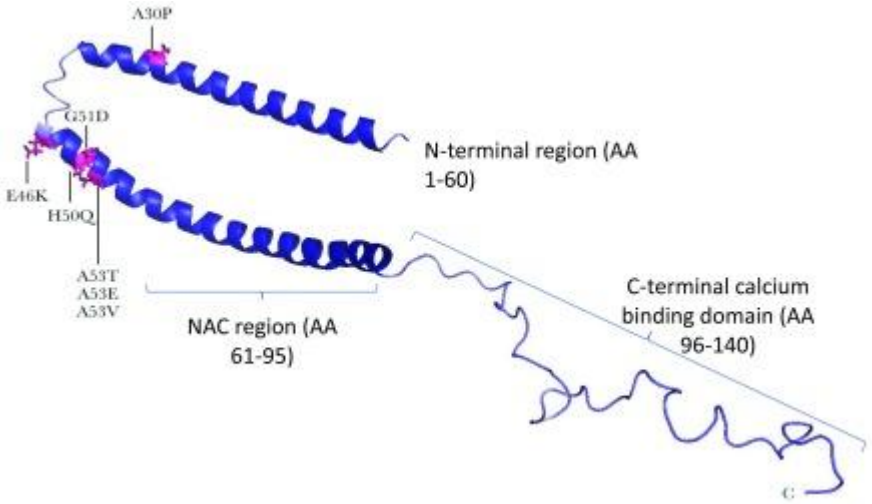

Figure 1.11: Membrane-bound structure of α-synuclein.
Structure of membrane-bound α-synuclein based on nuclear magnetic resonance measurements. The structure consists of a "broken" amphipathic α-helix between residues 1-95, with a flexible and disordered C-terminal region. Parkinson's disease missense mutations are highlighted. Figure from Whittaker et. al. 2017 [266].

Membrane binding of α-synuclein tends to favour membranes with high curvature and a negative charge [265, 267], consistent with that of presynaptic vesicles [263, 264]. Although the endogenous function of α-synuclein is still not precisely known, most evidence points towards a variety of neurotransmission-related roles including: clustering and maintaining a pool of synaptic vesicles at presynaptic termini [268, 269], membrane remodelling [270-273], interacting with dopamine and serotonin membrane transport proteins [274, 275], and neurotransmitter release from vesicles by promoting SNARE-complex formation [263, 264, 276, 277].

The pathogenic role of α-synuclein in Parkinson's disease is also somewhat unclear. The large fibrillar deposits of α-synuclein, which make up Lewy bodies, are not generally thought to be the main driver of neurodegeneration [278, 279]. Instead, smaller oligomeric assemblies, with high β-sheet structure, that are generated along the pathway to the final fibrillar structure, are most often perceived to be the primary toxic element [280-283]. Lewy bodies themselves, are mainly thought to sequester and deplete monomeric α-synuclein, leading to a loss of endogenous function [284]. Additionally, fibrils have been shown *in vitro* to dissociate into toxic oligomers, as part of a dynamic equilibrium [280], and therefore may also help to maintain the levels of toxic oligomer species within neurons.

The term "oligomer" in this context applies to a very wide range of assemblies. Many oligomers are generated *in vitro*, under different conditions, yielding different assemblies with various potentially toxic properties. Unfortunately, it is often challenging to assess which of these assemblies, often induced by somewhat non-physiological means, such as with agitation [285, 286], ethanol [287] or lyophilisation [288, 289], may actually exist in Parkinson's disease and cause a significant proportion of the pathology. Among the many reported effects of toxic α-synuclein oligomers, reviewed in Robert and Brown 2015 [278], one often cited mechanism of toxicity involves aggregation on membrane surfaces and subsequent membrane permeabilisation [285, 286, 290-292]. This results in mitochondrial dysfunction [286, 293] and release of reactive oxygen species [293], as well as destruction of transport vesicles [285].

Multiple sources of evidence have emerged that support mechanisms for membrane-mediated aggregation as one of the primary methods of α-synuclein toxicity. α-synuclein spontaneously oligomerises on membrane surfaces as part of its regular functions [272, 294]. These "healthy" oligomers are likely to be the starting point for misfolding and aggregation of the toxic forms *in vivo*, which go on to cause membrane rupture by destructive remodelling. Furthermore, all currently known familial missense mutations of α-synuclein that induce Parkinson's disease occur within the membrane binding helical regions [295], which are also known to enhance oligomerisation and fibrillisation [279, 296]. Damaged mitochondria and fragmented membranes are usually found in close proximity with Lewy bodies [242, 244, 245] and some structures of α-synuclein fibrils in Lewy bodies have also been shown to sequester lipids around them [297]. Finally, a recent drug trial, specifically targeting membrane binding of monomeric α-synuclein, has shown promise by recently extending its phase II clinical trials [109, 110].

The study of α-synuclein aggregation into both oligomers and fibrils, as with other neurodegenerative disease aggregating proteins, tends to focus on *in vitro* aggregates formed from monomer or seeded *ex vivo* using end-stage aggregates found in patient tissue. More recently, the

importance of membranes as surfaces for both catalysing nucleation and dictating the aggregate structure of α-synuclein in Parkinson's disease has been recognised. While *ex vivo* seeded aggregates can inform upon the final fibrillar structure of α-synuclein in the disease context, oligomers and early protofibrillar structures derived from membrane-mediated aggregation may prove to be disease-relevant species.

1.9 Membrane-Mediated Toxicity of α-Synuclein

The current literature surrounding α-synuclein's membrane-related mechanisms of toxicity can be classified into three broad categories: membrane permeabilisation and membrane remodelling, which both result in disruption of normal membrane functions; and vesicle clustering, where α-synuclein drags vesicles and other membranes together, resulting in loss of vesicle and organelle functions. These characteristics involve both monomeric and pre-formed oligomers of α-synuclein in the presence of negatively charged lipid membranes, and are expanded upon in this section.

Firstly, α-synuclein is thought to, in some way, permeabilise the membranes they bind to. This occurs either by embedding into a membrane and altering lipid packing, creating thin sections that allow otherwise impermeable particles to leak through [298-300], or by α-synuclein oligomers directly forming pore-like channels in a membrane surface [286, 290, 301].

Monomeric α-synuclein inserts into a bilayer via an N-terminal α-helix which lays across the membrane surface and embeds itself deeply, between the lipid head groups, which disrupts lipid packing and has been shown to cause thinning of both supported bilayers [298], and vesicles [273]. Many studies have explored adding pre-formed oligomers, generated through a variety of different methods, to bilayers or vesicles *in vitro* and observe permeabilisation [286, 291, 292, 301]. These oligomers are typically small annular structures and are often described as ellipsoid with high β-sheet content (Figure 1.12) [285, 290, 292].

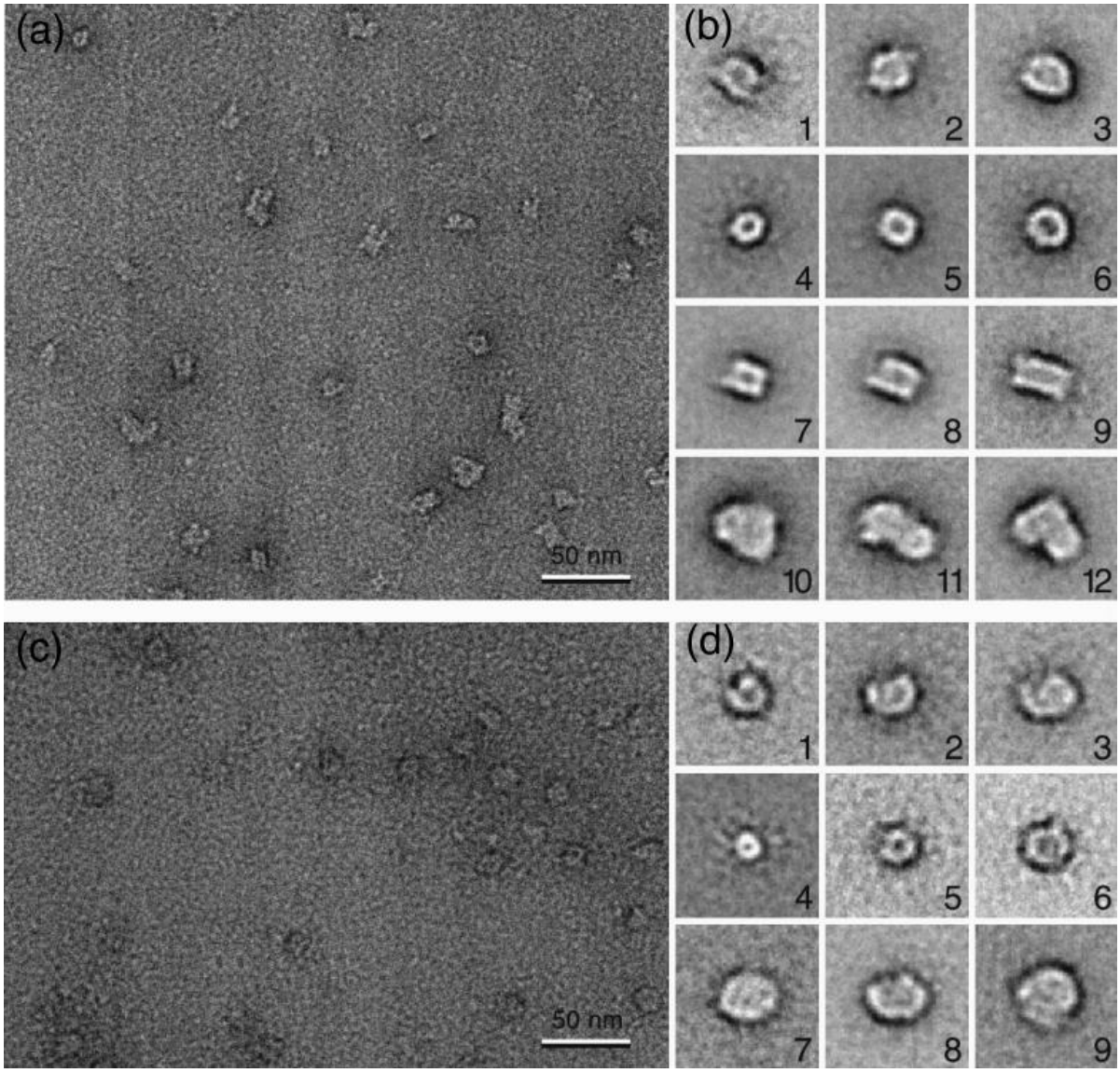

Figure 1.12: Electron microscopy of α-synuclein annular oligomers.
Negative-stain EM of size-exclusion chromatography purified oligomers, generated by lyophilisation of a-b) A53T and c-d) A30P mutants of α-synuclein. These ring-like oligomers display high β-sheet content by CD and are hypothesised to form pores in membranes. Figure from Lashuel et. al. 2002 [290].

These ring-like structures are soluble and create channels by simply embedding directly into the membrane [292, 301]. As previously stated, these oligomers are usually prepared by somewhat non-physiological means and it is therefore uncertain if these structures actually exist in the disease case. While most studies seem to support the embedding of these oligomers to form discrete pores within membranes [290-292, 301], some have also argued that pore-formation may not actually occur and that disruption of lipid packing is to blame for membrane permeability in these cases [299, 300, 302]. In both

cases, the type of lipid used affects permeability, with α-synuclein showing stronger binding to membranes with larger spacings between lipid headgroups [286].

Next is vesicle clustering, for which there is both *in vitro* and *in vivo* evidence. Single vesicle imaging and electron microscopy techniques have shown that negatively charged vesicles will spontaneously co-localise and fuse in the presence of α-synuclein monomer (Figure 1.13) [303, 304]. Overexpression of α-synuclein in yeast creates local clusters of vesicles [245] that are reminiscent of the lipid aggregation in Lewy bodies [242, 244, 245]. Extensive work by Fusco et. al. 2016 has provided a model for vesicle clustering by monomeric α-synuclein, in which the protein is able to bind to two vesicles simultaneously and anchor them together (Figure 1.14) [305]. Clustering of pre-synaptic vesicles is an endogenous function of α-synuclein [268, 269]. However, in the disease form overexpression, changes in cytosolic conditions or regulatory malfunction may lead to aberrant clustering of many other membranes, resulting in the large number of vesicles and organelles trapped within Lewy bodies [242, 244, 245].

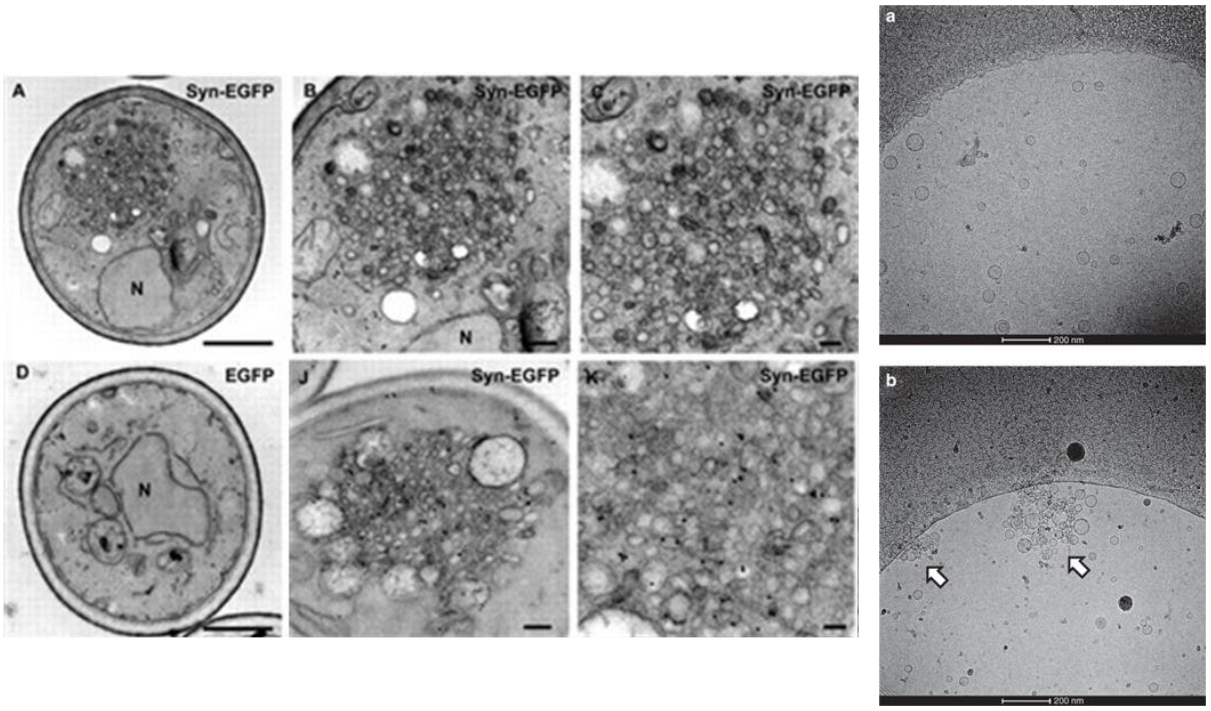

Figure 1.13: Electron microscopy of vesicle clustering by α-synuclein.
(Left) Yeast cells overexpressing either D) EGFP or A-C, J-K) an α-synuclein-EGFP fusion protein. A-C) A dense accumulation of vesicles caused by α-synuclein-EGFP expression. J-K) Immuno-EM using a polyclonal antibody for α-synuclein tagged with gold nanoparticles (black dots) shows localisation within vesicle clusters. A, D) Scale bars = 500 nm. B, J) Scale bars = 100 nm. C, K) Scale bars = 50 nm. Figures from Soper et. al. 2008 [245]. (Right) TEM of α-synuclein and lipid at a 500:1 L:P ratio with either a) DOPC and b) DOPS:DOPC (12%:88% ratio). Vesicle clustering can be observed when a negatively charged lipid is included in the vesicles (DOPS). Scale bars = 200 nm. Figure from Cai et. al. 2020 [304].

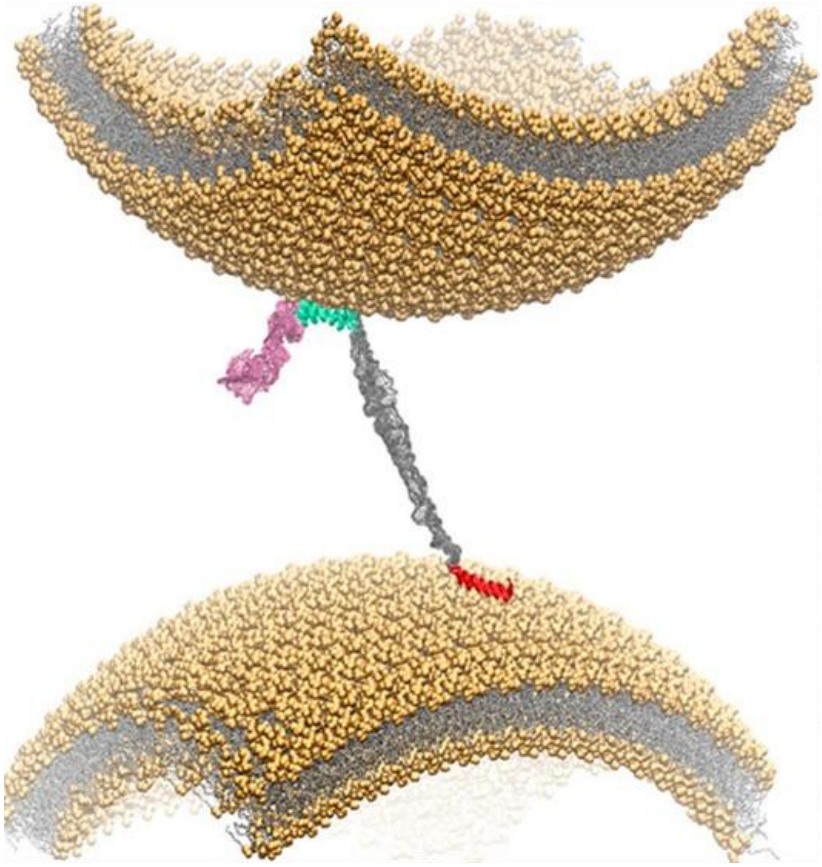

Figure 1.14: The double-anchor mechanism of vesicle clustering by α-synuclein.
A molecular model of 50 nm diameter vesicles anchored by a single α-synuclein monomer, containing two amphipathic helices at residues 1-25 (red) and 65-97 (cyan). The C-terminal is shown in pink. The linker between both helices is shown in grey. The maximum distance between anchored vesicles is 150 Å using this model. Figure from Fusco et. al. 2016 [305].

Finally, there is a growing body of literature on the remodelling of large membranes and vesicles by α-synuclein, which could imply an alternative mechanism for destruction of vesicles and organelles in Parkinson's disease neurons. Monomeric α-synuclein incubated with lipids will often spontaneously form either lipid-protein nanodisc particles [271, 306, 307] or large tubular assemblies, which are either bilayer tubes [270, 271, 308] or cylindrical micelles [271, 307, 308] (Figure 1.15). Unlike other mechanisms of membrane disruption, membrane remodelling is not necessarily limited to negatively charged membranes, as one study found that α-synuclein was also able to remodel vesicles of POPC a neutral lipid [270]. This is especially interesting considering that POPC makes up roughly 50% of neuronal cell lipids [309]. However, there is conflicting evidence against the remodelling of POPC by α-synuclein [308].

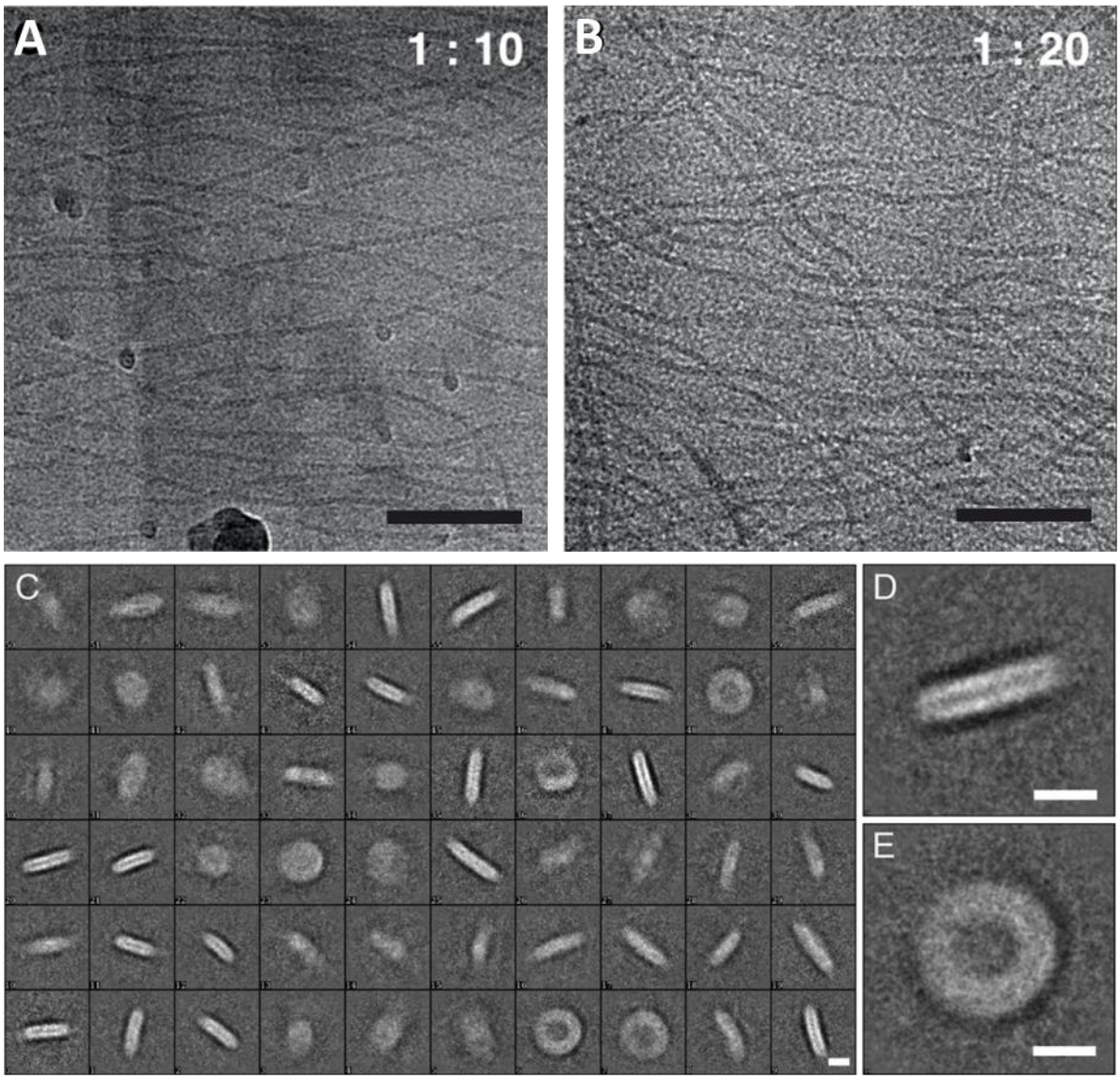

Figure 1.15: Representative Cryo-EM of lipoprotein particles of α-synuclein.
A) 1:10 and B) 1:20 molar ratios of α-synuclein:POPG, showing the presence of cylindrical micelles. C-E) 2D-classification of nanodisc particles from a preparation of α-synuclein and DOPS after size-exclusion chromatography. A-B) Scale bars = 100 nm. Figures from Mizuno et. al. 2012 [271]. C-E) Scale bars = 10 nm. Figures from Eichmann et. al. 2016 [306].

The type of lipoprotein structure that forms is a result of the lipid used and the lipid:protein ratio (L:P), with lower L:Ps favouring nanodiscs and high L:Ps favouring bilayers, with cylindrical micelles in between [271, 308]. These structures form rapidly and secondary structural analysis confirms high α-helical content, which shows α-synuclein to remain monomeric or be part of non-β sheet oligomers [294, 306, 307]. Coarse-grained molecular dynamics, by Braun et. al. 2014 [272], predicts that α-synuclein binding imposes a positive curvature upon membranes surfaces. This local curvature then recruits additional monomers to the surface, forming a ring of associated α-helices, that tubulates the

membrane (Figure 1.16) [272]. Tubulation of vesicles into bilayer tubes and cylindrical micelles has also been directly observed by microscopy techniques (Figure 1.17) [273, 308] and by X-ray/Neutron scattering [307].

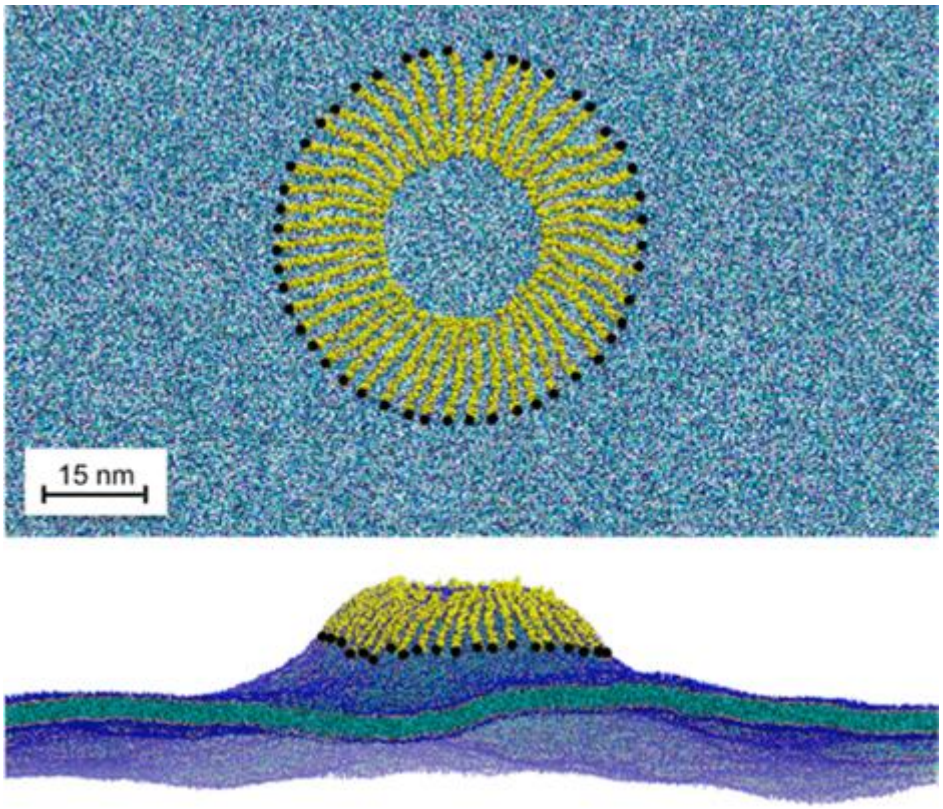

Figure 1.16: Molecular Dynamics Simulation of Membrane Remodelling by α-synuclein.
Coarse-grain model of 48 α-synuclein proteins (residues 1-100 only) (yellow) induce membrane curvature to form a budding tubule on a POPG lipid bilayer (blue). Figure from Braun et. al. 2014 [272].

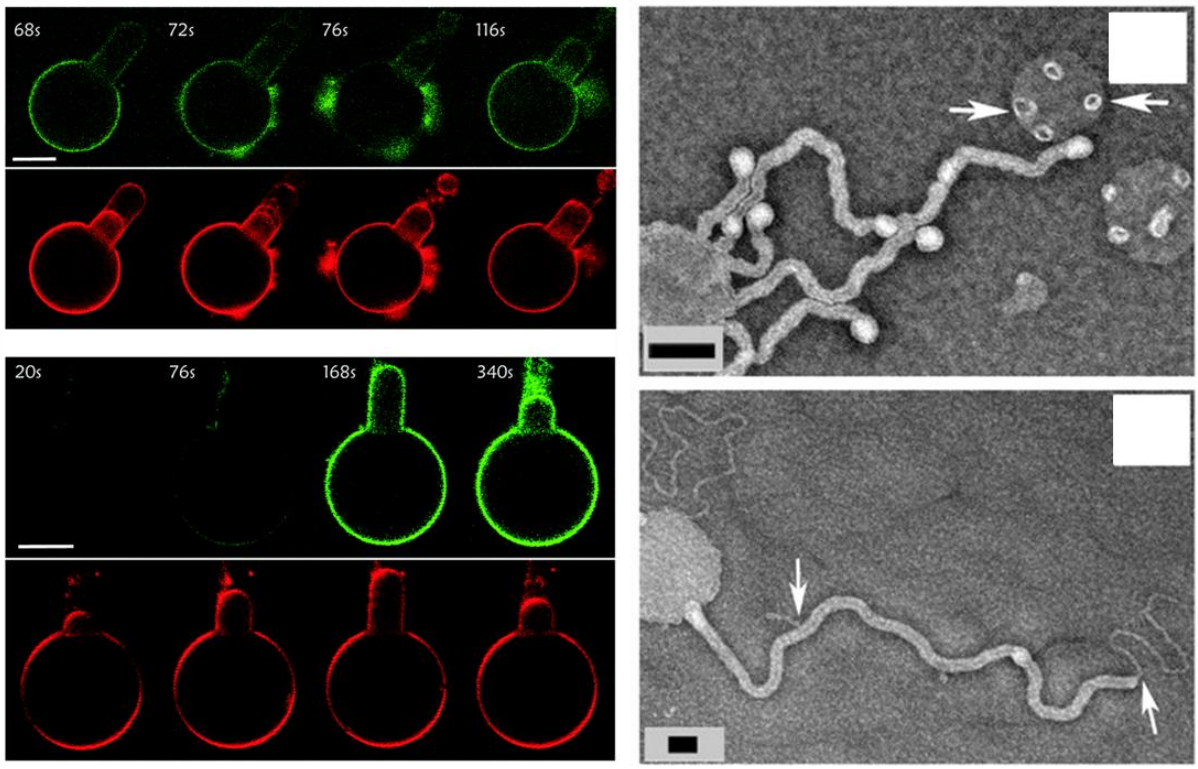

Figure 1.17: Tubulation of vesicles visualised by microscopy.
(Left) Timelapse confocal microscopy of giant DOPS lipid vesicles, tracked by red fluorescence, undergoing tubulation and fragmentation by α-synuclein, tracked by green fluorescence. Figure from Shi et. al. 2015 [273]. (Right) Electron microscopy showing vesicle tubulation. (Top right) POPG/POPC (1:1 molar ratio) incubated with α-synuclein at a 20:1 L:P ratio. Arrows indicate budding on a vesicle. (Bottom right) POPG/POPC (1:4 molar ratio) incubated with α-synuclein at a 10:1 L:P ratio. Arrows show a bilayer tube that is further extruded into a cylindrical micelle. Scale bars are 100 nm. Figure from Varkey et. al. 2010 [308].

Mizuno et. al. 2012 generated a series of α-synuclein cysteine mutants for single-residue labelling with either fluorescent or spin-label tags [271]. These labels allowed them to determine which residues of membrane-bound α-synuclein were embedded or exposed to solvent, via changes in fluorescence intensity or electron paramagnetic resonance. Their results suggested that α-synuclein forms full-length α-helices, rather than two separate helical regions, which stabilise cylindrical micelles and nanodisc structures by embedding almost completely between lipid headgroups (Figure 1.18) [271].

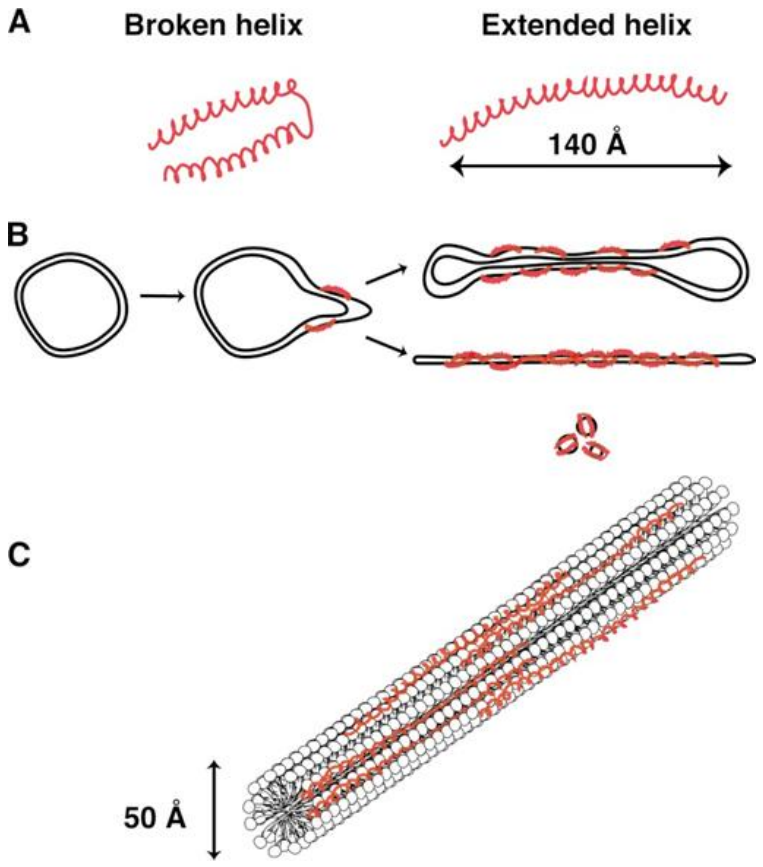

Figure 1.18: Model of α-synuclein lipoprotein particles.
A) Comparison of the regular membrane-bound "Broken helix" structure, with an inferred vesicle remodelling "Extended helix" structure that spans the full length of the protein. B) Schematic of vesicle remodelling, with α-synuclein binding initiating tubulation and eventually forming compact nanodiscs (top) or cylindrical micelles (bottom). C) Cylindrical micelles are predicted to be stabilised by extended helix α-synuclein, embedding parallel along the length of tubes, and is somewhat randomly distributed. Figure from Mizuno et. al. 2012 [271].

Furthermore, aggregation of α-synuclein on the surface of fixed bilayers has been shown to remove lipids from the surface and incorporate them into large aggregates that eventually become fibrillar amyloids [310]. Meanwhile, aggregates formed by vesicle preparations of α-synuclein were structurally characterised and shown to form amyloids with incorporated lipids that shield exposed hydrophobic regions of the fibre from solvent (Figure 1.19 and 1.20) [297, 311]. This leaching of lipids from membrane structures into aggregates is clearly destructive and thought to be another mechanism by which Lewy bodies incorporate lipids during disease.

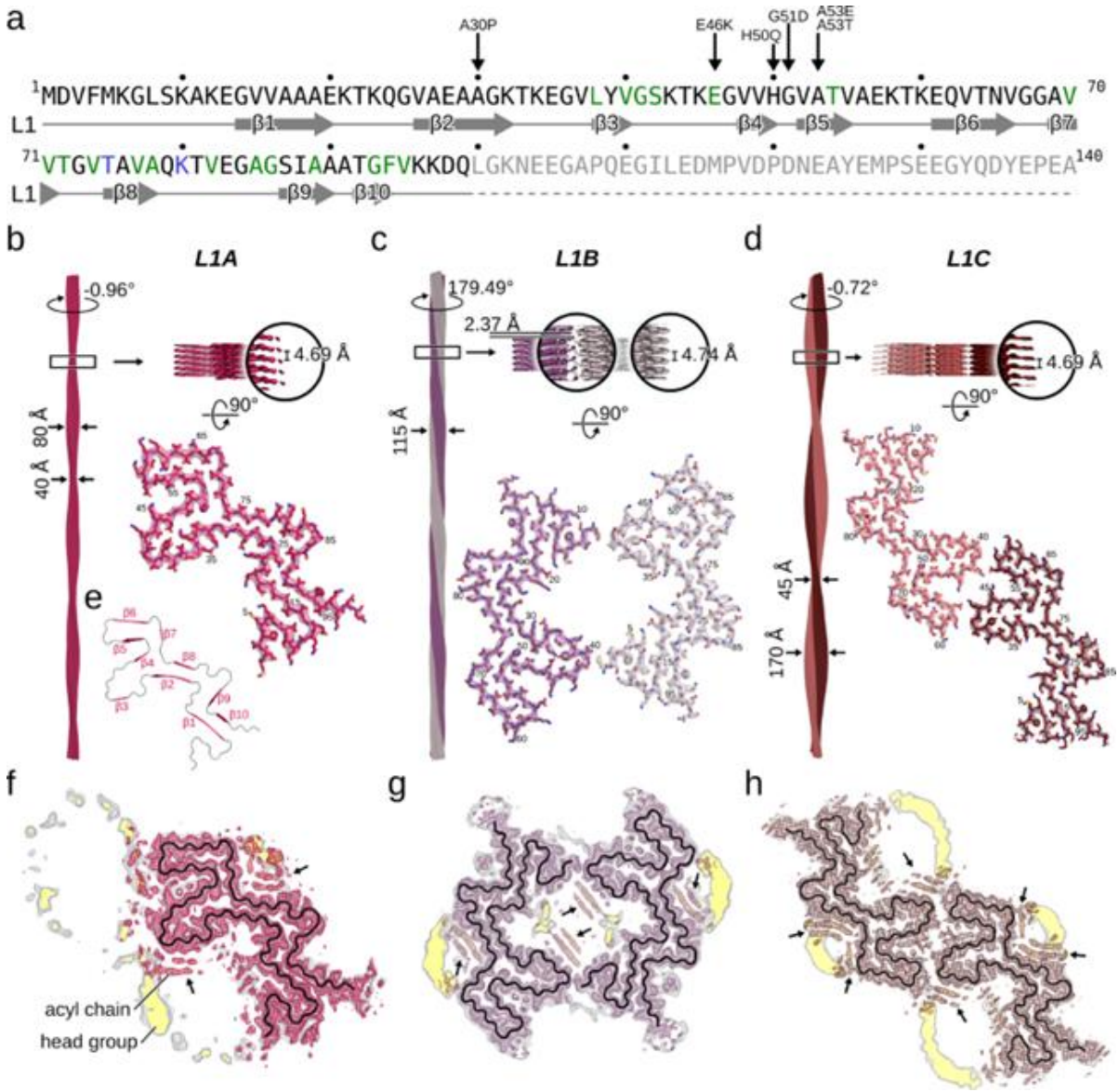

Figure 1.19: Structures of lipidic amyloids of α-synuclein.
a) The sequence and secondary structural fold of α-synuclein, with familial PD mutations highlighted. Residues binding to lipid acyl groups (green) and choline groups (blue) are highlighted. b-d) Cryo-EM structures of α-synuclein amyloid fibrils which each share the same secondary structure, labelled 'L1'. f-h) The electron density map for each fibril, with the protein backbone overlaid in black and densities attributed to lipids shown in yellow. Figure from Frieg et. al. 2022 [297].

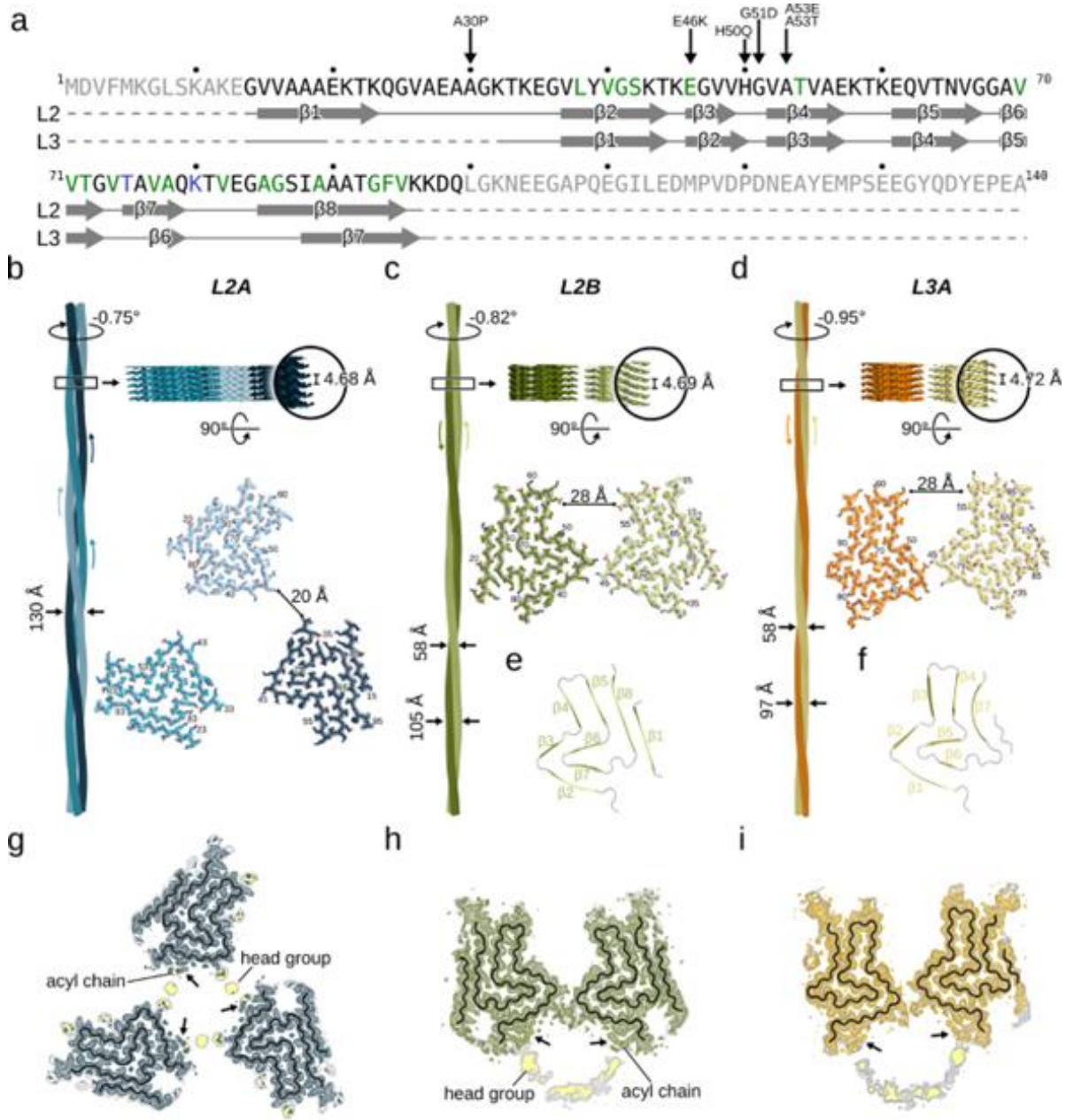

Figure 1.20: Structures of lipidic amyloids of α-synuclein.
a) The sequence and secondary structural folds of α-synuclein amyloid fibrils, with familial PD mutations highlighted. Residues binding to lipid acyl groups (green) and choline groups (blue) are highlighted. b-d) Cryo-EM structures of amyloid fibrils. The fibrils labelled 'L2A' and 'L2B' share the same secondary structure, labelled 'L2'. f-h) The electron density map for each fibril, with the protein backbone overlaid in black and densities attributed to lipids shown in yellow. Figure from Frieg et. al. 2022 [297].

There is a wide range of potential mechanisms by which α-synuclein may disrupt membranes, making it tough to determine which of these is likely to have pathological effects inside Parkinson's disease neurons. In this case, we chose to replicate a model *in vitro* system of α-synuclein incubated with POPG vesicles, which was used to design a drug molecule for Parkinson's disease currently in

phase II clinical trials [109, 110]. The main feature of this small molecule, minzasolmin, is to bind α-synuclein and interfere with its membrane binding capabilities [110]. The success of this therapeutic approach, so far, lends credence to the *in vitro* model's disease relevance. Here we expand upon previous work by P.J. Davis (unpublished) in optimising α-synuclein oligomer production and separation, in the presence of POPG vesicles, and attempt to structurally characterise potentially relevant steps of aggregation in Parkinson's disease.

Chapter 2: Materials and Methods

2.1 Buffers and Reagents

All reagents were Fisher Scientific (USA) or Sigma-Aldrich (DE) unless otherwise stated. Buffers were made using type 1 ultrapure water from a Purelab 611 Classic UVF dispenser (ELGA LabWater, UK). Buffer pHs were verified using a benchtop pH meter and, when necessary, adjusted to the correct pH with HCl or NaOH. Buffers were vacuum filtered through 0.2 µm pore size membrane filters (Whatman, UK). 1 mM sodium azide (NaN_3) was added to all buffers, except those used for cell growth.

Commonly referenced buffers:

- hCC working buffer (50 mM $NaPO_4$, pH 7.4)
- α-Syn working buffer (20 mM $NaPO_4$, pH 7.1)
- α-Syn resuspension buffer (20 mM Tris-HCl, pH 8.0)

2.2 Growth Media and Stock Solutions

Luria-Bertani Media (LB):

Per litre of water

- 10 g Tryptone
- 5 g Yeast Extract
- 10 g NaCl

LB solutions were sterilised by autoclaving, followed by addition of required antibiotics after cooling.

LB-Agar:

LB solution was made with the addition of Agar powder (15 g/L) and sterilised by autoclaving. Required antibiotics were added after cooling to less than 40 ^oC, after which the LB-Agar was cast in petri dishes and left to solidify under sterile conditions before storage at 4 ^oC. Plates were used for transformations generally on the same day and no more than 1 week after casting.

M9 Minimal Media:

Per litre of water:

- 6 g Na_2HPO_4
- 3 g KH_2PO_4
- 0.5 g NaCl

This solution was adjusted to pH 7.4 before sterilisation by autoclaving.

The following is added to the autoclaved media immediately before use (per litre):

- 650 µL trace elements (autoclaved)
- 2 g glucose
- 100 µL thiamine (10 mg/mL) (filter sterilised)
- 2 mL $(NH_4)_2SO_4$ (0.5 mg/mL) (filter sterilised)
- 1 mL $MgSO_4$ (1 M) (autoclaved)
- 100 µL $CaCl_2$ (1 M) (autoclaved)

The $CaCl_2$ was always added last with vigorous swirling to avoid precipitation.

Trace Elements:

Per 100mL of water:

- 550 mg $CaCl_2.2H_2O$
- 140 mg $MnSO_4.H_2O$
- 40 mg $CuSO_4.5H_2O$
- 220 mg $ZnSO_4.H_2O$
- 45 mg $CoCl_2.6H_2O$
- 26 mg $Na_2MoO_4.2H_2O$
- 40 mg H_3Bo_4
- 26 mg KI

The above solution was made up to 70 mL and pH adjusted to 8.0 before adding:

- 500 mg EDTA

This was pH adjusted again to 8.0 before adding:

- 375 mg $FeSO_4.7H_2O$

The solution was then made up to 100 mL and sterilised by autoclaving.

MDAG-135 Minimal Media:

The following is a recipe adapted from Studier (2005) [312]. The only change is the use of soy-based tryptone instead of individually adding each amino acid.

Per litre of water:

- 3.55 g Na_2HPO_4
- 3.40 g KH_2PO_4
- 2.67 g NH_4Cl
- 0.71 g Na_2SO_4

This solution is adjusted to pH 7.4 and autoclaved before the following additions:

- 3.5 g glucose
- 1 g aspartic acid
- 10 g soy-based tryptone
- 2 mL $MgSO_4$ (1 M) (autoclaved)
- 200 µL 1000x WFS trace elements

Antibiotic was added at this stage and media was used immediately.

1000x WFS trace elements:

The following is an adapted recipe from Studier (2005) [312], with the exception of Na_2SeO_3, which was not able to be sourced.

Per 100mL of water:

- 20 mL $FeCl_3$ (0.25 M) in 0.3 M HCl (filter sterilised)
- 2 mL $CaCl_2$ (1 M)
- 1 mL $MnCl_2$ (1 M)
- 1 mL $ZnCl_2$ (1 M)
- 1 mL $CoCl_2$ (0.2 M)
- 2 mL $CuCl_2$ (0.1 M)
- 1 mL $NiSO_4$ (0.2 M)
- 2 mL Na_2MoO_4 (0.1 M)
- 2 mL H_3BO_4 (0.1 M)

Except $FeCl_3$, all component stock solutions were autoclaved prior to addition. This solution was made up under sterile conditions to prevent contamination.

Isopropyl-β-D-galactosidase (IPTG):

120 mg/mL IPTG was dissolved in type 1 water to produce a 1 M stock solution. This was then filter sterilised through a 0.2 µm filter. Aliquots of 1 M IPTG stock were stored at -20 °C and thawed before use.

Antibiotic solutions:

All antibiotic solutions were stored in 1000x concentration aliquots at -20 °C and gently thawed before use. All stocks were made by dissolving a powered antibiotic salt in type 1 water, with the exception of chloramphenicol, which was dissolved in 100% ethanol.

List of antibiotics, their working concentrations and use cases:

- Ampicillin (100 µg/mL)
    - pET22b-pelB-hCC
    - pINIII-ompA-hCC
    - pJONEX4-pelB-hCC
    - pET32a-TrxA-hCC
- Carbenicillin (100 µg/mL)
    - Used as a more thermostable alternative to ampicillin
- Kanamycin (50 µg/mL)
    - pACGFPN1-hCC
    - Origami *E.coli* strain
    - pET28a-αSyn (at 34 µg/mL kanamycin)
- Chloramphenicol (20 µg/mL)
    - pSigP
    - Origami *E.coli* strain

2.3 General Data Handling Software

Data handling, outside of specifically mentioned software, was performed in Microsoft Excel 2019 and GraphPad Prism 9 and 10 (graphpad.com). ImageJ (imagej.net), with the Fiji package installed, was used to process, add scale bars and make figures from microscopy images.

The use of screenshots for purification graphs in Chapter 3 was an unfortunately necessity, due to a technical error at the time of writing which restricted access to the raw data files.

2.4 Protein Expression and Purification

2.4.1 Preparation of Competent Cells

E.coli strain BL21-DE3 or XL10-GOLD (Kan^r) was thawed on ice and streaked onto LB agar plates using a sterile loop and incubated at 37 °C overnight. Single colonies were picked and used to inoculate 10 ml LB broth starter cultures and incubated at 37 °C, 180 rpm shaking overnight. Starter cultures were then added to 50 ml LB broth in 250ml conical flasks and incubated 37 °C, 180 rpm shaking until an OD_{600} of 0.5 was reached.

Cultures were then transferred to sterile 50ml Falcon tubes and incubated on ice for 15 minutes. Cells were pelleted by centrifugation at 3000xg for 10 minutes at 4 °C and the supernatant was discarded. Pellets were resuspended in 15 ml of pre-chilled competency buffer (100 mM RbCl, 50 mM $MnCl_2$, 30 mM CH_3COOK, 10 mM $CaCl_2$ and 15% (v/v) glycerol, pH 5.8) and incubated on ice for at least 30 minutes.

Finally, cells were pelleted by centrifugation at 3000xg for 10 mins at 4 °C and the supernatant was discarded. Pellets were resuspended in 4 ml of pre-chilled storage buffer (10 mM MOPS, 75 mM $CaCl_2$, 10 mM RbCl, 15% (v/v) glycerol. Competent cells were separated into 200 µl aliquots in sterile cryovials then flash-frozen in liquid nitrogen before storage at -70 °C.

2.4.2 Cell Transformations

Competent cell aliquots were thawed on ice before 1 µl plasmid per 200 µl aliquot was added. After a 30-minute incubation on ice, cells were heat shocked for 90 seconds at 42 °C, then placed on ice for 2 minutes. 800 µl of pre-chilled LB broth was added and cells were incubated at 37 °C for 1 hour before plating 120 µL on LB agar, with a plasmid-selective antibiotic, and incubated at 37 °C overnight.

2.4.3 Plasmid Replication

Replication of all plasmid stocks was carried out in *E.coli* strain XL10-GOLD (Kan^r) (Agilent Technologies), except in the case of pAcGFPN1 derived vectors, which were replicated in a DH5α strain. Single transformed colonies were grown overnight in 5-10 mL LB at 37 °C. Plasmids were extracted using the Monarch® Plasmid Miniprep Kit (New England Biolabs) according to the

manufacturer's protocol and eluted in ultrapure water. Plasmid concentration was quantified by UV absorbance (Thermo Scientific NanoDrop One) and stored at -20 °C.

2.4.4 Growth and Expression of Cystatin C in *E.coli*

Cystatin C that was used for aggregation experiments was expressed in *E.coli* strain BL21-DE3, containing either the pET22b-pelB-hCC or pINIII-OmpA-hCC plasmids.

Single transformed colonies were picked from agar plates and used to inoculate 25 mL LB starter cultures at 37 °C, 180 rpm shaking overnight. 6 mL of starter culture was used to inoculate each 600 mL culture of M9 minimal media in baffled flasks, incubated at 37 °C, 180-220 rpm shaking.

The OD_{600} of each culture was periodically checked until it reached between 0.6-0.8, after which expression of hCC was initiated by addition of 0.5 mM IPTG. Cultures were then additionally grown for either 2-4 hours at 42 °C or overnight at 18 °C before harvesting. Cells were pelleted by centrifugation at 46,254 g for 15 minutes at 4 °C, then stored at -20 °C.

2.4.5 Purification of Cystatin C from Cell Pellet

Method 1:

Purification of hCC by this method was carried out by Dr. Svetlana Sedelnikova using the following protocol.

Cell pellets were resuspended in 50 mL 50 mM MES-NaOH, pH 6.2 supplemented with protease inhibitor (Pierce, Thermofisher) and sonicated on ice for 4x20 second cycles using a medium probe at 18 microne amplitude on a Soniprep150 machine. Cell debris was removed by centrifugation at 70000 g for 15 minutes.

Cell free extract was applied on 2x5 mL HiTrap SP-HP columns (Cytiva), at a flow rate of 5 mL/min. Elution was performed using a gradient of NaCl concentration from 0 to 0.5 M in the same buffer. Fractions containing the sample were identified by SDS-PAGE, combined and concentrated in a 5kDa MWCO polyethersulfone centrifugal concentrator (Sartorius Vivaspin® 20, VS2011).

Combined fractions were then applied on a HiLoad 16/600 Superdex 200 (Cytiva) gel filtration column, at a flow rate of 1.5 mL/min, with a running buffer of 50 mM Tris-HCl, pH 8.0, 0.5 M NaCl. Fractions were collected and assessed by SDS-PAGE. Purified hCC fractions were exchanged into hCC working buffer and concentrated again using a centrifugal concentrator, then stored in aliquots at 4 °C.

Method 2:

Cell pellets were resuspended in 50 mL 20 mM $NaPO_4$, pH 8.0, supplemented with protease inhibitor (Pierce, Thermofisher or Roche Diagnostics) and sonicated on ice for 6x30 second cycles at 40% power by a Fisherbrand 505 sonicator (20 kHz) with a 12 mm probe. Cell debris was removed by centrifugation at 46,254 g for 15 minutes.

Cell-free extract was treated for nucleic acids by addition of 2 mM $MgSO_4$ and 25 units/mL Benzonase endonuclease (Millipore), incubated at 37 °C for 30 minutes. Digested nucleic acids were removed by flowing the sample through 2x5 mL HiTrap Q-HP columns (Cytiva), at a flow rate of 5 mL/min and collecting the unbound fraction. This fraction was then pH adjusted to pH 6.0 with HCl.

The unbound fraction was applied on a 2x5 mL HiTrap SP-HP columns (Cytiva), at a flow rate of 5 mL/min, with a running buffer of 30 mM MES, pH 6.2. Elution was performed using a gradient of NaCl concentration from 0 to 0.5 M in the same buffer. Fractions containing the sample were identified by SDS-PAGE, combined and concentrated in a 5 kDa MWCO regenerated cellulose centrifugal concentrator (Sartorius Vivaspin® 15R, VS15RH12).

Combined fractions were then applied on a HiLoad 16/600 Superdex 75 (Cytiva) gel filtration column, at a flow rate of 1.0 mL/min, with a running buffer of 50 mM Tris-HCl, pH 8.0, 0.5 M NaCl. Fractions were collected and assessed by SDS-PAGE. Purified hCC fractions were exchanged into hCC working buffer and concentrated again using a centrifugal concentrator, then stored in aliquots at 4 °C.

2.4.6 SDS Polyacrylamide Gel Electrophoresis

All electrophoresis was carried out using a Bio-Rad Mini Protean II apparatus.

SDS-PAGE Buffers:

4x Upper Buffer – 0.5 M Tris-HCl, pH 6.8, 0.4% (w/v) SDS

4x Lower Buffer – 1.5 M Tris-HCl, pH 8.8, 0.4% (w/v) SDS

Running Buffer – 25 mM Tris-HCl, pH 8.3, 190 mM Glycine, 0.1% (w/v) SDS

4x Loading Buffer – 200 mM Tris-HCl, pH 6.3, 400 mM DTT, 8% (w/v) SDS, 0.4% (w/v) bromophenol blue, 60% (v/v) glycerol

Stain – 45% (v/v) methanol, 10% (v/v) acetic acid, 0.25% (w/v) Coomassie Brilliant Blue R250

Destain – 45% (v/v) methanol, 10% (v/v) acetic acid

Commercial stains: Instant Blue (Expedeon), ReadyBlue (Sigma-Aldrich), InstantBlue (Abcam), SimplyBlue (Invitrogen), QuickBlue (BDL)

Gel Casting:

4.8% polyacrylamide stacking gels were cast above 16% polyacrylamide resolving gels using the following recipes (per gel):

16% Resolving gel:

- 2.5 mL 4x Lower Buffer
- 4 mL 40% acrylamide (37.5:1 acrylamide:bisacrylamide ratio) (Serva)
- 3.5 mL H_2O
- Mixed with gentle inversion before and after adding:
    - 100 µL 10% (w/v) ammonium persulphate (APS)
    - 10 µL N, N, N', N'-tetramethylethylenediamine (TEMED) (VWR)

4.8% Stacking gel:

- 1.25 mL 4x Upper Buffer
- 0.6 mL 40% acrylamide (37.5:1 acrylamide:bisacrylamide ratio) (Serva)
- 3.15 mL H_2O
- Mixed with gentle inversion before and after adding:
    - 55 µL 10% (w/v) ammonium persulphate (APS)
    - 5.5 µL N, N, N', N'-tetramethylethylenediamine (TEMED) (VWR)

Samples were prepared at a 3:1 ratio with 4x loading buffer and 8-15 µL were loaded depending on sample concentration. Samples were not heated prior to loading as this was not required to see either protein. Gels were run in running buffer at 180-220 V until the bromophenol dye band reached the end of the gel.

Generally, gels were stained using a commercial stain on a rotating platform overnight, then rinsed with water. Occasionally, gels were stained for 1 hour with Coomassie stain, followed by destain until clear, then rehydrated in water.

2.4.7 Determination of Protein Concentration

Measurements of protein UV absorption at 280 nm were made using a NanoDrop One (Thermo Scientific). Concentrations were calculated using the Beer-Lambert Law:

$$A = \varepsilon . l . c$$

Where 'A' is the absorbance, c is the concentration (M), 'ε' is the molar extinction coefficient ($M^{-1}cm^{-1}$) and 'l' is the pathlength (cm). Molar extinction coefficients of each protein are: hCC (ε = 11100 $M^{-1}cm^{-1}$); α-synuclein (5960 $M^{-1}cm^{-1}$).

2.5 Cystatin C *in vitro* Methods

2.5.1 Yeast RNA Extract Solvation

Whole yeast RNA extract (Sigma Aldrich, prod. code, 10109223001) was measured out to the desired concentration and dissolved in hCC working buffer. RNA was added in small amounts and the resulting solid aggregates were broken up mechanically using a magnetic stirrer at high speed. The solution pH was periodically measured and NaOH was added to maintain above pH 7. Once all RNA had dissolved, NaOH or HCl was used to alter the pH back to pH 7.4.

2.5.2 Cystatin C Aggregation Screening

hCC was added to solutions containing desired amounts of DTT, NaCl or RNA in hCC working buffer in clear 1st hydrolytic class glass vials (Postnova, prod. code: Z-VIA-11090500). Solutions were incubated overnight at lab temperature (18-20 °C) and then assessed for aggregation by eye or quantified using 500 nm wavelength 90° light-scattering measurements in a Varian Cary Eclipse Fluorescence Spectrophotometer (Agilent Technologies). Aggregated samples were shaken by hand to form a suspension before pipetting for downstream microscopy imaging.

2.5.3 Differential Interference Contrast (DIC) Microscopy

DIC microscopy is an optical microscopy technique, which emphasises regions of higher or lower sample density. Split polarised light enters the sample at two separate points, which is then recombined after passing through the sample. Any interference caused during recombination is the

result of differences in optical path length travelled by each beam, which is affected by the refractive index of the sample at relevant points.

Samples were pipetted onto glass slides and sealed with a coverslip. DIC was performed on an Eclipse Ti-E Widefield Microscope (Nikon), with images taken using a Zyla sCMOS camera (ANDOR). The system was controlled using the NIS Elements software (Nikon).

2.5.4 ^{1}H-NMR Titration of Cystatin C with DTT

Unlabelled hCC was expressed and purified using method 1 (Section 2.4.5). Samples for NMR each included 10% D_2O and 5mM TSP (Trimethylsilylpropanoic acid). NMR spectra were recorded using a 500 MHz Bruker Avance II 3-channel liquid-state spectrophotometer with a 5 mm TXI probe and 5mm BBO operated using the Topspin 4 software (Bruker). Following each addition of DTT, the system was fully recalibrated before spectra were recorded. Figures showing overlaid spectra were made using Topspin 4.

2.5.5 2D-NMR Titration of Cystatin C with RNA

^{15}N-labelled hCC was expressed in ^{15}N-labelled M9 media and purified using method 1 (Section 2.4.5). Samples for NMR each included 10% D_2O and 5 mM TSP (Trimethylsilylpropanoic acid). Additions of RNA to the sample included 10% D2O and 5 mM TSP so as not to dilute any of these concentrations in the final sample.

NMR spectra were recorded using an 800 MHz Bruker Neo 4-channel liquid-state spectrometer with a high sensitivity TCI cryoprobe operated using the Topspin 4 software (Bruker). Following each addition of RNA, the system was fully recalibrated before spectra were recorded. 2D HSQC measurements were captured using the following parameters: ^{1}H increments = 1024, ^{15}N increments = 128, 16 scans, 8 dummy scans, ^{1}H spectral width of 12.5 ppm, ^{15}N spectral width of 36 ppm.

HSQC spectral peaks were mapped using a previously assigned spectrum of cystatin C [313] in CCPNmr (ccpn.ac.uk). Weighting of changes in ^{15}N (δ^2_N) and ^{1}H (δ^2_H) chemical shifts into combined shifts (δ^2_{HN}) was calculated according to the following equation from Williamson (2013) [314]:

$$\delta^2{}_{HN} = \sqrt{\frac{1}{2}[\delta^2{}_H + (\alpha \,.\, \delta^2{}_N)]}$$

Where 'α' is a scaling factor that is calculated as the ratio between the range of peak shifts in the ^{1}H dimension and the range of peak shifts in the ^{15}N dimension:

$$\alpha = \frac{\delta_{H(max)} - \delta_{H(min)}}{\delta_{N(max)} - \delta_{N(min)}}$$

Combined shifts were then mapped onto 3D structures of cystatin C monomer and dimer, and figures produced using PyMOL 2.4 (pymol.org).

2.5.6 DIC Microscopy Timelapse of Cystatin C, PEG and DTT

Individual PEG and DTT conditions were each made up in a 96-well quartz microplate and hCC was added to relevant wells as quickly as possible to start the aggregation process. The timelapse was set up using the NIS Elements software (Nikon) to automatically control the stage and take DIC microscopy images at a pre-defined location in each well, every 2 hours. The initial dead-time between adding hCC and setting up the timelapse was 1.33 hours and the final images were recorded at 19.33 hours after hCC addition.

2.5.7 Computational Analysis of DIC Microscopy Timelapse

Timelapse microscopy images of cystatin C aggregation in PEG and DTT conditions featured accumulation of small particles on the bottom surface of the microplate. There was an uneven brightness gradient across the images, which was difficult to correct for between images without losing image resolution.

In order to accurately track the increase in particle density between each micrograph, images were divided into a grid of 100x100px squares. A thresholding algorithm (Huang, ImageJ) was applied, based on the central 50% of each image, and used to differentiate between background (black) and particles (white) (Figure 2.1b). Note that due to the brightness gradient, this thresholding was only effective for parts of the image, hence the need to subdivide the image to find representative sections.

Plotting the change in proportions of white-to-black pixels for each given grid square over time, gave graphs similar to the one shown in Figure 2.1d (top). These time courses were filtered, based on general assumptions, using the following two constraints for each individual grid square: the initial timepoint must contain less than 10% white pixels and final timepoint must include more white pixels than any other timepoint in the time course. Using just these constraints was enough to

restrict measurements of particle density to properly thresholded regions of the micrographs (Figure 2.1c), which results in the filtered graphs in Figure 2.1d.

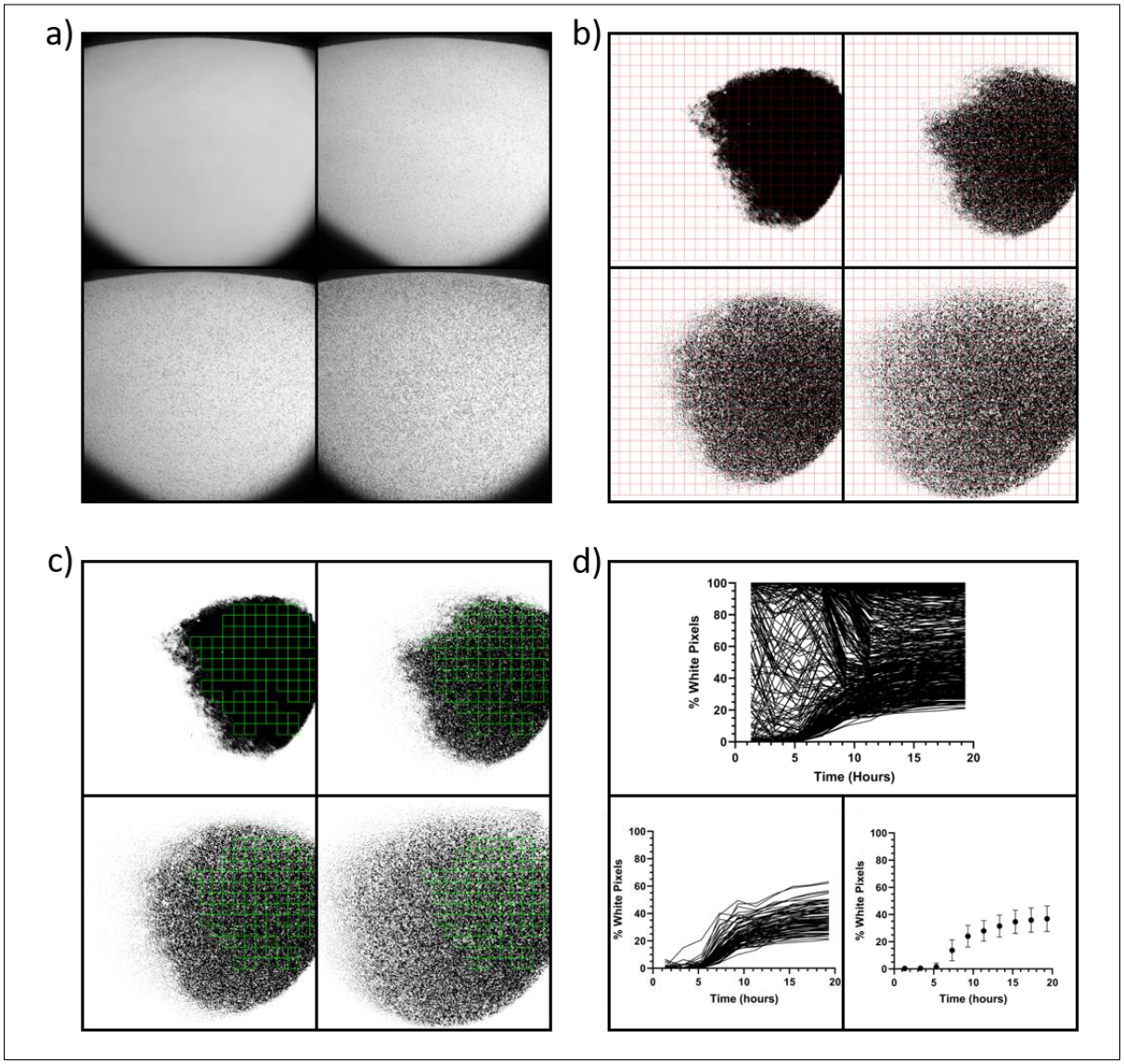

Figure 2.1: Box-sampling method for determining aggregate increases over time.
a) Representative timelapse DIC microscopy images of a single condition show aggregates appearing over time. b) The same images shown in (a), which are converted to binary (black-white) images using the Huang thresholding algorithm on the central 50% of the image. The red grid represents box-sizes of 100x100px used to sample across the image. c) Green boxes show accepted grid squares based on the filtering method described in the text. d) The change in percentage of white pixels within each grid square over time is shown without filtering (top), after filtering (left) and as an average of filtered traces (right). Standard error is shown for the averaged graph.

In order to determine the start-time of aggregation or lag-phase for each condition, the filtered curves were fit using a conditional exponential growth function that combines the initial plateau before aggregation, with a typical exponential growth function, such that both can be fit simultaneously. This removes the need to exclude early timepoints in order to fit an exponential, and reduce the risk of bias in cases where the "start" of aggregation was ambiguous. The conditional fitting equation is described as follows:

$$Y = \begin{cases} A\left(1 - e^{-kx}\right) + C, & if\ A\left(1 - e^{-kx}\right) + C > Plat, \\ Plat, & otherwise. \end{cases}$$

Where 'A', 'k', 'C' and 'Plat' are all fitted parameters. The value of 'Plat' fits to the y-axis value of the lag-phase plateau and forces the fitted curve to remain at this fixed value where the exponential curve would extend below. Lag-phase estimates are generated from where the exponential curve function would intercept the x-axis, using the following equation:

$$x_{int} = -\left(\frac{\ln\left(1 + \frac{C - Plat}{A}\right)}{k}\right)$$

2.6 Cystatin C *in vivo* Methods

2.6.1 Transfection of tagged Cystatin C in HeLa cells

All transfections were performed by either Rachel Hodgson or Sarah Granger (Sheffield Institute of Translational Neuroscience).

Cells were seeded in 24-well plates, with coverslips, at a density of $5x10^4$ cells. Transfection with pAc-hCC-GFP or pCIneo-CST3-HA was performed 24 hours after plating, using Lipofectamine 2000 (ThermoFisher) according to the manufacturer's instructions.

2.6.2 Live-Cell Confocal Fluorescence Microscopy

pAc-hCC-GFP transfected HeLa cells were imaged for GFP fluorescence in glass-bottomed dishes, incubated at 37 ^oC, using a Nikon A1 HD25 Confocal Microscope, controlled using the NIS Elements (Nikon) software.

2.6.3 Fixing HeLa Cells and Fluorescent Marker Staining

Cell fixing and staining was performed by Rachel Hodgson.

Transfected HeLa cells were fixed in 4% paraformaldehyde and permabilised in methanol. Primary antibodies were incubated with cells for 2 hours at room temperature, then washed off with phosphate buffered saline and incubated with Alexa-Fluor conjugated secondary antibodies (1:500 dilution) for 1 hour at room temperature. Cells were then incubated with DAPI stain and mounted using ImmunMount mounting medium.

2.6.4 Fixed-cell Fluorescence Imaging

Fixed cells were imaged with the assistance of either Rachel Hodgson or Tatyana Shelkovnikova.

Transfected and fixed HeLa cells were imaged for GFP or HA, DAPI and marker fluorescence using an Olympus BX57 microscope controlled by cellSens Dimension software (Olympus). Images were taken with an ORCA-Flash 4.0 camera (Hamamatsu).

2.7 Preparation of α-Synuclein Lipoprotein Particles

2.7.1 Growth and Expression of α-Synuclein

Single transformed colonies containing pET28a-αSyn were picked from agar plates and used to inoculate 50 mL LB-Kan starter cultures at 37 ^{o}C, 180 rpm shaking overnight. Roughly 21 mL of starter culture was used to inoculate each 750 mL culture of LB-Kan in baffled flasks, for a starting OD_{600} of 0.1, which were incubated at 37 ^{o}C, 200 rpm shaking.

The OD_{600} of each culture was periodically checked until it reached above 0.8, after which expression of α-synuclein was initiated by addition of 0.3 mM IPTG. Cultures were then grown for an additional 4 hours at 37 ^{o}C before harvesting. Cells were pelleted by centrifugation at 46,254 g for 15 minutes at 4 ^{o}C, then stored at -20 ^{o}C.

2.7.2 Purification of α-Synuclein from cell pellet

Each 750 mL culture cell pellet was resuspended in 50 mL α-Syn resuspension buffer, supplemented with 12.5 units/mL Benzonase endonuclease (Millipore) and 5 mg Lysozyme (Sigma-Aldrich). The cell suspension then underwent 3 cycles of freezing in dry-ice and thawing at room temperature. Cell debris was removed by centrifugation at 46,254 g for 15 minutes.

Cell free extract was applied on 2x5 mL HiTrap Q-FF columns (Cytiva), at a flow rate of 5 mL/min in α-Syn resuspension buffer. Elution was performed using a gradient of NaCl concentration from 0 to 0.5 M in the same buffer. Fractions containing α-synuclein, assessed by SDS-PAGE, were combined and ran through 2x HiPrep 26/10 desalting columns (Cytiva) to remove excess NaCl.

The desalted sample was then applied to a 6 mL ResourceQ column (Cytiva) at a flow rate of 5 mL/min in α-Syn resuspension buffer. Elution was again performed using a gradient of NaCl concentration from 0 to 0.5 M in the same buffer. Fractions containing α-synuclein, assessed by SDS-PAGE, were combined and concentrated in a 5 kDa MWCO polyethersulfone centrifugal concentrator (Sartorius Vivaspin® 20, VS2011).

The concentrated fractions were then loaded onto a HiLoad 16/600 Superdex 75 (Cytiva) gel filtration column, at a flow rate of 1.0 mL/min, running in α-Syn working buffer. Pure α-synuclein fractions, assessed by SDS-PAGE, were combined and concentrated in a centrifugal concentrator, then stored in aliquots at -70 °C.

2.7.3 Preparation of POPG SUVs

POPG stored in chloroform or as powder then dissolved in chloroform (Avanti 840457C or 840457P) was added to a glass round-bottomed flask. The chloroform was slowly evaporated with a stream of nitrogen gas, while swirling the mixture to create an even lipid film. Residual chloroform was further evaporated overnight using a freeze-dryer.

The film was resuspended in α-Syn working buffer using a vortex mixer and through 5 consecutive freeze-thaw cycles in dry-ice and a 60 °C water bath. The final volume after freeze-thaw was made up to 6.5 mL per 100 mg of POPG, equating to 15.4 mg/mL (20 mM) stock concentration. Stocks were aliquoted and stored at -70 °C.

Small unilamellar vesicles (SUVs) were prepared by thawing POPG stocks and passing them through an Avanti Polar Lipids mini-extruder 20 times with a 100 nm membrane, followed by at least 30 times with a 50 nm membrane.

2.7.4 α-Synuclein Aggregate Preparation in the Prescence of POPG SUVs

This protocol was optimised previously by Peter Davis and the main modification is scaling up the original protein and lipid concentrations, previously 30:900 μM α-Syn:POPG, for preparative use by maintaining a 1:30 stochiometric ratio of α-Syn:POPG.

α-synuclein and 50 nm POPG SUVs were combined in α-Syn working buffer to give final concentrations of 3.90 mg/mL α-synuclein (270 μM) and 6.24 mg/mL POPG (8100 μM) and incubated in glass vials (Postnova, prod. code: Z-VIA-11090500) at 45 ^{o}C for 2 hour and 30 minutes.

2.7.5 Separation of α-Synuclein:POPG Aggregates by AF4

Asymmetric-flow field-flow fractionation (AF4) separates molecules by size in a thin liquid channel, generally smallest to largest. Buffer is pumped through a membrane spanning the base of the channel, generating a “cross-flow” force acting on all molecules in the channel pulling them towards the membrane (Figure 2.2). The dimensions of the channel create a parabolic flow profile that allows small molecules, which more easily diffuse against the cross-flow and into the middle of the channel, to move more quickly down the channel.

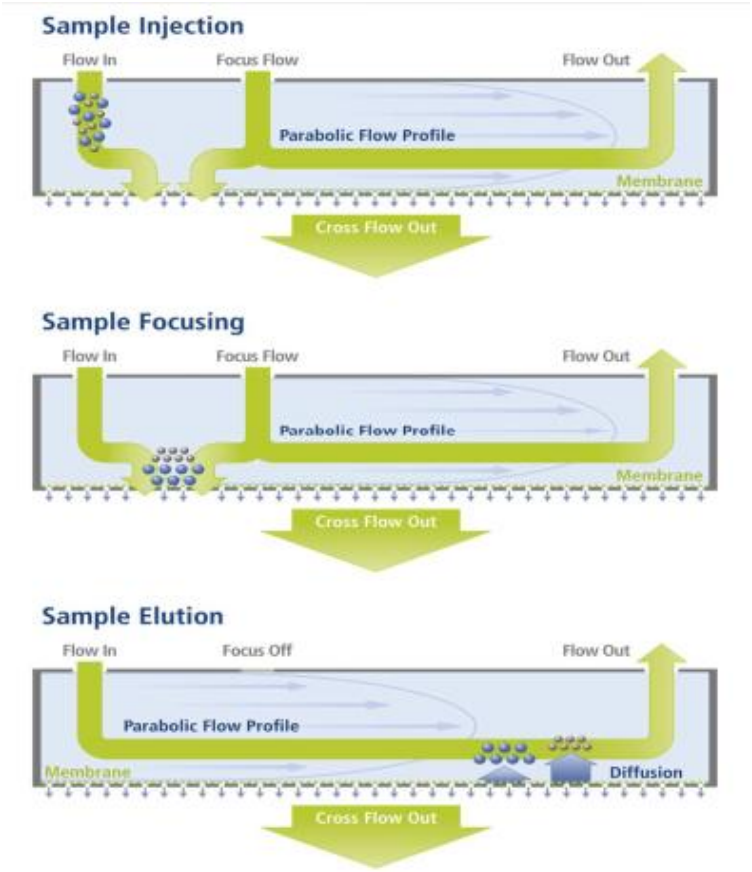

Figure 2.2: Steps of an AF4 run.
Sample is injected into the channel and concentrated into a single band by an opposing "Focus Flow" and is kept at the base of the channel by the "Cross-Flow" going through a membrane at the base of the channel. Elution begins once the focus flow is removed, allowing material to proceed down the channel. Smaller molecules more easily diffuse against the cross-flow into the centre of the channel, where they flow faster due to a parabolic flow profile. Eventually, cross-flow rate is reduced, allowing larger molecules to elute.

During the course of a run, the cross-flow can be reduced over time to gradually allow larger molecules to exit the channel. Samples exiting the channel pass through UV and multi-angle light scattering (MALS) detectors to give information on concentration and molecular size distribution, before being fractionated for downstream applications.

AF4 was performed with a Postnova AF2000 AT system, using a standard channel, 350 µm spacer and 5 kDa MWCO polyethersulfone membrane. Samples were injected with a PN5300 autosampler (Postnova), or by manual injection, and detection performed with a Shimadzu (JP) UV detector at 280nm and Postnova MALS detector. Sample separation follows the flow-profile in Figure 2.3, with an injection flow-rate of 0.5 mL/min and a slot flow-rate of 0.2 mL/min. Data was analysed using the AF2000 software (Postnova). MALS data for mixed or α-synuclein only samples was fit using a second-order Berry plot, while POPG SUVs could be fit using a Zimm plot.

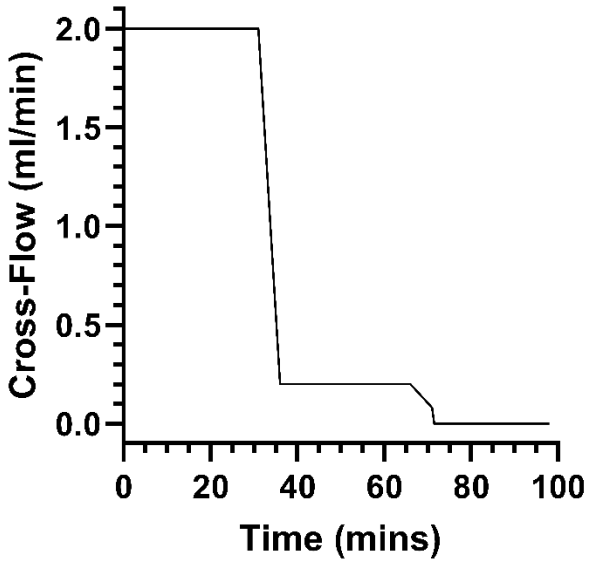

Figure 2.3: Typical AF4 cross-flow profile.
AF4 runs of α-synuclein and POPG were separated starting at a 2 mL/min cross-flow, gradually reduced to 0.2 mL/min after 31 minutes, before removing the cross-flow at 71 minutes.

The AF4 method described above was originally developed by Peter Davis. Various optimisations were attempted to improve this method, including: removal of the slot flow, adding more plateau steps in the cross-flow rate, and using a 250 µm channel spacer. However, these changes generally had a negative impact on separation efficacy or sample yield and they were not used for downstream experiments.

2.8 Biophysical Techniques

2.8.1 Multi-Angle Light Scattering

Direct MALS measurements were made by injection at 0.5 mL/min through the AF4 detectors, including a Shimadzu (JP) UV detector at 280 nm and Postnova MALS detector. Data was analysed using the AF2000 software (Postnova) and fit in the software using either the Zimm or second-order Berry equations.

The Zimm equation is a generalisation of the Debye standard static light scattering equation that assumes scattering particles are not interacting in the sample, in order to simplify the equation to a linear angular dependence that can be more reliably extrapolated to give an average particle radius. This method was used for POPG vesicle controls, as the simplest equation that fit the data well, and indicates that there were not many inter-vesicle interactions in those samples.

The Berry equation is also a generalisation, but allows for the inclusion of higher order parameters, which roughly account for scattering dependence due to inter-molecular interactions in the sample. The “second-order” Berry plot includes terms that account for 2-body interactions between particles, but not 3-body or higher. It was the simplest equation that fit the data for mixtures of α-synuclein and POPG. Due to the structural complexity of the mixed samples, the radii reported by this model are most likely qualitatively comparable, but not quantitative. A more appropriate model would incorporate the tube-like shape of the particles into the equation; however, an option did not exist in the software to do this.

2.8.2 Liquid Chromatography Mass-Spectrometry

LC-MS measurements were performed and analysed by Adam Hold (UCB Pharma). The system consisted of a reverse-phase chromatography column, upstream of a time-of-flight mass spectrometer. Concentration of α-synuclein in AF4 fractions was determined by integrating peak UV absorbance at 220 nm. A calibration curve for the absorbance at 220 nm was generated using known α-synuclein stock concentrations and is displayed in Figure 2.4.

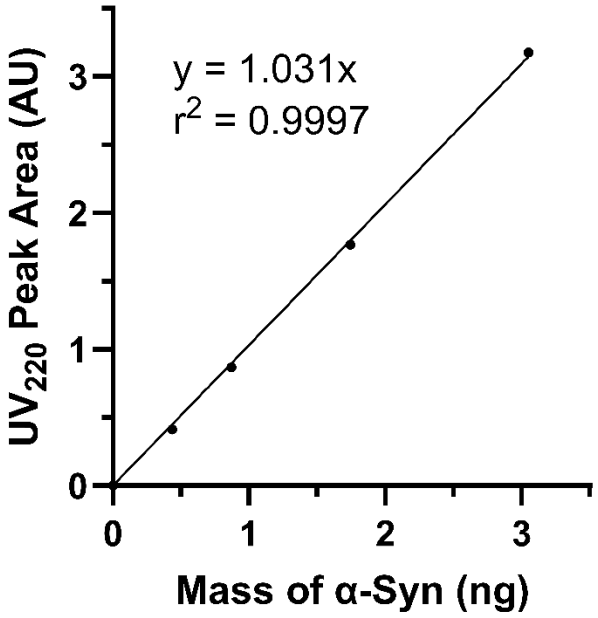

Figure 2.4: Calibration curve for α-synuclein peak absorbance at 220 nm.
Known concentrations of α-synuclein stocks were injected onto the reverse-phase chromatography column and the resulting UV peaks were integrated and plotted to give a calibration curve to determine the α-synuclein concentration in AF4 fractions.

2.8.3 ATR-FTIR of α-Synuclein and POPG mixtures

Attenuated total reflection (ATR) Fourier-transform infra-red (FTIR) spectroscopy was carried out on a nicolet 380 spectrometer (Thermo Instruments, UK) equipped with a Golden Gate 45° single-reflection diamond ATR system (Specac, UK), with assistance from Thomas Braxton. Samples were dried on the surface of the ATR crystal with a nitrogen stream. To increase the initially poor signal-to-noise ratio, samples were applied and dried 5 times each to increase the concentration before measuring. IR-absorbance of each sample was measured across the range of 4000-800 cm^{-1} wavenumber, with a resolution of 1.93 cm^{-1} and 128 scans.

In order to align and compare the amide region (1700-1350 cm^{-1}) between samples, each spectrum was shifted with a Y-offset by least-squares fitting the nearby 2200-1800 cm^{-1} region to an average of all spectra. This was necessary due to the complexity of these spectra and variable signal contribution by water, which made traditional baselining challenging. The full spectrum, with this alignment, is shown in Figure 2.5.

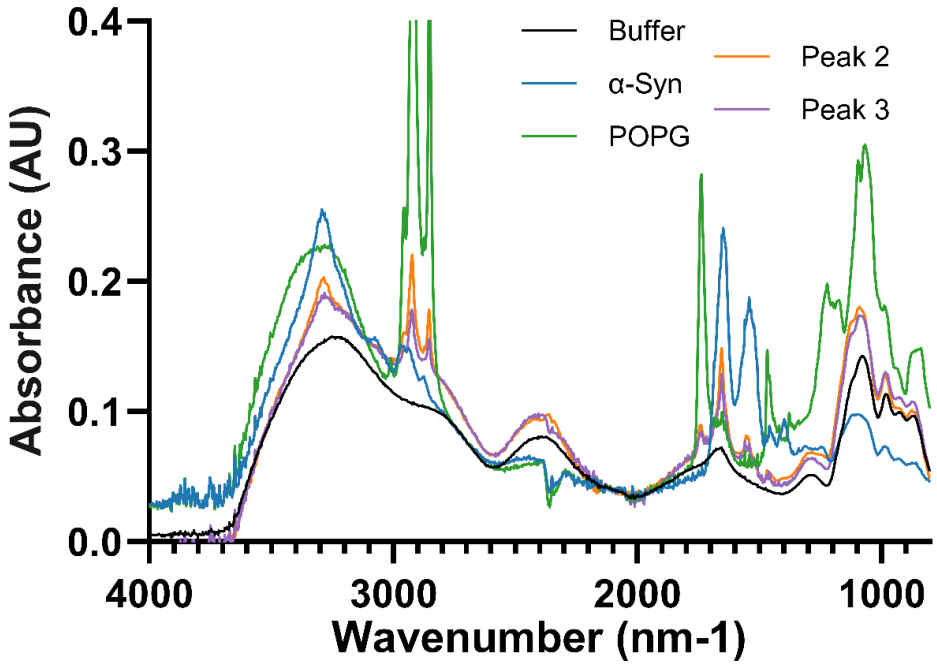

Figure 2.5: ATR-FTIR full spectrum overlay with baseline adjustment.
The spectra shown are aligned according to a least-squares fit within the region of 2200-1800 cm^{-1}. This allows for a better comparison between the primary region of interest (1800-1350 cm^{-1}) without trying to subtract an arbitrary baseline that could negatively manipulate the data.

2.8.4 Circular Dichroism

Circular Dichroism measurements were performed using a JASCO J-810 spectropolarimeter across the 190-260 nm range, with a bandwidth of 1 nm and scan speed of 20-50 nm/min. Spectra were recorded as the average of 3 scans. Samples were placed in a 1 mm pathlength quartz cuvette (Hellma, UK), which was thoroughly cleaned between samples. The 45 °C CD timelapse used a PTC-3515 Peltier Temperature Controller (Jasco) attached to an external water bath to incubate the cuvette inside the spectropolarimeter.

2.8.5 CD Methanol Titration of α-Synuclein and POPG

333 µg/mL α-synuclein (23 µM) and 532.5 µg/mL POPG (692 µM) were mixed to give a 1:30 stochiometric ratio and incubated at 45 °C for 2 hours 30 minutes. This mixture was then added to dilutions of methanol to give final sample concentrations of 30% α-Syn:POPG mixture in 0-70% methanol in 10% increments. The methanol dilutions were pre-chilled and samples kept on ice to reduce further α-synuclein aggregation prior to CD measurement.

2.8.6 Spectrophotometry Time Courses

Absorbance and fluorescence time courses were both monitored in hydrophilic coated polystyrene 96 half-well microplates (Corning, prod. no. 3881) using a FLUOstar Omega microplate reader (BMG Labtech, UK) controlled by the MARS analysis software (BMG Labtech, UK). In all cases, samples were measured as 5-well replicates, averaged and then blank corrected against appropriate controls measured at the same time. Samples were incubated at the specified temperature in the microplate reader, without shaking.

2.8.7 Negative-Stain Electron Microscopy

Copper grids with a carbon support film were glow discharged for 15 seconds using a Cressington (UK) 208 glow-discharge unit. 5 µL of sample was applied to each grid and allowed to adsorb for 1 minute. Grids were then blotted and washed twice by dipping into water droplets and re-blotting. Sample was stained by dipping grids into 0.75% uranyl formate for 20 seconds before blotting and gently drying with a vacuum pump.

Imaging was performed using a Philips CM100 electron microscope with a LaB6 cathode operating at 100 kV with a spot size of 2. Images were captured at 8900x and 28500x magnification using a 1024x1024px Gatan camera.

2.8.8 Cryo-Electron Microscopy

The majority of samples were applied to grids, blotted and vitrified using a Leica Automatic Plunge Freezer, performed at 12 ^{o}C and maximum humidity, with a 45-second wait after sample application before blotting. A variety of grids, glow discharge times and blotting parameters were attempted, discussed in Section 5.8. Glow discharge of grids was carried out using a Cressington (UK) 208 glow-discharge unit. Imaging was performed on a Technai Arctica microscope, with assistance from Dr. Svetomir Tzokov (University of Sheffield, electron microscopy manager), at 200 kV, 2.7 mm spherical aberration and a dosage of 30 e/Å^2. Some preliminary data was collected with the assistance of Chris Adams (UCB Biopharma, electron microscopy technician), using a Vitrobot plunge freezer at 4 ^{o}C and maximum humidity, and a Glacios (Thermo Scientific) electron microscope.

Micrographs were processed in CryoSPARC (cryosparc.com) by first running the motion correction and CTF estimation jobs. Particle picking was attempted both using an untemplated “filament tracer” job, as well as manually picking particles and generating 2D classes for templating the filament tracer. Neither method appeared to generate significantly different 2D classes. The 2D class averages were then used to generate 3D reconstructions using the “Helical refinement” and “Ab initio” jobs, which are also discussed in Section 5.8.

2.8.9 Atomic Force Microscopy

Single crystalline silicon substrate (Active Business Company GmbH) was prepared by oxygen plasma treatment for 5 minutes. Samples were applied to the substrate and allowed to adsorb for 5 minutes at room temperature before being dried using a nitrogen stream. AFM was carried out using a Veeco Dimension 3100 AFM microscope, equipped with a Scout ultrasharp probe of a 5 nm radius (Nunano) and operated by a nanoscope 4 controller in tapping mode. Heightmaps were processed by mean plane subtraction and row alignment using the 5^{th} order polynomial option in Gwyddion 2.60. Figures were also produced in Gwyddion.

2.8.10 AFM Grain Fitting of AF4 Peak 2

Atomic force microscopy of AF4 Peak 2 revealed a repeating pattern of pore-like structures across the surface of the silica. These structures were treated as individual grains and fit in Gwyddion 2.60 using the “watershed” and “segmentation” algorithms.

Watershed first locates grains by simulating small drops of liquid across the whole image, which flow into local minima. Minima whose area is below a set threshold are ignored. These parameters were optimised to ensure every pore contained a single merged “droplet”, identifying them as individual grains. The fill stage, following grain location, continues adding simulated liquid to fill up each grain until liquid from different grains meet, creating a fixed boundary between them. An example of the watershed algorithm and the parameters used can be found in Figure 2.6.

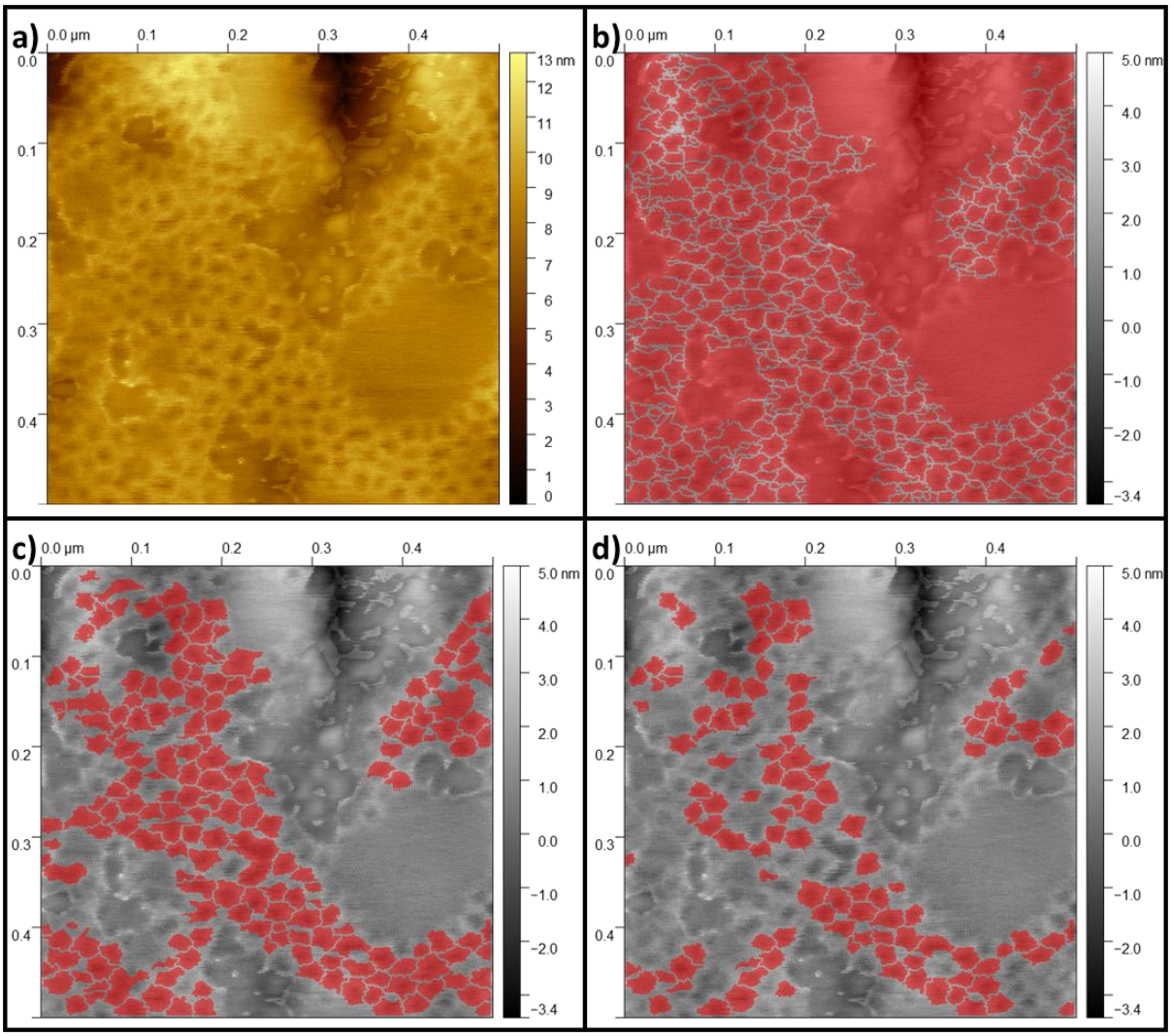

Figure 2.6: Watershed algorithm applied to AF4 Peak 2.
a) The AFM heightmap of AF4 Peak 2. b) Overlaid grain locations after applying the watershed algorithm using the following parameters: Grain location: number of steps = 50, drop size = 1%, threshold = 15 px^2; Segmentation: number of steps = 100, drop size = 10%. c) Remaining grains after applying a soft filter (κ_1 lower threshold = 0.001 nm^{-1}, κ_2 = 0.002-0.028 nm^{-1}). d) Remaining grains after applying a strict filter (κ_1 lower threshold = 0.005 nm^{-1}, κ_2 = 0.009-0.028 nm^{-1}).

The segmentation algorithm instead treats every local minimum as a grain, except those with a similar height close-by, and fills from each minimum, preserving boundaries between them. This approach tends to be noisier than watershed so Gaussian smoothing is applied to remove the very small grains produced by local minima in background noise, by combining them into a single grain. An example of the segmentation algorithm and the parameters used can be found in Figure 2.7.

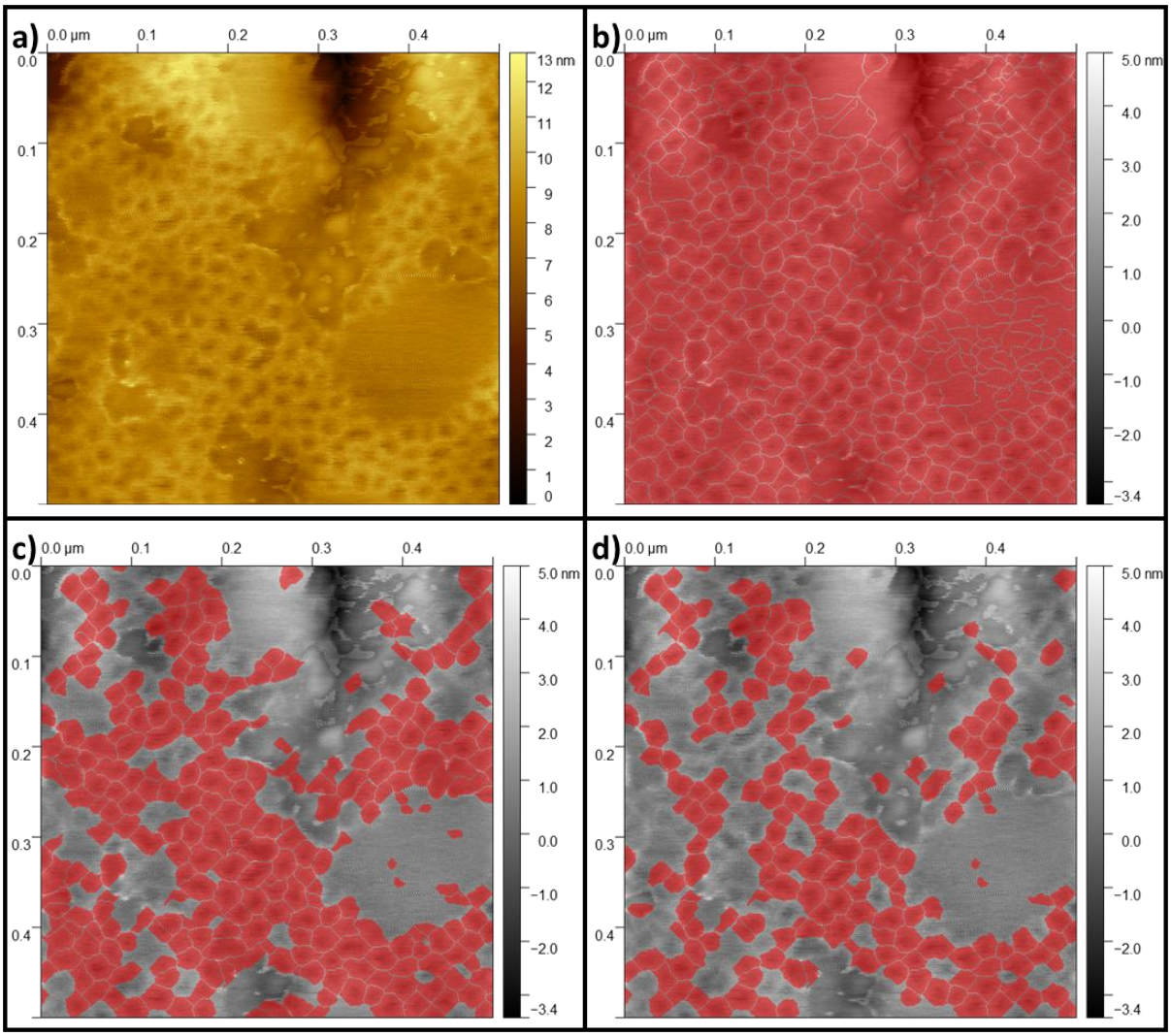

Figure 2.7: Segmentation algorithm applied to AF4 Peak 2.
a) The AFM heightmap of AF4 Peak 2. b) Overlaid grain locations after applying the watershed algorithm using the following parameters: prefill from minima to 0.5% of image height, Gaussian smoothing of 5 px (4.88 nm). c) Remaining grains after applying a soft filter (κ_1 lower threshold = 0.001 nm^{-1}, κ_2 = 9-28 μm^{-1}). d) Remaining grains after applying a strict filter (κ_1 lower threshold = 0.005 nm^{-1}, κ_2 = 9-28 μm^{-1}).

In order to remove grains that don't correspond to an underlying pore structure, filters were applied based on height curvature. To reduce the inherent bias in applying a filter subjectively, a soft and strict filter was applied to both algorithms, with the aim of selecting for either all the relevant pores with many false positives, or only pores with many false negatives.

2.8.11 Small-Angle X-Ray and Neutron Scattering

Perdeuterated α-synuclein was produced recombinantly in fully deuterated M9 media. Cells were transformed and plated, as in Section 2.7.1, then grown in successive 20 mL overnight cultures of M9 media with D_2O percentages of 0%, 90% and 100%. This was used to inoculate 2 L (4x500 mL) of 100% deuterated M9, which was induced at an OD_{600} of 0.8 with IPTG and allowed to express for 4 hours at 37 ^oC. The perdeuterated protein was then purified following the protocol in Section 2.7.2 and buffer exchanged into the relevant D_2O percentage buffers for SANS experiments. Deuterated POPG-d64 was purchased from ANSTO (Sydney, Australia) and extruded to form 50 nm small unilamellar vesicles (SUVs) using the technique described in Section 2.7.3.

Scattering experiments and analysis were performed with help from Dr. Andrew Parnell (University of Sheffield, Department of Physics). Small-angle X-ray scattering (SAXS) was carried out at the Xeuss SAXS facility (University of Sheffield, Department of Chemistry), where solutions were measured in quartz capillary tubes in a temperature-controlled sample holder set to 25 ^oC or 45 ^oC.

Small-angle neutron scattering (SANS) experiments were performed on the SANS2D instrument at the ISIS spallation neutron source (Oxfordshire, UK). Sample solutions were measured in banjo-style quartz cuvettes with a path length of 1 mm. These were mounted in a temperature-controlled sample holder at 25 ^oC or 45 ^oC during time course measurements. Different mixtures of hydrogenous and deuterated forms of α-synuclein and POPG were measured in pre-calculated deuterium concentrations to contrast match either the protein or lipid (Table 2.1). Contrast matching aims to adjust the solvent to have a similar scattering power as one of the experimental components, in this case protein or lipid, such that the component's scattering becomes indistinguishable from the solvent background signal. Contrast matching allows for the unmatched component to then be visible in isolation, without any additional signal contributed by the solvent-matched component.

α-Synuclein	POPG	Solvent D2O Concentration (%)	Visible Species	Temperatures
Hydrogenated	-	100%	α-Synuclein monomer	25 ºC and 45 ºC
Deuterated	-	0%	α-Synuclein monomer	25 ºC and 45 ºC
-	Hydrogenated	100%	POPG Vesicles	25 ºC and 45 ºC
-	Deuterated	0%	POPG Vesicles	25 ºC and 45 ºC
Hydrogenated	Hydrogenated	100%	Both α-Synuclein and POPG	25 ºC and Timecourse at 45 ºC
Deuterated	Deuterated	0%	Both α-Synuclein and POPG	25 ºC and Timecourse at 45 ºC
Hydrogenated	Deuterated	36%	POPG	25 ºC and Timecourse at 45 ºC
Hydrogenated	Deuterated	77%	α-Synuclein	25 ºC and Timecourse at 45 ºC
Deuterated	Hydrogenated	12.8%	α-Synuclein	25 ºC and Timecourse at 45 ºC
Deuterated	Hydrogenated	94%	POPG	25 ºC and Timecourse at 45 ºC

Table 2.1: Measured SANS solutions.
Mixtures of hydrogenated and deuterated α-synuclein and POPG with their respective solvent deuterium concentrations and temperature measurements. The "visible species" column refers to which components of the mixture are distinguishable from background noise, which is important for the final four rows where contrast matching is used to remove the signal from one component.

Scattering dependence fits of both SAXS and SANS data were performed by Dr. Parnell, using standard model functions within SasView 6.0. Documentation for each model can be found on the SasView website and are provided in the following references: Monodisperse gaussian coil model [381], vesicle model [382], Guinier-Porod model [383], flexible cylinder model [384], rigid cylinder model [385].

2.9 Plasmid Maps

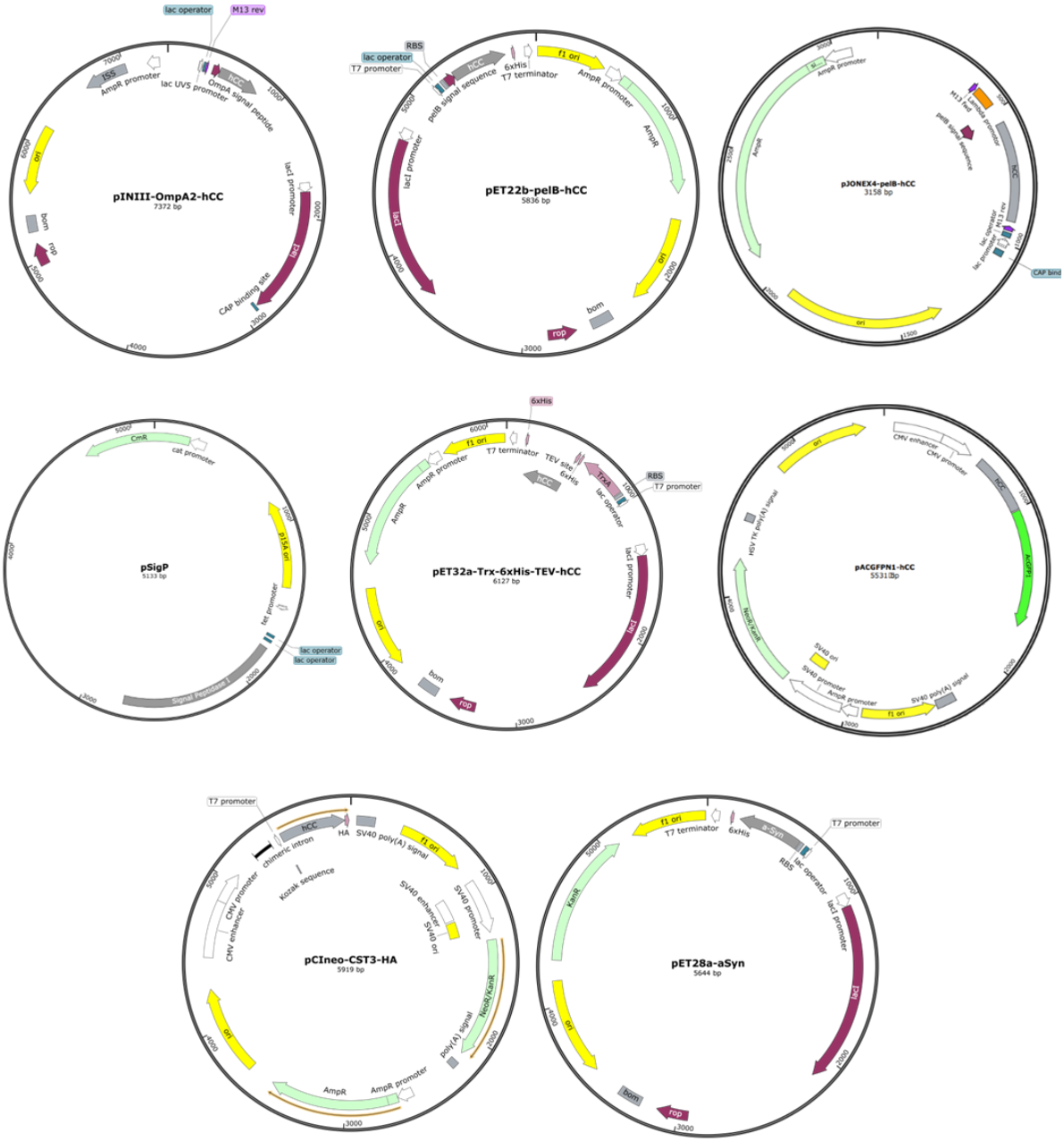

Figure 2.8: Maps of plasmids used for cystatin C and α-synuclein expression.
Shown are genetic maps of bacterial expression vectors for cystatin C, mammalian expression vectors for cystatin C fused with GFP or HA-tags and the bacterial expression vector for α-synuclein expression. pCIneo-CST3-HA was provided by Sarah Granger (Sheffield Institute of Translational Neuroscience). pET28a-aSyn was provided by Marco Kriek (UCB Biopharma).

Chapter 3: Expression Optimisation of Human Cystatin C

3.1 Introduction to Expression Optimisation

In order to carry out an *in vitro* study of human cystatin C (hCC) aggregation it must first be produced in sufficient quantities to facilitate screening a wide-range of conditions. Recombinant expression of cystatin C was first carried out by Abrahamson et. al. 1988 [315] in *Escherichia coli* (*E. coli*). The system involved secretion of hCC into the periplasm and purification by ion exchange and size exclusion chromatography [316]. Alternative methods and strategies developed by other groups involve: use of codon optimisation [317], expression in yeast [318], addition of purification tags for metal affinity chromatography [319], fusion protein solubility tags [320] and addition of a PelB secretory signal peptide to enhance cellular export [321]. A cytoplasmic pTWIN1 expression system produces inclusion bodies of Intein-cystatin C fusion protein, that can be denatured and renatured during a single-step using chitin column purification [322]. However, this system produces high molecular weight oligomers and refolding proteins from inclusions bodies is often problematic (Abrahamson, pers. comm.). By far the most extensively used and successful method appears to be the original used by the Abrahamson group [316], which reports a yield of 15 mg/L cell culture.

3.2 History of the Sheffield Lab Constructs

Initial cloning of the human cystatin C gene was carried out by Dr. Rosie Staniforth. The original *CST3* gene was obtained from the American Type Culture Collection, which have a cDNA genebank, and cloned into the pINIII-ompA2 system obtained previously for high yield expression of chicken cystatin (10 mg/L cell culture [323]). Miss Emma Keeley deleted the additional N-terminal amino acids that occur as a result of a cloning site between the OmpA leader sequence and the cystatin gene, as had been performed successfully by the Abrahamson group with a similar OmpA construct [313, 316]. The pINIII-ompA2 system is IPTG-inducible under the control of the lipoprotein promoter and the lactose promoter and operator [324] and seemed like a good substitution for the temperature-induced OmpA-hCC system favoured by the Abrahamson group, but not available at the time.

Subsequent experience of various *E. coli* expression strains (pLysS, Origami, Rosetta and Rosettagami), expression conditions (pH, temperature, IPTG tuning and salts), was mostly thanks to Miss Emma Keeley [248]. The conclusion from these studies was that nothing helped expression, except for use of minimal growth media, which, surprisingly, doubled the yield. She reported an

average expression yield of 4 mg/L cell culture, but noted somewhat unreliable expression of cystatin C.

Codon optimisation of the gene was then performed by Mr. Adham El Shawaihde [325], who carried out site-directed mutagenesis on the pINIII-ompA2 construct. He looked for codons which were known to correspond with rare tRNAs in *E. coli* and replaced them with more common ones. His final, optimised construct of pINIII-ompA2 is the main construct that has been used by the Staniforth lab. In 2015, Miss Abigail Williams designed a PelB-hCC construct, in which the cystatin C gene was commercially synthesised (Genscript) with codons optimised for *E. coli* expression [210]. The periplasmic leader sequence, PelB, was used in place of OmpA2 as this was a more modern sequence found in pET vector systems. The synthetic gene allowed the design for a direct fusion of PelB-hCC, with no intervening cloning site, ensuring the hCC N-terminal is not modified after PelB is cleaved upon secretion, similar to the pINIII construct. None of these constructs made much difference to overall expression of cystatin C, which remained somewhat variable and unreliable [210, 325, 326].

When starting this project, I aimed to investigate why there was such a disparity between cystatin C expression in the Staniforth lab, compared with reported expression by the Abrahamson group. I also hoped to improve upon a lengthy periplasmic extraction protocol, previously used to purify the protein, which involved an overnight dialysis step, thought to considerably reduce final yields due to both proteolysis and co-precipitation with nucleic acids. Nucleic acids, in particular, were an unusual occurrence in periplasmic extracts, which was not observed for equivalent preparations of chicken cystatin (Staniforth, pers. comm.). The relationship between cystatin C and nucleic acids, namely RNA, is examined further in chapter 4.

Table 3.1: Summary of optimisations for the expression of human cystatin C in *E.coli*

Expression Strategy	Construct	Strain	Media + Antibiotic(s)	Induction	Culture Volume	Purification Method [1]	Yield (mg/L)	Notes
New purification method (pINIII)	pINIII-ompA2-hCC	BL21-DE3	M9-Amp	42 °C - 2 hours	8x600 mL	Method 1	1.1, 1.35, 0.86*	[* = 15N-labelled growth]
New purification method (pET22b)	pET22b-pelB-hCC	BL21-DE3	M9-Amp	18 °C - O/N	500 mL	Method 1	1.7	
Scaled up expression	pET22b-pelB-hCC	BL21-DE3	M9-Amp	18 °C - O/N	8x600 mL	Method 1	1.19, 1.23, 0.30, 0.30	High nucleic acid contamination in CFE Switch from PES to RC spin concentrators
Additional purification steps	pET22b-pelB-hCC	BL21-DE3	M9-Amp	18 °C - O/N	8x600 mL	Method 2	0.36	Changed resolubilisation buffer from pH 6.2 MES to pH 8.0 NaP Addition of $MgSO_4$ and Benzonase treatment after sonication Start with Q-Seph to remove excess nucleic acids Adjust Q-Seph unbound fraction to pH 6.2 before SP-Seph
Change of induction temp.	pET22b-pelB-hCC	BL21-DE3	M9-Amp	42 °C - 2 hours	8x600 mL	Method 2	0.41	
Temperature-sensitive expression system	pJONEX4-pelB-hCC	M72	2YT-Amp	42 °C - 2 hours	500 mL	Method 2	n.s, n.s	SDS-gels show bands at ~11 kDa, indicating proteolysis
Change of growth media (MDAG-135 + Carb)	pET22b-pelB-hCC	BL21-DE3	MDAG-135-Carb	42 °C - 2 hours	8x500 mL	Method 2	n.s, n.s, n.s	MDAG-135 instead of M9 media Carbenicillin instead of ampicillin No significant gel band after SP-Seph in 3 separate batches
Small-scale trial (pINIII)	pINIII-ompA2-hCC	BL21-DE3	M9-Carb	18 °C - O/N	500 mL	Method 2	5.16, 5.40, 4.68	
Small-scale trial (pET22b)	pET22b-pelB-hCC	BL21-DE3	M9-Carb	18 °C - O/N	500 mL	Method 2	3.44, 3.12, 3.76	
Bioreactor growth	pINIII-ompA2-hCC	BL21-DE3	M9-Amp	N/A	22 L	Method 2	n.s	No 13kDa band visible in cell extract, pellet or column fractions
Signal-peptidase I co-expression trial (pINIII)	pINIII-ompA2-hCC; pSigP	BL21-DE3	M9-Carb+Chlor	18 °C - O/N	500 mL	Method 2	3.84	Lower expression than without pSigP in equivalent volume trials
Signal-peptidase I co-expression trial (pET22b)	pET22b-pelB-hCC; pSigP	BL21-DE3	M9-Carb+Chlor	18 °C - O/N	500 mL	Method 2	2.08	Lower expression than without pSigP in equivalent volume trials
Thioredoxin fusion protein expression trial	pET32a-Trx-6xHIS-TEV-hCC	Origami™ B (Novagen)	LB-Carb+Kan+Tet	18 °C - O/N	500 mL	desc. in relevant section	1.2*	[* = hCC was mostly insoluble after cleavage by TEV protease]
Smaller volume expression batches	pINIII-ompA2-hCC	BL21-DE3	M9-Carb	18 °C - O/N	2x500 mL	Method 2	2.1, 2.1*	[* = Two separate growths combined and purified gave 2.1 mg/L overall]

1 - Purification methods are described in Section 2.4.5

3.3 A New Purification Method

The first step in optimising the cystatin C expression was to adopt a more streamlined approach to purification. A more straightforward purification method was used, as proposed by Dr. Svetlana Sedelnikova (University of Sheffield, departmental officer for protein preparations), in which cystatin C was separated from whole cell lysate by SP-Sepharose cation exchange, taking advantage of its unusually high positive charge at neutral pHs. Fractions from SP-Sepharose were then further purified by size-exclusion gel filtration. The full details of this method can be found in Section 2.4.5 listed as "Method 1".

This was performed three times using the pINIII-ompA2 expression system in 5-litre batches, one of which being ^{15}N-labelled for downstream NMR, and gave final yields of around 1.1 mg/L of culture. Figures 3.1 and 3.2 show a representative SP-Sepharose run, while Figures 3.3 and 3.4 show size-exclusion. An expression trial of 500 mL using the pET22b-pelB expression system was also purified using this method, which yielded an impressive 1.7 mg/L. This is shown in Figures 3.5 and 3.6.

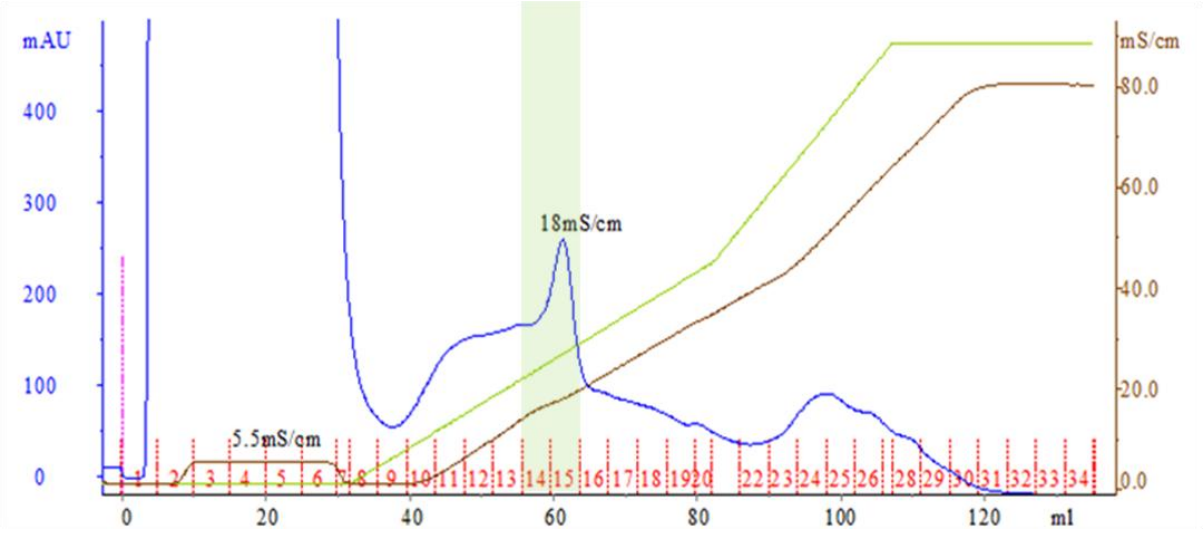

Figure 3.1: Cation exchange chromatography of pINIII-ompA2-hCC following purification method 1. The chromatogram of SP-Sepharose cation exchange is shown. The following is represented by each graph line: (blue) UV signal; (green) NaCl gradient concentration from 0 to 0.5 M; (brown) conductivity. Fractionated samples are represented by the red numbers along the x-axis. The green highlighted region represents fractions which were used for the next step of purification.

1	Ladder
2	Cell Debris
3	CFE
4	CFE
5	Fr12
6	Fr13
7	Fr14
8	Fr15
9	Fr16
10	Fr17
11	Fr18
12	Fr19
13	Fr20
14	Fr22
15	Fr24
16	Fr26
17	Fr28

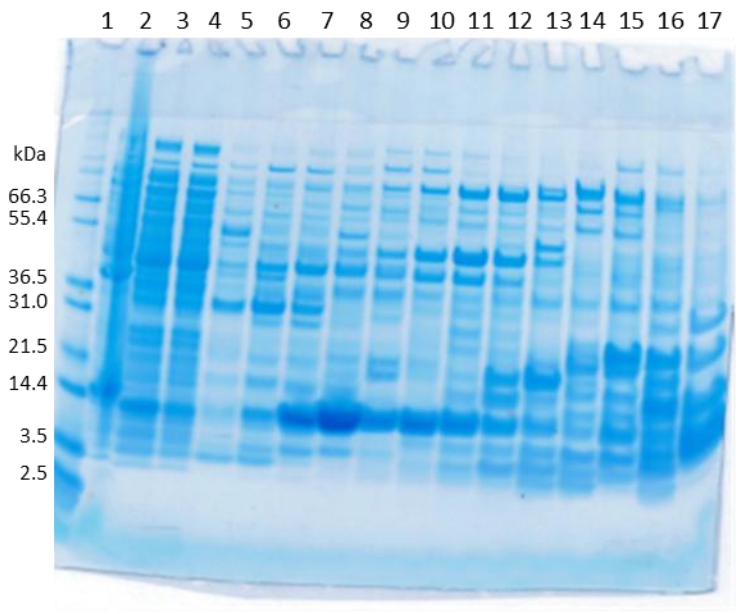

Figure 3.2: SDS-PAGE of SP-Sepharose fractions from Figure 3.1.
Protein-containing bands are separated by size and stained visible by SDS-PAGE. The numbers above each gel lane correspond to the table (left). Cell-free extract (CFE) is the supernatant after sonication. "Fr" are fractions taken from the SP-Sepharose run in Figure 3.1. The green highlighted region represents fractions which were used for the next step of purification.

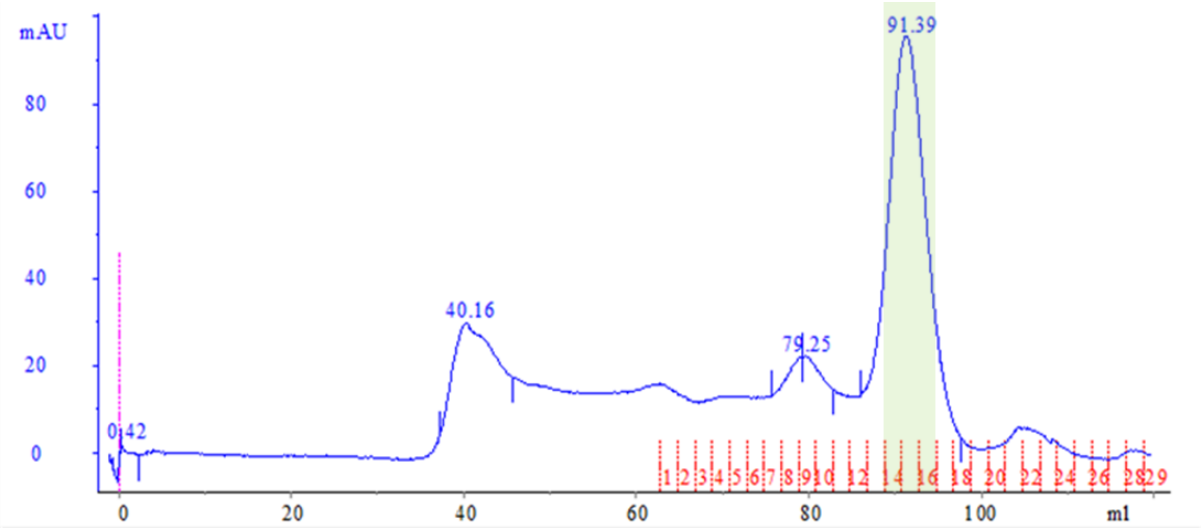

Figure 3.3: Size-exclusion chromatography of pINIII-ompA2-hCC following purification method 1.
The chromatogram of gel-filtration is shown. The graph line represents UV signal. Fractionated samples are represented by the red numbers along the x-axis. The green highlighted region represents fractions which were concentrated to give the final product.

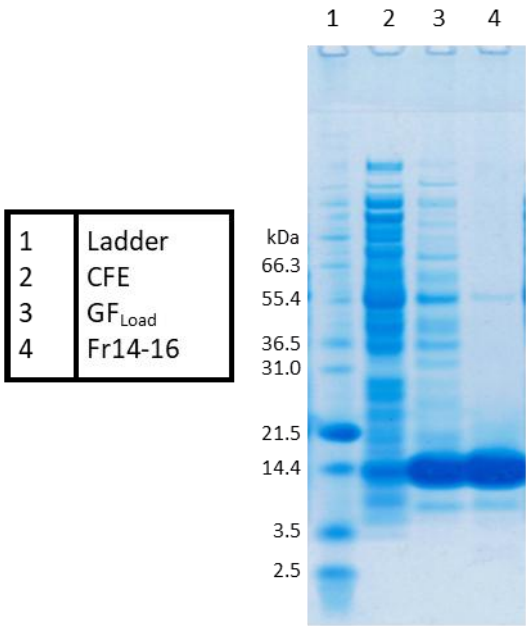

Figure 3.4: SDS-PAGE of gel-filtration from Figure 3.3.
Protein-containing bands are separated by size and stained visible by SDS-PAGE. The numbers above each gel lane correspond to the table (left). Cell-free extract (CFE) is the supernatant after sonication. "Fr14-16" are the combined fractions taken from the gel-filtration run in Figure 3.3.

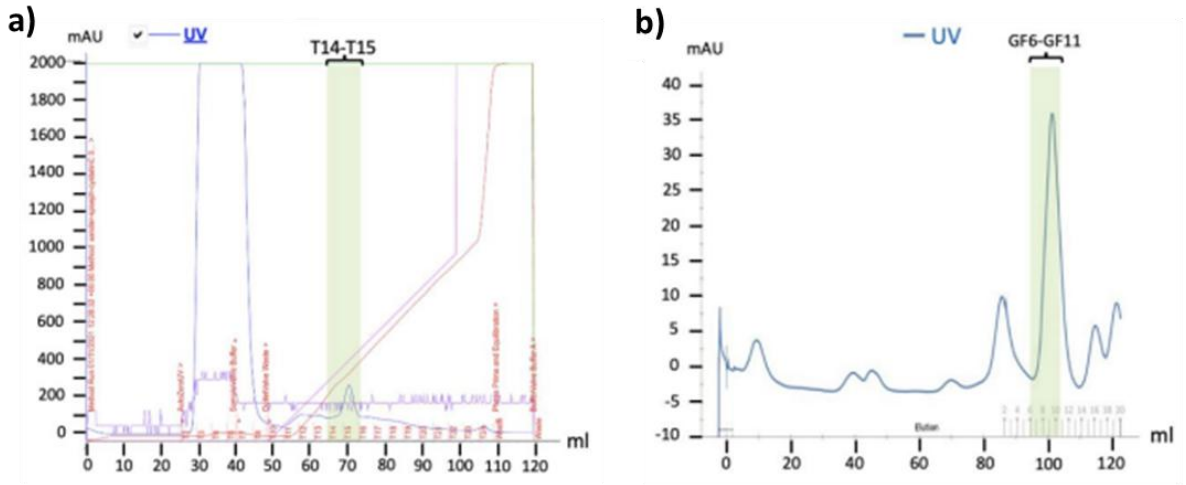

Figure 3.5: Purification of pET22b-pelB-hCC expression trial following purification method 1.
a) Chromatogram of SP-Sepharose cation exchange. The blue graph line corresponds to UV signal. The pink graph line shows a NaCl gradient from 0-0.5 M, followed by a wash at 1 M NaCl. b) Size-exclusion gel filtration of SP-Sepharose fractions 14+15. The graph line corresponds to UV signal. The green highlighted region on both graphs represents fractions which were used in the next step of purifications.

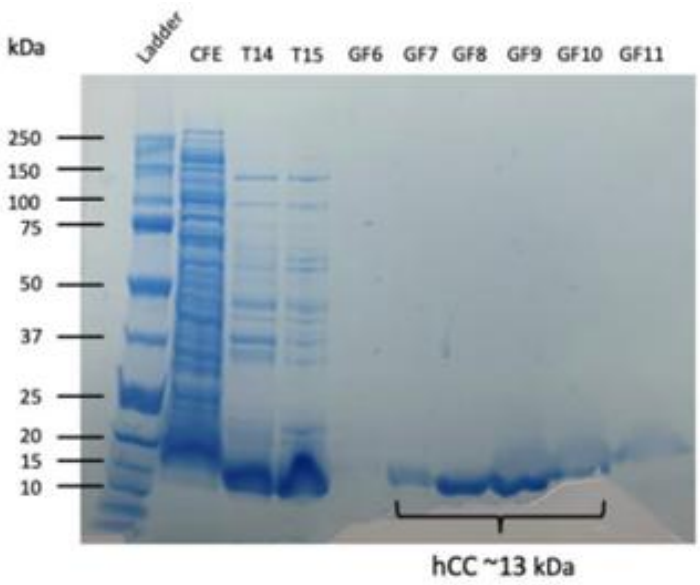

Figure 3.6: SDS-PAGE of purification steps in Figure 3.5.
Protein-containing bands are separated by size and stained visible by SDS-PAGE. Cell-free extract (CFE) is the supernatant after sonication. “T14” and “T15” are SP-Sepharose fractions that contained hCC (Figure 3.5a). “GF” are fractions from the gel filtration run (Figure 3.5b). hCC is labelled as a ~13 kDa band in GF7-10.

In order to verify the integrity of the purified proteins from both plasmids, they were assessed by mass spectrometry. Both plasmids produced a strong signal at 13.343 kDa (Figures 3.7 and 3.8), which is equivalent to the non-hydroxylated form of cystatin C [327], with no significant alternative peaks. This indicates no aberrant proteolysis or post-translational modification from these methods of expression. The lack of significant peaks elsewhere in the mass spectrum shows that this purification method was sufficient to produce pure hCC with very low contaminants (Figure 3.9).

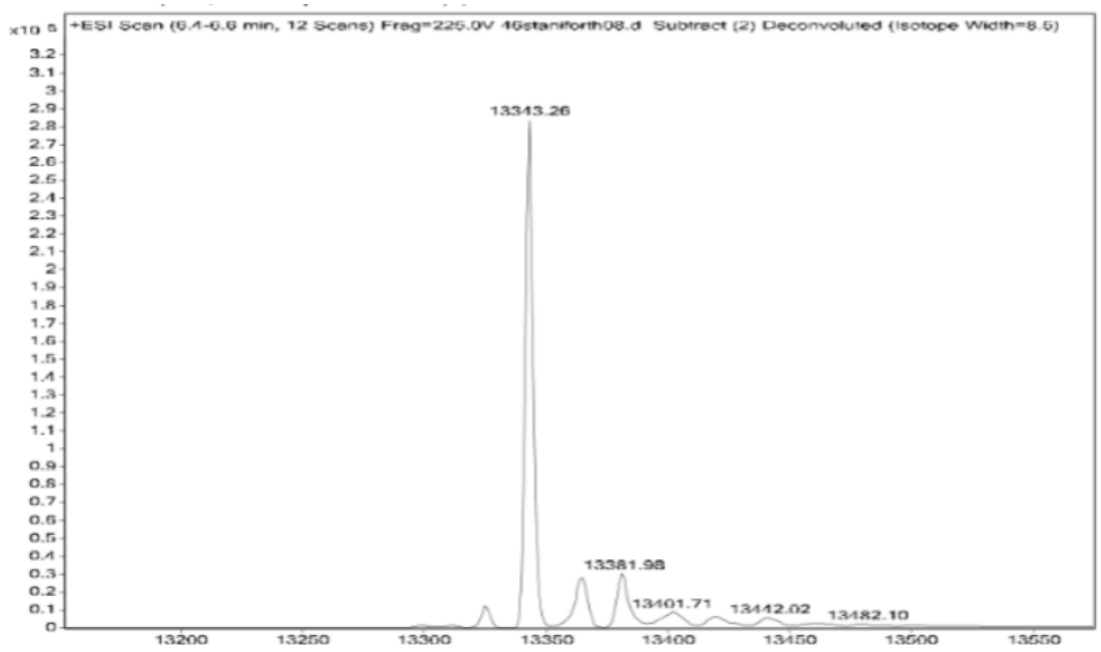

Figure 3.7: Mass-spectrometry of purified hCC from the pINIII-ompA2 expression system.
The mass spectrum of hCC shows a substantial peak at 13343 Da, which corresponds to non-hydroxylated hCC [327]. The lack of significant alternative peaks shows high purity of this form of hCC.

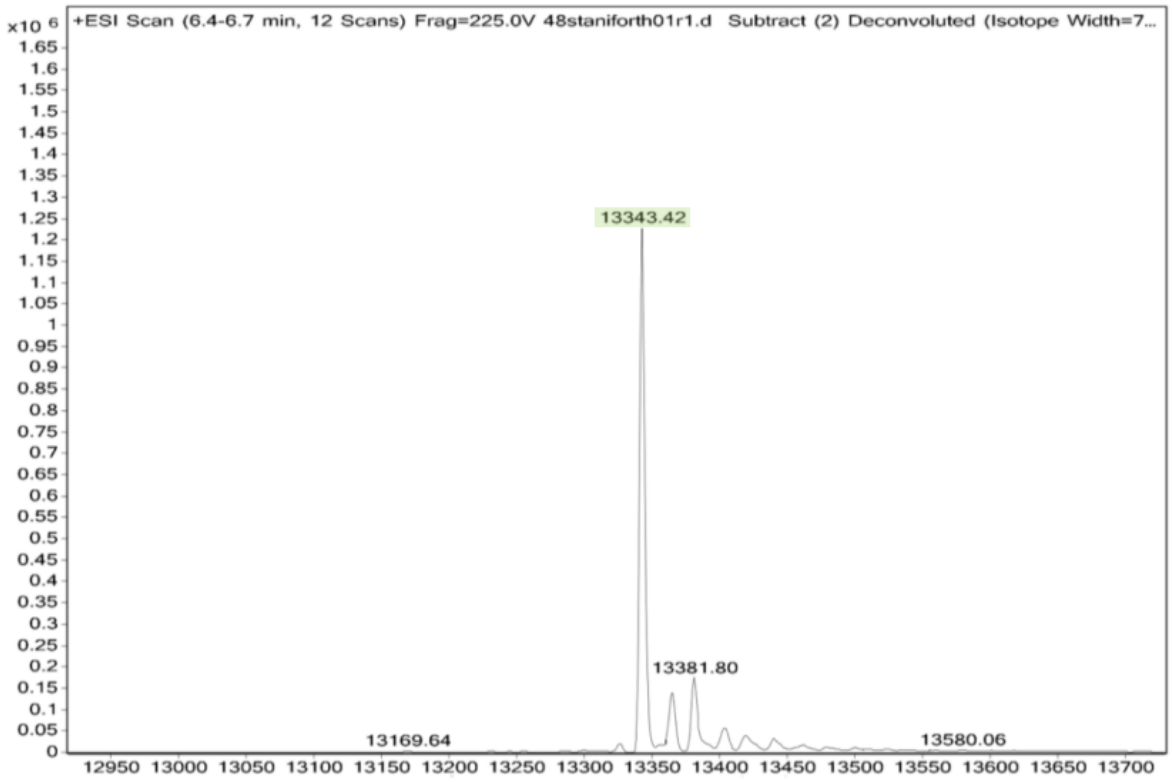

Figure 3.8: Mass-spectrometry of purified hCC from the pET22b-pelB expression system.
The mass spectrum of hCC shows a substantial peak at 13343 Da, which corresponds to non-hydroxylated hCC [327]. The lack of significant alternative peaks shows high purity of this form of hCC.

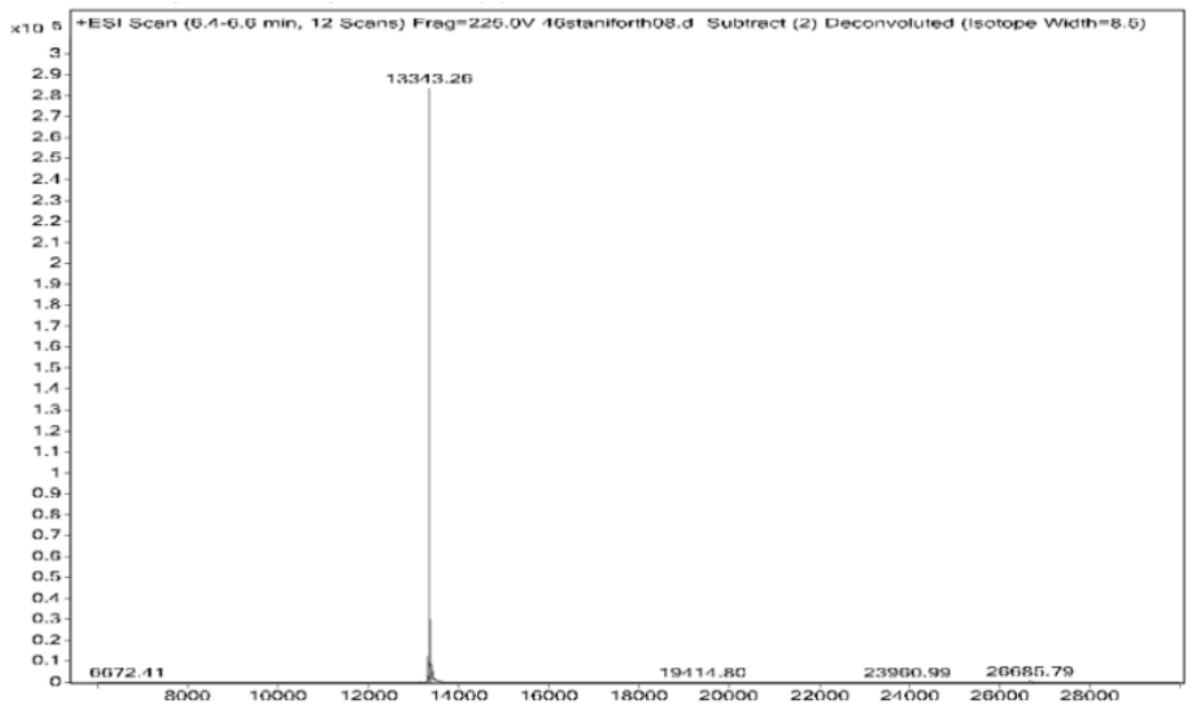

Figure 3.9: Full mass-spectrum of purified hCC from the pINIII-ompA2 expression system.
When looking at a broader range of masses from 6 kDa to 30 kDa, there is no contamination of hCC by other, similar mass proteins.

Upon scaling up the growth culture of the pET22b vector, from 500 mL to 5 L split between 8 flasks, the yield dipped significantly down to about 1.2 mg/L culture. Representative SP-Sepharose and SDS-PAGE can be seen in Figure 3.10. This remained slightly better than pINIII until, without changing any conditions, subsequent yields dropped again to just 0.3 mg/L. One particularly notable difference of the pET22b system was that cell lysates were very viscous and fractions after cation exchange had high 260/280 nm UV absorbance ratios of 0.69-1.52, indicating significant nucleic acid content was co-eluting with hCC [328]. This effect is visible through the smearing of bands in lanes 2-4 of the SDS-gel (Figure 3.10b) and could potentially be reducing the protein yield.

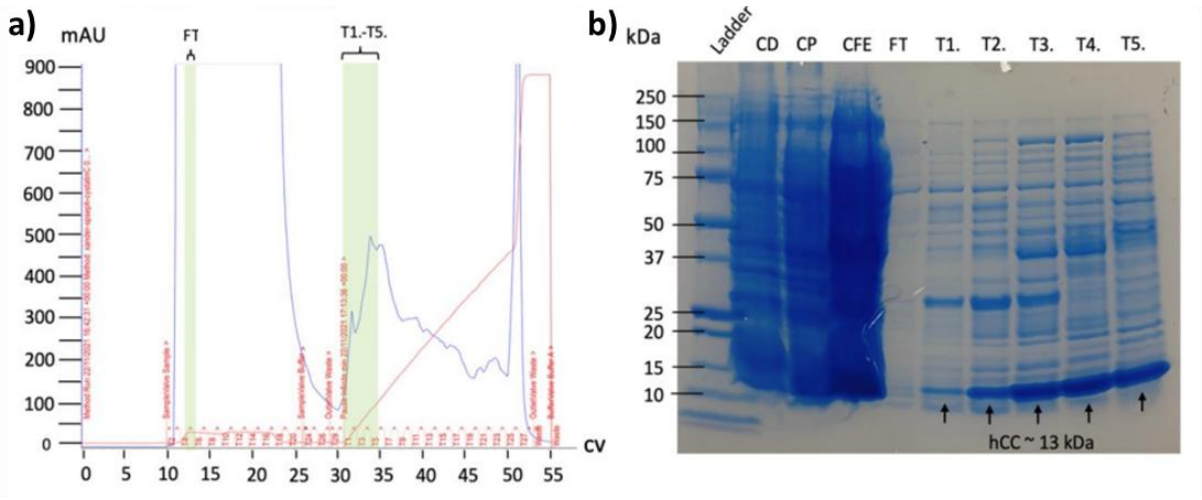

Figure 3.10: Purification of hCC from a large-scale growth using the pET22b-pelB expression system.
a) SP-Sepharose cation exchange chromatogram from 5 L of cell culture. The graph lines are (blue) UV signal and (red) NaCl gradient from 0 to 0.5 M, followed by a wash step at 1 M. The green highlighted regions show fractions used on the SDS-PAGE gel. b) SDS-PAGE of total cell debris (CD), cell pellet (CP) and cell-free extract (CFE) after sonication. "FT" is the unbound fraction of the SP-Sepharose run. "T1-5" are shown as having a strong band at 13 kDa, corresponding to hCC.

3.4 Modifying Purification to Reduce Nucleic Acid Contamination

To combat the high levels of nucleic acids using the pET22b vector, additional steps were added to the purification protocol to try and pre-filter contaminants. The primary additions were treating cell lysate with benzonase endonuclease to digest excess nucleic acids, which were then separated from hCC using a Q-Sepharose anion exchange step before SP-Sepharose. The resolubilisation buffer was changed from MES to sodium phosphate, which was capable of buffering at pH 8.0 for anion exchange and then at pH 6.2 for the subsequent cation exchange step, without the need to buffer exchange between them. The full details can be found in Section 2.4.5 as "Method 2".

Implementing this filtering step helped to remove both nucleic acids and a large proportion of contaminant proteins remained bound to the Q-Sepharose column, while hCC does not. When compared with previous purifications, the SP-Sepharose chromatogram and SDS-PAGE gel are much cleaner (Figure 3.11). The UV absorbance at 260 nm is also significantly reduced, which indicates nucleic acids contamination was successfully removed by these changes.

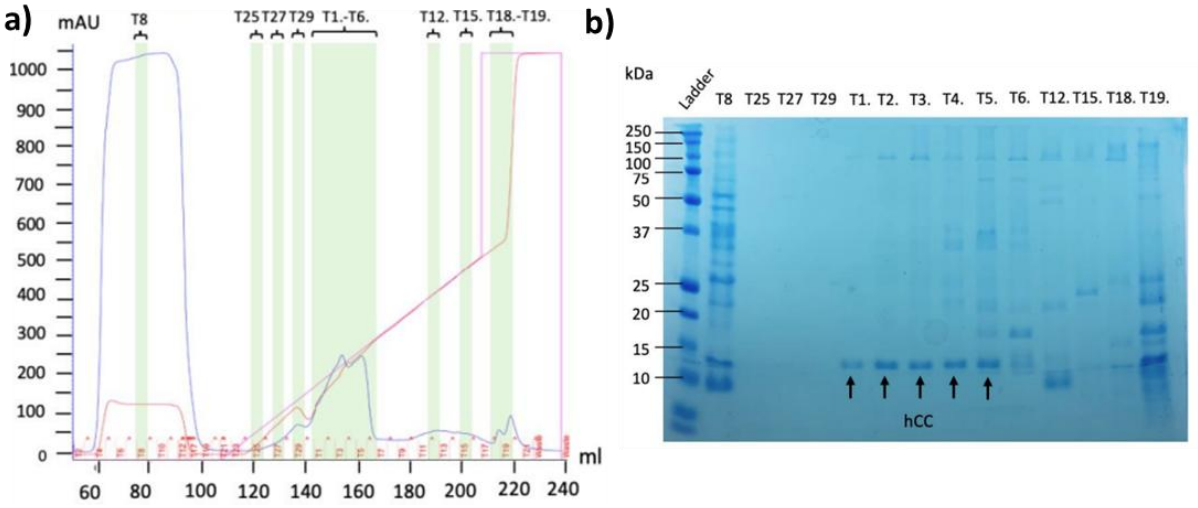

Figure 3.11: Purification of hCC after endonuclease treatment and anion exchange.
Purification of a large-scale growth (5 L) of culture, using the pET22b-pelB-hCC vector. a) SP-Sepharose cation exchange chromatography. The graph lines are (blue) UV signal and (red) NaCl gradient from 0 to 1 M. The green highlighted regions show fractions used on the SDS-PAGE gel. b) SDS-PAGE of fractions highlighted in a), with bands corresponding to hCC molecular mass labelled.

Unfortunately, removal of nucleic acid contamination by this method did not increase the overall yield of hCC. One 5 L culture using this method still only produced 0.36 mg/L under the same growth conditions which previously produced 0.30 mg/L. A slight improvement was made using a heat-shock induction at 42 °C, with the aim of inducing heat-shock proteins to help chaperone unfolded hCC in the bacterial cytosol. This change produced 0.41 mg/L cell culture, but clearly the problem that initially caused the yield to drop still persisted. Regardless, the additional filtering steps were successful at removing excess nucleic acid contamination and continued to be used in all future purifications.

3.5 Temperature-sensitive Expression System

Due to the low yields of the pINIII and pET22b vectors and the need for a high quantity of cystatin C, necessary to fuel phase-separation screening experiments, the aim was to generate alternative expression systems that may improve upon past yields. Abrahamson et. al. report extensive use of a temperature-sensitive expression system for their work with recombinant cystatin C, which appears to produce quantities up to 10% of the total protein content in their cell lysates [315]. Their extensive work with the protein, compared with expression work published by other groups, suggests their construct may be more successful than others. The plasmid they used (pHD313) is not commercially available and we could not make contact with the group in order to obtain it for our own use.

As an alternative, Prof. Jon R. Sayers (University of Sheffield, School of Medical Sciences) generously donated the pJONEX44 temperature-sensitive plasmid, which is featured in their previous paper [329]. This plasmid includes a λP_L promotor, which can be repressed by the cl857 heat-sensitive repressor protein, expressed by the M72 *E.coli* strain. cl857 repression of the λP_L promotor is lifted upon shifting the temperature to 42 °C, allowing heat-sensitive expression of a target protein [330].

The *pelB-hCC* gene sequence was cloned into the pJONEX44 plasmid, resulting in the pJONEX44-pelB-hCC construct, which was transformed into M72 cells and expressed in 2YT media as per recommendation by Prof. J.R. Sayers. These were grown normally and then induced for 2 hours at 42 °C before harvesting. Figure 3.12 shows the results of one of two growth attempts using this system.

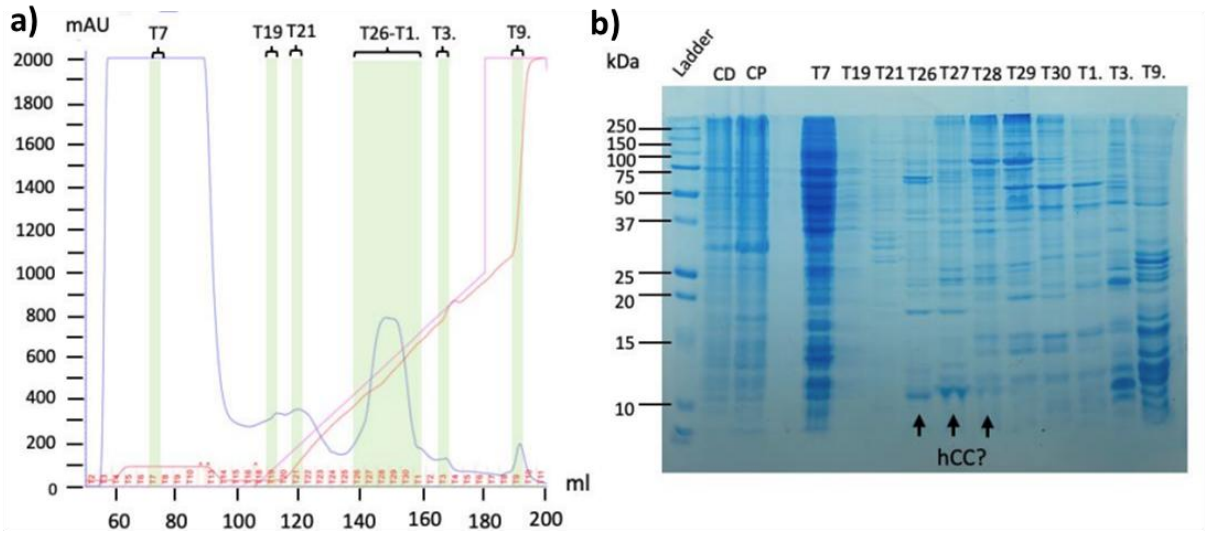

Figure 3.12: Purification of hCC from expression trials using the pJONEX44-pelB-hCC expression system.
a) SP-Sepharose cation exchange chromatogram from 5 L of cell culture. The graph lines are (blue) UV signal and (red) NaCl gradient from 0 to 1 M. The green highlighted regions show fractions used on the SDS-PAGE gel. b) SDS-PAGE of total cell debris (CD), cell pellet (CP) after sonication. SP-Sepharose fractions are labelled. Some faint bands at ~11 kDa are labelled as potentially hCC, although they appear smaller in mass than normally expected.

Although the SP-Sepharose chromatogram does show a significant peak in the expected region for hCC, this is not reflected by the SDS-PAGE gel (Figure 3.12). Neither the cell debris nor cell pellet have any significant bands around the 13 kDa region, expected of overexpression. Meanwhile, the SP-Sepharose peak does produce some faint bands across 2-3 fractions, which are significantly less prominent than previous purifications, indicating low protein concentration. Finally, the bands are

suspiciously lower down on the gel, compared with previous gels, and appear at around 11 kDa. This may suggest some proteolysis to have occurred, which is also problematic for this system.

It was very apparent from the first few attempts that this system was producing smaller quantities of hCC, compared to the pET22b or pINIII vectors. While much more optimisation could have been performed, the potential problem of hCC proteolysis was also a significant concern and so further work on this system was abandoned to pursue other avenues.

3.6 Exploring Alternative Growth Conditions

Returning to the pET22b system, one clear issue was that expression of cystatin C was likely to be toxic to the cells by inhibiting bacterial cysteine proteases from carrying out normal functions. It has been observed that pET vectors typically have a low level of persistent expression, even in the absence of IPTG [312]. This has been attributed to small amounts of lactose contamination from digests of the milk protein casein, commonly used in LB media [312]. Starter cultures grown in LB, prior to inoculation of M9 media, may therefore select for poorly expressing variants of the transformed *E.coli*, in order to avoid basal expression of cystatin C [312].

To attempt to remedy this potential problem, expression tests were performed using MDAG-135 in the starter and final cultures. MDAG-135 is an alternative minimal media, similar to M9, but supplemented with additional glucose and free amino acids. Like M9, this media does not include any casein derived digest, as a soy-based alternative was used to supplement the amino acids. The additional nutrients should allow this media to be better suited for use as a starter culture, whilst also increasing the growth rate of the final cultures to better combat toxic expression of hCC during induction [312].

Coincident with this change in growth media, carbenicillin was used as an alternative antibiotic to ampicillin. Carbenicillin is another β-lactam derivative and is more stable than ampicillin at incubation temperatures [331]. The rationale behind this substitution was to better maintain antibiotic selectivity during ongoing incubations and ensure the pET22b vector is not discarded, as may be the case when ampicillin breaks down during incubation.

The use of MDAG-135 did not appear beneficial, as SDS-PAGE gels of the pellet and cell lysate did not show a strong band at 13 kDa, as is normally observed in M9 cultures (Figure 3.13a). Further purification showed thin bands of hCC at the SP-Sepharose stage (Figure 3.13b). However, the yield of these preparations, measured by UV absorbance, were already below that of previous results,

without accounting for the gel-filtration step that would likely further reduce protein yield. The best expression was still using M9 media, although carbenicillin continued to be used in place of ampicillin, but this did not appear to have significant effects on the yield of subsequent M9 cultures.

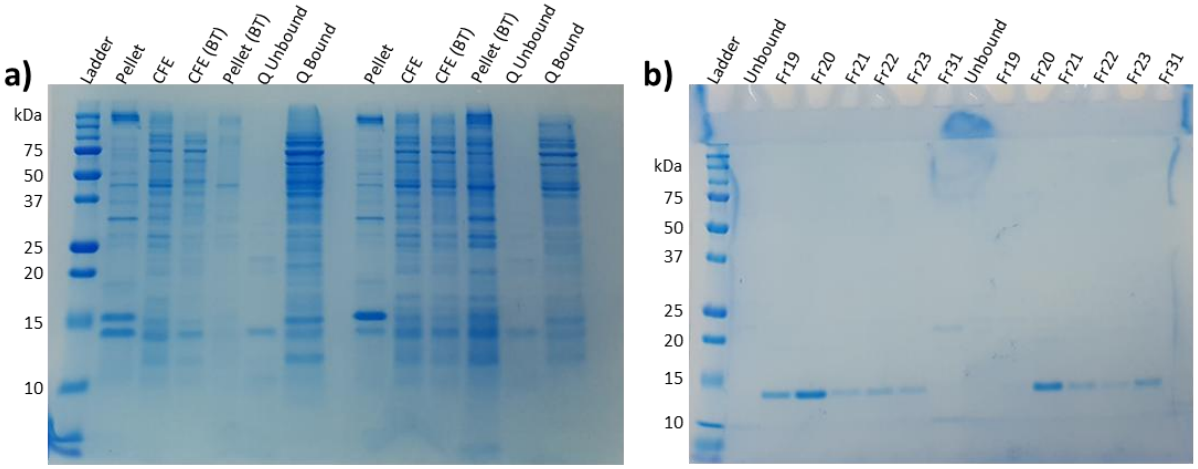

Figure 3.13: SDS-PAGE of hCC purification from MDAG-135 cultures.
a) SDS-PAGE of two separate MDAG-135 expression tests, grouped in lanes 2-7 and 9-14. Cell pellet and cell-free extract (CFE) are shown before and after benzonase treatment (BT). Q-Sepharose bound and unbound fractions are also shown. b) SDS-PAGE of the same two MDAG-135 expression tests, grouped in lanes 2-8 and 9-15, showing SP-Sepharose fractions using the same gradient elution shown by previous chromatograms.

3.7 Revisiting Small-Scale Expression Trials

Roughly two years on from the initial expression trials of both the pINIII and pET22b constructs, they were both re-examined in small-scale expression tests (500 mL) to get a new benchmark for their expression going forward. The only significant differences between these trials and those previously mentioned are the substitution of carbenicillin for ampicillin and the extra purification steps involved in “Method 2” rather than “Method 1”. Initial trials of the pINIII construct were also performed at preparative scale, with 8 flasks of 600 mL each, and using a 42 ^{o}C induction temperature, rather than at small-scale, with 18 ^{o}C overnight induction (See Table 3.1).

The results of these trials were surprising and were repeated multiple times. The pET22b vector yielded around 3.4 mg/L, roughly double its previous yield. Meanwhile, the pINIII vector, which at scale yielded roughly 1.2 mg/L, now yielded over 5 mg/L in small-scale trials. The origin of this significant yield increase remains unclear, as both carbenicillin and the additional purification steps of “Method 2” had not previously shown such dramatic increases. More puzzling still, is that virtually

identical conditions performed at larger scale, just using multiple identical flasks containing 500 mL of culture, yields much less.

Our best interpretation for this phenomenon is that temperature changes within an incubator happen more slowly for 4 L of culture, even when divided into separate flasks, compared with just a single 500 mL flask by itself. This may have the effect of slowing down the transition from 37 ^{o}C growth temperature to the 18 ^{o}C induction temperature, which may allow cultures to overgrow prematurely. Overgrown cultures can reduce protein yield as a result of cell stress or cell death, due to depletion of nutrients or accumulation of waste products in the media. Additionally, dense cultures can deplete the antibiotic and remove plasmid selectivity, allowing them to get rid of the expression vector in order to avoid overexpressing a foreign protein.

3.8 Bioreactor Growth and Expression

As part of our efforts to obtain usable quantities of cystatin C for aggregation screening experiments, a large-scale bioreactor growth was attempted, using the most-effective expression system at the time. Bioreactors allow for large volumes of culture to be maintained by constantly aerating and feeding in new media while removing waste products from the bacteria. A sample of the pINIII-ompA2-hCC plasmid and our protocol for expression was sent to the Biochemical and Bioprocessing facility (Manchester University), who grew and expressed 22 L of culture.

The resulting cell pellet was 66 g and a small portion of this was separated and purified to assess overall yield. SDS-PAGE gels of the cell lysate and of subsequent purifications steps did not appear to show any evidence of hCC expression (Figure 3.14). It is unfortunate that there was no expression during this attempt, as even a low yield could have provided a substantial amount of hCC, once purified.

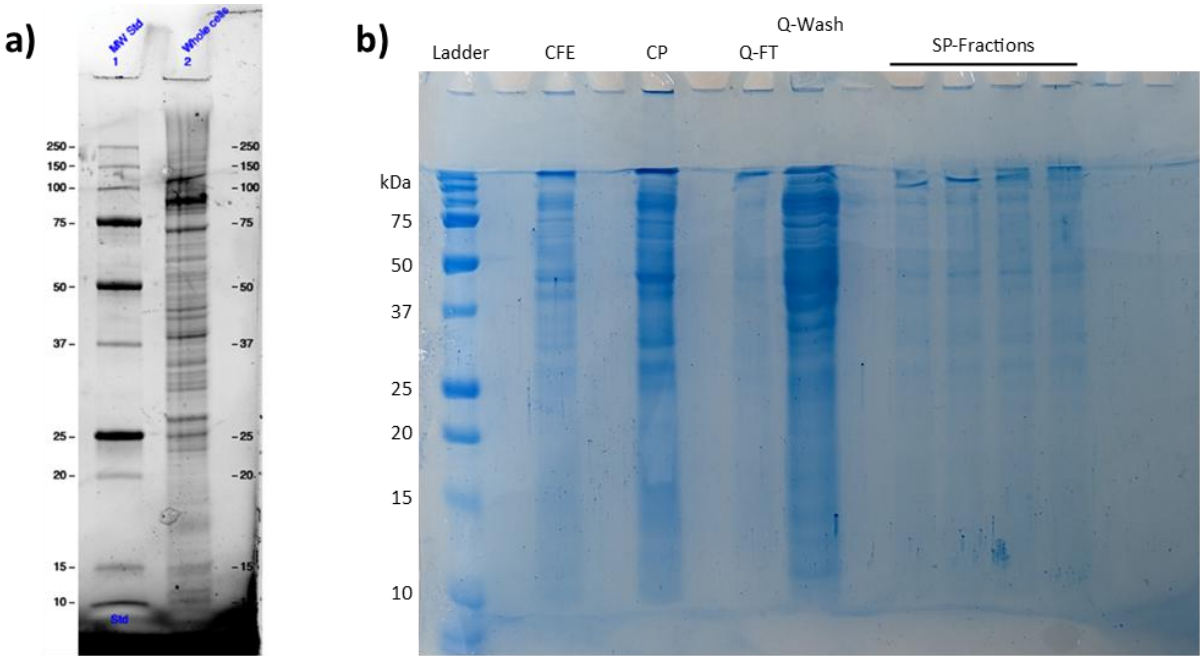

Figure 3.14: SDS-PAGE of Bioreactor Growth.
a) SDS-PAGE performed by a technician in Manchester University, showing whole-cell lysate from a 22 L bioreactor culture. The lack of strong band at ~13 kDa implies no expression of cystatin C. b) SDS-PAGE from the same culture, featuring whole-cell lysate (CFE), insoluble fraction after lysis (CP) and Q-Sepharose and SP-Sepharose purification steps. There is no evidence of a 13 kDa hCC band in any of the lanes.

3.9 Signal Peptidase I Co-expression System

Both the pINIII and pET22b vectors express cystatin C with an N-terminal periplasmic secretory sequence, taken from either the ompA2 or pelB bacterial proteins. These secretory sequences are cleaved off as the protein passes into the periplasm through signal peptidase I membrane-bound proteins [332-334]. Expressed cystatin C must enter the periplasm in order to remove this sequence, to fold and to form its disulphide bonds. Any hCC that remained within the cytosol upon cell lysis stayed insoluble and could be visualised as a ~15 kDa band on SDS-PAGE gels, best visualised in Figure 3.2 and 3.13a.

In an attempt to reduce the insoluble fraction of hCC and potentially increase overall yield, the gene for signal peptidase I and a T5 promotor region was commercially synthesised and cloned into the pACYC184 vector. This vector was isolated from a donated *E. coli* strain containing pLysS, a construct that is also built upon pACYC184. Of particular note is that pACYC184 uses an alternative origin of replication to pINIII or pET22b, meaning they can more easily co-exist in the same bacteria. This construct containing signal peptidase I, referred to as pSigP, also includes the chloramphenicol

resistance cassette, ensuring selectivity for both a hCC construct and pSigP using dual antibiotic media.

Although it has been reported that co-expression of signal peptidase can enhance periplasmic protein expression for other systems, including pelB and ompA2 [332-334], the same cannot appear to be said for hCC. Under near-identical conditions to the small-scale trials detailed in Section 3.5, co-expression of pSigP reduced the final yields by approximately one third (Table 3.1). An SDS-PAGE gel of the pET22b and pSigP expression showed similar proportions of soluble to insoluble hCC and no clear band for signal peptidase I itself (data not shown).

There are a few potential reasons for why this co-expression route did not work as intended. Firstly, the lack of signal peptidase I on the SDS-PAGE gel could indicate it was not properly expressed. It was cloned with an upstream T5 promoter, which should also become induced upon addition of IPTG. However, as a membrane-bound protein, signal peptidase I may simply become insoluble during cell lysis and therefore difficult to visualise on a gel. Secondly, the need to use two antibiotics, chloramphenicol and carbenicillin, may stress the cells to the point where any benefits of pSigP are outweighed. Finally, despite using different replication origins, having two separate plasmids may decrease the genetic load of the hCC expression plasmid, leading to less total production of hCC before cell death occurs.

This system may require further optimisation and future work would first focus on determining expression of signal peptidase I from pSigP alone, to ensure the construct was functioning as intended. While it did produce some hCC, it was not as effective as using only pINIII or pET22b.

3.10 Thioredoxin Fusion Protein Cytoplasmic Expression

In the same vein as co-expression with signal peptidase I, another aim was to bypass the need for periplasmic secretion, avoiding the problem altogether. To do this, a vector containing a fusion protein of cystatin C and thioredoxin was developed to be expressed in the Origami cell line. Origami *E. coli* contains mutations in both thioredoxin reductase and glutathione reductase, which are aimed at enhancing disulphide bond formation within the cytosol [335]. Thioredoxin is a 12 kDa soluble protein which can oxidise or reduce disulphide bonds in other proteins.

Thioredoxin has previously been used in fusion proteins, both to increase solubility during purification, and catalyse disulphide bond formation of a target protein, before it is removed by proteolytic cleavage [336-338]. Following a previous study [336], a fusion gene of hCC and thioredoxin,

alongside a cleavage and nickel-affinity purification tag, was commercially synthesised and cloned into the pET32a vector (Figure 3.15). The fusion protein was designed to be cleaved, after purification, with TEV protease, such that it would preserve an intact N-terminal on hCC with no additional amino acids. A C-terminal poly-histidine tag was included on thioredoxin, allowing the fusion protein to be purified from cell lysate, and for thioredoxin to be separated from hCC post-cleavage, using nickel affinity chromatography.

Figure 3.15: Schematic of the thioredoxin-hCC fusion protein.
A representation of the fusion protein structure including thioredoxin (Trx) and cystatin C (hCC). The cleavage site for TEV protease (TEV) is found at the N-terminal of hCC and does not cause any additional residues to the final hCC sequence when cleaved. The C-terminal of thioredoxin includes a poly-histidine repeat (6xHIS), which is used to separate cleaved thioredoxin from hCC via nickel affinity chromatography.

The concentration of fusion protein, purified by affinity chromatography from cell lysate, appeared exceptionally high, visible on SDS-PAGE gels as a huge band at roughly 27.5 kDa (Figure 3.16). The purified fusion protein was then cleaved by TEV protease, causing a large amount of precipitation to occur, which indicated insoluble protein had formed. The remaining soluble fraction, after TEV cleavage, could be purified to give a small amount of hCC (Figure 3.16, left). The insoluble fraction was resolubilised in 6 M guanidine and dialysed, in an attempt to refold any precipitated hCC. While some hCC appeared to be recovered using this method (Figure 3.17), it was later determined to be fairly unstable and prone to further precipitation. This indicates hCC is not folding properly and forming its disulphide bonds as part of the fusion protein, leading to immediate precipitation after thioredoxin is cleaved, which cannot be recovered by refolding in guanidine.

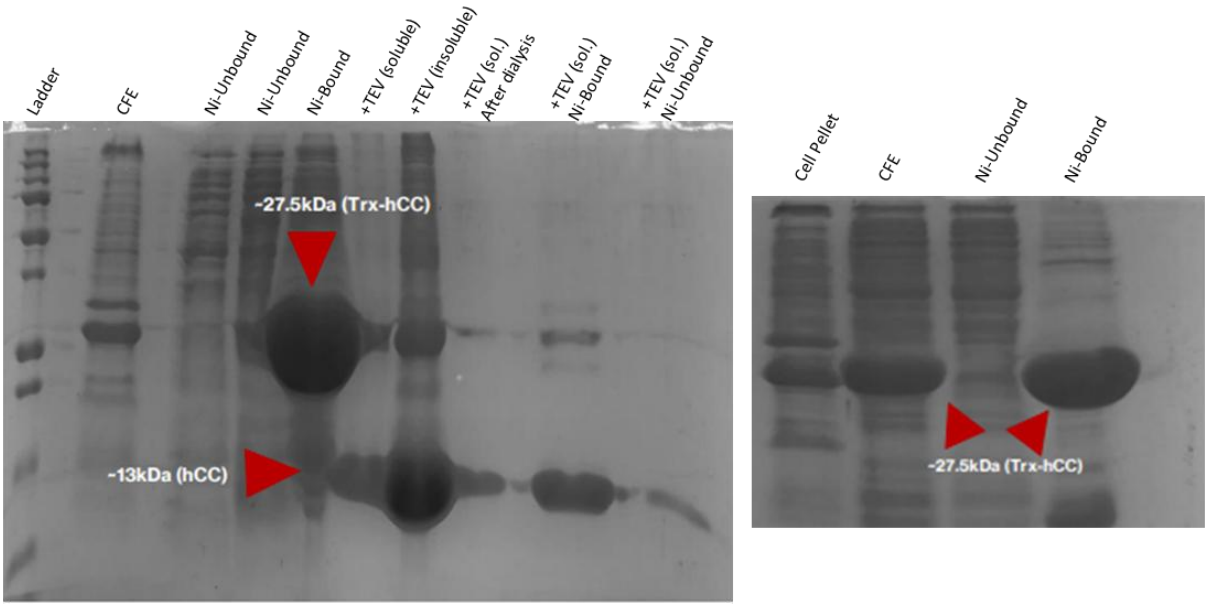

Figure 3.16: Initial purification of Trx-hCC fusion protein and TEV cleavage.
SDS-PAGE gels showing very large 27.5 kDa bands, corresponding to the Trx-hCC fusion protein, in the cell lysate (CFE) and nickel-bound fraction (Ni-Bound). The left-hand gel also shows the soluble fraction after TEV cleavage (+TEV (soluble)), as well as its downstream purification including dialysis, to remove excess imidazole, and a second round of Ni-affinity to remove TEV and thioredoxin (+TEV (sol.) Ni-Bound) from hCC (+TEV (sol.) Ni-Unbound). The insoluble fraction after TEV cleavage was resolubilised in 6 M guanidine and then dialysed to slowly reduce the guanidine concentration (+TEV (insoluble)).

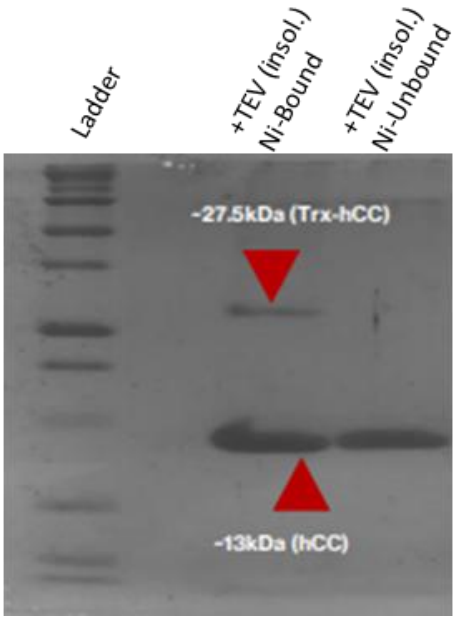

Figure 3.17: Affinity chromatography of insoluble fraction after TEV cleavage.
The insoluble fraction following TEV cleavage was resolubilised in 6 M guanidine, which was dialysed to remove guanidine slowly. This resolubilised fraction was then applied to a Ni-affinity column to remove TEV, thioredoxin and any Trx-hCC that had escaped cleavage. Both the bound and unbound fractions contain a significant 13 kDa band, which could correspond to hCC or thioredoxin in the case of the bound fraction.

The TEV proteolysis usually requires a reducing agent, such as DTT, to regenerate the active site thiol group after cleavage. A standard DTT concentration of 1 mM was used for cleavage, which unfortunately generated a large insoluble fraction. As discussed in Chapter 4, 1 mM DTT is sufficient to partially aggregate purified hCC by reducing its disulphide bonds. Alternative TEV cleavage conditions, without DTT at the same or higher TEV concentrations, were tested to see whether soluble hCC yield could be improved (Figure 3.18). This showed that the proportional soluble fraction could be greatly increased by removing DTT and increasing TEV concentration, at the cost of total protein yield.

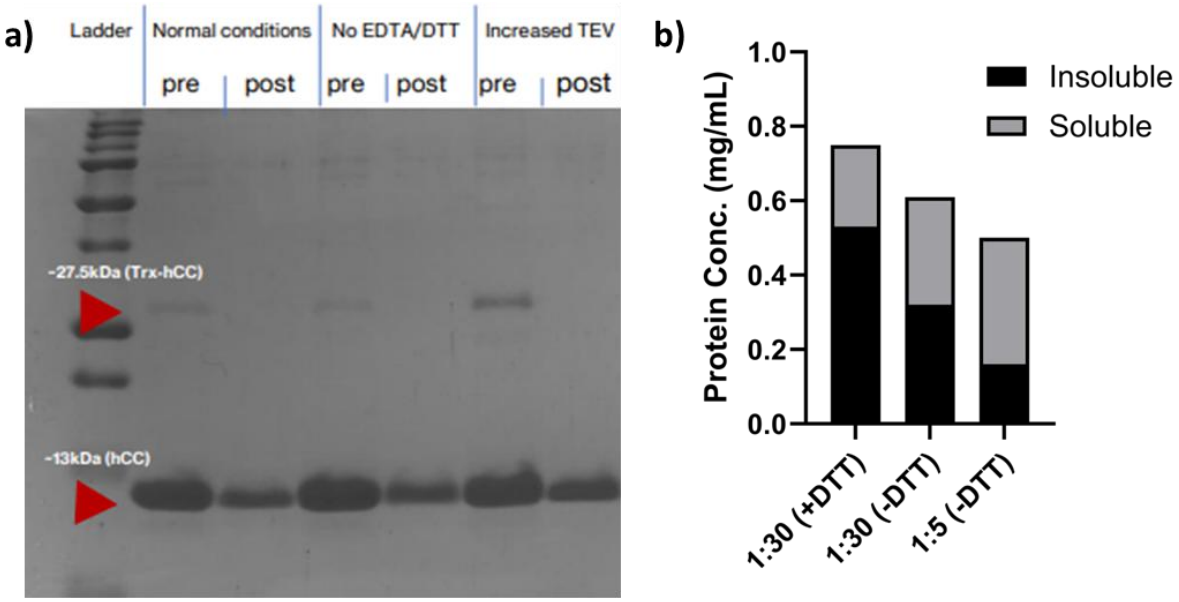

Figure 3.18: The effect of TEV cleavage conditions on soluble hCC concentration.
a) SDS-PAGE showing pre- and post-purification of the soluble fraction, after TEV cleavage, by Ni-affinity chromatography. "Normal conditions" describes standard TEV cleavage conditions of 1:30 TEV:sample protein concentration, with 1 mM DTT and 0.5 mM EDTA. Alternative cleavage conditions without EDTA and DTT (no EDTA/DTT), or at a TEV ratio of 1:5 without EDTA and DTT (Increased TEV), are also shown. b) A graph representing the final hCC concentrations of soluble and insoluble fractions after TEV cleavage in the above conditions.

The stability of the soluble fraction was assessed by 1D NMR (data not shown), which gave uncharacteristically wide peaks compared with previous measurements. This is an indication of partial unfolding and suggests that despite remaining soluble, the cleavage product of the fusion protein is not likely to be correctly folded. The high level of expression of the fusion protein shows promise in this method for considerably increasing hCC yield. However, further work would need to be done to ensure hCC is properly folded, and remains so after TEV cleavage, in order for this method to generate usable protein.

3.11 Small volume expression trials

The sudden increase in hCC yield when expressing single 500 mL cultures of pINIII or pET22b, when compared to batches of 8x500 mL flasks (Section 3.5), raised questions about how this may be affecting expression. To further test this phenomenon, a series of 2x500 mL flask batches were grown and expressed to see whether the total volume of culture in an incubator affected the final yield. Two separate batches using the pINIII vector, totalling 2 L of culture, were combined and purified for a yield of 2.1 mg/L culture (Figure 3.19).

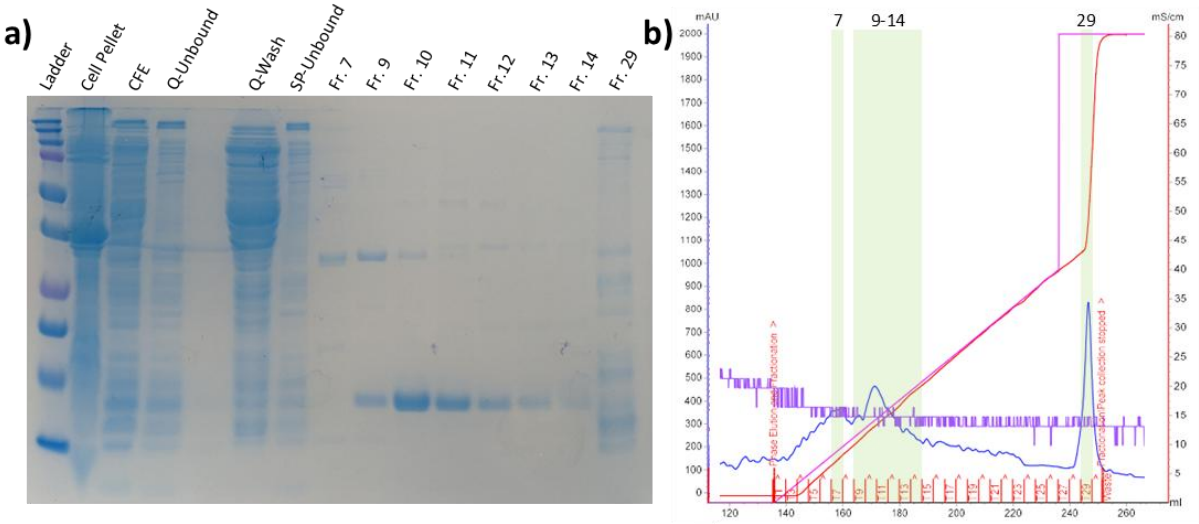

Figure 3.19: Purification of hCC from smaller growth batches using the pINIII-ompA2-hCC expression system.
a) SDS-PAGE showing insoluble pellet and soluble cell lysate (CFE), alongside Q-Sepharose and SP-Sepharose purification steps. SP-Sepharose fractions, corresponding to green highlighted regions on the SP-Sepharose chromatogram in (b), are shown in lanes 8-15. A 13 kDa band of hCC can be seen in SP-Sepharose fractions 9-13.

A yield of 2.1 mg/L with 2x500 mL batches is considerably better than previous yields of 0.3-1.1 mg/L with either 8x500 mL or 8x600 mL batches. However, it doesn't match the single flask expression tests, which yielded around 5 mg/L. This shows a clear, albeit confusing, link between the number of flasks used per growth batch and final protein yield. As mentioned before, this could be the result of more overgrowing during induction in larger batches, due to a slower rate of temperature change when cooling down to 18 ^{o}C induction temperature. An alternative explanation could be that degradational processes, such as proteolysis or disulphide breakage, may have more time to occur when handling larger volumes of culture.

3.12 Summary and Conclusion of hCC Growth Optimisation

To summarise, using the original pET22b and pINIII constructs remains the most consistent method for purifying hCC. However, there is a clear issue involving the total volumes of individual growth batches. At best, one can expect to receive around 5mg total from a 4.8 L culture using 8 flasks of 600 mL each. Meanwhile, half of this amount (2.55 mg) can be purified from just a single flask of 500 mL culture, if grown separately. The rapid diminishing returns for increased batch volume impose a strict upper limit on hCC production without access to additional incubators to run such batches in parallel.

The three alternative expression systems: temperature-sensitive expression with pJONEX4-pelB-hCC, signal peptidase I co-expression with pSigP, or thioredoxin fusion protein with pET32a-Trx-6xHIS-TEV-hCC in Origami B cells, have each failed to improve expression. The pJONEX4 construct shows proteolysed hCC bands and low protein quantity by SDS-PAGE, while pSigP co-expression resulted in a reduction in purified hCC vs. controls. Although, this may be due to a lack of signal peptidase expression. The most promising alternative system was the Trx-hCC fusion protein, which showed clear overexpression, but any hCC produced did not appear to be correctly folded after cleavage. Future work focussing on this system may seek to adapt the Trx-hCC construct to use a serine protease tag, instead of a cystine protease, and to treat isolated Trx-hCC fusion protein with a gradual titration of an oxidising agent, such as glutathione, to promote thioredoxin-mediated disulphide formation in cystatin C prior to cleavage.

Even though there has not been much improvement in hCC expression yields, a variety of potential avenues to explore and optimise are now available for future yield increases. Future work in this area should focus on: identifying precisely why increased batch volumes have such diminished yield; expression of signal peptidase from pSigP to verify the construct integrity before future trials; and optimising the processing of Trx-hCC fusion protein to induce hCC folding prior to cleavage, including disulphide formation, and maintain its folded state after TEV cleavage occurs.

Chapter 4: Investigating Intracellular Cystatin C Aggregation

4.1 Introduction to Cystatin C Results

The overall aim of this section is to develop a model system with cystatin C, that displays similar features of Bunina bodies. Bunina bodies are large, spherical aggregates, containing cystatin C, which form intracellularly. Based on the spherical shape and large size of these aggregates, and the simultaneous depletion of soluble cystatin C in affected neuronal cells, I hypothesise that Bunina bodies form via a phase-separated intermediate state.

To validate this hypothesis, and find conditions where cystatin C might aggregate into Bunina body-like inclusions, I first conducted simple *in vitro* screens of cystatin C in a range of conditions that could induce aggregation and are relatively physiological. Commonly screened conditions when searching for phase-separation include pH, temperature, salt and addition of specific biomolecules known to interact with the target [339-341].

In the following screens, pH and temperature were kept constant at pH 7.4 and 37 ^{o}C in line with reported temperature and cytosolic pH in human cells [342, 343], while salt was varied to investigate the effect of electrostatic interactions on cystatin C aggregation. Different concentrations of RNA were also screened, due to its abundance intracellularly and previously reported ability to induce phase-separation in some systems [141, 148, 344].

Cystatin C contains a secretory leader sequence, which results in its export through the cell secretory pathway and into the extracellular matrix. Intracellular Bunina bodies may therefore form either from full-length cystatin C prior to its export, or from re-imported cystatin C which has lost its secretory sequence. This thesis focuses on the leaderless form of cystatin C, under the hypothesis that the majority of cytosolic cystatin C arrives via endocytosis and lysosomal leakage, rather than by escaping the secretory pathway. Protein production constraints prohibited assessment of both forms.

Another important consideration of cystatin C intracellular mislocalisation is the presence of two disulphide bonds in cystatin C's structure [345]. These stable covalent bonds help stabilise the structure and are generally only found in extracellular proteins, due to the reducing environment of the cell cytosol [346, 347]. To mimic this condition for screening, dithiothreitol (DTT) was used to reduce and break the disulphide bonds in cystatin C.

In order to detect and quantify the presence of aggregation in these screens, a mixture of light-scattering measurements (Section 2.5.2) and differential interference contrast (DIC) microscopy (Section 2.5.3) was used. The advantage of DIC microscopy is that it can be used to visualise liquid

phase-separated droplets by the change in refractive index between dense and dilute liquid phases. However, phase-separation was never observed in these screens.

A major limitation of this work is the difficulty in producing sufficient quantities of recombinant cystatin C (Chapter 3). The protein concentration is an important factor that dictates which conditions will lead to phase-separation and concentrations above or below certain thresholds will not undergo phase-separation [348]. The majority of *in vitro* work in this chapter uses a cystatin C concentration of 10 µM, which may be outside the range necessary for phase-separation to occur. Use of polyethylene glycol (PEG) as a crowding agent is common practice to help induce phase-separation by increasing the local concentrations of other molecules in solution by volume exclusion [349, 339].

This chapter ends with some *in vivo* expression of cystatin C in HeLa cells, a standard human cell line for protein expression [350, 351]. The cystatin C expressed in these cells include one of two tags that can be visualised using fluorescence microscopy. This allows detection of cystatin C localisation in the HeLa cells, which is paired with a series of markers for various common cytosolic structures that cystatin C may localise to. The aim of this section is to determine whether cystatin C exhibits Bunina body-like morphology in these cells and whether it co-localises to other cell components, such as mRNA or stress granules.

4.2 The Effect of Dithiothreitol on Cystatin C Stability

Whilst aiming to determine which conditions may lead to the formation of Bunina bodies, I first targeted the pair of disulphide bonds that help to maintain cystatin C's structure. Although the typical environment for cystatin C is extracellular in tissue fluid and blood plasma [352], Bunina bodies are found intracellularly, which is a more reducing environment [346, 347] that would likely lead to breakage of existing disulphides.

To mimic this environment, cystatin C was titrated with different concentrations of dithiothreitol (DTT), a reducing agent commonly used to break disulphide bonds [353, 354]. The resulting aggregation of cystatin C was then monitored by a combination of light-scattering (Figure 4.1b), light microscopy (Figure 4.1c) and 1D-NMR (Figure 4.2).

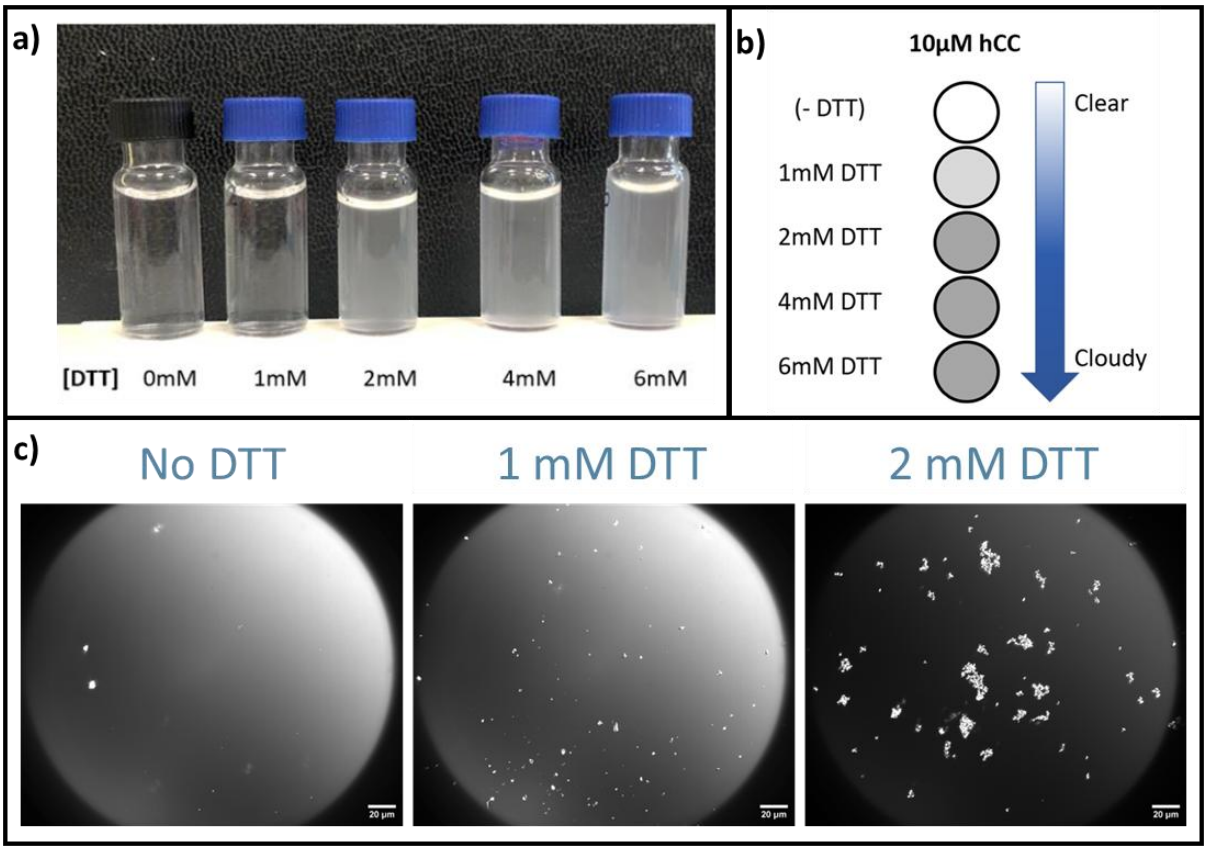

Figure 4.1: Cystatin C aggregation in the presence of dithiothreitol.
a) Picture displaying increasing cloudiness of solutions of 10 µM hCC and varying concentrations of DTT. b) Graphic showing relative light-scattering measurements of the hCC and DTT conditions. c) Differential interference contrast microscopy of hCC aggregates formed in the presence of 0, 1 and 2 mM DTT.

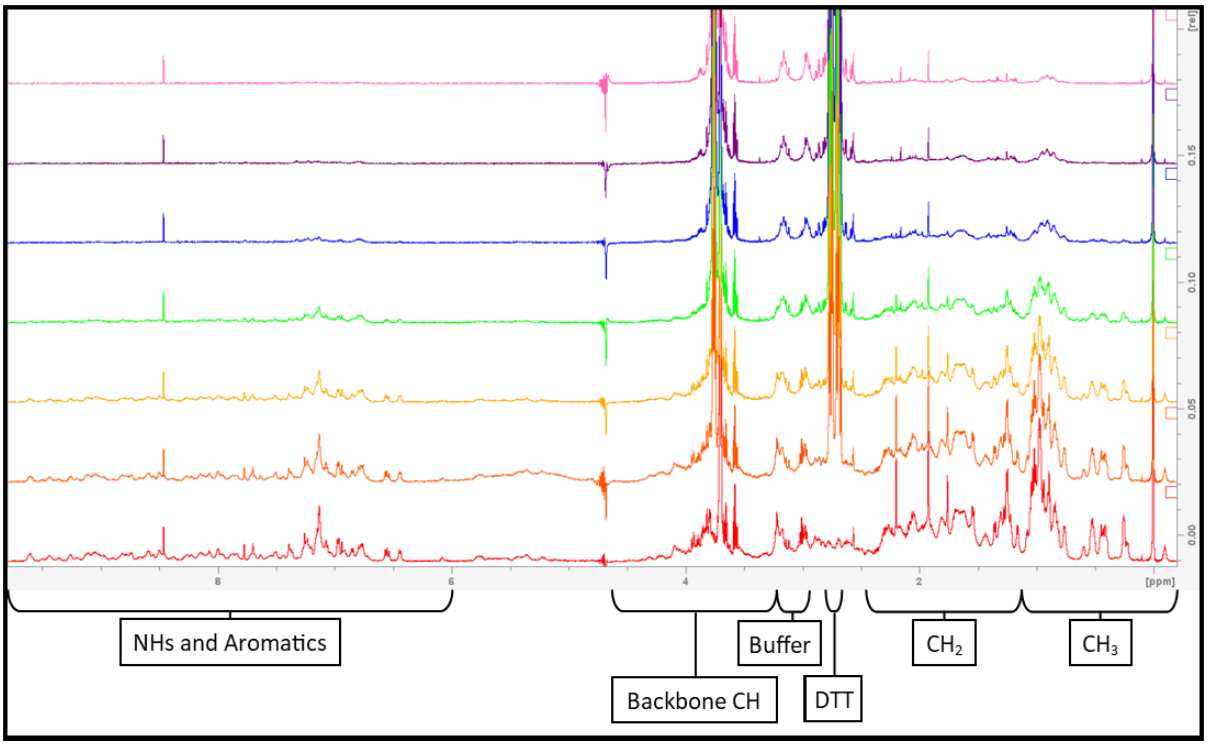

Figure 4.2: 1D NMR titration of cystatin C with DTT.
Shown are ^{1}H chemical shifts of cystatin C with increasing concentration of DTT: 0 mM (red), 1 mM (orange), 2 mM (yellow), 3 mM (green), 4 mM (blue), 5 mM (purple), 6 mM (pink). The positions of the different chemical groups involved are annotated.

At the 10 µM concentration used, cystatin C can already be seen forming small solid aggregates in 1 mM DTT, which are considerably larger at 2 mM DTT (Figure 4.1c). The light-scattering measurements do not increase significantly at concentrations higher than 2 mM DTT (Figure 4.1b). However, the NMR would suggest that some folded cystatin C remains until around 4 mM DTT (Figure 4.2).

The even reduction in signal intensity across the amide and methyl bands of the NMR spectra shows a loss in the visibility of cystatin C, whilst what remains is fully folded. This is in contrast with what might be observed if partially unfolded forms of cystatin C remained soluble, which would be marked by the loss of specific peaks in these bands. This indicates that cystatin C rapidly aggregates to form particles too large to be observed by NMR due to faster relaxation rates [355, 356].

4.3 The Effect of Salt on Cystatin C Stability with Dithiothreitol

To continue probing conditions for cystatin C phase-separation, I next looked at varying the solution ion concentration using Sodium Chloride. Increasing ion concentration has the effect of screening electrostatic interactions on the protein surface, which can lead to unfolding by disrupting salt bridges between the protein residues. However, in some cases the presence of ions can instead stabilise protein structure. In these cases, low concentrations of ions may enhance specific protein-ion binding interactions, while high concentrations increase the hydrophobic effect, which can lead to a more stable collapsed protein structure [357-359].

The cell cytosol of a typical mammalian neuron contains a relatively small amount of sodium and chloride ions (< 30 mM) [360, 361], as these are mostly transported extracellularly to maintain the electric potential across the neuronal membrane. Instead, the majority of ions present intracellularly are potassium and membrane-impermeable anions, including most proteins and RNA. Potassium is reported to have an intracellular neuronal concentration of 75 or 140 mM [360, 361], which is presumably similar to the overall negative charge contribution from impermeable anions. The decision to use sodium chloride in this case was due to a previous lack of consideration for the above. In hindsight, solutions involving potassium, with either phosphate or acetate to mimic RNA or protein anions, would have been more suitable.

Sodium chloride was added to cystatin C at concentrations up to 200 mM to provide a similar ionic strength to intracellular neuronal conditions, whilst removing the complexity of having a range of different ions and large molecules that might have specific interactions beyond charge. Cystatin C, at concentrations of 10, 40 and 80 µM, did not aggregate in the presence of sodium chloride alone over a 24-hour time period.

1 mM DTT was then added to each condition, which is sufficient to induce some cystatin C aggregation alone, to explore any moderating effects that sodium chloride might have on the aggregation process. The microscopy of 10 µM cystatin C (Figure 4.3) shows a small amount of aggregation in the no salt condition, which does not appear to occur in 200 mM NaCl. Meanwhile, at the higher 80 µM cystatin C concentration (Figure 4.4), aggregation occurs in both NaCl conditions and does not appear particularly different.

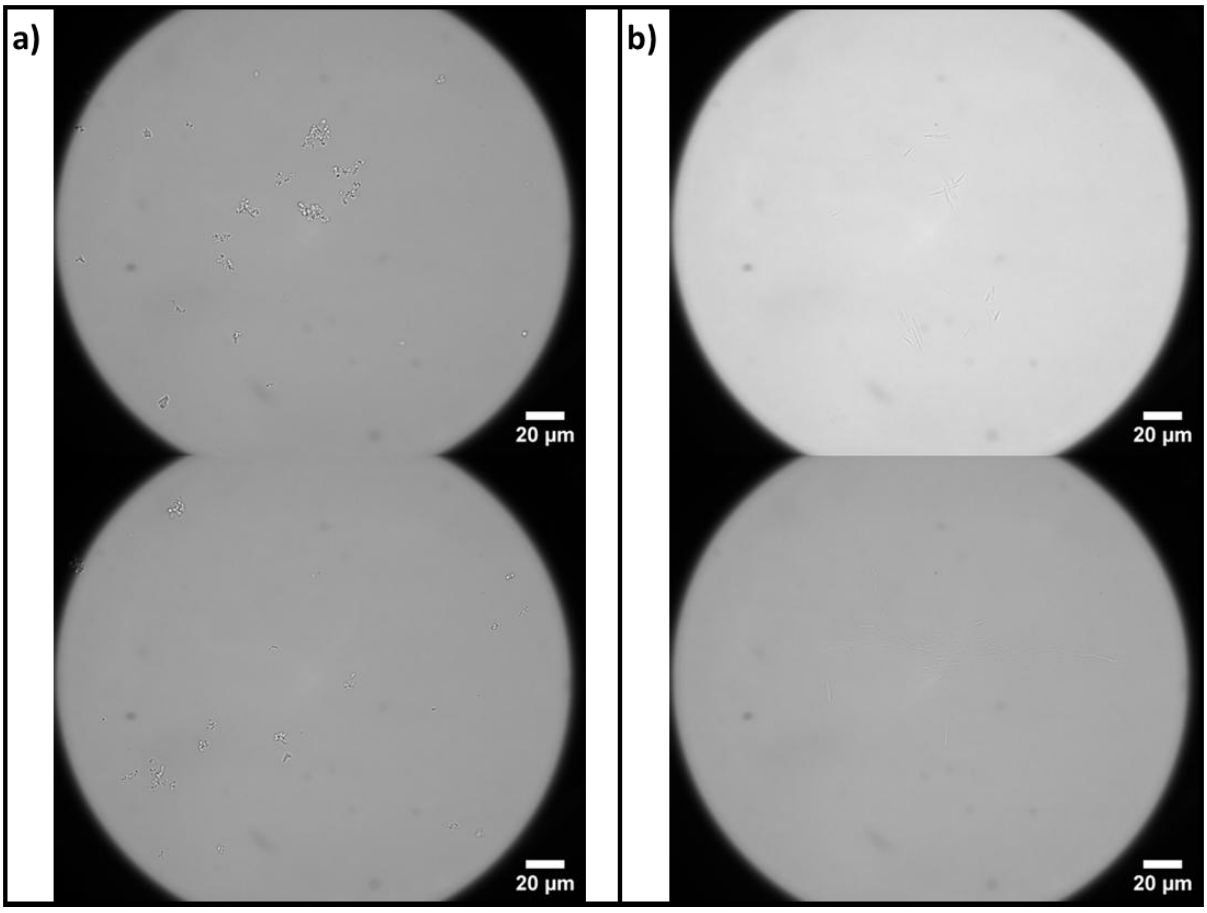

Figure 4.3: DIC microscopy of 10 µM cystatin C and 1 mM DTT in the presence or absence of salt. a) 10 µM hCC and 1 mM DTT forming small aggregates. b) Addition of 200 mM NaCl appears to prevent aggregate formation.

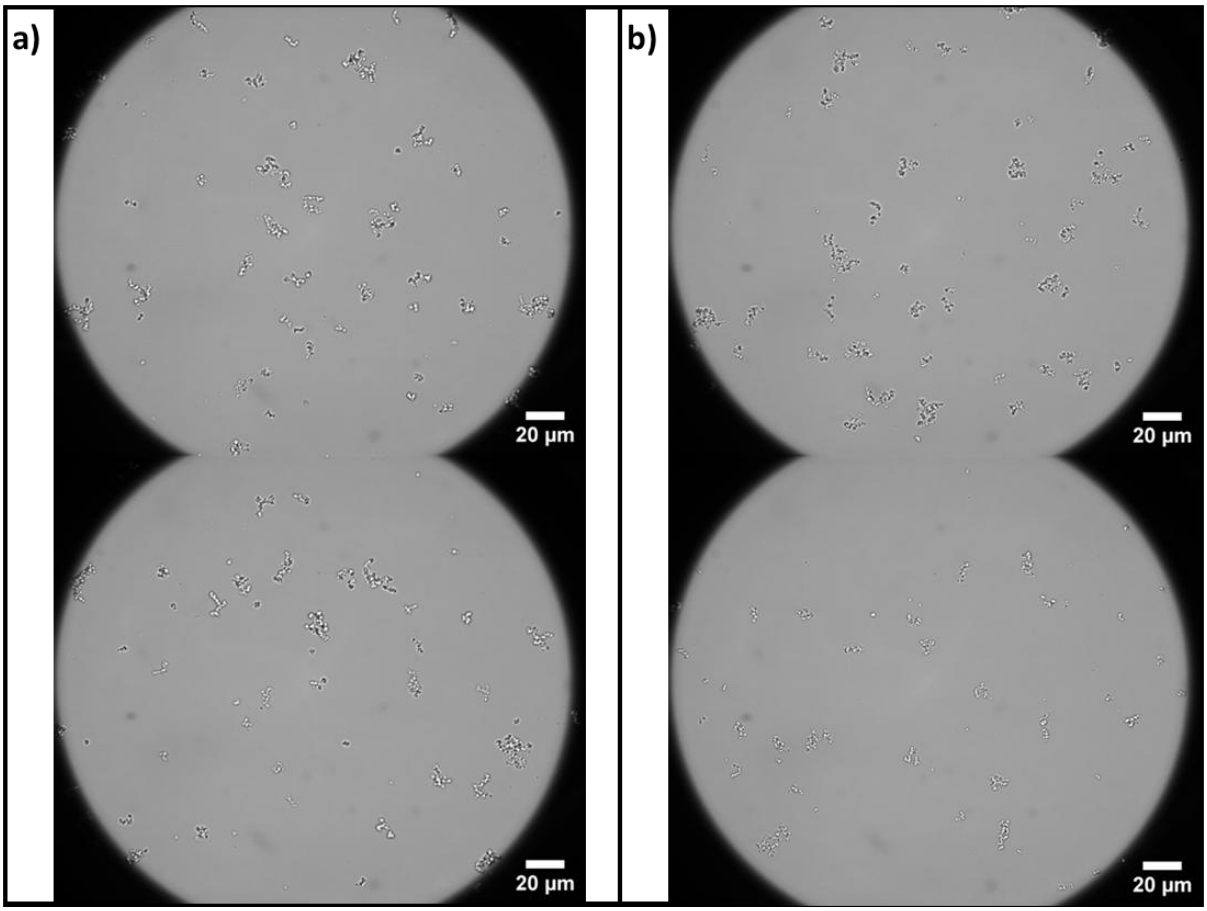

Figure 4.4: DIC microscopy of 80 µM cystatin C and 1 mM DTT in the presence or absence of salt. a) 80 µM hCC and 1 mM DTT forming small aggregates. b) Addition of 200 mM NaCl does not seem to moderate the aggregation.

These data, while not quantified, would suggest that addition of NaCl alone will not cause cystatin C aggregation and, in fact, inhibits aggregation at lower protein concentrations, presumably through ion stabilising interactions [357-359]. It can be concluded that bulk-ionic effects are not a major factor in cystatin C aggregation, when compared to the influence of disulphide bond breakage caused by the intracellular reducing environment.

4.4 The Interaction of Cystatin C with RNA

An important feature of biomolecular condensates is the formation of a scaffold, comprised of multivalent biomolecules, which typically bind to each other and to "client" molecules. The scaffold molecules can more easily phase-separate and associate to form an interconnected network. Client molecules are then able to partition into the condensate, driven by their interactions with the scaffold network [141, 148, 362].

One commonly cited scaffold molecule, found abundantly in the cytosol, is RNA [141, 148, 344]. While cystatin C is not reported to have specific RNA-binding activity, it's unusually high isoelectric point of 9.3 results in it being highly positively charged in most instances [363]. I hypothesise that this charge potentially allows for non-specific electrostatic interactions with negatively charged RNA, that could drive Bunina body formation.

Cystatin C was first screened with different concentrations of whole yeast RNA extract, up to 150 mM RNA nucleotide concentration, which are laid out in Table 4.1. None of the conditions listed displayed any aggregation, as observed by light scattering and microscopy. Therefore, RNA alone does not appear to be sufficient to initiate phase-separation or aggregation of cystatin C.

RNA Concentration in NMPs	Buffer Control	10 µM hCC (0.13 mg/mL)	40 µM hCC (0.53 mg/mL)
Control (no RNA)	✓	✓	✓
1 mM (0.34 mg/mL) RNA	✓	✓	
2 mM (0.68 mg/mL) RNA	✓	✓	
4 mM (1.3 mg/mL) RNA	✓	✓	✓
6 mM (2.0 mg/mL) RNA	✓	✓	
8 mM (2.7 mg/mL) RNA	✓	✓	
10 mM (3.4 mg/mL) RNA	✓	✓	✓
15 mM (5.1 mg/mL) RNA	✓	✓	
25 mM (8.5 mg/mL) RNA	✓	✓	✓
30 mM (10 mg/mL) RNA	✓	✓	
50 mM (17 mg/mL) RNA	✓	✓	✓
100 mM (34 mg/mL) RNA	✓	✓	✓
150 mM (51 mg/mL) RNA	✓	✓	✓

Table 4.1: List of screened RNA and cystatin C conditions *in vitro*.
This table shows the range of conditions screened for cystatin C aggregation in the presence of whole yeast extract RNA (Section 2.5.1). In all cases no aggregation was observed through either light-scattering measurements or direct observation by microscopy. Upon addition of 2 mM DTT, all conditions appeared to aggregate equally well, as observed in 2 mM DTT without RNA.

Additionally, ^{15}N isotopically labelled cystatin C was titrated with RNA, up to 34 mM nucleotide concentration, and changes in the protein residues were observed using 2D-NMR (Section 2.5.5). These data can be processed to obtain weighted chemical shifts changes for each cystatin C residue (Figure 4.5), showing how significantly the addition of 34 mM RNA affected the local chemical environment of each amino acid. These changes could then be mapped to a 3D-structure of cystatin C, in both its monomer and dimer states, to visualise the changes (Figure 4.6).

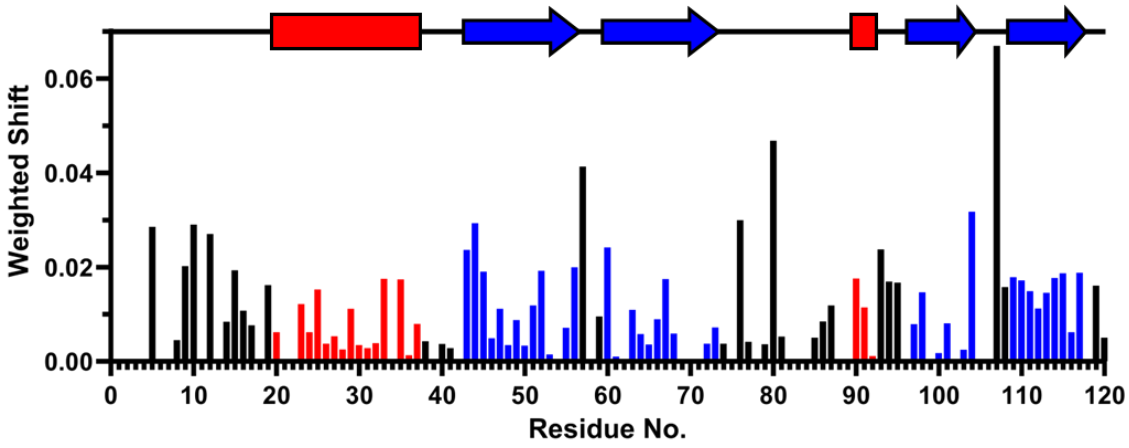

Figure 4.5: Weighted chemical shift changes of cystatin C RNA titration.
The peaks of an NMR-HSQC spectra of cystatin C were mapped to a previously assigned spectrum of cystatin C [313]. The movement of each peak was then tracked during successive additions of up to 34 mM RNA. The graph displays the chemical shift changes in δH and δN for each residue upon addition of 34 mM RNA, combined into a "weighted shift" as described in Section 2.5.5. The top part of the graph displays the secondary structure layout of cystatin C monomer, showing α-helical (red) and β-sheet (blue) regions of the sequence.

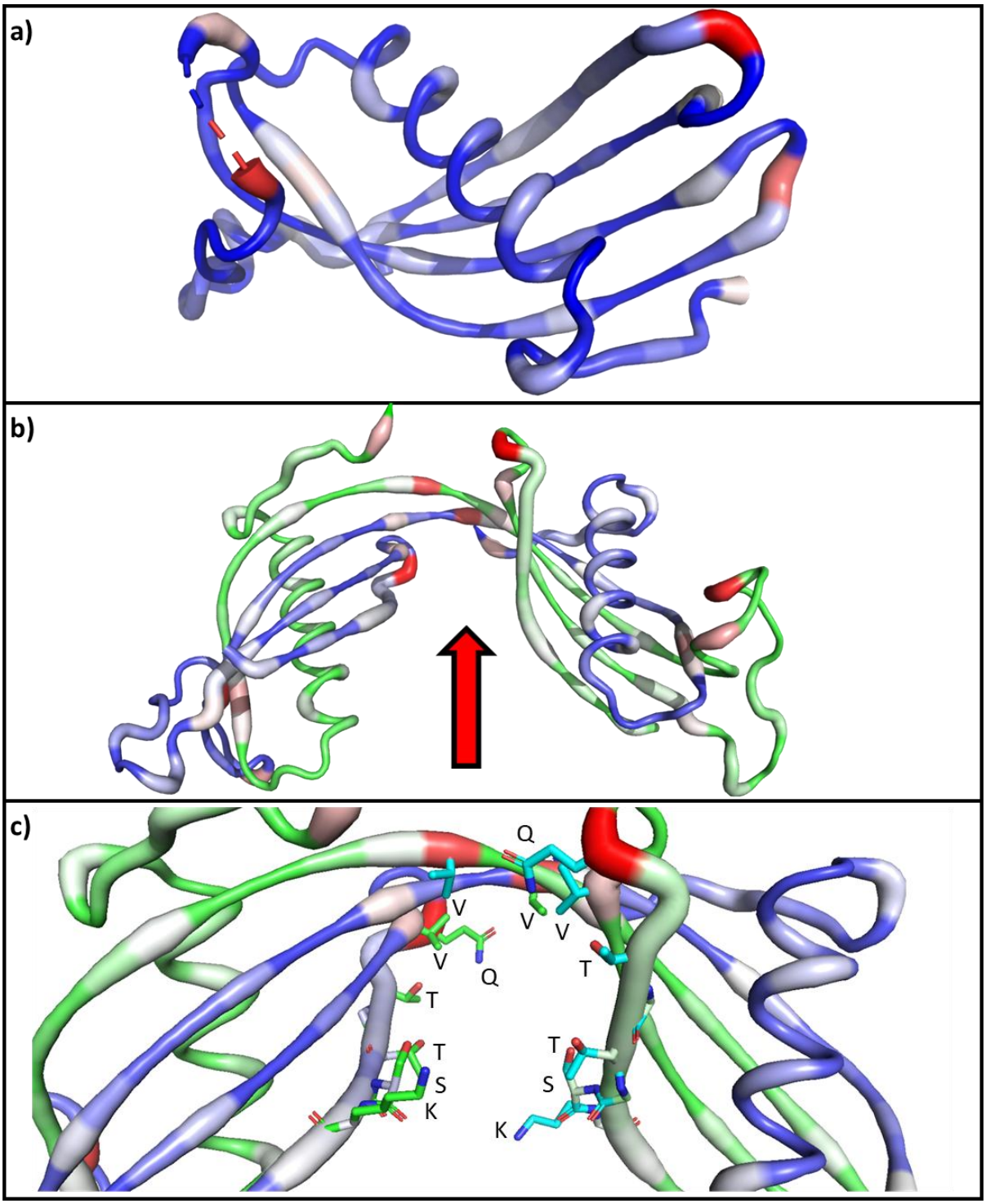

Figure 4.6: Mapped chemical shifts upon RNA interaction to cystatin C structure.
The weighted chemical shift changes, shown in Figure 4.5, are displayed in each image by colour and strand thickness. Individual cystatin C molecules are shown as either blue or green. Thicker parts of the strands, that also transition in colour to white then to red, indicate increasing chemical shifts of those residues. Structures shown are: a) monomer cystatin C (PDB: 3GAX) [177] and b) dimer cystatin C (PDB: 1R4C) [202], which includes an arrow pointing at a potential RNA binding pocket with higher chemical shifts. c) displays a zoom in of the dimer binding pocket with relevant amino acids shown and labelled.

It should be noted that this NMR data is very preliminary. Due to a lack of protein concentration in the starting sample, there was a significant dilution effect caused by titrating RNA that limited the final RNA concentration. The chemical shift changes observed were very small, with maximum shifts of 0.06 ppm in δH and 0.19 in δN, that could have been improved at higher RNA concentrations.

The monomer structure (Figure 4.6a) shows the largest shifts occur in the β-turn elements between β-strands 1-2 (residue 57) and 3-4 (residue 107), and in the extended loop region (residues 76 and 80). There is also an extended region of chemical shifts along β-strand 4, between residues 107-119. There does not appear to be an obvious binding location for the RNA in the monomer structure.

Mapping these shifts onto the dimer structure of cystatin C shows localisation of many of the high-shift residues to something resembling a binding pocket between the two domains (Figure 4.6b). This seems promising, as a series of charged resides can be found facing in on one side of the groove (K, S, T and Q), which could potentially coordinate the RNA phosphate backbone (Figure 4.6c). Meanwhile, residues available on the face of the linker between the two domains are hydrophobic, primarily valine (V), which could participate in pi-interactions with the RNA bases.

These data might suggest a previously unreported RNA binding pocket that forms when cystatin C dimerises. However, as previously stated, the quality of the data is not sufficient to make any concrete claims. Therefore, repeating this experiment with a higher starting concentration of cystatin C, or using pre-dimerised protein, and higher final concentration of RNA would be required to verify these observations.

4.5 Cystatin C Aggregation Timelapse in DTT and PEG Conditions

In order to find conditions where cystatin C might phase-separate, I attempted to map the aggregation landscape of cystatin C at 10 µM in varying concentrations of DTT and polyethylene glycol (PEG). In doing so, I aimed to find conditions where aggregation occurs slowly, which could become the starting point for future screens looking for phase-separation specifically.

PEG was introduced as a crowding agent to mimic the volume exclusion effect in the cytosol from the high concentration of macromolecules [349]. This also helps to partially counteract the limited amount of cystatin C available by increasing its effective concentration in conditions with higher PEG concentration. Crowding agents, including PEG, are also commonly found to promote the formation of biomolecular condensates that form via liquid-liquid phase-separation [339].

A series of 20-hour light microscopy timelapses were recorded for a range of conditions between 0 – 2 mM DTT and 0 – 10%$^{(w/v)}$ PEG. Representative images from some of these conditions can be viewed in Figure 4.7, while a phase-diagram displaying aggregation onset times is displayed in Figure 4.8. The phase-diagram shows clearly that increases in both PEG and DTT lead to faster aggregation of cystatin C. However, PEG alone does not induce cystatin C aggregation, at this protein concentration and buffer conditions, up to 10%$^{(w/v)}$.

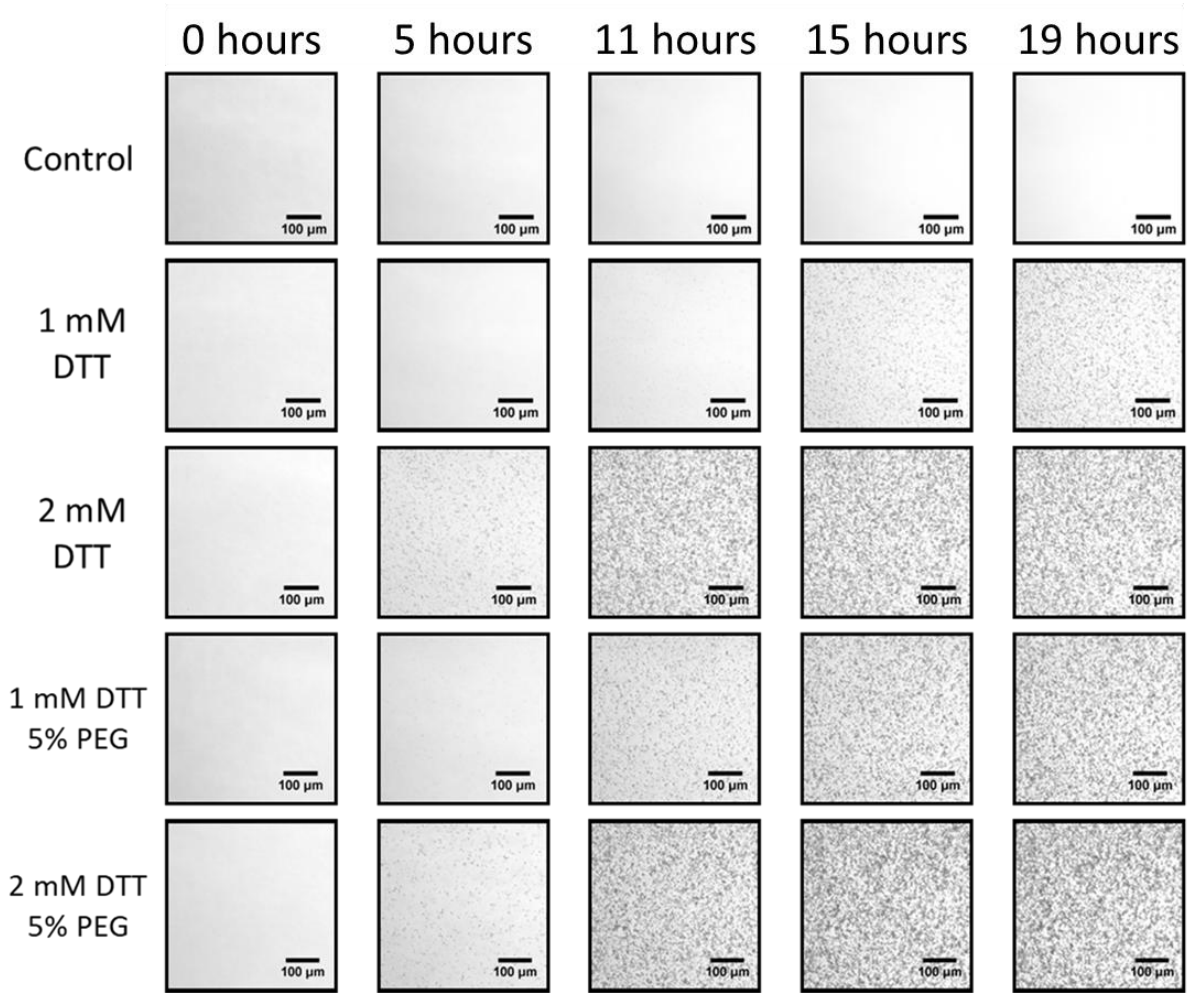

Figure 4.7: Representative microscopy of cystatin C aggregation in the presence of PEG and DTT. The images show a selection of differential interference microscopy images recorded in succession during a timelapse of cystatin C aggregation. The focal plane of the microscope is at the bottom of each microplate well, thus increasing numbers of aggregates are observed over time as they fall out of solution onto this surface.

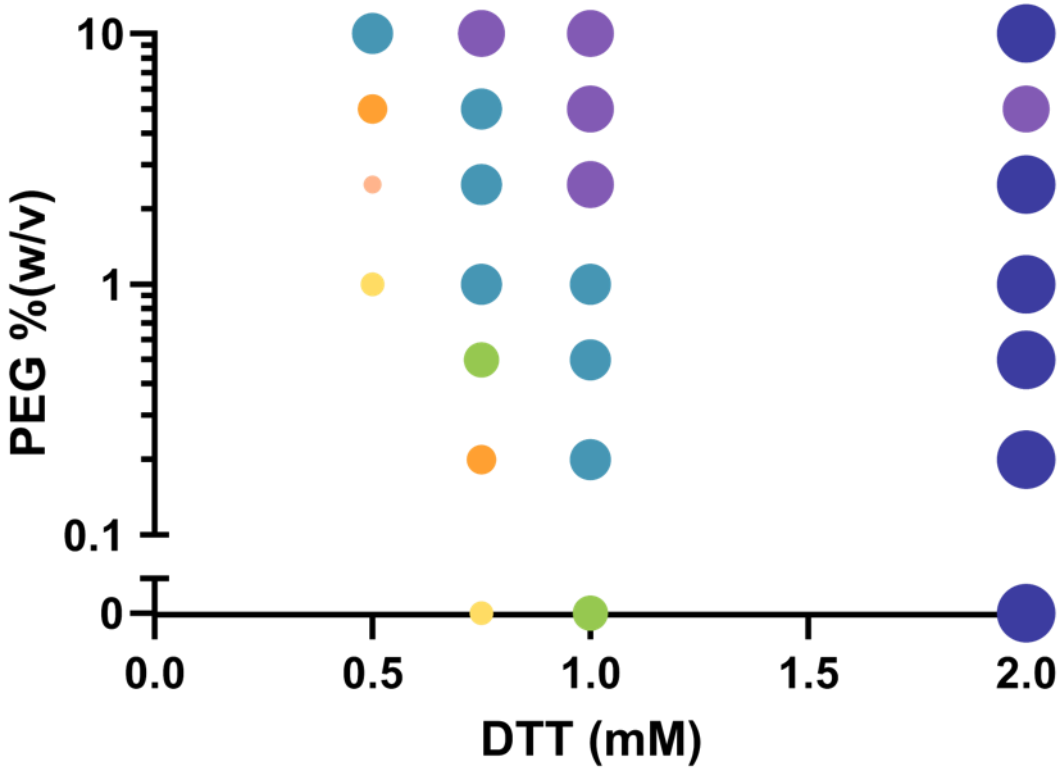

Figure 4.8: Phase diagram of cystatin C aggregation in PEG and DTT conditions.
The rate of cystatin C aggregation in solutions of 10 µM hCC at the given PEG and DTT concentrations is shown by the size and colour of each dot, as measured by the first microscopy timepoint where aggregation was observed. The dots largest to smallest display fastest to slowest onset of aggregation, with specific timepoints being: 5.3 hours (dark blue), 7.3 hours (purple), 9.3 hours (light blue), 11.3 hours (green), 13.3 hours (orange), 15.3 hours (yellow), 17.3 hours (peach).

Using a computational approach to determine the relative number of particles in each image (Section 2.5.7), the data was converted into a series of concentration curves over time (Figure 4.9). A lag-phase estimate, which is the time taken for noticeable aggregation to occur, was calculated for each curve as the X-intercept for an exponential fit through points that are not part of the initial plateau. To remove any bias caused by manually excluding near-zero data points, fitting of the initial plateau was included as part of the overall algorithm, via a conditional function (Section 2.5.7).

From these data it is obvious that increasing DTT concentration dramatically reduces the lag-time before aggregation occurs. When plotting changes in lag-time due to PEG concentration, it is again clear that increasing PEG concentration leads to lag-time reduction in conditions of 0.75 mM and 1 mM DTT (Figure 4.10). However, PEG concentration does not appear to influence aggregation rate at 2 mM DTT, which remains roughly constant at 5 hours. This implies that aggregation at 2 mM DTT is not dependent on any intermolecular interactions, which are amplified at higher concentrations of

protein or crowding agent. Therefore, this rate-limiting step is likely to be an intramolecular conversion, such as structural rearrangement within a soluble oligomeric intermediate, that is required to nucleate further aggregation. A previously discussed feature of other cystatins is the need for a trans- to cis- proline isomerisation step to allow the formation of tetrameric intermediates, that then go on to aggregate [209, 210]. Considering this proline is also conserved in cystatin C (Pro105), it seems reasonable to hypothesise this as the rate-limiting mechanism.

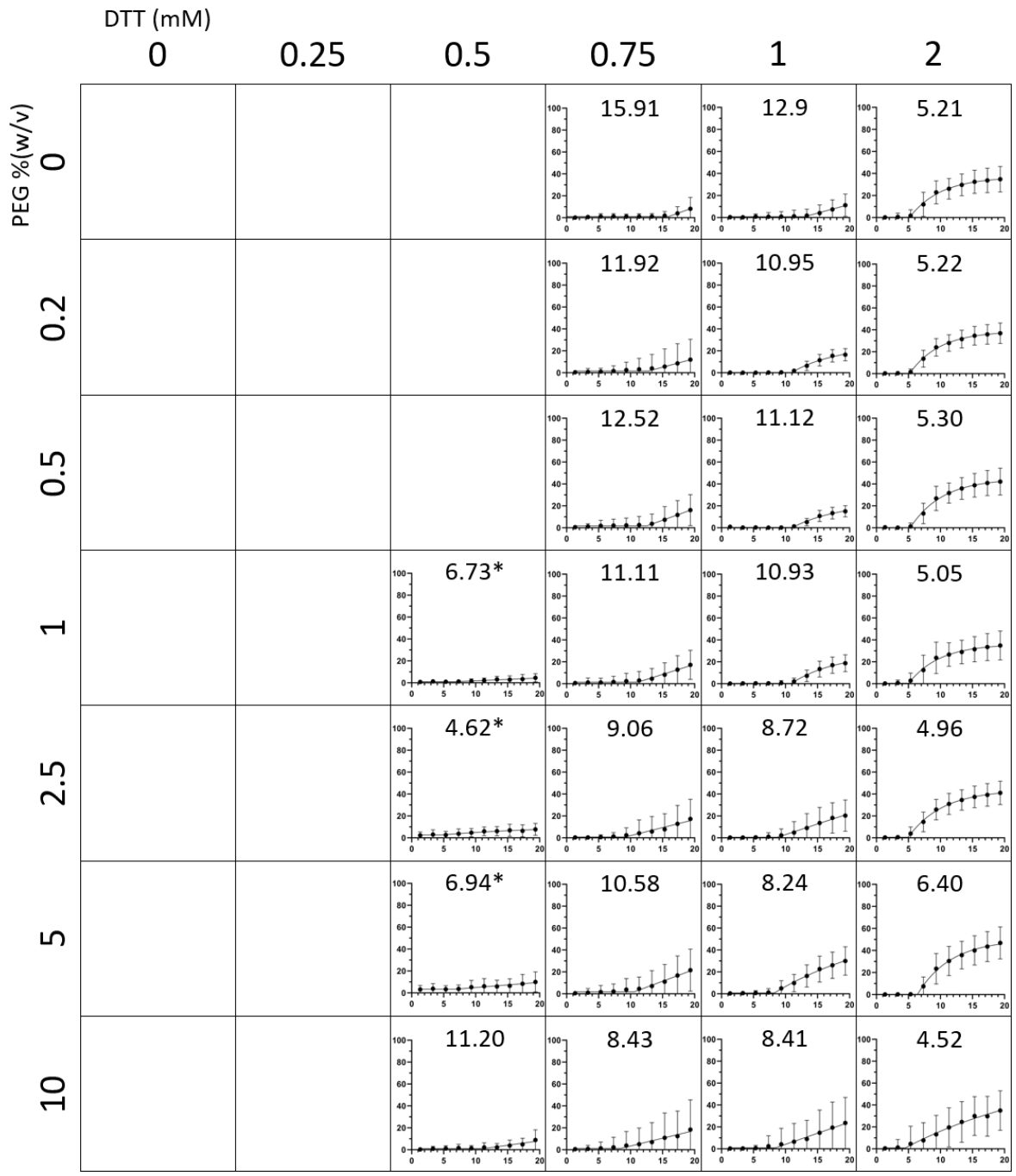

Figure 4.9: Cystatin C aggregation timelapses in conditions of PEG and DTT, with computational analysis.

20-hour microscopy timelapses were collected for each condition shown and cystatin C aggregation was tracked computationally as described in Section 2.5.7. The graphs show the percentage of each image's background that is obscured by aggregate particles, as a means to measure the relative number of aggregates (y-axis) over time in hours (x-axis). Error bars show the standard error of each data point, which relates to the number of subsections of each image that could be appropriately tracked. The line through each graph is a best-fit for a conditional exponential curve function (Section 2.5.7). Numbers above each graph represent a lag-phase estimate in hours, based on the fit. An '*' is used where estimates are heavily influenced by poor fitting. Conditions without a graph did not show any aggregation over the 20-hour time period.

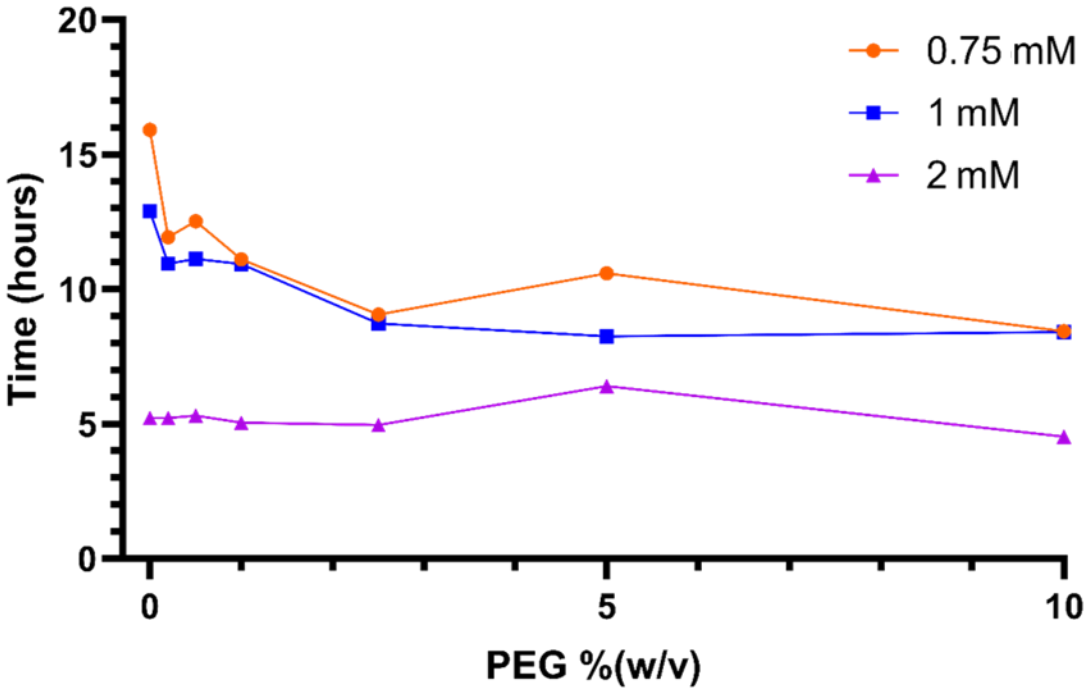

Figure 4.10: Change in lag-phase estimate by DTT concentration.
Changes in lag-phase estimates are shown as a function of PEG concentration for 3 DTT concentrations: 0.75 mM (orange), 1 mM (blue) and 2 mM (purple). For the first two, lag-phase decreases with PEG concentration. For 2 mM DTT, lag-phase is independent of PEG concentration.

4.6 Microscopy of Fluorescently-tagged Cystatin C in HeLa cells

As part of this project's aim to create a Bunina body model system, I explored expressing cystatin C without its secretory signal to ensure it remains intracellular and study its localisation. To visualise the protein, cystatin C was expressed with a C-terminal GFP (green fluorescent protein) tag, commonly used to study protein localisation *in vivo* [364]. The construct that was designed for GFP-cystatin C expression can be found in Section 2.9. The C-terminal was chosen to accommodate the fluorescence tag to reduce its interference with the N-terminal secretory sequence and because N-terminal modifications have been shown to inhibit dimerisation and aggregation in cystatin B [209].

HeLa cells are a known standard for mammalian cell expression [350, 351] and were chosen for ease of use and general robustness to protein overexpression. Despite this, overexpression of cystatin C in HeLa cells was highly toxic and many cells appeared dead or highly stressed upon imaging. Localisation of cystatin C in these cells fell under two main categories, discrete puncta or web-like, both of which are shown in the live-cell images in Figure 4.11.

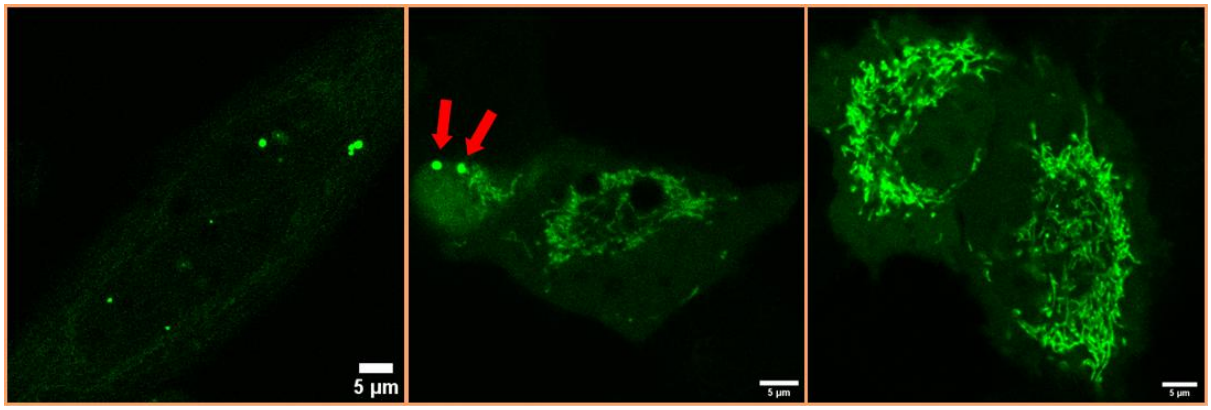

Figure 4.11: Live-cell fluorescence microscopy of GFP-cystatin C in HeLa cells.
Confocal microscopy of live HeLa cells expressing hCC-GFP display two main phenotypes: discrete puncta, shown in the left image and marked by red arrows in the middle image; and a web-like phenotype, clearly visible in the middle and right images.

Cells expressing the GFP construct were also fixed and stained with a series of markers to determine whether cystatin C co-localised to any of them (Figure 4.12). Antibody markers corresponding to stress granules (G3BP1) and aggresomes (γ-tubulin) did not share any localisation with GFP-cystatin C.

mRNA localisation was visualised using fluorescence in-situ hybridisation, which did not match with GFP-cystatin C localisation. This is in agreement with previously mentioned screens (Section 4.4), where cystatin C would not aggregate in the presence of RNA. This does conflict with the NMR data, which suggested dimeric cystatin C may be able to interact with RNA, however this is not particularly surprising due to the low confidence of that dataset. Additionally, the presence of a large C-terminal GFP tag may also simply interfere with normal cystatin C localisation.

The LAMP2 marker, identifying late endosomes and lysosomes, potentially shares some co-localisation with the GFP signal. However, due to the preliminary nature of these images, it is difficult to determine whether the overlapping fluorescence signals are due to actual co-localisation of these features or just an overabundance of GFP-cystatin C throughout the cell.

Surprisingly, the web-like phenotype, but not the puncta, does appear to co-localise with mitochondrial marker Tomm20, which explains its unusual distribution and distinct mitochondrial morphology. It is currently unclear why GFP-cystatin C would localise to the mitochondria, although it has been reported that mitochondrial surfaces can act as condensation sites for the formation of some cytosolic protein aggregates [386]. The aggregation is likely to disrupt mitochondrial function, which may explain the cell stress and toxic phenotype seen in these cells.

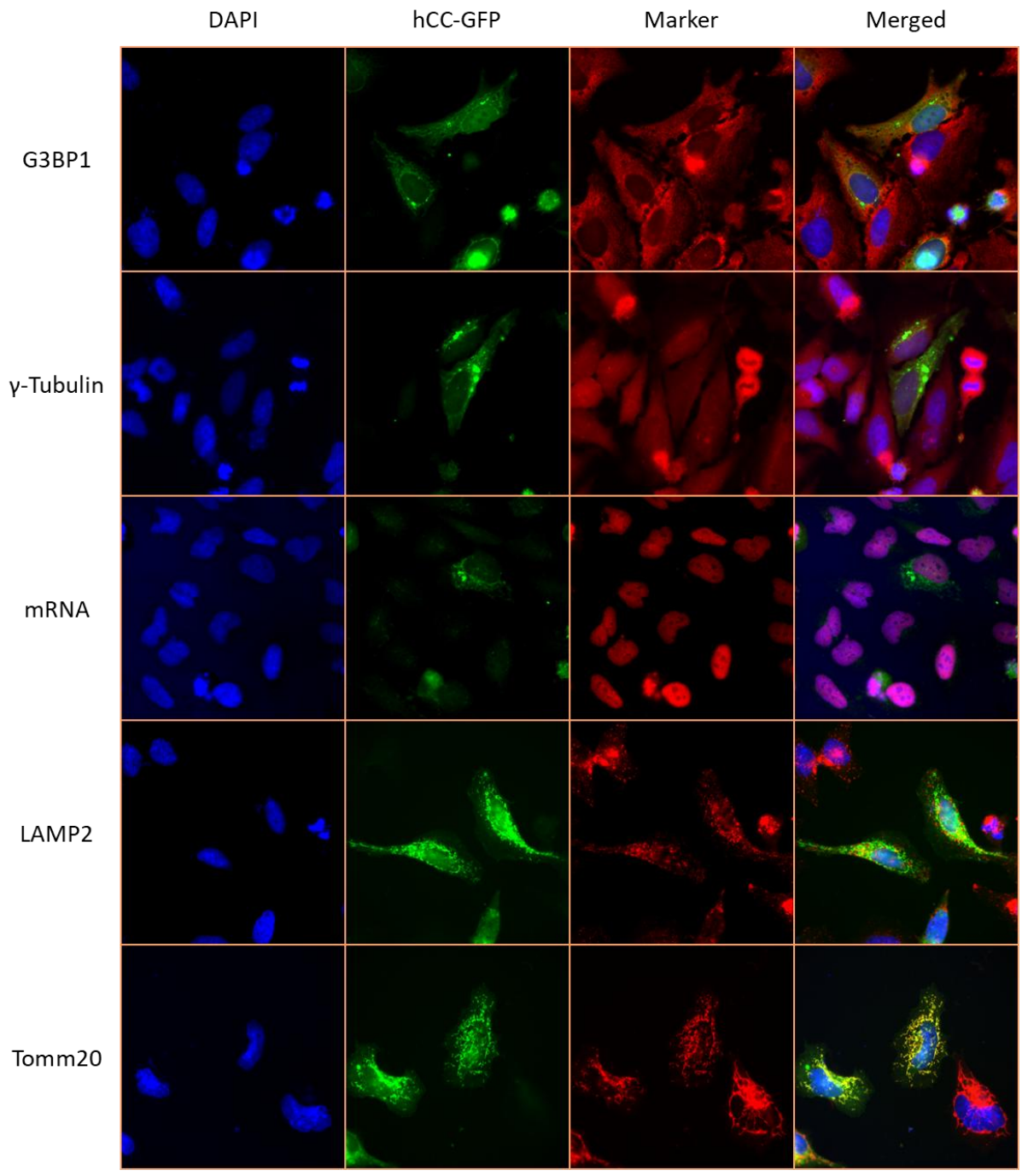

Figure 4.12: Fixed-cell fluorescence microscopy of GFP-cystatin C stained with a variety of biomarkers.
Fixed HeLa cells expressing hCC-GFP, shown in green are stained with DAPI (DNA stain), shown in blue and one of a selection of cytoplasmic biomarkers to determine co-localisation with hCC-GFP. The markers, shown in red, and their associated cytoplasmic components are: G3BP1 antibody (Stress granules), γ-tubulin antibody (centrosome), mRNA poly(A) fluorescence in situ hybridisation (mRNA), LAMP2 antibody (late endosome and lysosomes) and Tomm20 (mitochondria). A merged overlay including stain, hCC-GFP and DAPI is also shown.

To verify whether this mitochondrial association was the result of interaction by cystatin C or by GFP, an alternative construct (Section 2.9) using a hemagglutinin tag (HA-tag) was also expressed and stained with Tomm20 and LAMP2 (Figure 4.13). HA-cystatin C, visualised using fluorescent antibodies for the HA-tag (Section 2.6.3), appeared to form small granular inclusions which concentrated around the nucleus of the HeLa cells, which mimics observations of perinuclear Bunina body formation in patient neurones with granular Bunina body staining [213]. HA-cystatin C does not seem to share the same localisation pattern as GFP-cystatin C and did not co-stain with Tomm20 (Figure 4.13). However, similar to the previous images, it is difficult to distinguish whether there was co-localisation with the LAMP2 marker due to an overabundance of GFP signal.

The difference in localisation between GFP and HA-tagged cystatin C likely comes down to the influence of the tags themselves. The HA-tag is a short, nine amino acid peptide (YPYDVPDYA) [365], which is unlikely to affect the cystatin C structure or localisation. Meanwhile, GFP is a 238 amino acid protein, making it slightly larger than double the size of cystatin C. This makes GFP much more likely to alter the localisation of cystatin C, leading to the unexpected mitochondrial localisation. GFP on its own usually appears diffuse throughout the cell [365], so the exact reason why the GFP-cystatin C fusion localised to the mitochondria remains a mystery.

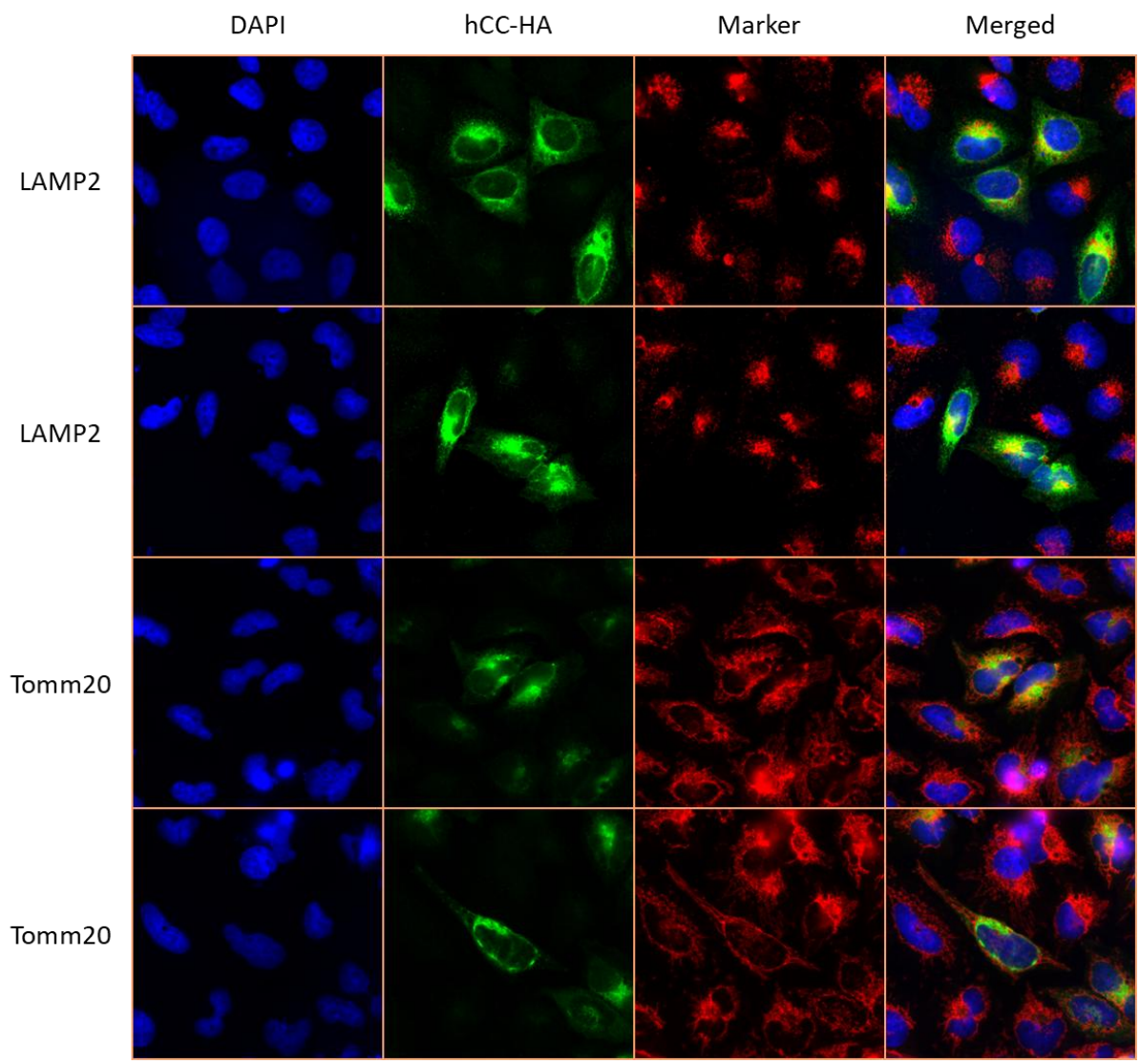

Figure 4.13: Fixed-cell fluorescence microscopy of HA-cystatin C stained with LAMP2 and Tomm20. Fixed HeLa cells expressing hCC-HA, shown in green using a fluorescent antibody for the HA-tag, are stained with DAPI (DNA stain), shown in blue. Cells were stained with either fluorescent antibodies, shown in red, for LAMP2 (late endosome and lysosome) or Tomm20 (mitochondria) to determine their co-localisation with hCC-HA. A merged overlay including stain, hCC-HA and DAPI is also shown.

4.7 Nocodazole Treatment of HeLa Cells Expressing Cystatin C

The fluorescence microscopy of HA-tagged cystatin C, expressed in HeLa cells (Section 4.6), showed the presence of small granules of cystatin C, which appeared to concentrate around the perinuclear region of the cytoplasm. To determine whether this localisation was actively maintained, or due to a preferential interaction at the nuclear membrane, cells expressing HA-tagged cystatin C were incubated with nocodazole.

Nocodazole is a small organic compound, which binds to β-tubulin and disrupts the microtubule network in cells [366]. Cells without a microtubule network are then unable to actively transport molecules around the cytoplasm. An antibody for α-tubulin, the other main component of microtubules, is used to confirm the effects of the nocodazole. Figure 4.14 shows α-tubulin as part of the microtubule network in DMSO controls, which is then clearly disrupted in nocodazole treated cells.

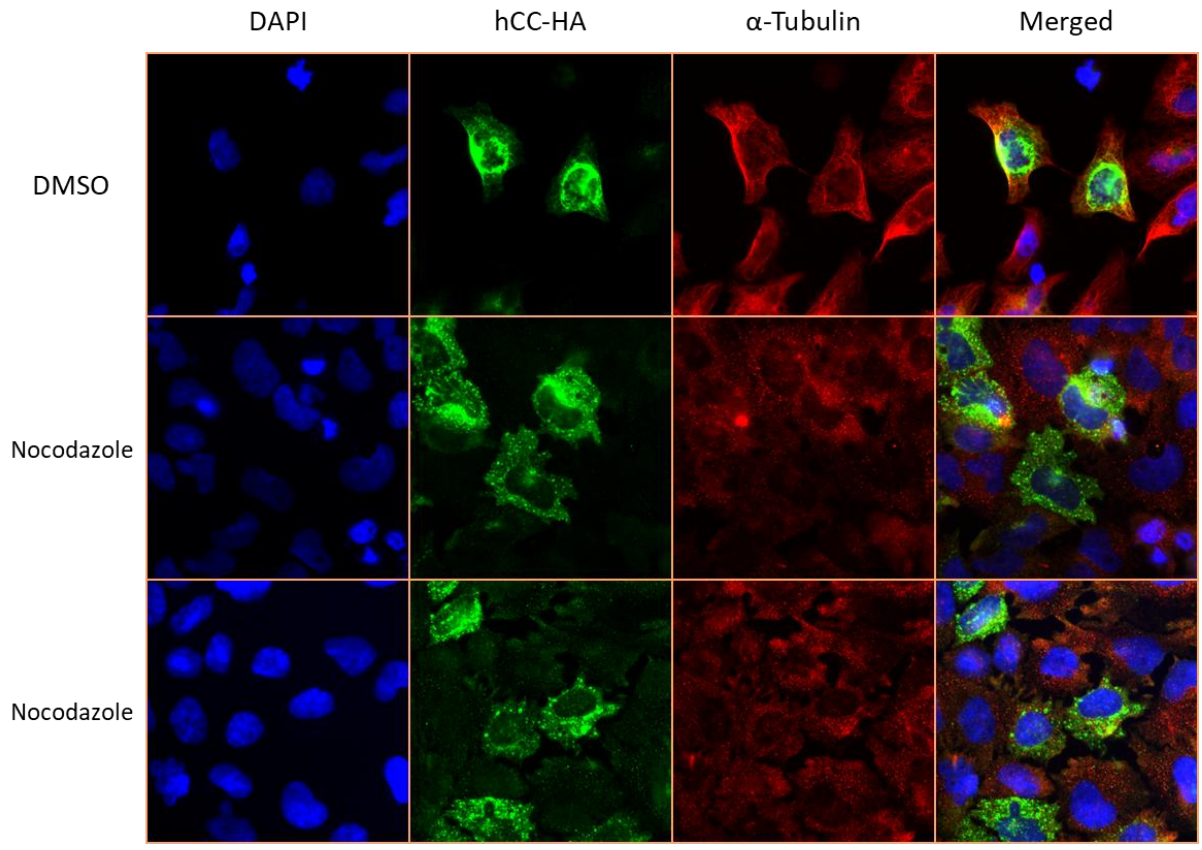

Figure 4.14: Fixed-cell fluorescence microscopy of HA-cystatin C nocodazole treatment.
Fixed HeLa cells expressing hCC-HA, shown in green using a fluorescent antibody for the HA-tag, are stained with DAPI (DNA stain), shown in blue, and α-tubulin antibody, shown in red. In the DMSO control (top), α-tubulin staining shows an intact cytoplasmic microtubule network. Upon incubation with nocodazole for 1 hour (middle and bottom), microtubules can be seen to be disrupted and the localisation of hCC-HA changes from peri-nuclear to evenly distributed puncta.

HA-tagged cystatin C localisation changes from perinuclear to diffuse granules throughout the cytoplasm, upon addition of nocodazole (Figure 4.14). This could therefore indicate an active transport process is the cause of the perinuclear localisation in untreated cells. As a side note, GFP-cystatin C expressing cells were also treated with nocodazole, but this did not appear to change the mitochondrial localisation (Figure 4.15).

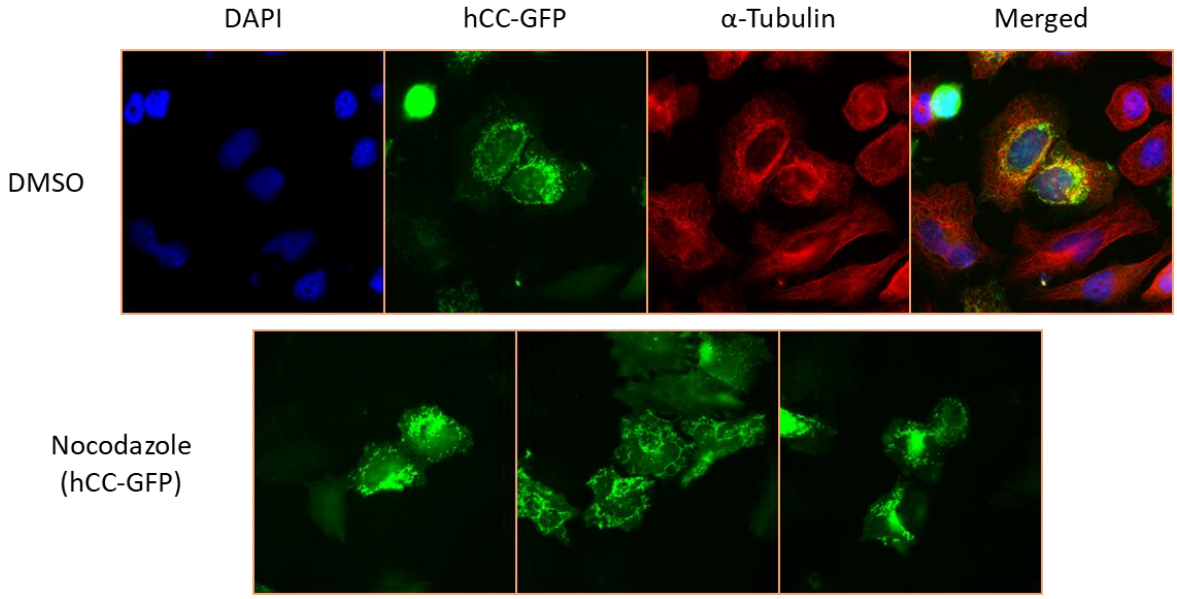

Figure 4.15: Fixed-cell fluorescence microscopy of GFP-cystatin C nocodazole treatment.
Fixed HeLa cells expressing hCC-GFP, shown in green, are stained with DAPI (DNA stain), shown in blue, and α-tubulin antibody, shown in red. In the DMSO control (top), α-tubulin staining shows an intact cytoplasmic microtubule network. Upon incubation with nocodazole for 1 hour (bottom), microtubules can be seen to be disrupted. Due to file corruption, DAPI and α-tubulin fluorescence are not show. All three images are of hCC-GFP fluorescence after nocodazole treatment. The localisation of hCC-GFP did not appear to change very significantly following treatment.

4.8 Summary of Cystatin C Results

In this thesis, I have screened low concentrations of cystatin C for phase-separation and aggregation under a range of physiological conditions. From these data, it is clear that cystatin C is unstable in a reducing environment (>1 mM DTT) and in the presence of a molecular crowding agent (PEG). Both of these were intended to mimic key differences experienced by cystatin C when transitioning from its normal extracellular or lysosomal environment, to a cytosolic environment where Bunina bodies are observed [213, 227]. Currently, it is unclear whether cystatin C's disulphide bonds are reduced under these conditions, as DTT is also a known denaturant and the 1D NMR (Section 4.2) does not show any evidence of individual disulphide breakage. Reduced or not, low concentrations of DTT are sufficient to aggregate the protein, forming amorphous particles visible by light microscopy. Future work should aim to determine the state of disulphides under these conditions using mass spectrometry.

Timelapse microscopy of aggregation in varying conditions of DTT and PEG showed that both separately enhance the rate of cystatin C aggregation in a concentration dependent manner. However, aggregation is rate-limited above 2 mM DTT, with a lag phase of approximately 5 hours. The current hypothesis explaining this phenomenon is a trans- to cis- proline isomerisation step in the aggregation pathway, which occurs on hours-long timescales, and has been observed as part of the aggregation of other cystatins [209, 210].

An increase in ionic strength, via addition of NaCl, showed that it may be slightly stabilising for cystatin C after disulphides are disrupted. Although a significantly more comprehensive screen would be required to verify this one-time result. The effect of RNA concentration was investigated, based on its propensity to enhance liquid-liquid phase-separation and subsequent aggregation in other neurodegenerative inclusions of ALS [115-117]. However, this did not yield any significant alterations in the aggregation of cystatin C under conditions reported here. Interestingly, a titration of cystatin C with RNA, observed using 2D NMR, suggests a potential unreported binding pocket in the dimer form of cystatin C. This NMR data should be taken with a grain of salt until replicated, as the concentration of protein used was quite low, leading to poor signal-to-noise, and the quality of the RNA for this type of experiment was questionable. Although liquid-liquid phase-separation was not observed, as it has been in other ALS aggregates [133-140], this may simply be due to a lack of protein concentration or screened conditions, stemming from an inability to manufacture recombinant cystatin C at scale.

Fluorescently tagged cystatin C was expressed in a standard mammalian cell line (HeLa), using both green fluorescent protein (hCC-GFP) and a hemagglutinin epitope tag (hCC-HA). The punctate inclusions of hCC-GFP, observed in both live and fixed cells, appear very reminiscent of Bunina bodies

in patient tissue. However, there is significant concern over whether this model is realistic as the alternative localisation of hCC-GFP to mitochondria, tracked via the Tomm20 marker, is not commonly observed and not replicated by hCC-HA.

The peri-nuclear localisation of HA-tagged cystatin C seems to better conform with the localisation of Bunina bodies, which tends to be peri-nuclear or in neurites (not present in HeLa cells) [213, 227]. Furthermore, the HA-tag is a short peptide, while GFP is roughly twice the size of hCC [364] and far more likely to influence its localisation in cells. Disrupting the microtubule network, via treatment with nocodazole, surprisingly removed the peri-nuclear localisation of hCC-HA, which instead formed small puncta throughout the cytoplasm. This indicates cystatin C is actively transported to the nuclear membrane by the cell. The small puncta, which greatly resemble the granular form of Bunina bodies [213, 227], may form at the nuclear membrane, prior to nocodazole treatment, or form afterwards, due to unknown interactions in bulk cytosol.

Overall, this chapter explores the effect of an intracellular environment on cystatin C aggregation, both *in vitro* and *in vivo*. It finds that disulphide breakage and molecular crowding, which can also be interpreted as increased hCC concentration, may form the underlying reasons that folded cystatin C aggregates when entering the cytoplasm, forming Bunina bodies that go on to contribute to ALS pathology. It also shows that the kinetics of cystatin C aggregation under these conditions imply a proline-isomerisation event and resolve a possible RNA binding site within the cystatin C dimer. Finally, I demonstrate Bunina body-like inclusions using fluorescently-tagged hCC in mammalian cells and show a microtubule-dependent process localises hCC to the nuclear membrane.

Chapter 5: Characterising α-Synuclein Membrane Aggregation

5.1 Introduction to α-Synuclein Results Chapter

This part of the project aimed to structurally characterise elements of the aggregation pathway of α-synuclein, in the presence of lipid membranes. This work builds upon previous data gathered by Dr. Peter J. Davis (University of Sheffield) (unpublished), in collaboration with UCB Biopharma UK. Their study initially focused on a system published by Galvagnion et. al. 2015 [311], which reported α-synuclein binding saturation of DMPS small unilamellar vesicles (SUVs) at roughly a 30:1 molar ratio of lipid:protein (L:P) (Figure 5.1a). They also showed that the final concentration of downstream aggregates, depended on the availability of DMPS vesicles, rather than protein concentration itself (Figure 5.1b). These aggregates were shown as thin fibrillar filaments that extend from existing vesicles with high flexibility and were assumed to be β-sheet amyloid, despite having very different morphology to traditionally rigid α-synuclein amyloids (Figure 5.1c-e).

Dr. Davis instead focused on POPG lipid, following recommendation by UCB Biopharma UK, who have developed a number of Parkinson's disease drug candidates using 50 nm POPG SUVs as a model membrane. The most successful of these drugs, which is currently in phase II clinical trials, blocks α-synuclein binding to POPG membranes, preventing aggregation, as its mechanism of action [109, 110]. The chemical structures of POPG and DMPS can be compared in Figure 5.2. Dr. Davis performed a similar circular dichroism titration at 222 nm using POPG SUVs, with a similar binding saturation at around a 30:1 L:P ratio (Figure 5.3).

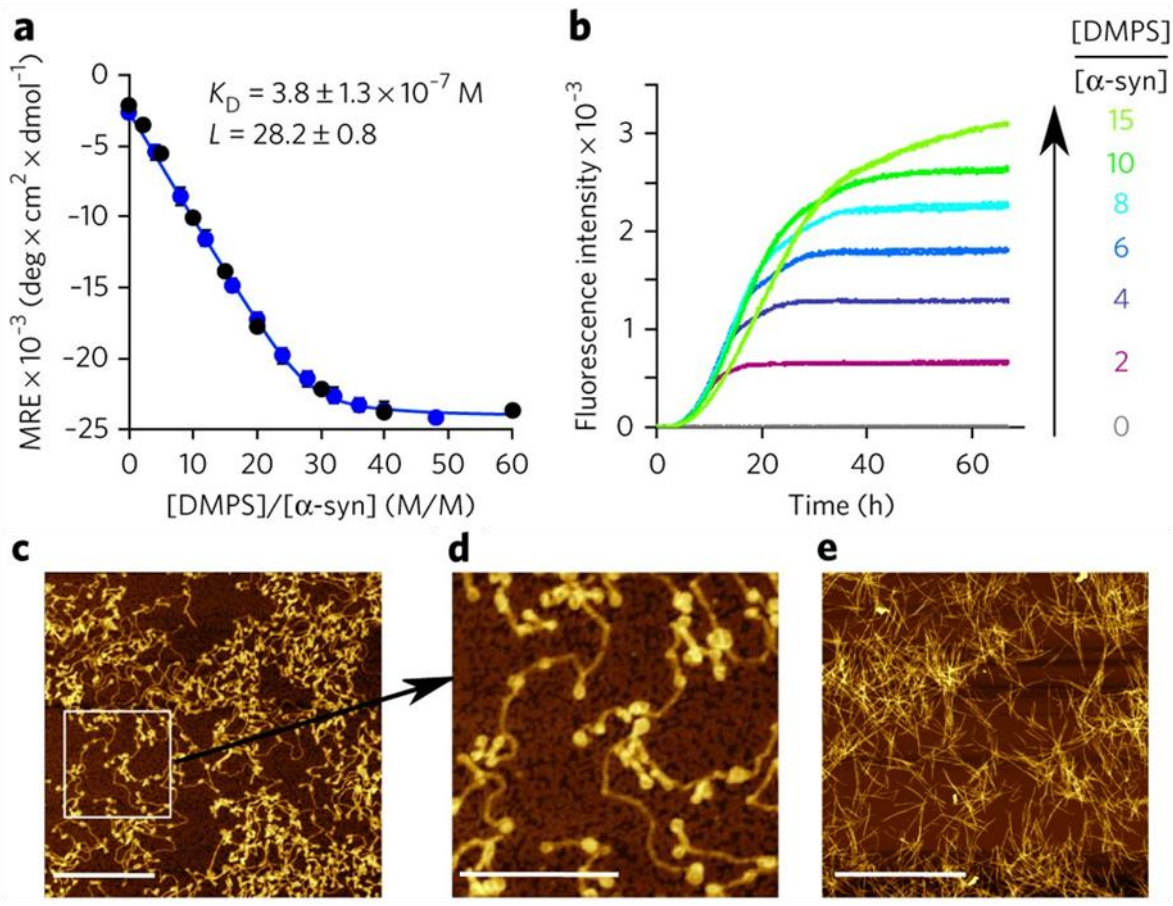

Figure 5.1: Experimental findings of Galvagnion et. al. 2015.
a) Circular dichroism at 222 nm for different L:P ratios of DMPS SUVs and α-synuclein, with a fitted binding stoichiometry of 28.2 molecules of lipid per protein. b) Thioflavin T (ThT) fluorescence of the different L:P ratios listed, shows total aggregate concentration increases at higher L:P ratios. c-d) AFM of fibrillar α-synuclein aggregates extending from vesicles (3:1 L:P ratio). e) α-synuclein aggregates formed without lipids by preformed seed fibrils. The scale bars for each AFM image are: c) 1 µm, d) 500 nm, e) 4 µm. Figures from Galvagnion et. al. 2015 [311].

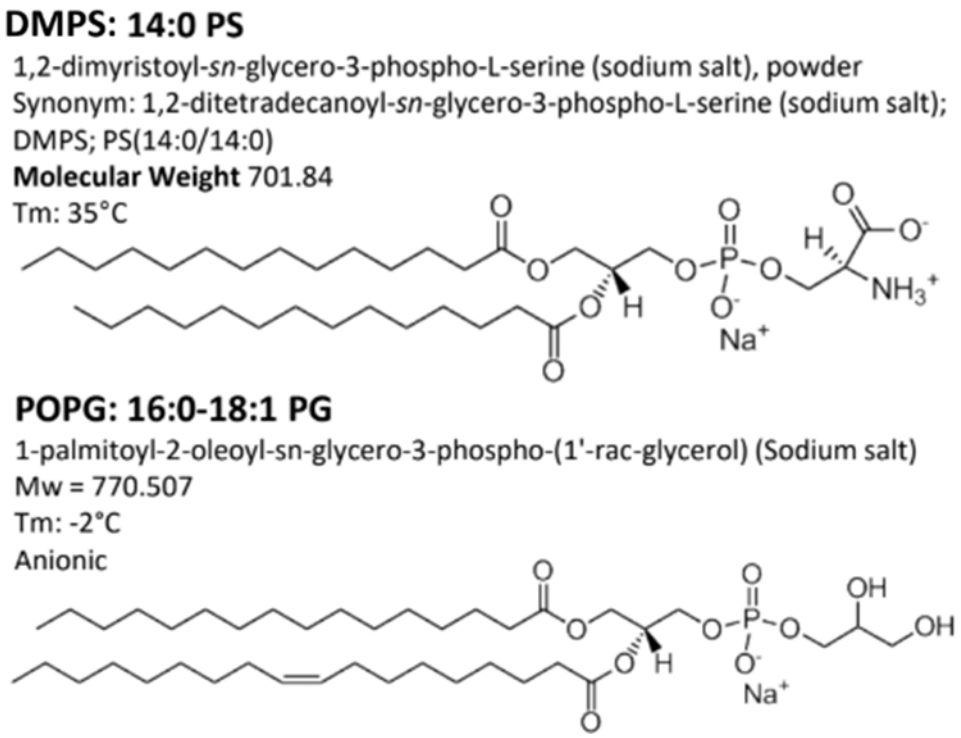

Figure 5.2: Chemical structures of DMPS and POPG.
Names, structures, masses and melting temperatures of DMPS and POPG lipids as stated by Avanti Polar Lipids.

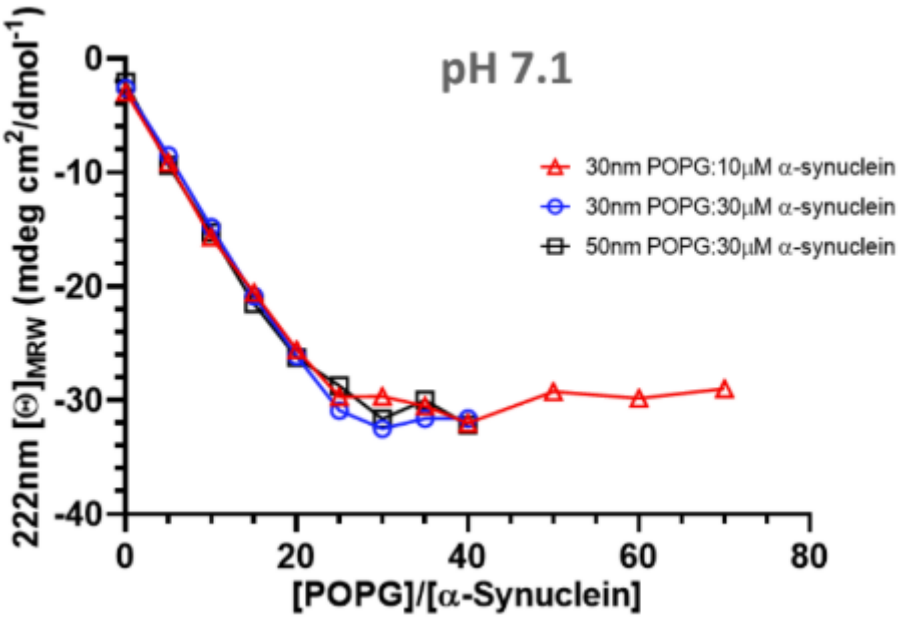

Figure 5.3: CD titration of α-synuclein with POPG SUVs.
Circular dichroism at 222 nm for different L:P ratios of POPG SUVs with 30 nm or 50 nm diameters and α-synuclein at 10 μM or 30 μM. Change in vesicle diameter or α-synuclein concentration did not appear to significantly alter binding. Data and figure by Dr. Peter J. Davis (University of Sheffield) (unpublished).

The main interest in this area stems from identifying the oligomeric and fibrillar species generated by this system, as their connection to ongoing drug trials, which are designed to block their formation, already establishes a strong disease-relevant connection for these aggregates. Dr. Davis provided significant efforts in optimising conditions for oligomer and aggregate assembly, and their separation by asymmetric-flow field-flow fractionation (AF4), yielding preliminary electron microscopy data for isolated aggregate species (Figure 5.4). The aim of this chapter is to demonstrate scaled-up separation of these aggregates by AF4 and perform various characterisations of their underlying structure, in an attempt to elucidate species and mechanisms along the pathway of membrane-mediated α-synuclein aggregation, with potential relevance to Parkinson's disease progression.

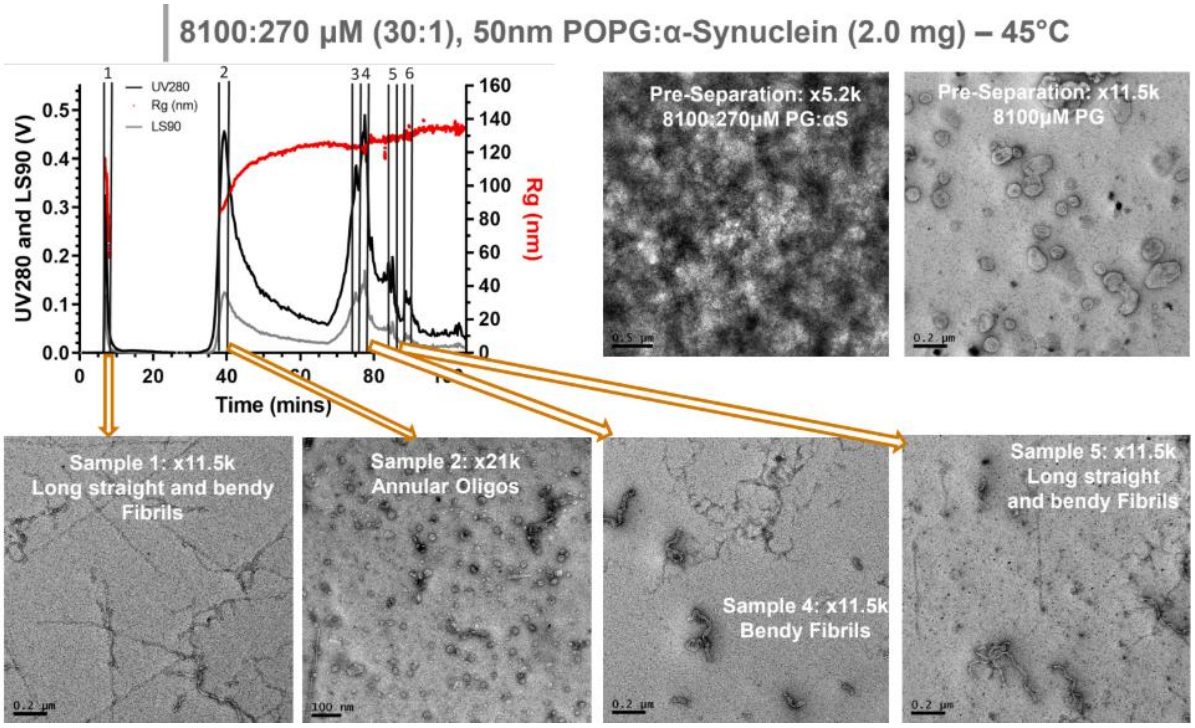

Figure 5.4: Electron microscopy of separated α-synuclein aggregates.
(Top left) Fractionation of a 30:1 L:P mixture of 50 nm POPG SUVs and α-synuclein, pre-incubated for 2.5 hours at 45°C, separated by AF4. Fractions 1-6 are highlighted between vertical lines and transmission electron micrographs of their contents shown below. (Top right) TEM micrographs of before AF4 separation (left) and POPG SUVs only (right). Details on image magnification and sample morphology are indicated on each micrograph. Data and figure by Dr. Peter J. Davis (University of Sheffield) (unpublished).

5.2 Separation of α-Synuclein Aggregate Species by AF4

In order to study the aggregation pathway of α-synuclein in the presence of lipid membranes, the first aim was to isolate oligomeric species of α-synuclein in the early stages of aggregation. Following an optimised protocol developed previously by P. J. Davis and outlined in Section 2.7.4, α-synuclein and POPG SUVs were mixed together and incubated at 45 °C for 2.5 hours to initiate aggregation. The mixture was then fractionated by asymmetric-flow field-flow fractionation, which separated it according to diffusion coefficient, resulting in three primary peaks (Figure 5.5c). These peaks will be referred to as AF4 peaks 1, 2 and 3.

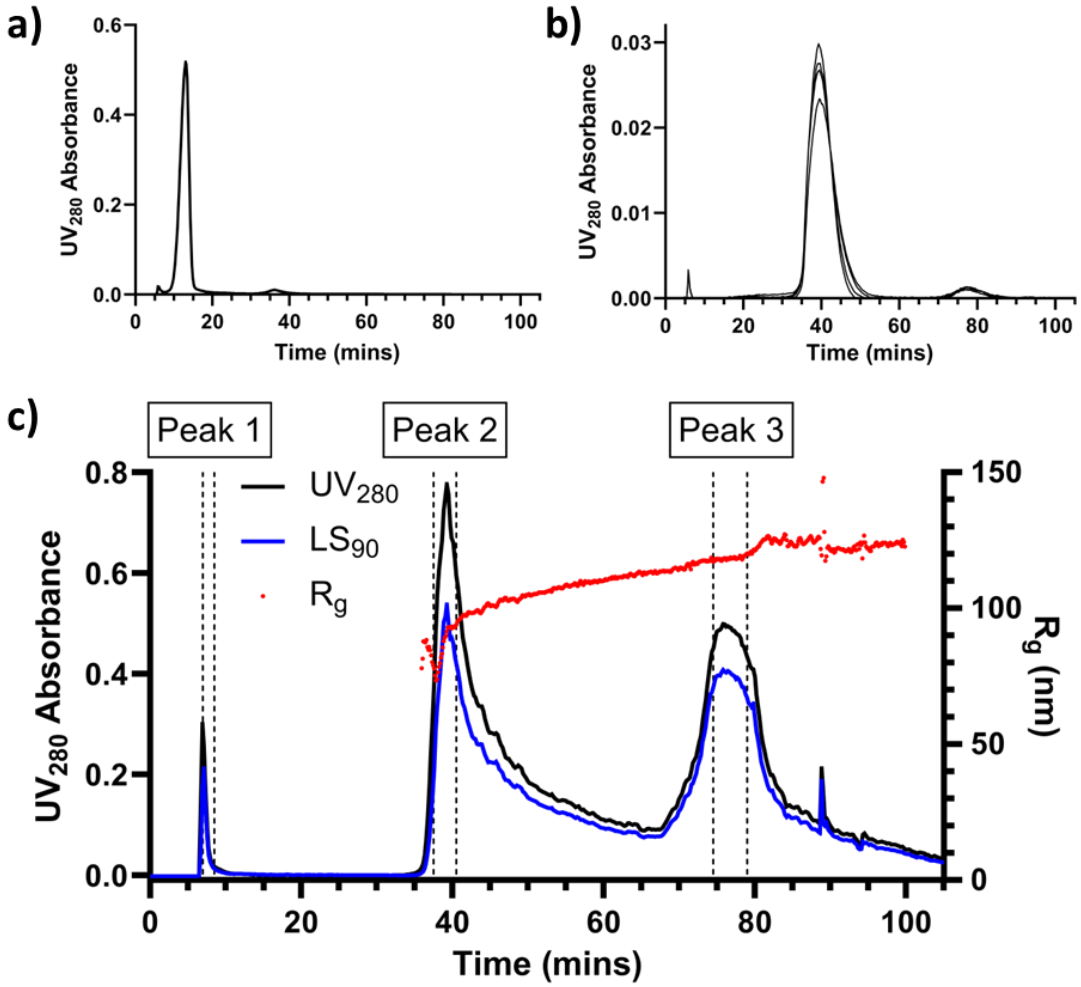

Figure 5.5: A standard AF4 separation of α-synuclein:POPG mixtures.
Shown are the elution profiles of a) α-synuclein monomer, b) multiple injections of 50 nm POPG SUVs and c) a pre-incubated mixture of 270 µM α-synuclein and 8.1 mM POPG SUVs as described in Section 2.7.4. All elutions were performed using the AF4 method detailed in Section 2.7.5. The graph of the mixed sample shows UV absorbance (UV_{280}), 90° light scattering (LS_{90}) and average radius of gyration (R_g) estimated by MALS fitting (Section 2.7.5). The fractionated regions referred to as AF4 peaks 1, 2 and 3 in the text are highlighted.

Peak 1, as labelled in Figure 5.5c, is a void peak in AF4 caused by the disruption of flows throughout the channel when transitioning from the focus step to elution step (Section 2.7.5). Some particles can escape the channel during this flow disruption, leading to a sharp UV and light scattering peak, which can also be seen to a lesser extent in the control samples (Figures 5.5a and b) and found in other examples of AF4 in the literature [367].

The absence of a peak at the position shown by the α-synuclein control (Figure 5.5a) indicates that very little α-synuclein monomer remains in the incubated sample. Peak 2 corresponds well to the POPG vesicle control peak (Figure 5.5b), but clearly includes much larger species with an average radius of gyration (R_g) of roughly 70-100 nm across the peak, rather than POPG SUVs normal R_g of around 25-30 nm, and continues to increase beyond the fractionated section of the peak. Peak 3 elutes at the end of the run and includes the largest species, approximately 120 nm average R_g.

This protocol was highly reproducible and was performed routinely to produce fractionated samples for downstream experiments. A broad series of optimisations on both the incubation and separation protocols were attempted to further separate the peak 2 species (data not shown), but these did not yield any significant improvements and were never used for downstream applications.

5.3 Liquid Chromatography Mass-Spectrometry of AF4 Fractions

Peak fractions collected from AF4 were likely to contain a mixture of protein and lipid, which were initially assessed using mass-spectrometry. Using reverse-phase liquid chromatography upstream of mass spectrometry (LC-MS) (Section 2.8.2), the protein and lipid components could be separated and measured individually in each fraction.

The AF4 peaks from two separate preparations, one made shortly before and the other 6 months prior, were analysed by LC-MS to give qualitative proportions of protein, lipid and an unknown third species, using the mass spectrometry total ion chromatogram (TIC) (Figure 5.6). The figures for each TIC peak are summarised in Table 5.1, along with estimated α-synuclein concentrations for each AF4 peak, based on integrals of UV absorption at 220 nm for the monomer elution peaks after chromatography.

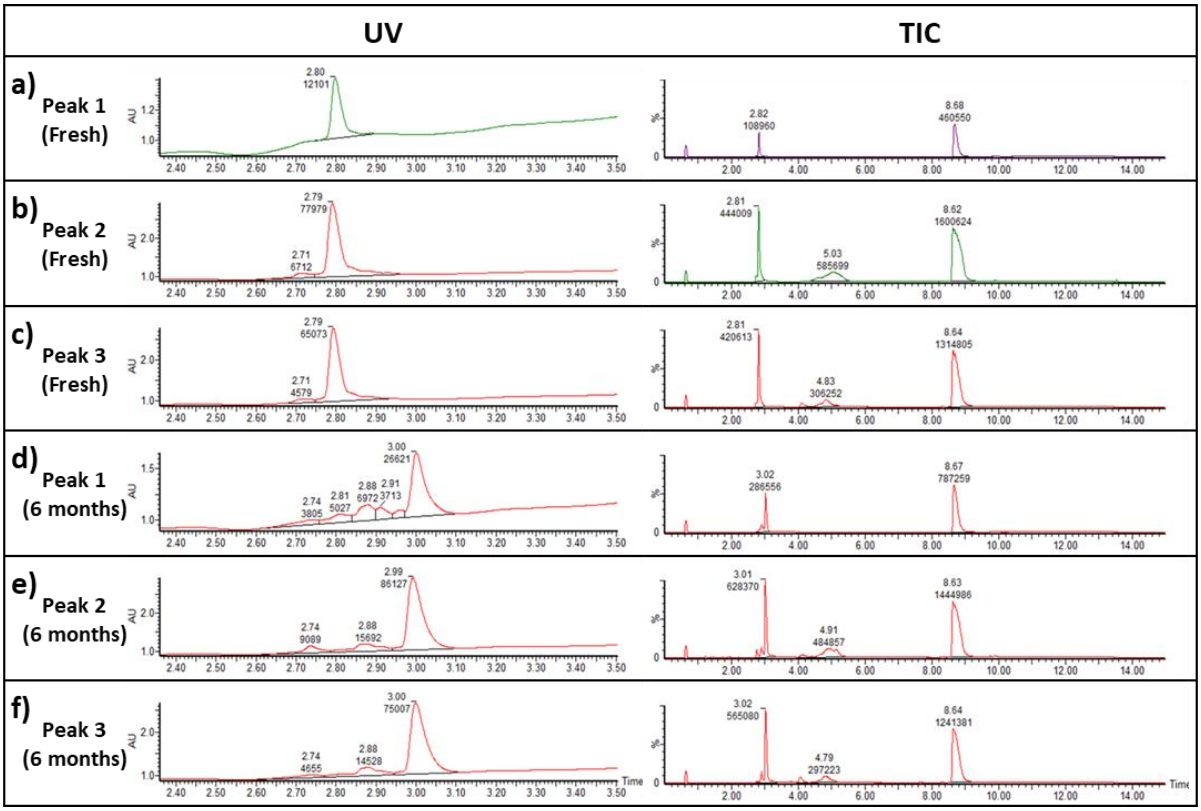

Figure 5.6: Liquid chromatography mass-spectrometry of AF4 peaks.
AF4 peaks 1-3 from two separate preparations are shown, one produced freshly beforehand (a-c) and the other 6 months prior (d-f). For each sample, graphs of UV absorbance at 220 nm (left) and total ion count (right) are shown against an x-axis of elution time using reverse-phase chromatography. All peaks are labelled with elution time and peak area, calculated using the baselines shown in black.

		Relative Area of TIC Peaks			Lipid:Protein Ratio	
Sample	Est. Conc. (µg/mL)	Protein Peak	Oligomer Peak	Lipid Peak	(Exc. Oligomer)	(Inc. Oligomer)
Peak 1 (Fresh)	23.8	108960	-	460550	4.23	4.23
Peak 2 (Fresh)	153.3	444009	585699	1600624	3.60	1.55
Peak 3 (Fresh)	127.9	420613	306252	1314805	3.13	1.81
Peak 1 (6 Months old)	52.3	286556	-	787259	2.75	2.75
Peak 2 (6 Months old)	169.3	628370	484857	1444986	2.30	1.30
Peak 3 (6 Months old)	147.4	565080	297223	1241381	2.20	1.44

Table 5.1: LC-MS peak statistics.
Peak statistics for the fresh and 6-month-old AF4 preparations, shown in Figure 5.6. Concentration estimates were made using peak integrals of the UV absorbance at 220 nm, compared with a calibration curve of α-synuclein monomer (Section 2.8.2). Total ion count (TIC) peaks integrals are shown for monomeric α-synuclein and lipid, as well as an unknown intermediate species labelled "oligomer" in AF4 peaks 2 and 3. The monomer, oligomer and lipid peaks are visible in the TIC graphs of Figure 5.6, with elution times at around 2.9, 4.9 and 8.6 mins respectively. The lipid:protein ratios shown are not a quantitative measure of actual lipid:protein concentration ratio, due to differences in ionisation efficiencies of each component that are not factored in.

The UV data (Figure 5.6) shows single, well-defined peaks for α-synuclein monomer, with retention times of 2.8 minutes for the first preparation and 3.0 for the second. These retention times correspond well with those of the α-synuclein monomer controls (data not shown), which were used to generate the absorbance calibration curve (Section 2.8.2). The presence of additional smaller peaks in the second preparation are likely to be the effect of protein degradation during the 6-month storage period before this measurement.

The total ion count (TIC) of each AF4 peak (Figure 5.6) shows a substantial amount of material elutes after 8.6 minutes, whose mass signal was attributed to POPG. AF4 peaks 2 and 3 of both preparations also included a broad intermediate peak eluting at roughly 4.8 minutes, which must either be oligomeric species of α-synuclein or protein-lipid complexes that are not fully disrupted during reverse-phase chromatography.

Comparing the peak areas for lipid and protein in each sample shows a similar ratio of lipid:protein between AF4 peaks 2 and 3 of the same preparation (Table 5.1). This trend remains true whether the oligomer peak is included as part of the protein component or not, which together shows that both peaks 2 and 3 contain similar amounts of protein, lipid and the unknown oligomer. However, this analysis cannot determine what the actual proportions of each component is, only that they are the similar in both samples. This is due to unaccounted differences in ionisation efficiencies for each component, which will affect their relative peak intensities.

Although the ratios for these peaks differ significantly between the fresh and 6-month-old preparations (3.60, 3.13 vs. 2.30, 2.20), they are much more similar when including the oligomer peak as part of the protein component of each sample (1.55, 1.81 vs. 1.30, 1.44). This could indicate that a higher proportion of protein exists in this oligomeric state in the fresh samples, when compared with the 6-month-old samples. Differences in these ratios between preparations after the oligomer peak is included may be explainable by slightly higher overall protein concentration in the 6-month-old sample, as shown by the UV concentration estimates (Table 5.1).

In summary, these data show that each AF4 peak contains significant protein and lipid components, and that the relative proportion of lipid and protein in peaks 2 and 3 are broadly similar. These peaks also contain an oligomeric or lipid:protein complex species that is not fully disrupted by reverse-phase chromatography, and which appears more prevalent in the fresh sample versus the 6-month-old sample. The relevance of this separated “oligomer” peak is unclear and future work could aim to specifically isolate and characterise this peak.

Finally, due to the evidence of potential sample degradation in the 6-month preparation stored at 4 ^{o}C and because these preparations are significantly altered by freeze-thawing and lyophilisation (data not shown), all downstream experiments using α-synuclein-POPG mixtures were prepared as close to measurement as possible to avoid any over-time degradation effects.

5.4 Fourier Transform Infrared Spectroscopy of AF4 Fractions

To further investigate the protein and lipid compositions of each AF4 peak, Fourier transform infrared (FTIR) spectroscopy was used. Attenuated total reflectance-FTIR (ATR-FTIR) (Section 2.8.3) allowed gathering whole sample spectra from dried samples, but had a variable signal baseline and low signal-to-noise for the AF4 peak samples.

The ATR-FTIR overlay in Figure 5.7 shows a clear distinction between the characteristic protein amide peaks of α-synuclein at around 1650 nm^{-1} and 1540 nm^{-1}, and the signal contributed by POPG at 1740 nm^{-1}. Based on these controls, similar peaks corresponding to both α-synuclein and POPG can be seen in both AF4 peaks 2 and 3. However, due to the low concentration of the fractionated samples and variable baseline, it does not seem reasonable to integrate these peaks for lipid and protein concentrations as these would very likely give inaccurate measurements. At best, this helps confirm observations from the LC-MS data that peak 2 and peak 3 contain similar ratios of lipid to protein. Access to multi-bounce FTIR or Raman spectroscopy, would likely improve signal for these low concentration samples.

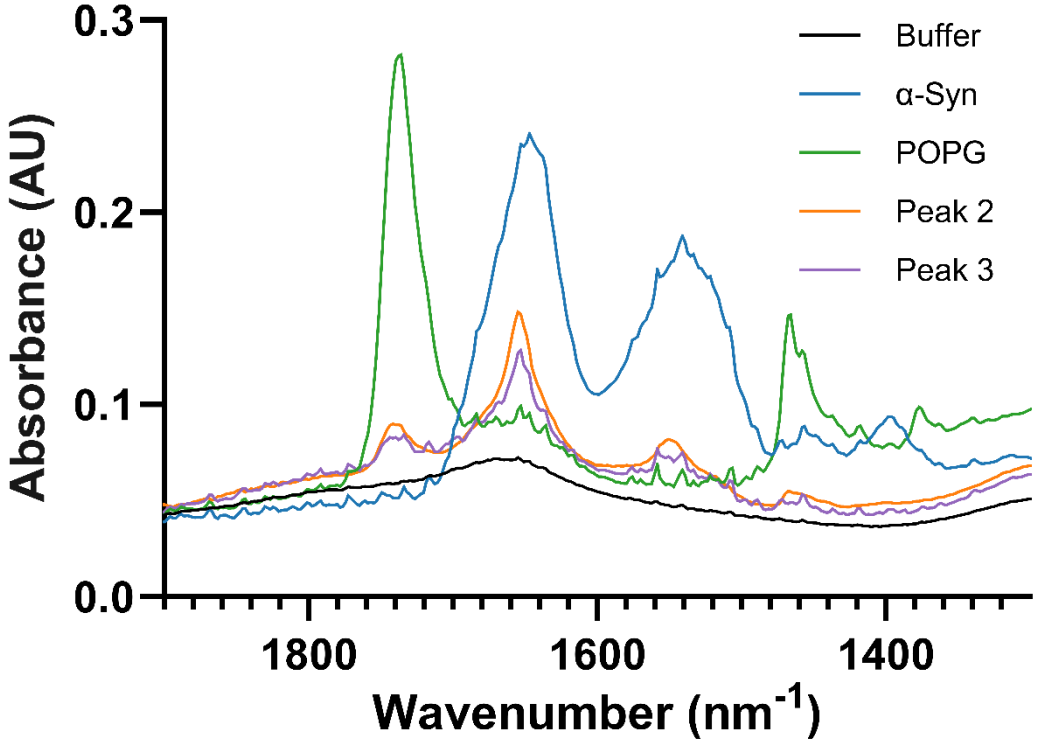

Figure 5.7: ATR-FTIR showing amide band overlay with baseline correction.
The amide band region of 270 µM (8.13 mg/mL) α-synuclein (blue) and 8.1 mM (6.25 mg/mL) POPG (green) controls is shown overlayed with AF4 separation peak 2 (orange) and peak 3 (purple). To align each spectrum, whilst maintaining a fair comparison between them, spectra were fit to each other in a flat portion of the spectrum between 1900-2200 nm^{-1}. The details of the alignment can be found in Section 2.8.3.

5.5 Circular Dichroism of AF4 Fractions

Circular Dichroism was used to determine differences in α-synuclein secondary structure between the AF4 peaks. The expectation was that peak 2, which elutes at a similar time to liposome controls, would show a strong α-helical signal that relates to the membrane-bound structure of α-synuclein [245, 263-266]. In contrast, peak 3 was expected to contain β-sheet amyloid as this often dominates the larger species formed during α-synuclein aggregation *in vitro* [311, 368].

Surprisingly, both AF4 peaks (Figure 5.8c and d) and a pre-fractionation sample (Figure 5.8b) appeared strongly α-helical (Figure 5.8), indicating that β-amyloid had not yet formed during this timescale and that the majority of protein in this system remains in the helical membrane-bound form. A control sample of α-synuclein is also shown to be in its native random coil solution state (Figure 5.8a).

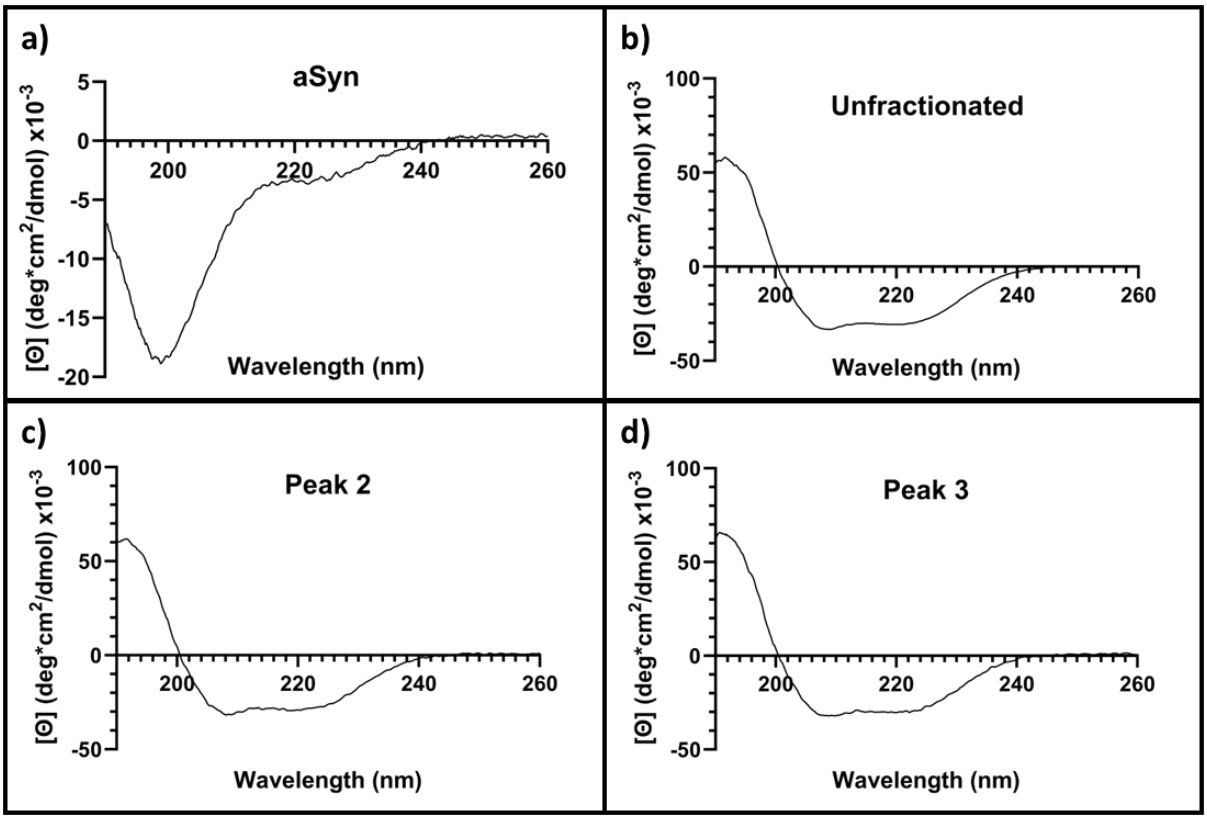

Figure 5.8: Circular Dichroism of α-synuclein and POPG incubation and separated AF4 peaks. Spectra shown are of a) 270 µM α-synuclein, b) 270:8100 µM (30:1 L:P) α-Syn:POPG as 50 nm SUVs, incubated for 2.5 hours at 45 °C, c) AF4 separation peak 2 and d) AF4 separation peak 3. The Y-axis displays molar ellipticity, which was calculated for peak 2 and 3 using α-synuclein concentration estimates from LC-MS data (Section 5.3). The calculated % α-helicities were: b) 84.9%, c) 77.4%, d) 82.3%.

Using the signal for ellipticity at 222 nm, the proportion of α-synuclein structured as an α-helix could be determined based on the calculation by Chen et. al. 1972 [369]:

$$\% \, \alpha - helicity = (\theta_{222nm} - \theta_{min}) \cdot \left(\frac{100}{\theta_{max} - \theta_{min}} \right)$$

Where θ_{222nm} is the molar ellipticity at 222 nm for an observed protein, θ_{min} is the minimum molar ellipticity at 222 nm for a fully disordered protein and θ_{max} is the maximum ellipticity at 222 nm for a fully helical protein. Chen et. al. report θ_{min} = 2340 based on CD of disordered sections of 5 globular proteins and θ_{max} = 30300 using the helical regions of those proteins. Due to observations that the length of unbroken α-helices also increases 222 nm ellipticity in proteins with identical α-helical content [370], I opted to instead use a θ_{max} of 35700, following the value obtained for polylysine, which forms a long unbroken α-helix [371].

These calculations show that the helical content of both unfractionated and peak 3 samples is particularly high (84.9% and 82.3%), while only a slight decrease is observed for peak 2 (77.4%). This shows that all species isolated in this system, including apparently fibrillar aggregates, are likely to be strongly α-helical in structure.

5.6 Destabilising α-Synuclein and POPG Mixtures with Methanol

One attempt to isolate α-synuclein aggregates formed by this system was to destroy the POPG liposomes, thereby releasing any bound aggregates into solution for downstream purification and analysis. Candidates to remove the liposomes included: increasing the concentration of solvent ions to shrink and destabilise the POPG SUVs, adding a phospholipase which could break down liposomes by digesting POPG, or dissolving the liposomes in an organic solvent such as methanol.

The preferred method would have been to use a phospholipase as this would have the least chance of affecting the aggregate structure compared to the addition of salts or methanol. Phospholipase A_1 from *Aspergillus oryzae* (Merck L3295) was added to POPG SUVs at concentrations reaching well in excess of what should be required to hydrolyse the majority of POPG in each sample. Despite using optimal conditions, including an appropriate buffer of 25mM $CaCl_2$ and 10mM $MgSO_4$ at pH 7.1, only slightly below the optimal pH of 8.5 [372], there were no changes in liposome structure as measured by solution absorbance and multi-angle light-scattering.

Similar observations have been made using other fungal phospholipases, showing difficulty in penetrating liposome bilayers to hydrolyse lipid molecules in DOPG [373], which shares high similarity with POPG. These include phospholipases from *Rhizopus arrhizus*, *Candida rugosa*, and species of *Mucor* and *Geotrichum* [373]. Future experiments could potentially make use of phospholipase A_2 from bee venom (*Apis mellifera*), as this has previously been shown to be much more effective at penetrating and degrading liposomes [374]. Unfortunately, due to availability issues, this enzyme was not able to be sourced, so instead methanol was used to disrupt the liposomes.

Addition of POPG liposomes to different concentrations of methanol showed that these liposomes were disrupted immediately by 60-70% methanol and after around 10 minutes in 50% methanol at 37 °C. The UV absorbance of the liposomes was shown to decrease significantly at these methanol concentrations, which should be due to a reduction in light scattering as the liposomes are disrupted (Figure 5.9).

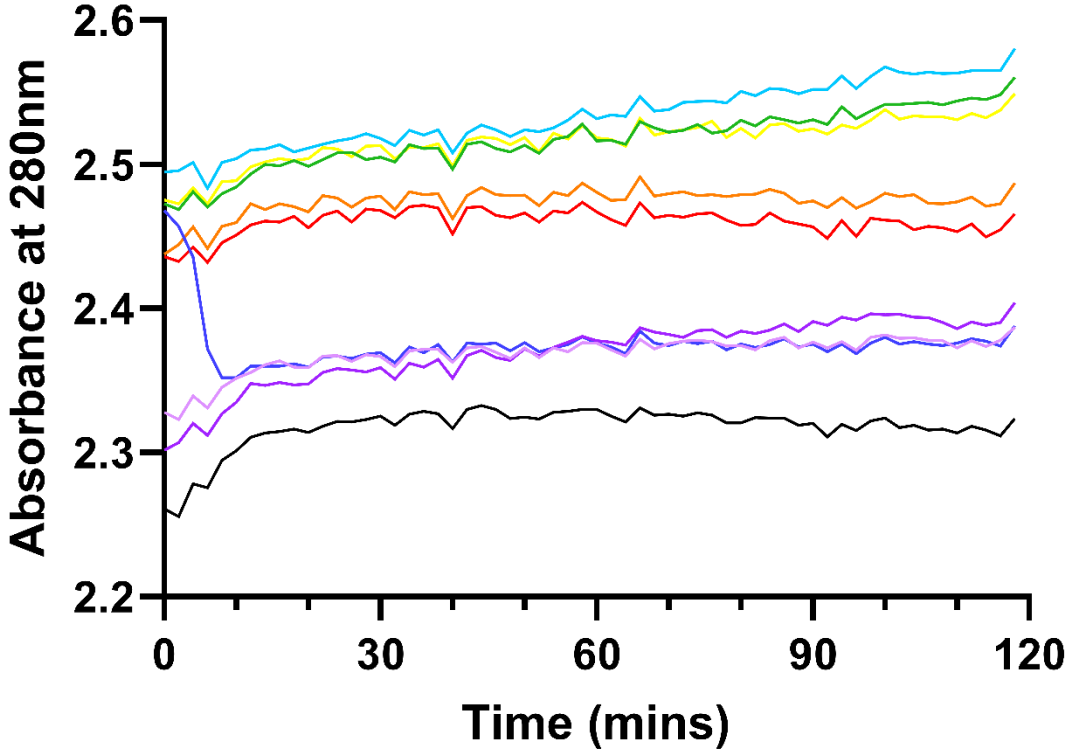

Figure 5.9: Disruption of POPG SUVs by increasing methanol concentration.
Shown is UV absorbance at 280 nm of 50 nm POPG SUVs. Traces each represent the average of 5 replicates, containing 900 µM POPG incubated at 37°C in either 0% (red), 10% (orange), 20% (yellow), 30% (green), 40% (cyan), 50% (blue), 60% (purple) or 70% (pink) methanol. The black trace represents buffer only as a control. The high absorbance values are caused by the use of polystyrene microplates, which also absorb in the UV spectrum.

The CD spectra of α-synuclein and POPG preparations, incubated as before, also shifts from α-helical to β-sheet upon addition of at least 60% methanol (Figure 5.10). Similarly, each AF4 fractionated peak converts from α-helical to β-sheet upon addition of 70% methanol (Figure 5.11). The restructuring of α-synuclein in this condition could be attributed to either the high concentration of methanol, which is likely to affect both hydrophobic interactions and hydrogen bonding, or to the removal of the liposomal surface upon which α-synuclein was bound. The native structure of α-synuclein is random coil [261, 262], therefore this methanol-induced structure is distinct from both the native and liposome-bound forms.

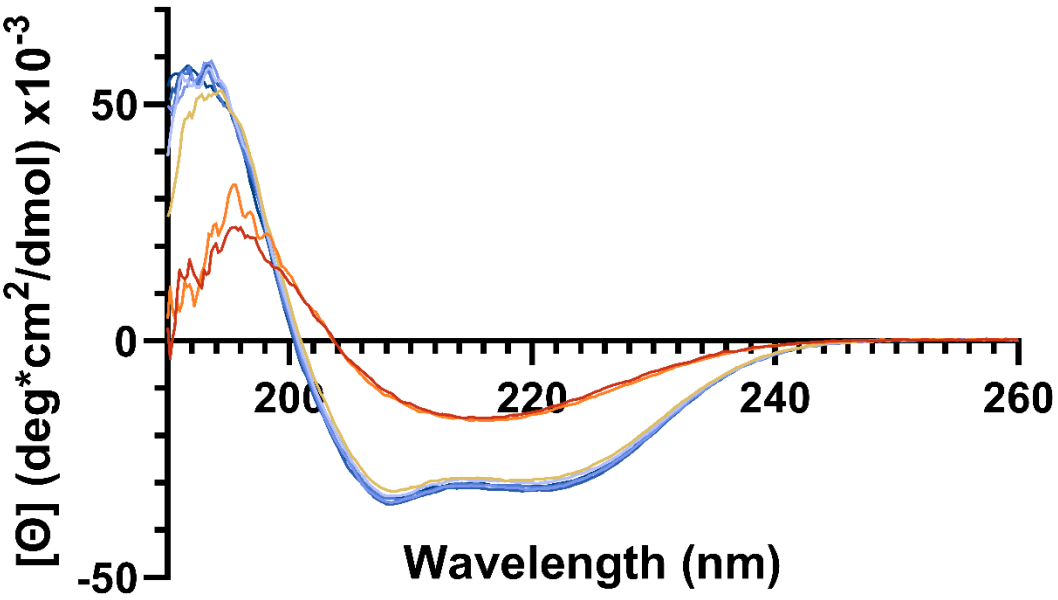

Figure 5.10: Circular Dichroism of α-synuclein and POPG incubation titrated with methanol.
A 1:30 ratio of α-Syn:POPG was first incubated then diluted with different concentrations of methanol according to Section 2.8.5. Displayed is molar ellipticity of each methanol concentration: 0-40% (blues), 50% (yellow), 60% (orange), 70% (red). Traces for 0-50% methanol show a strong α-helical signal, while 60-70% show a strong β-sheet signal.

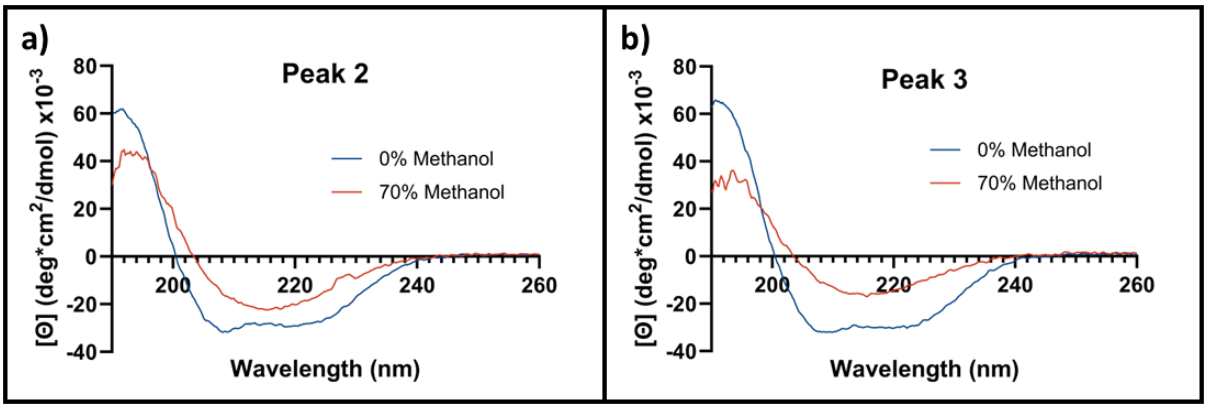

Figure 5.11: Circular Dichroism of AF4 separation peaks with and without methanol.
Molar ellipticity of (a) AF4 separation peak 2 and (b) peak 3 are displayed in the presence of 70% methanol (red), showing predominantly β-sheet signal. For comparison, the spectra without methanol are also displayed (blue) showing the α-helical signal.

5.7 Transmission Electron Microscopy of AF4 Fractions

To more directly visualise the components of each AF4 peak and the methanol-induced β-sheet structure, electron microscopy was employed. Negatively stained grids of each AF4 peak and of peak 3 in 70% methanol were screened and representative images for each shown in Figure 5.12.

AF4 peak 1 is characterised by a relatively small number of both small particles (< 10 nm) and short, thin and flexible fibril structures (Figure 5.12a). As stated previously, peak 1 is the void peak for AF4 and can contain a variety of particles from later peaks. Peak 2 (Figure 5.12b) appears to contain spherical particles which compare well with the POPG liposome control and can also be seen occasionally forming disc-shaped structures, which have been reported for similar α-synuclein:lipid systems at different ratios [271, 306, 307]. Some wide (~25 nm) ribbon-shaped structures can be seen, which the liposomes appear to cluster around.

It is difficult to determine which elements of peak 2 are lipid or protein. However, there is a clear background signal present in both peak 2 and the α-synuclein only control (Figure 5.12e), which would suggest that unbound α-synuclein is present in these images. Comparing the POPG control and the large spherical particles of a similar size range in peak 2 makes their designation as liposomes a reasonable assumption. There are a few thin particles that could be interpreted lipid nanodiscs, which is another known feature of α-synuclein lipid remodelling [271, 306, 307]. The generally intact shape and size of the peak 2 liposomes, compared to controls also implies stabilisation by an outer layer of bound α-synuclein. Clustering of the liposomes could therefore be caused either by the effect of drying during sample preparation, although similar clustering is not really observed in the control, or it may be caused by α-synuclein drawing the liposomes together by anchoring between them as has been shown to be possible in the literature [245, 304, 305].

Peak 3 (Figure 5.12c) is considerably more homogeneous than peak 2, consisting purely of long, thin fibrillar structures that appear very flexible. I hypothesise this to be a bilayer tube or cylindrical micelle of POPG, whose structure is stabilised by α-synuclein in extended α-helices embedded along the length of the tubes as described by Mizuno et. al. [271] (Section 1.9). This hypothesis is supported by the CD data in Section 5.5 showing a strong α-helical signal for peak 3 and by the mass spectrometry and FTIR shown previously in Sections 5.3 and 5.4, which indicate substantial amounts of both lipid and protein in this peak. Further examples of α-synuclein and lipid mixtures generating similar structures can also be found in the literature [307, 308].

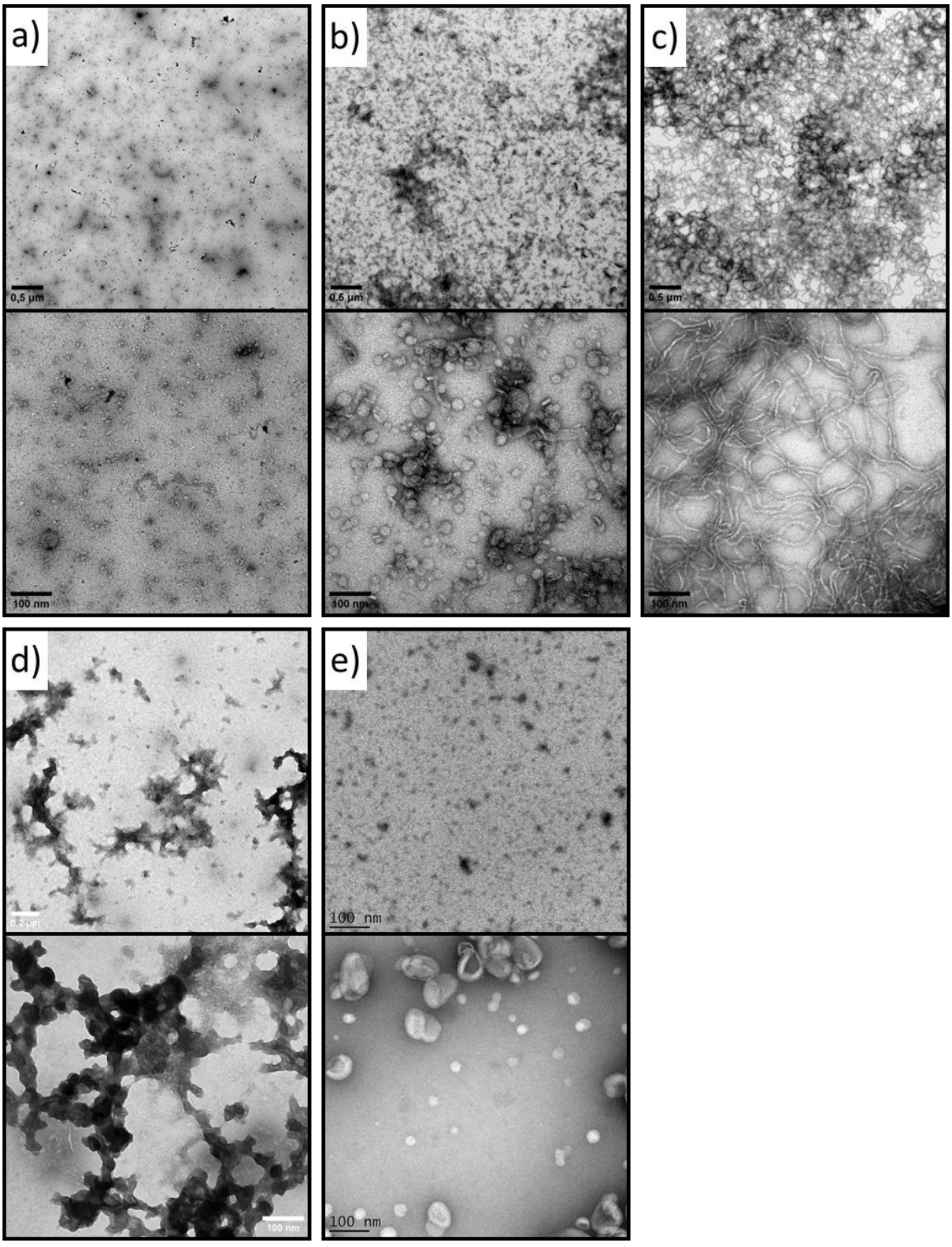

Figure 5.12: Electron microscopy of α-synuclein and POPG fractions.
Negative-stain transmission electron microscopy of a 30:1 L:P mixture of 50nm POPG SUVs and α-synuclein fractionated by AF4 to give a) Peak 1, b) Peak 2 and c) Peak 3. d) A sample of AF4 peak 3, in 70% methanol. e) Controls of α-synuclein only (top) and POPG SUVs (bottom). The bottom panels of a), b) and c) are 5x magnifications of the top panels. The bottom panel of d) is a 2x magnification of the top panel.

Finally, peak 3 in 70% methanol was also screened (Figure 5.12d) to help answer the question of what effect methanol had on this system. The addition of methanol appears to have completely disrupted the POPG lipid tubes and resulted in the formation of large structures resembling amorphous protein aggregation [375]. As such, it seems unlikely that this product shares any relevant similarities to the structures seen in peak 2 and 3, and is probably primarily caused by the denaturing effects of the methanol rather than any previous interaction of α-synuclein on the lipid surface.

5.8 Cryo-Electron Microscopy of AF4 Peak 3

To further examine the hypothesised lipid tube structure of AF4 peak 3, an attempt was made to resolve the structure by cryo-electron microscopy. By aligning many sections of these lipid tubes, the hope was to obtain a regular pattern for the any bound α-synuclein, which could inform on the protein structure bound to the lipid. The POPG:α-synuclein tubes proved challenging to vitrify at an appropriate ice thickness to visualise them despite optimisation through a variety of grid types and vitrification parameters, which are summarised in Table 5.2. Representative micrographs of the best condition can be seen in Figure 5.13.

The sample appears to maintain a strong preference for thicker sections of ice, which introduce additional background noise to the micrographs. Thinner sections of ice, even on the same grid, were completely devoid of these tubes and so the main focus was attempting to process the thicker sections despite the reduced signal-to-noise. Examples of 2D classes with a range of box sizes can be found in Figure 5.14.

Batch No.	Hole Size	Grid Name	Grid Material	Grid Film	Glow Discharge	Vitrification System	Blotting Time	Sample Conc. Factor	Result
1	R1.2/1.3	Quantifoil Copper	Copper	Holey Carbon	1 minute	Vitrobot	4 seconds	0.5	No sample in holes
								1	No sample in holes
								6.7	Very few tubular structures observed in thicker sections
	R1.2/1.3	Carbon Support Film	Copper	Holey Carbon with Carbon Support Film	1 minute	Vitrobot	4 seconds	0.5	No sample in holes
								1	No sample in holes
	R1.2/1.3	UltrAuFoil	Gold	Holey Gold	1 minute	Vitrobot	4 seconds	6.7	**Data Collected:** Many overlapping tubes, thick ice giving lower resolution
2	R1.2/1.3	UltrAuFoil	Gold	Holey Gold	10 seconds	Lecia	4s front-blot	1	No sample in holes
							4s back-blot	1	No sample in holes
	R1.2/1.3	Quantifoil Gold	Gold	Holey Carbon	10 seconds	Lecia	4s front-blot	4	Very few tubular structures observed in thicker sections
							4s back-blot	4	No sample in holes
	R1.2/1.3	Quantifoil Copper	Copper	Holey Carbon	10 seconds	Lecia	4s front-blot	4	No sample in holes
3	R1.2/1.3	UltrAuFoil	Gold	Holey Gold	1 minute	Lecia	5s front-blot	10	Mainly thin sections with no sample, a few thick ice sections had good sample concentration
								20	Ice too thick to image
								5	Ice too thick to image
	R1.2/1.3	Quantifoil Gold	Gold	Holey Carbon	1 minute	Lecia	5s front-blot	10	Ice too thick to image
								20	Ice too thick to image
					15 seconds	Lecia	5s front-blot	10	Ice too thick to image
								20	Ice too thick to image
4	R3.5/1	Quantifoil Gold	Gold	Holey Carbon	15 seconds	Lecia	5s back-blot	1	Ice too thick to image
								10	Ice too thick to image
							7s back-blot	1	No ice (too dry)
								10	**Data Collected:** Good ice, but low conc. sample
5	R3.5/1	Quantifoil Gold	Gold	Holey Carbon	15 seconds	Lecia	7s back-blot	10	Microscope warm up de-vitrified grids
							8s back-blot	10	Microscope warm up de-vitrified grids
	R2/2	Quantifoil Copper	Copper	Holey Carbon	15 seconds	Lecia	8s back-blot	10	Microscope warm up de-vitrified grids
6	N/A	CLC300Cu25-UT	Copper	Lacy Carbon with Carbon Support Film	15 seconds	Lecia	4s back-blot	10	Ice too thick to image
							8s back-blot	10	Ice too thick to image
							6s front-blot	10	Very dry, with a few spots of thick ice containing low sample conc.
							10s front-blot	10	Very dry, with a few spots of thick ice containing low sample conc.
7	R3.5/1	Quantifoil Gold	Gold	Holey Carbon	15 seconds	Lecia	6s back-blot	1*	Good ice, low sample conc.
	R3.5/1	Quantifoil Copper	Copper	Holey Carbon	15 seconds	Lecia	6s back-blot	1*	Good ice, low sample conc.
							8s back-blot	1*	No ice (too dry)
	R2/2	Cu-GO	Copper	Graphene Oxide	None	Lecia	6s front-blot	10	No ice (too dry)
							8s front-blot	10	No ice (too dry)

Table 5.2: Cryo-EM grid conditions and outcomes.
Screened conditions for cryo-EM visualisation of AF4 peak 3, using different types of grids, sample concentrations, glow-discharge times and blotting methods. Refer to Section 2.8.8 for differences between the Vitrobot and Lecia systems. Sample concentrations are expressed as a multiple of AF4-fractioned peak 3 concentration. '*' Indicates sample was applied and blotted 3-times before vitrification, which will increase its final concentration.

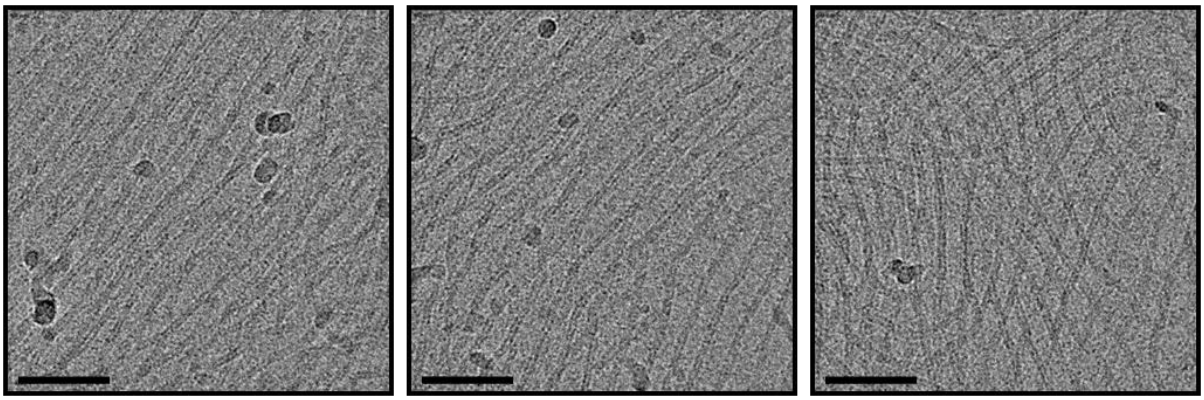

Figure 5.13: Cryo-electron microscopy of α-synuclein lipoprotein tubes.
Representative micrographs of the AF4 peak 3 fraction, showing tubular structures with unusually regular spacing and alignment. Scale bars = 60 nm.

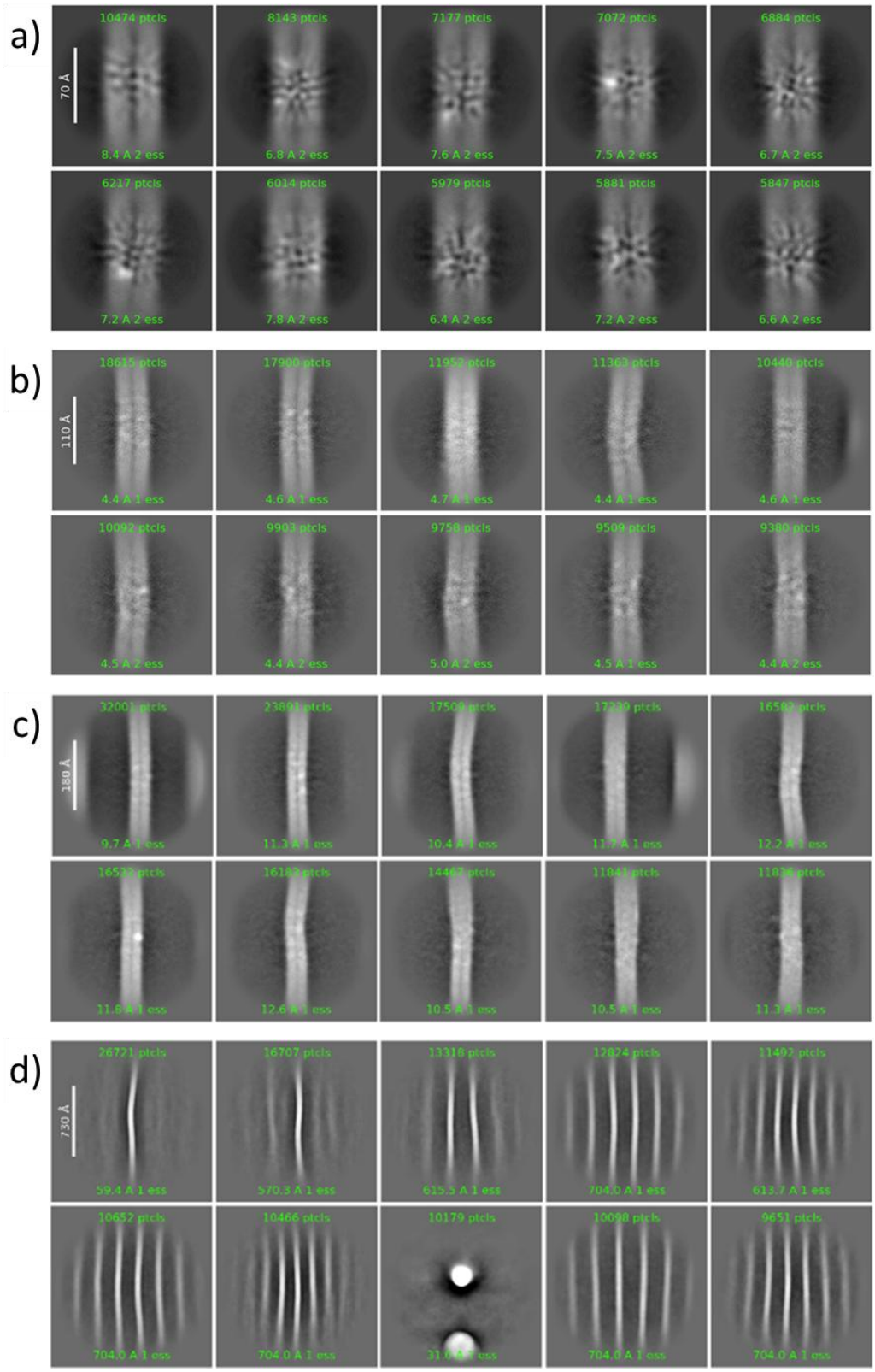

Figure 5.14: 2D-classification of lipoprotein tubes by cryo-EM.
A series of 2D-classifications are shown, which were obtained considering different box-sizes during particle alignment. The box-sizes used are: a) 156 Å, b) 273 Å, c) 431 Å and d) 1760 Å. Scale bars are shown on the left of each image.

2D classifications generated by aligning many sections of these tubes are useful for determining some of the general structural traits of this sample. From these, it can be determined that the diameter of the tubes is 5-6 nm across, with a hollow space running down the centre most visible with medium box-sizes (Figure 5.14b-c). The size of this diameter excludes the possibility of a bilayer tube, as the thickness of a POPG bilayer is ~40 Å [376]. Therefore, it can be concluded that a lipid structure of this diameter must be a cylindrical micelle.

Using a much larger box size (Figure 5.14d), there appears to be a lack of any regular twist or periodicity in the tubes, as well as an intriguing preference for highly regular spacing between each tube. The inter-tube spacing indicated by the 2D classes is a range between 16-26 nm measured from the centre of each tube or 10-20 nm from the outer edges. This spacing is particularly exciting, considering the double-anchor model, proposed by Fusco et. al. 2016 [305], in which an individual α-synuclein monomer is capable of binding two separate membranes up to 15 nm apart. As a result, this separation distance may be due to inter-micelle binding by some of the α-synuclein monomers. For such a regular spacing to be enforced implies the presence of rigid linkers. In the case of α-synuclein, this could be achieved via coiled-coil interactions along the long amphipathic helical regions of the protein, forming rigid dimers between micelles. 3D reconstructions were generated using either the Ab Initio or helical refinement tools of CryoSPARC [377]. The best results from each method are shown in Figures 5.15 and 5.16.

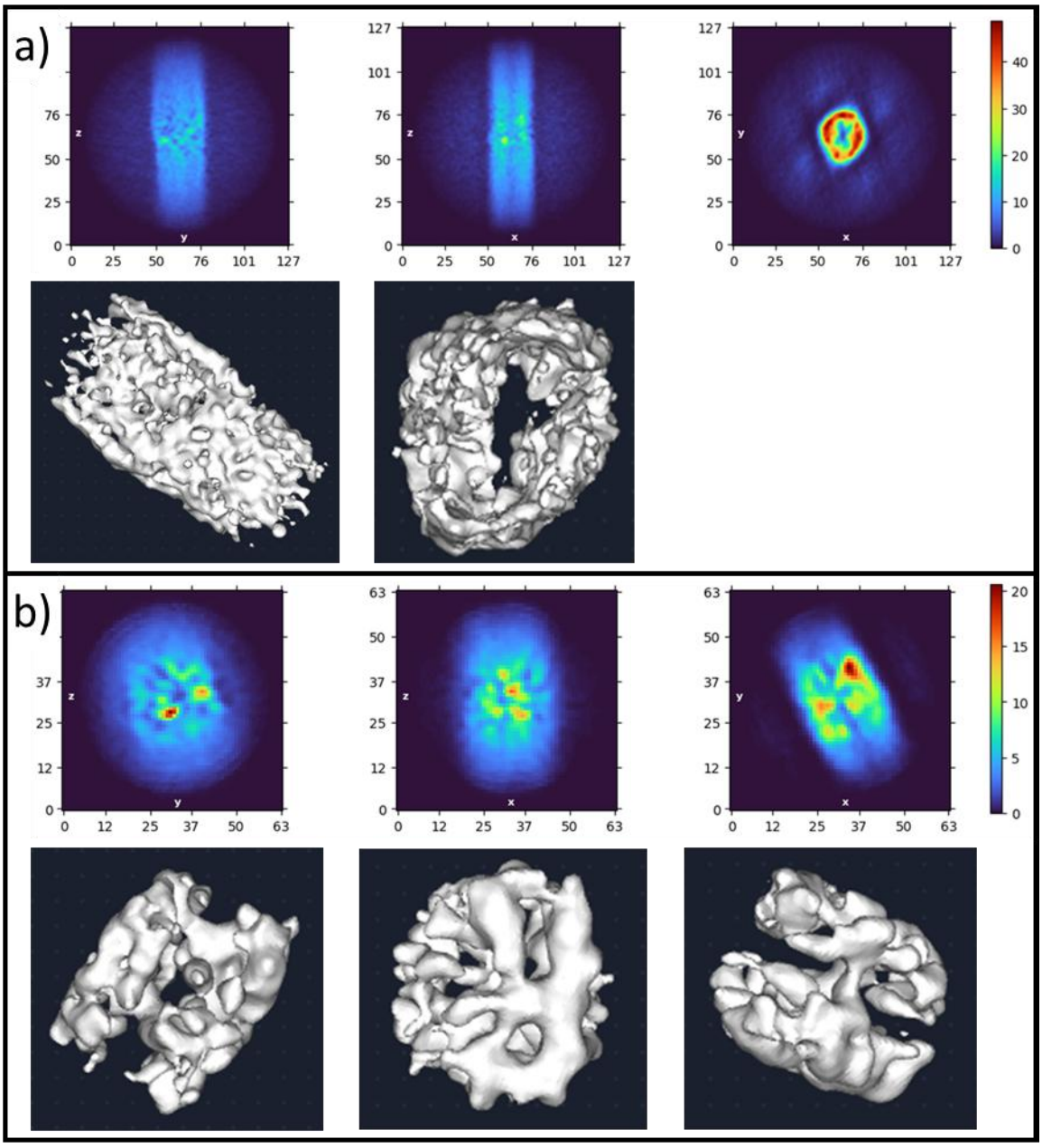

Figure 5.15: Ab Initio 3D reconstructions of lipoprotein tubes.
Two representative examples of untemplated 3D reconstruction from 2D classes with a box-size of 273 Å. a) Reconstruction provided a hollow tube, representing the expected structure of a micelle, with little structural detail. b) Reconstruction gave a small amorphous particle with no discernible structure, which is likely non-realistic.

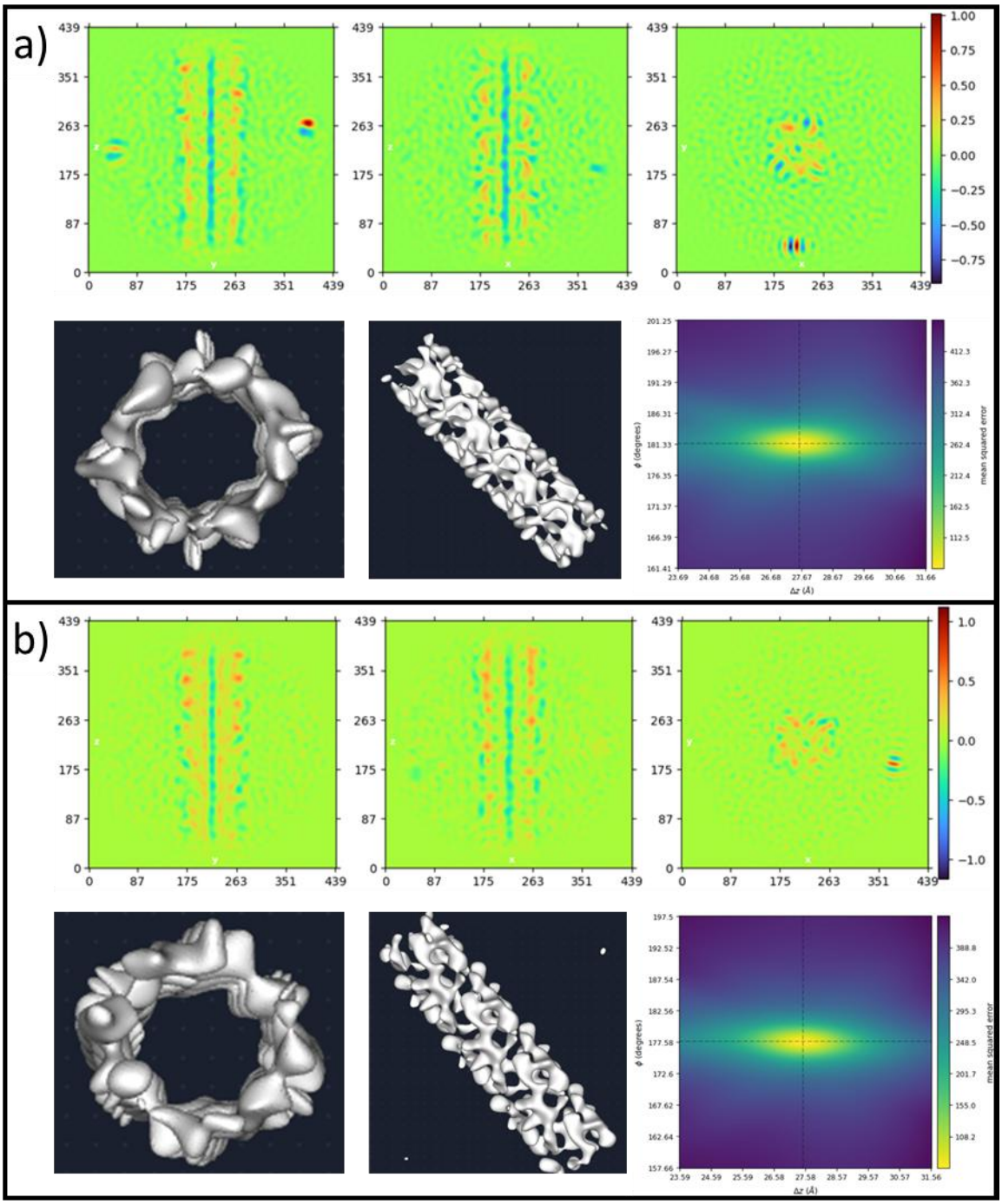

Figure 5.16: 3D reconstructions of lipoprotein tubes using helical refinement.
Two representative examples of 3D reconstructions using the helical refinement job in cryoSPARC. This forces a fibrillar structure, which fits better to lipid micelles, and searching for regularity along the fibril axes. Estimated helical rise and helical twist are shown (bottom right of each), which report virtually no twist and a regular rise of 27.6 Å. These measurements are unlikely to have meaning, considering no actual secondary structure can be made out from these reconstructions.

Ab Initio attempts to generate a 3D structure from 2D classes without a reference model or user-imposed restraints [377]. In this instance, Ab Initio has difficulty generating a coherent structure (Figure 5.15b) due to the relatively high background noise from imaging thicker ice sections and due to the apparent lack of any regular structural elements to align. It was able to capture the tube-like essence of the micelles, but had no further structural detail (Figure 5.15a).

The helical refinement feature was used to add constrains to the reconstruction by enforcing a fibrillar shape and searching for any repeated pattern along the length of the tubes (Figure 5.16). Both the shown reconstructions have a ~27.5 Å repeating pattern along a hollow tube with no apparent twist. Due to the lack of similarities in patterns between these and further helical reconstructions, it is likely that these patterns are mostly imposed by the fitting algorithm. However, the suggested lack of density in the centre of the tube does indicate a stronger regularity on the outer face of the tube.

These results appear to support the hypothesis of this system being a lipid micelle coated with α-synuclein as modelled by Mizuno et. al. [271]. POPG has a phase transition temperature of -2 °C, stated by Avanti Polar Lipids, well below ambient room temperature prior to vitrification. As such, there should be very little regularity present within the micelle, which is in a liquid-like state. Meanwhile, oligomeric complexes of α-synuclein or significant ordering of embedded α-helices should be susceptible to structural alignment and become visible during 2D classification and 3D reconstruction. The “noisy” structural alignment on the outer surface of these tubes could indicate a random distribution of loose associations made between the surface-bound α-helices, without a strong overall order or repeating pattern across the whole micelle, which is predicted by the Mizuno et. al. model (Figure 5.17) [271].

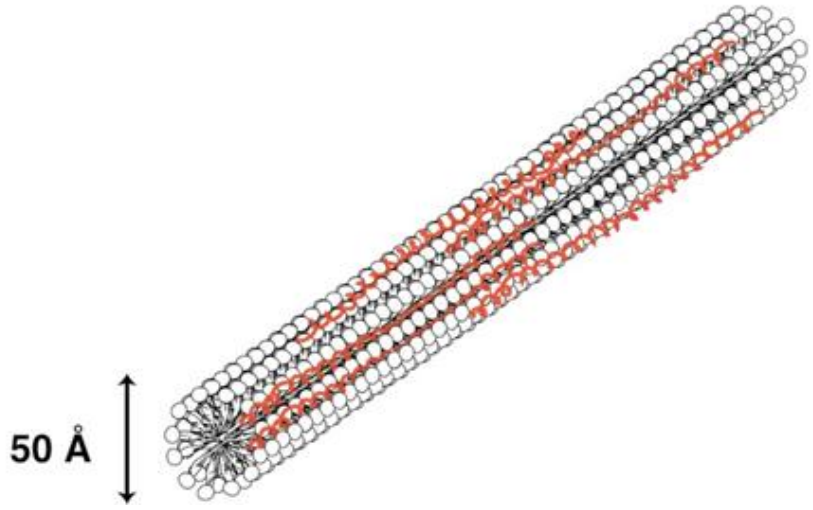

Figure 5.17: Model of α-synuclein distribution on lipid micelles by Mizuno et. al.
Shown is a model of α-synuclein bound to a POPG cylindrical micelle, based on observations by Mizuno et. al., discussed in Section 1.9. Figure from Mizuno et. al. 2012 [271].

5.9 Atomic Force Microscopy of AF4 Peaks

Atomic force microscopy (AFM) provides an alternative perspective, which can be compared to the electron microscopy results. An advantage of using AFM in this case is the ability to gather 3D height data. Though this work contains only initial screening of samples dried onto silica, one potential downstream application of this technique was to study our samples in more native liquid conditions than electron microscopy allows for. POPG liposome and α-synuclein controls can be found in Figure 5.18, while heightmaps of AF4 peaks 2 and 3, as well as an unfractionated sample, can be viewed in Figure 5.19.

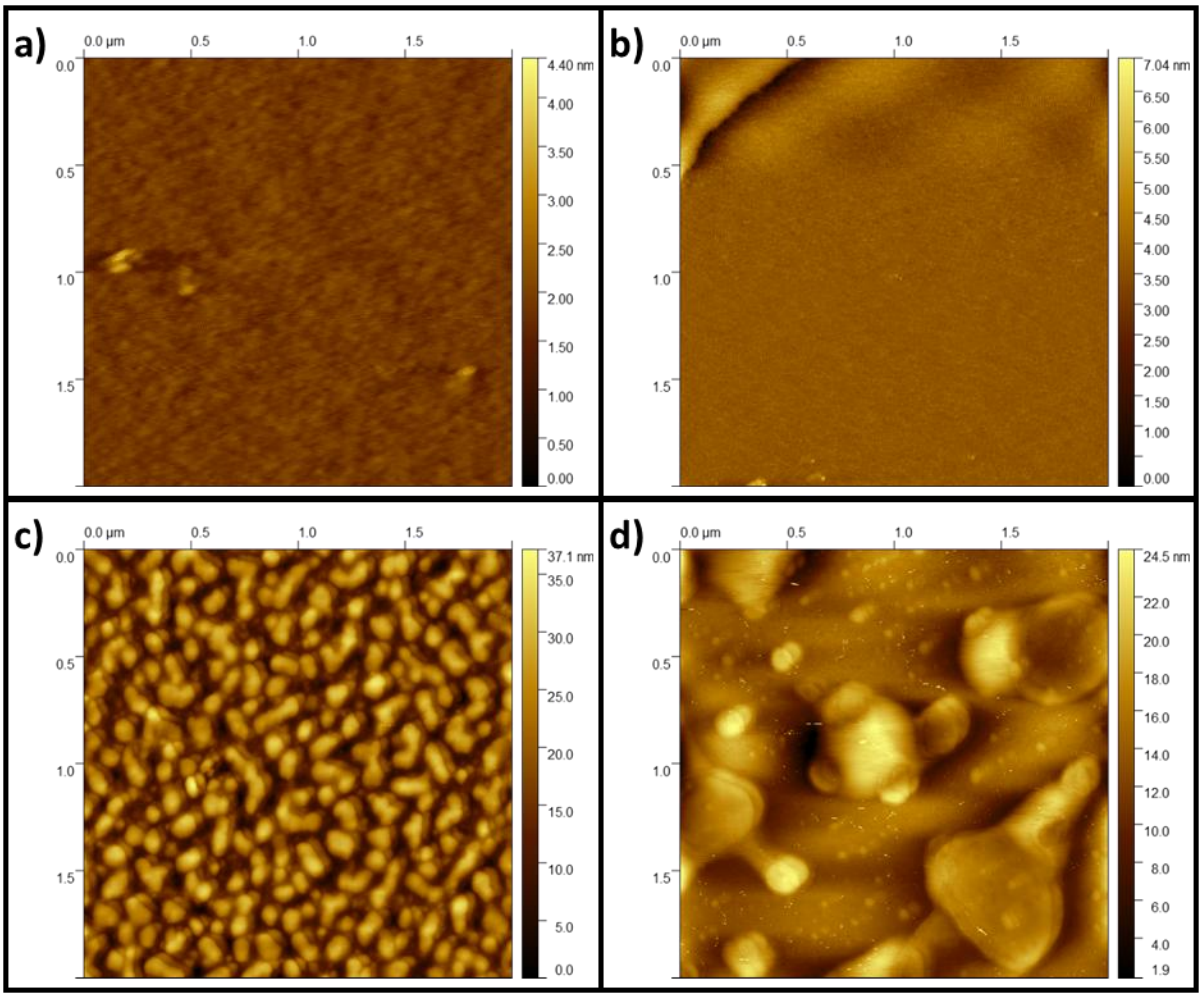

Figure 5.18: Atomic force microscopy control samples.
Representative height maps of control samples applied and dried onto atomically flat silica are shown. a) Bare silica with no sample. b) The sodium phosphate buffer only. c) 270 µM α-synuclein. d) 8100 µM POPG as 50 nm SUVs.

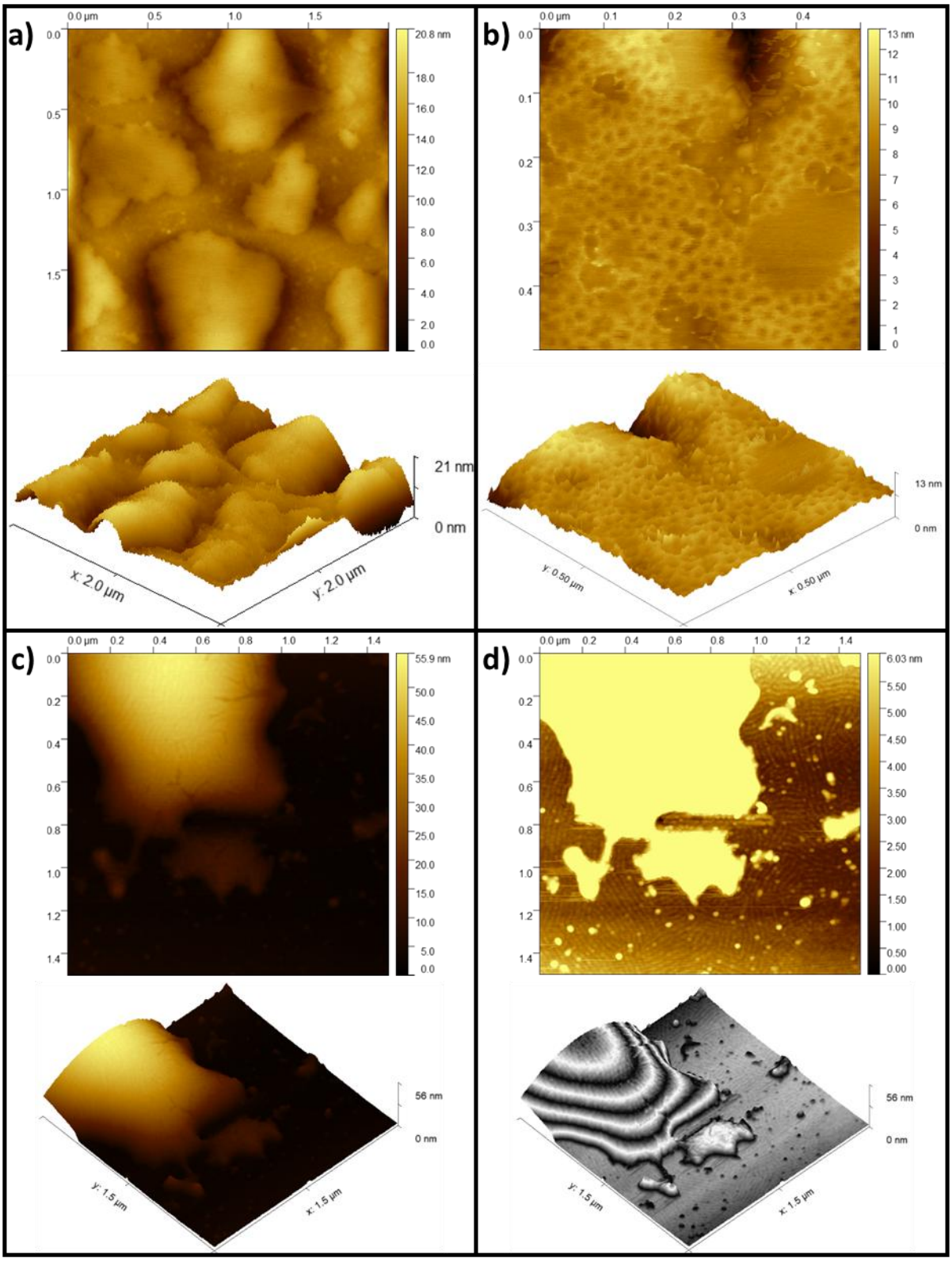

Figure 5.19: Atomic force microscopy of AF4 fractions.
Representative 2D and 3D height maps of an incubation of 270:8100 µM α-synuclein:POPG SUVs and its AF4 fractions, which were dried onto atomically flat silica, are shown. a) Unfractionated sample, which was 10x diluted in buffer before sample application. b) AF4 peak 2. c) AF4 peak 3. d) The same region shown in c), using a different height scale to highlight background features.

Controls of bare silica and dried buffer show virtually no contribution to height maps, as expected (Figure 5.18). The α-synuclein only control formed an assortment of relatively large spherical and elongated particles, much larger than a single protein (Figure 5.18c). Deposition of α-synuclein into this pattern is reminiscent of liquid-liquid phase-separation [141, 142], which may occur as the protein concentrates during the slow air-drying process. Similarly, drying of POPG controls appears to show large lipid droplets form (>500 nm diameter), with only a few intact liposomes remaining (Figure 5.18d).

Peak 2 features what appears to be a sheet of small pores packed tightly together (Figure 5.19b). Two separate grain fitting algorithms were used independently identify individual pores in the image (Figure 5.20). Both algorithms were employed using either a “strict” or “soft” filter as described in Section 2.8.10. The use of different filters and algorithms was to reduce any subjective bias introduced by picking between either algorithm or from choosing an arbitrary filter strictness. When assessing the grain statistics for each case, the average pore radius can be determined as between 10-15 nm (Figure 5.21). This size distribution fits well with the liposomes observed by negative stain EM (Section 5.7, Figure 5.12b), although they are much more closely packed in the AFM images, likely due to the effect of drying out the samples.

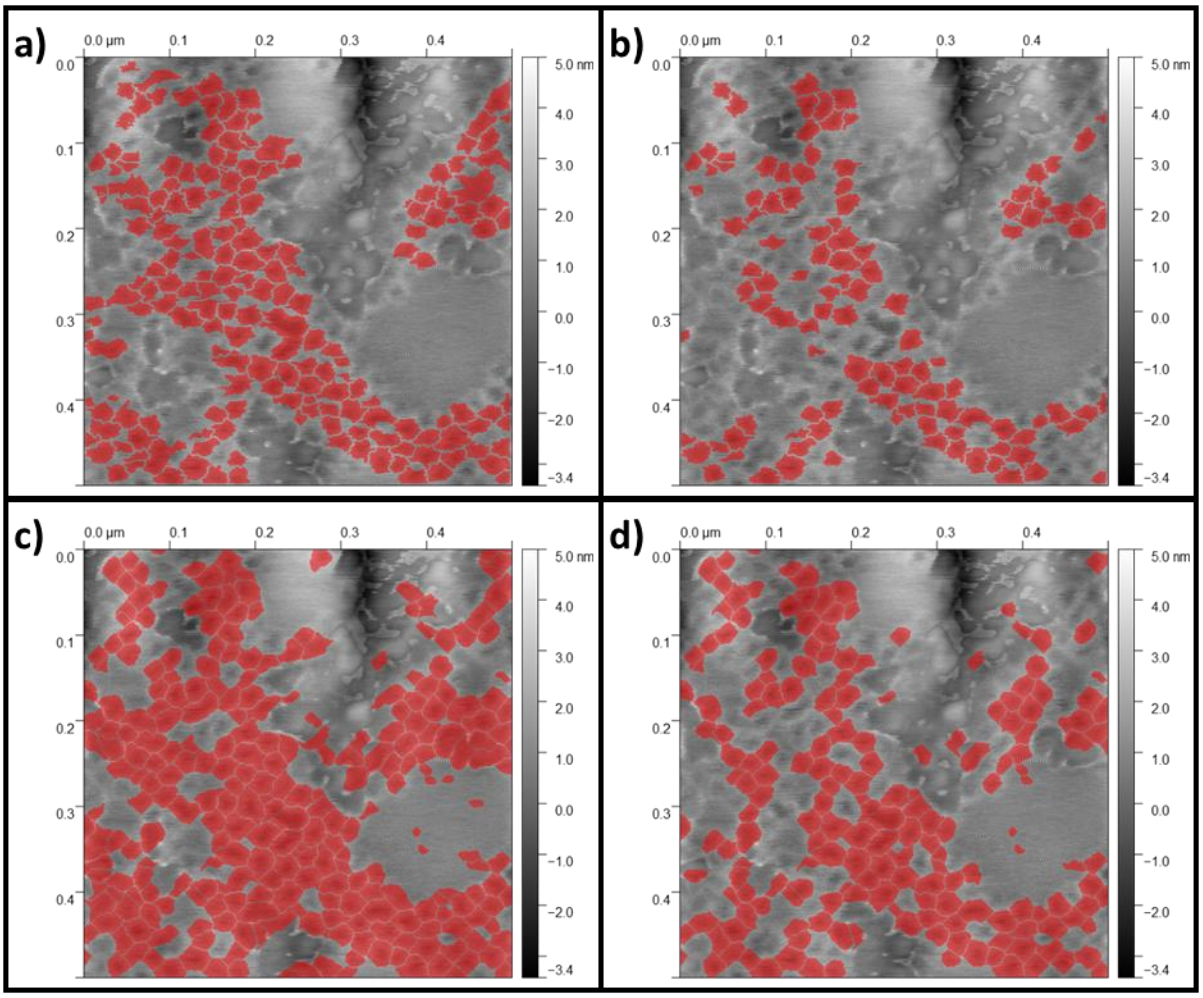

Figure 5.20: Grain fitting of AF4 peak 2 pores in AFM height maps.
The AFM height map of AF4 peak 2 (Figure 5.19b) is shown in all images overlaid with algorithmically fitted grains (red), mostly corresponding to pore-like structures in the image. Details of each fitting algorithm can be found in Section 2.8.10. a) Watershed (Soft filter). b) Watershed (Strict filter). c) Segmentation (Soft filter). d) Segmentation (Strict filter).

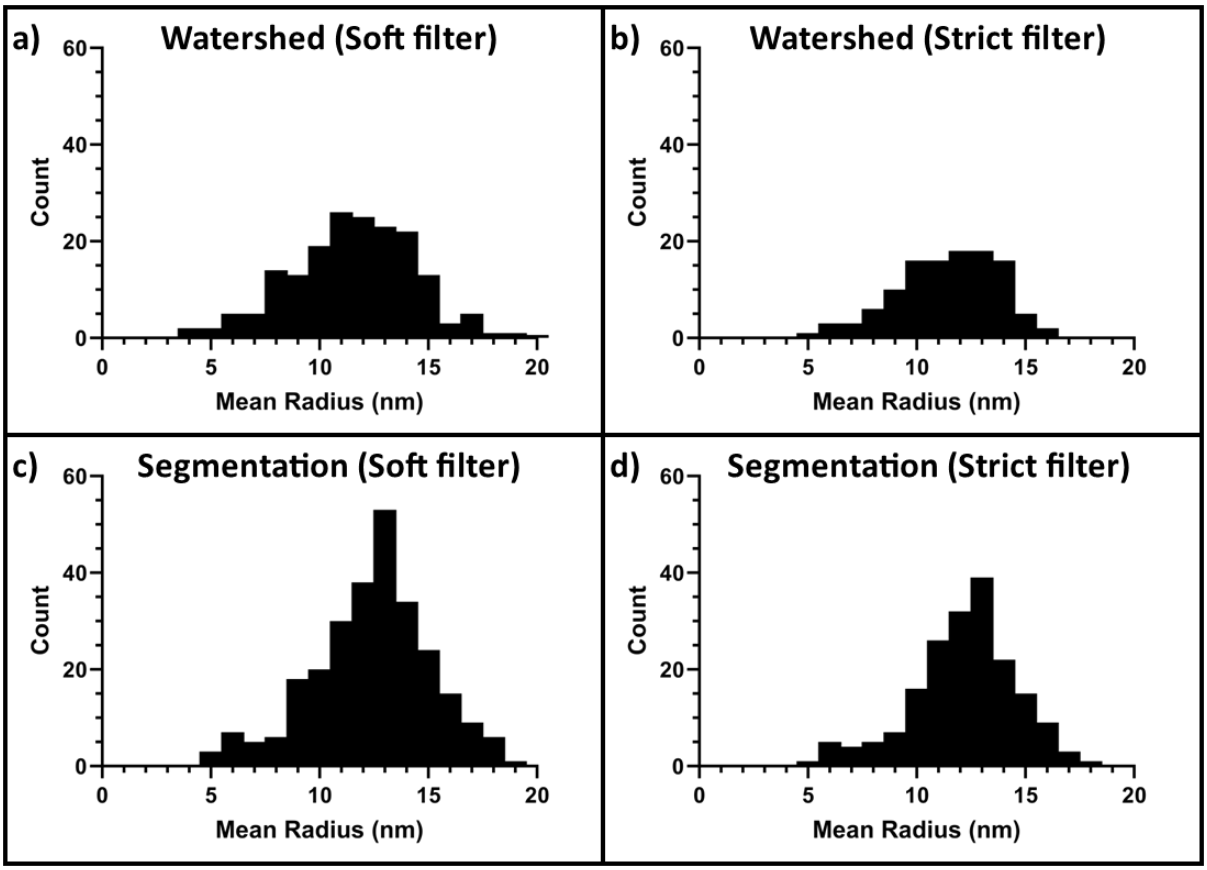

Figure 5.21: Histograms of grain radius with different fitting algorithms.
Histograms each show the numbers of individual grains with the same mean radius. Labels above each histogram indicate which grain fitting algorithm was used and whether the filtering was "soft" or "strict" as described in Section 2.8.10.

Based on the roughly circular shape and 10-15 nm radius, it seems likely that these pores are the liposomes, kept in close proximity by surface-bound α-synuclein and the effects of sample drying. The bilayer walls between each liposome are kept sturdy by these interactions, while the middle of each liposome appears to sag forming the pore-like appearance. Though this assumption is unable to be further substantiated with follow-up AFM data, it seems a reasonable conclusion given the sample composition, similar size distribution by electron microscopy and lack of similarity with liposome only controls.

At first glance, the AFM of peak 3 appears to show a large mass with a fibrillar pattern on its surface (Figure 5.19c). This is most likely an artefact of drying this sample, due to the high lipid content, causing large wetted droplets to form, with similar dimensions to those observed in the POPG control (Figure 5.18d) and unfractionated sample (Figure 5.19a). More interestingly, the fibrillar pattern seen on the surface of the droplet can also be seen coating the surface of the silica with a highly regular spacing (Figure 5.19d), reminiscent of the spacing between lipid micelles in previously

shown cryo-EM data (Section 5.8). As previously mentioned, this could be the result of α-synuclein interaction between micelles, maintaining a set distance of roughly 10-20 nm between them.

Unfortunately, the larger scan area required to capture a section of the droplet resulted in a reduced image resolution, which makes measurement of these fibrils challenging. A repeat experiment targeting just the background fibrillar pattern on a smaller scale would be required to make accurate measurements comparable with the cryo-EM.

Importantly, these data support the idea that inter-micelle anchoring by α-synuclein may be the native state of this system in solution. While AFM and cryo-EM dry or freeze a native sample, negative-stain EM requires changing the solution conditions with a stain, prior to drying. This might explain why regular spacing between these micelles is not observed in negative-stain EM, as the addition of uranyl formate stain may disrupt the interactions that allow α-synuclein to bridge between two micelles at once.

5.10 Multi-Angle Light-Scattering Time Course of α-Synuclein POPG incubations

Multi-angle light-scattering (MALS) measurements can be used to determine the average radial distribution of particles in a solution. MALS was used to detect size changes in POPG liposomes incubated with or without α-synuclein at both ambient temperature (25 ^{o}C) and at 37 ^{o}C. The aim was to evaluate whether size-changes in the mixed sample during incubation are due to liposome fusion caused by higher temperatures or by the membrane-remodelling activity of α-synuclein. The use 37 ^{o}C, rather than 45 ^{o}C used in most other incubations, was due to an upper limitation of the incubator attached to the MALS system.

Size distributions from several timepoints during an 8-hour incubation at 37 ^{o}C show that POPG liposomes by themselves are fairly stable and do not grow over this time period (Figure 5.22). In contrast, a 30:1 POPG:α-synuclein mixture increases rapidly in average particle size, immediately after mixing, even at ambient temperature (Figure 5.23). This growth process plateaus after around 2 hours incubation at 37 ^{o}C, or 2.5 hours after initial mixing, and is likely to represent α-synuclein membrane-binding and subsequent remodelling to cylindrical micelle structures. These data show the stability of POPG SUVs over experimental timescales and the necessity for α-synuclein to be present for any significant size changes to occur.

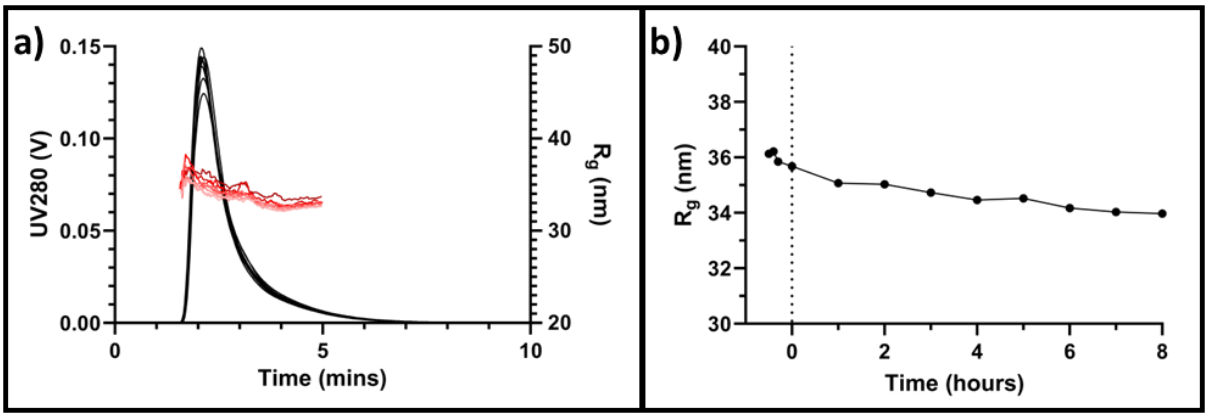

Figure 5.22: MALS time course of POPG SUVs at 37 °C.
810 µM of 50 nm POPG SUVs were incubated at 37 °C and periodically injected through a UV and multi-angle light-scattering detectors over 8 hours. Radius of gyration (R_g) was calculated from the angular dependence by Zimm plot. a) The UV (black) and R_g (red) for individual timepoints is plotted against elution time through the detectors. R_g is colour-coded from 0-8 hours as dark-light red. b) The average R_g between 1.8-3.0 mins elution time for each time-point, plotted against incubation time. Negative incubation time corresponds to pre-incubation measurements after mixing at 25 °C.

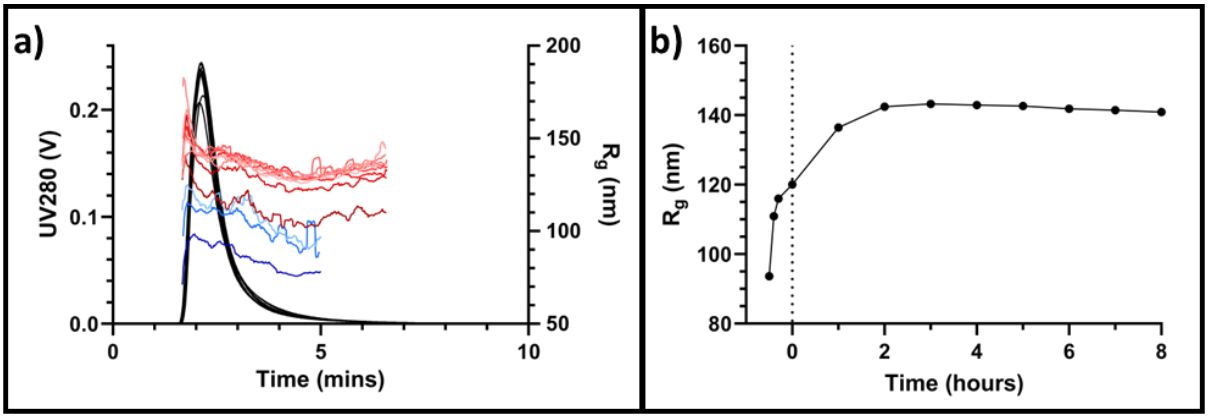

Figure 5.23: MALS time course of α-synuclein and POPG SUVs at 37 °C.
810 µM of 50 nm POPG SUVs and 27 µM α-synuclein were incubated at 37 °C and periodically injected through a UV and multi-angle light-scattering detectors over 8 hours. Radius of gyration (R_g) was calculated from the angular dependence by 2nd-order Berry plot. a) The UV (black) and R_g (blue and red) for individual timepoints is plotted against elution time through the detectors. R_g is colour-coded from 0-8 hours as dark-light red. Pre-incubation measurements are shown for 0, 6 and 12 minutes after mixing (dark to light blue). b) The average R_g between 1.8-3.0 mins elution time for each time-point, plotted against incubation time. Negative incubation time corresponds to pre-incubation measurements after mixing at 25 °C.

5.11 Circular Dichroism Timelapses of α-Synuclein and POPG Incubation

Most of the data shown in this chapter was derived from AF4 separations after relatively short incubations (2.5 hours) of α-synuclein and POPG at 45 °C. In an attempt to characterise any species that occur downstream of this system, a much longer circular dichroism timelapse was recorded during the 45 °C incubation of α-synuclein and POPG SUVs at the same lipid:protein ratio, which is displayed in Figure 5.24.

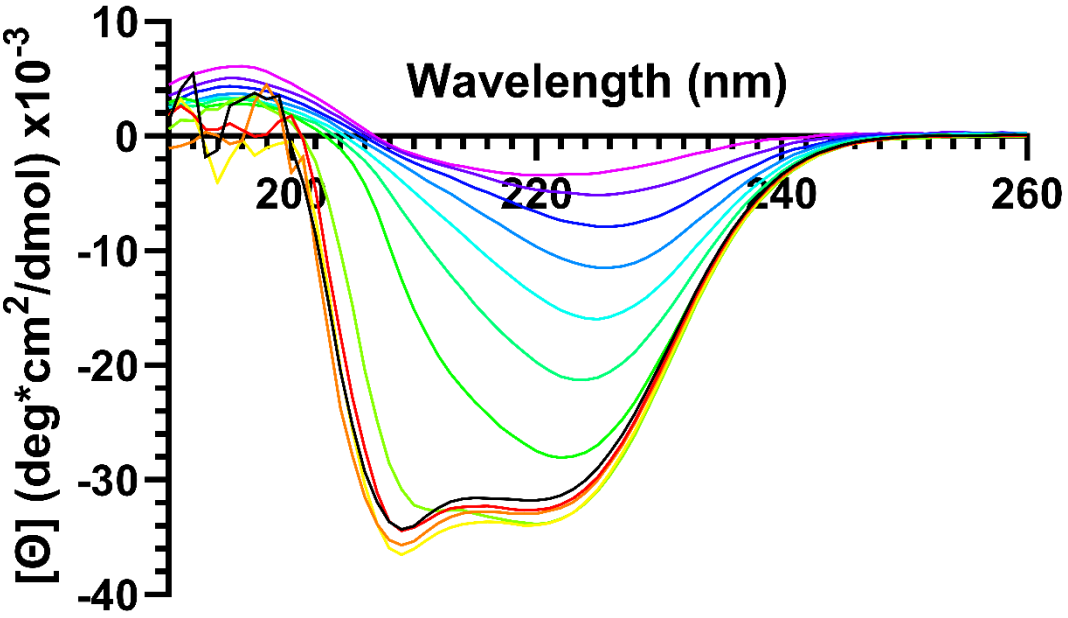

Figure 5.24: Circular dichroism timelapse of incubated α-synuclein and POPG SUVs.
An incubation of 27 µM α-synuclein and 810 µM POPG as 50 nm SUVs at 45 °C was monitored continuously by circular dichroism. The initial measurement is shown in black, with subsequent measurements after 20 h, 30 h and 40 h shown in red, orange and yellow respectively. The remaining measurements shown follow on in 4-hour increments from 44 h (lime) to 72 h (pink).

The CD spectrum clearly shows a large shift in α-synuclein from a primarily α-helical structure, with characteristic minima at 208 nm and 222 nm, to primarily β-sheet with a single minimum close to the characteristic minimum of 218 nm. This transition is more easily visualised by plotting these wavelengths as a function of time (Figure 5.25). From this, it is clear that there is actually a gradual increase in α-helical signal over time, shown by increasingly negative ellipticity, after about 20 hours. This is followed by a rapid transition to β-sheet, with the majority of 208 nm signal lost between the 40-hour to 50-hour timepoints.

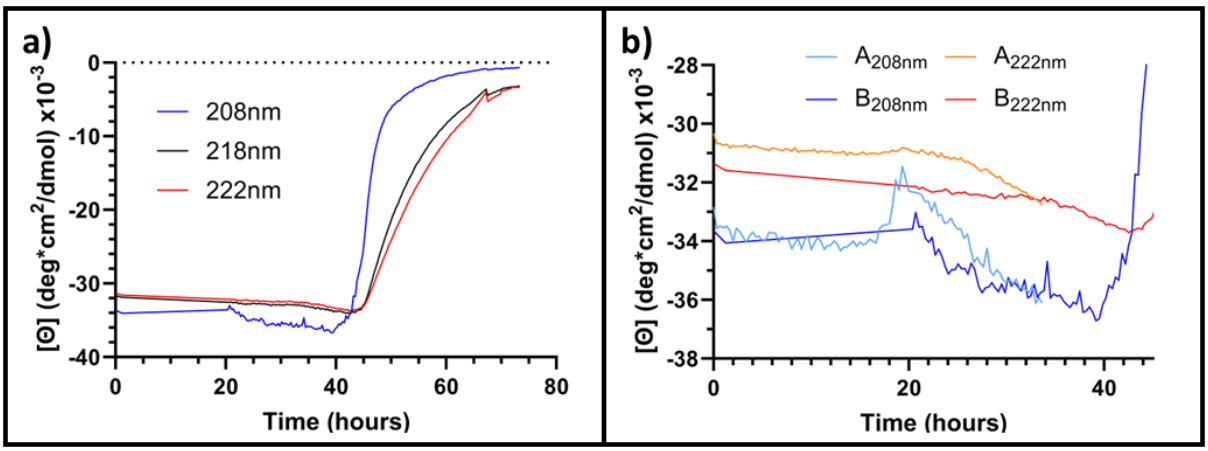

Figure 5.25: Change in characteristic CD wavelengths during α-synuclein:POPG incubation. Incubations of 27 µM α-synuclein and 810 µM POPG as 50 nm SUVs at 45 °C were monitored continuously by circular dichroism. a) Changes in molar ellipticity for the wavelengths 208 nm (blue), 218 nm (black) and 222 nm (red) over a single 73-hour timelapse. b) Wavelengths 208 nm and 222 nm from the first 45 hours shown in (a), labelled as B_{208nm} and B_{222nm}, accompanied by a replicate incubation that was recorded for only 34 hours, labelled A_{208nm} and A_{222nm}.

Following on from conclusions arising from the cryo-EM data (Section 5.8), reasonable speculations can be made on the changes occurring here. During the first 20 hours, there is very little change in the CD signal, which still appears strongly α-helical. This is likely the result of the extended helical structure of α-synuclein which embeds within the lipid layer and stabilises the cylindrical micelle structure, as discussed previously.

After 20 hours, there is a gradual increase in helicity. It is unlikely that this is the result of any additional α-helical structure in α-synuclein, as the extended helical structure already involves the entire protein chain. However, an increase in apparent α-helical signal can arise due to an increase in intermolecular interactions between the α-helices [370, 371]. From the cryo-EM it is hypothesised that α-synuclein must be randomly distributed along the surface of the micelles, due to the lack of structural alignment in 2D and 3D reconstruction attempts. Therefore, this increase in helicity over time could potentially indicate closer packing of α-synuclein helices together during this period.

Finally, after α-synuclein packing reaches a certain threshold level, marked by the maximum helicity at around 40 hours, there is a switch to a β-sheet-like structure. This change happens relatively rapidly throughout the whole sample, indicating a co-operative change towards a new secondary structure. It is easy to imagine that this β-structure, once nucleated, could potentially propagate along the length of the lipid micelles, through the now more tightly packed α-synuclein, templating the structural conversion throughout the whole mixture.

The exact nature of the β-structure cannot be further inferred from this information alone. However, due to the potential relevance of this model system in Parkinson's disease pathology, it is tantalising to speculate that this may emulate a disease-associated amyloid of α-synuclein, shown to form in the proximity of membranes *in vivo* [108, 242] and may also encapsulate lipids from the micelles within their structure [297, 311]. A priority of further work would be therefore be to elucidate this new, potentially more regular, structure by techniques such as cryo-EM.

5.13 X-Ray and Neutron Scattering of α-Synuclein and POPG Mixtures

A more detailed investigation of the structural changes observed over time by circular dichroism (Section 5.12) was carried out by small-angle light scattering using both X-rays (SAXS) and neutrons (SANS). While circular dichroism broadly reports on the protein secondary structure, SAXS and SANS techniques are able to distinguish shape, size and interaction distances between particles, including both protein and lipid. The primary difference between SAXS and SANS is that X-rays are scattered by atomic electrons and neutrons are scattered by the atomic nuclei themselves.

Neutron scattering is especially useful in this context as the strength of neutron scattering, called the scattering length density (SLD), can be manipulated for different parts of the sample by altering the composition of atomic nuclei, in this case through swapping some hydrogens to deuterium. The difference between the SLD of each sample component from the SLD of the surrounding solvent determines how strongly each signal is detected independently from the background solvent signal, termed signal contrast. By deuterating either α-synuclein or POPG, then mixing them into specific ratios of H_2O and D_2O, the SLD of the solvent and one of the two components can be made roughly equivalent to each other, thereby rending the component signal indistinguishable from background noise, leaving only the remaining component signal visible. Section 2.8.11 includes a table detailing each of the mixtures visualised using SANS, as well as a description of the fitting algorithms used in the following analyses.

Controls of monomeric α-synuclein were measured by SAXS and in different combinations of hydrogenated or deuterated protein and solvent. Figure 5.26 shows representative scattering data from each approach. The data was fit using the monodisperse gaussian coil model, which describes a system containing only one type of polymer chain, with a gaussian distribution of lengths between each segment within the chain. In this case the model was used as an approximation for the random coil structure of monomeric α-synuclein. Model-fit radii of gyration (R_g) for each condition are displayed in Table 5.3. Though not particularly relevant to the conclusions of this work, it is

interesting to note the increase in R_g at higher temperatures under the same conditions. This is likely due to expansion of the random coil structure with the increased kinetic mobility.

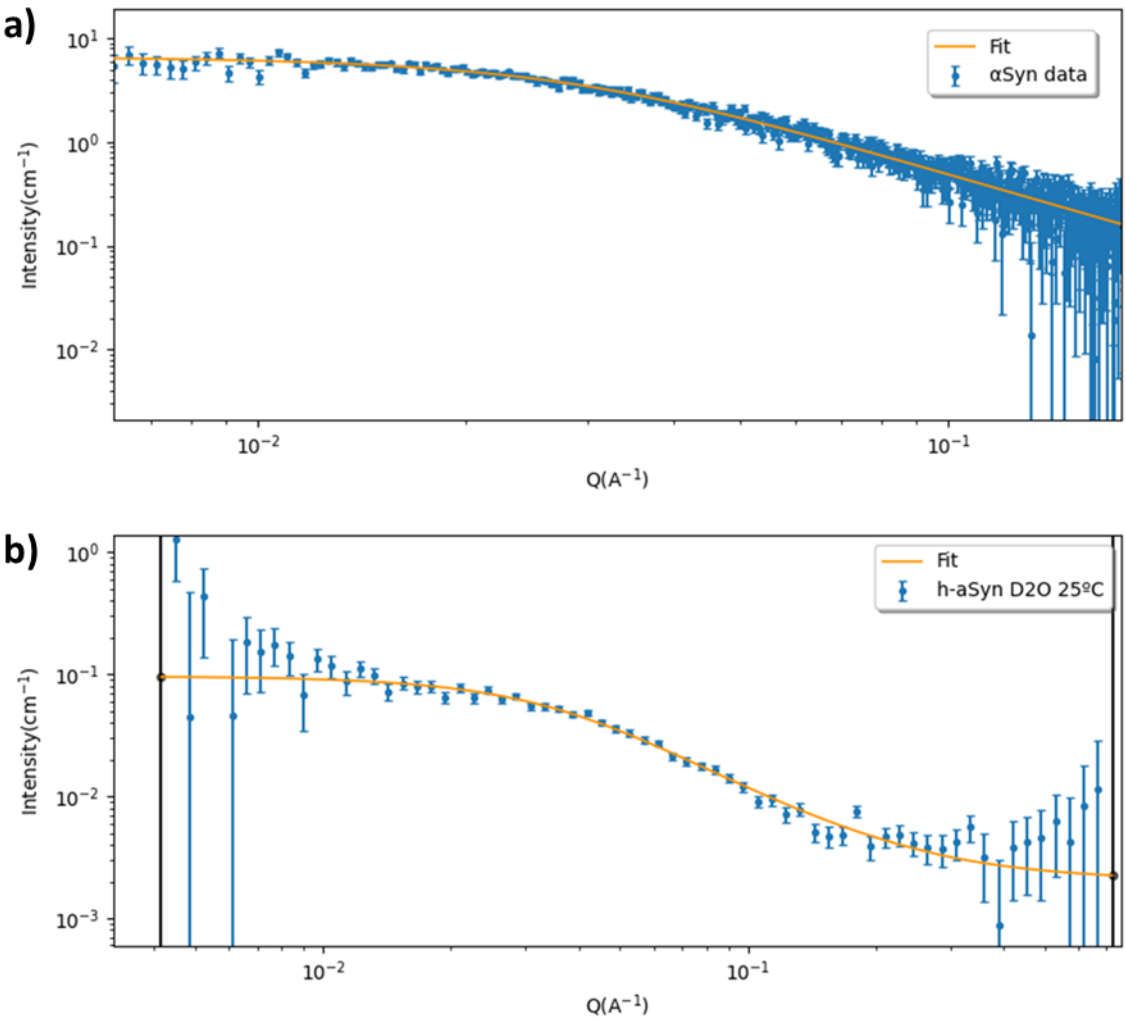

Figure 5.26: SAXS and representative SANS of monomeric α-synuclein.
Small-angle scattering measurements of α-synuclein monomer by a) SAXS or b) SANS. The SANS graph of hydrogenated α-synuclein (h-aSyn) in deuterated solvent (D2O) at 25 °C is representative of similar measurements made at 45 °C and with deuterated α-synuclein. The scattering vector (Q) is inversely proportional to distance and is graphed against scattered intensity as a function of Q. The orange line in both graphs was fit using the monodisperse gaussian coil model (Section 2.8.11). Figures and data fitting produced by Dr. Andrew Parnell (University of Sheffield).

Sample	Technique	Temperature (ºC)	Radius of Gyration (Å)
α-Syn	SAXS	25	51.3 ± 0.5
α-Syn	SANS	25	42.8 ± 1.3
α-Syn	SANS	45	50.4 ± 1.6
deuterated α-Syn	SANS	25	36.5 ± 2.6
deuterated α-Syn	SANS	45	59.8 ± 3.5

Table 5.3: Monodisperse gaussian coil model fitting statistics for α-synuclein controls.
Model fitting results of small-angle scattering measurements by SAXS and SANS for monomeric α-synuclein. The monodisperse gaussian coil model (Section 2.8.11) was used to fit an average radius of gyration (R_g) for each sample measured. Data fitting produced by Dr. Andrew Parnell (University of Sheffield).

Similarly, hydrogenated and deuterated POPG controls were assessed by SANS and fit using a vesicle scattering model (Figure 5.27). The outcome of these fits, displayed in Table 5.4, show a bilayer thickness of around 32.3 Å, which is slightly thinner than the reported thickness of a flat POPG bilayer (36.7 ± 0.7 Å) [378]. This is to be expected of small liposomes, whose shape imposes penalties to lipid ordering, which results in thinner bilayers [379]. There also appears to be a roughly 50 Å disparity between the radii of hydrogenous vs. deuterated POPG liposomes. The most likely explanation for this difference is simply operator differences during extrusion, as these particular stocks were extruded by different people. Regardless, this variance in liposomes size is unlikely to make a significant difference downstream, due to the apparently rapid remodelling into lipid micelles by α-synuclein upon mixing.

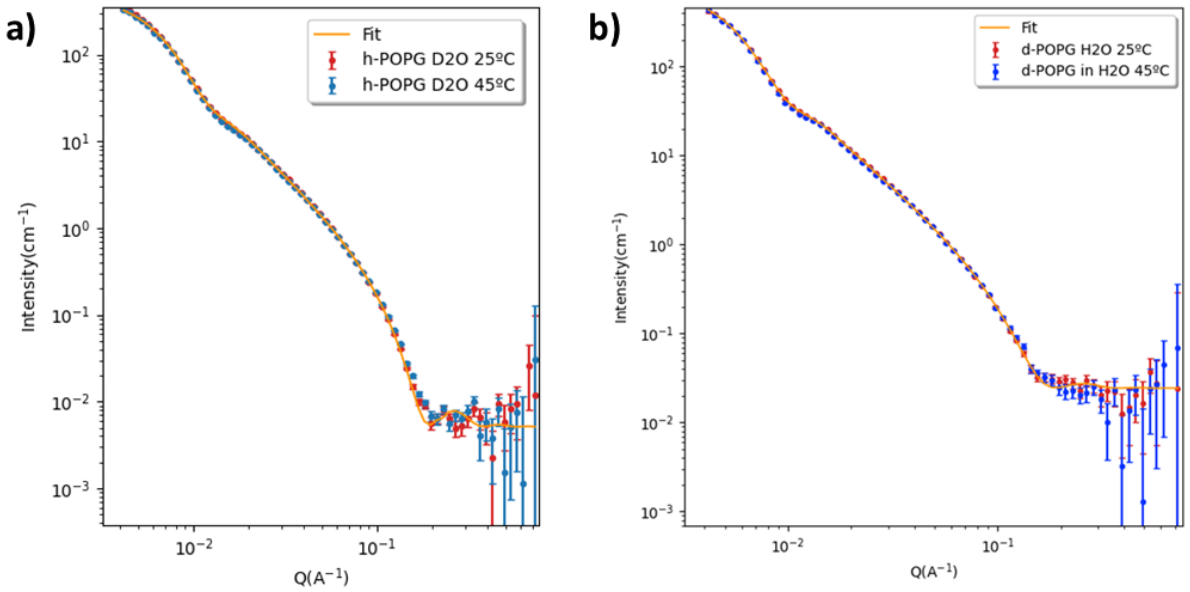

Figure 5.27: SANS of POPG liposomes.
Neutron scattering of 50nm extruded POPG liposomes at 25 °C and 45 °C are shown. a) Hydrogenated POPG (h-POPG) in deuterated solvent (D2O). b) Deuterated POPG (d-POPG) in hydrogenated solvent (H2O). The scattering vector (Q) is inversely proportional to distance and is graphed against scattered intensity as a function of Q. The orange line in both graphs was fit to the 25 °C data using the vesicle model (Section 2.8.11). Figures and data fitting produced by Dr. Andrew Parnell (University of Sheffield).

Sample	Temperature (°C)	Vesicle Core Radius (Å)	Bilayer Thickness (Å)	Vesicle Total Radius (Å)
POPG	25	160.6 ± 0.8	32.9 ± 0.1	193.5 ± 0.9
POPG	45	166.1 ± 0.8	31.0 ± 0.7	197.1 ± 1.5
deuterated POPG	25	222.3 ± 1.4	33.5 ± 0.2	255.8 ± 1.6
deuterated POPG	45	235.4 ± 1.4	32.1 ± 0.1	267.5 ± 1.5

Table 5.4: Vesicle model fitting statistics for POPG liposome controls.
Model fitting results of SANS measurements for 50 nm extruded POPG liposomes. The data was fit using the vesicle model (Section 2.8.11) to obtain an inner vesicle core radius and bilayer thickness, which could be summed to give a total vesicle radius for each sample measured. Data fitting produced by Dr. Andrew Parnell (University of Sheffield).

Mixtures of α-synuclein and POPG produce markedly different scattering dependencies, when compared with liposome controls, even prior to incubation at 45 °C (Figure 5.28 and 5.29). Over-time X-ray scattering measurements of this system do not appear to change significantly over an 18-hour incubation at 45 °C (Figure 5.30). The high variance in data above a Q-value of about 0.05 $Å^{-1}$ is hard to interpret. Signals within this range report on any distances below 12.5 nm, where there is a high degree of overlap. Furthermore, the apparent lack of trend in these curves over time is not encouraging for further analysis. These data appear to be in contrast with clear changes observed by neutron scattering, described below, over the same time period. Currently, it is not clear why these changes are not visible by SAXS, with the most plausible explanation being that the SAXS equipment is not sensitive enough to resolve differences observed during SANS.

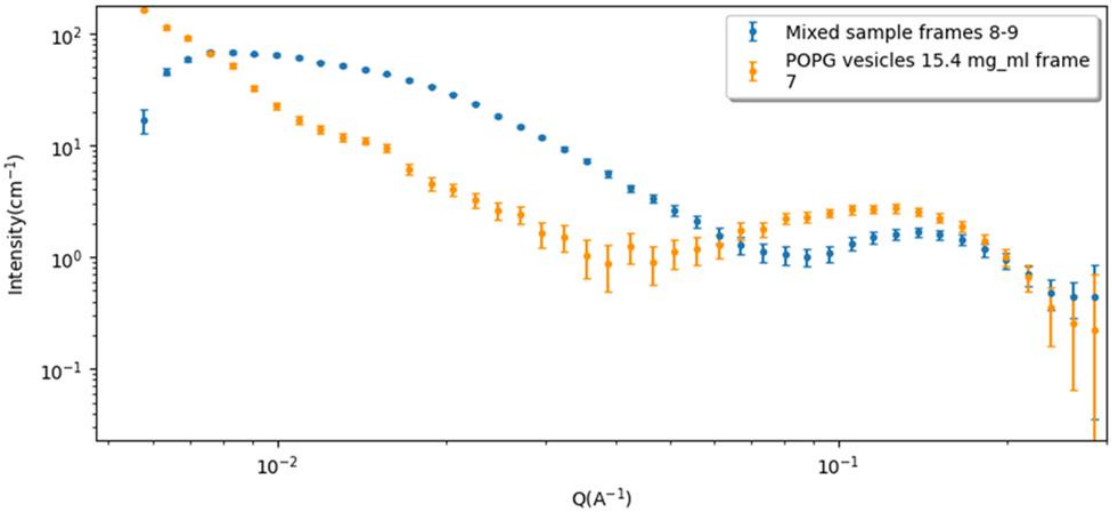

Figure 5.28: SAXS comparison of POPG liposomes against a mixture of POPG and α-synuclein. X-ray scattering of 50 nm extruded POPG liposomes (orange) and a 30:1 POPG:α-synuclein mixture (blue) both measured at 25 °C. Figure and data fitting produced by Dr. Andrew Parnell (University of Sheffield).

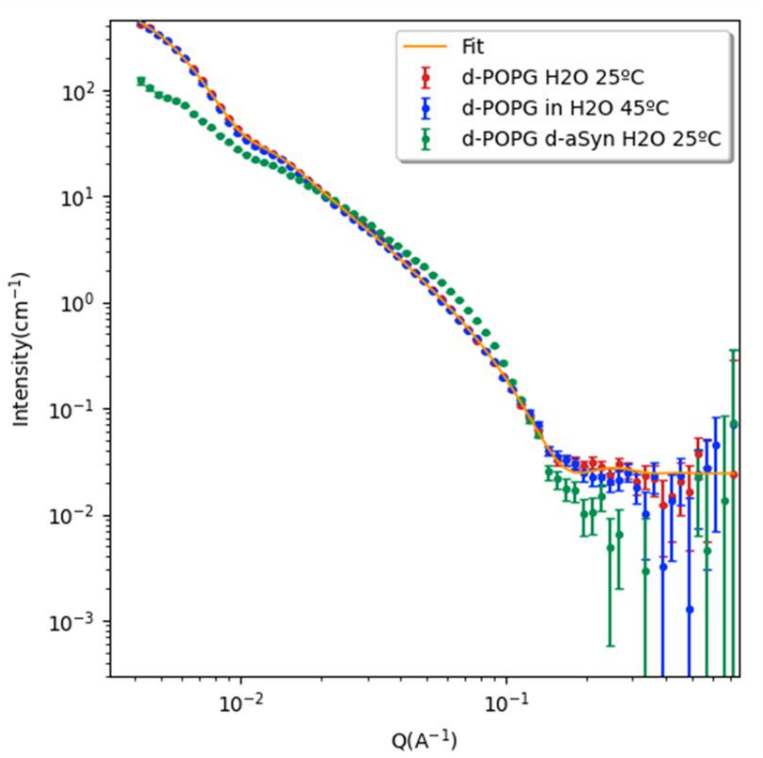

Figure 5.29: SANS comparison of POPG liposomes against a mixture of POPG and α-synuclein. Neutron scattering of 50 nm extruded POPG liposomes at 25 °C (red) and 45 °C (blue), compared to a 30:1 POPG:α-synuclein mixture at 25 °C (green). All three samples used deuterated POPG. The orange fit line represents a vesicle model fit (Section 2.8.11) to the 25 °C POPG liposome data. Figure and data fitting produced by Dr. Andrew Parnell (University of Sheffield).

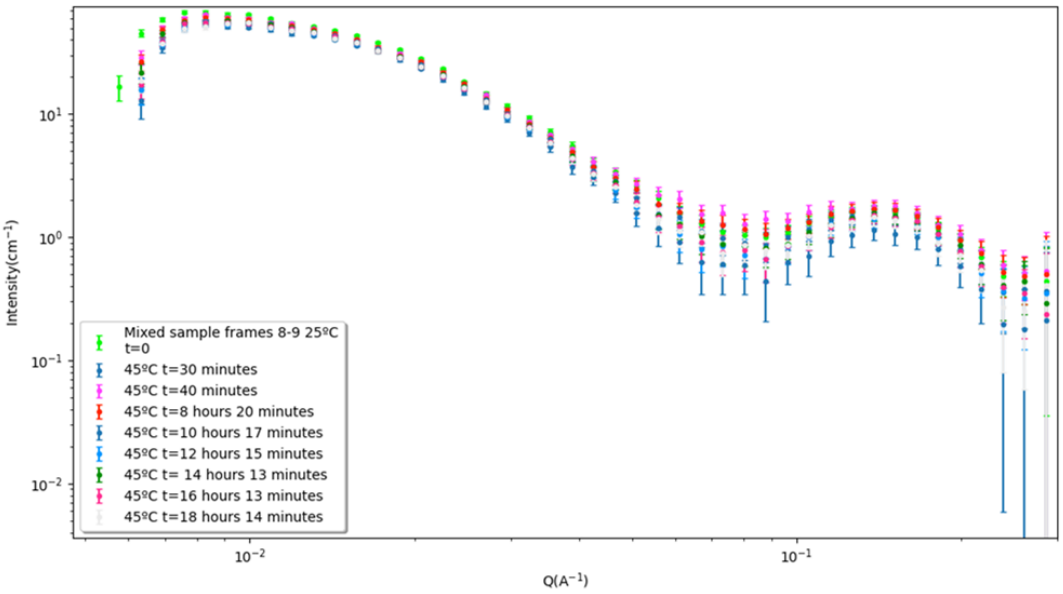

Figure 5.30: SAXS time course of α-synuclein and POPG mixture at 45°C. X-ray scattering of a 30:1 POPG:α-synuclein mixture at 25 °C (lime) and a series of 45 °C incubation time points, as listed on the figure, up to 18 hours. Figure produced by Dr. Andrew Parnell (University of Sheffield).

This SANS data was collected near the end of the project and, as such, has not been fully processed at the time of publishing. The remainder of this section presents preliminary figures and interpretations, but future work would aim to include a more thorough analysis of the entire dataset.

Visualising hydrogenated α-synuclein in a mixed sample, where deuterated POPG has been contrast matched to remove its signal, gives a scattering dependence that no longer fits monodisperse gaussian coil model (Figure 5.31). This indicates that α-synuclein is no longer in its random coil state and supports the previous circular dichroism data, which shows a fully folded structure. The Guinier-Porod model (Section 2.8.11) was employed to fit each time point curve for this sample (Table 5.5).

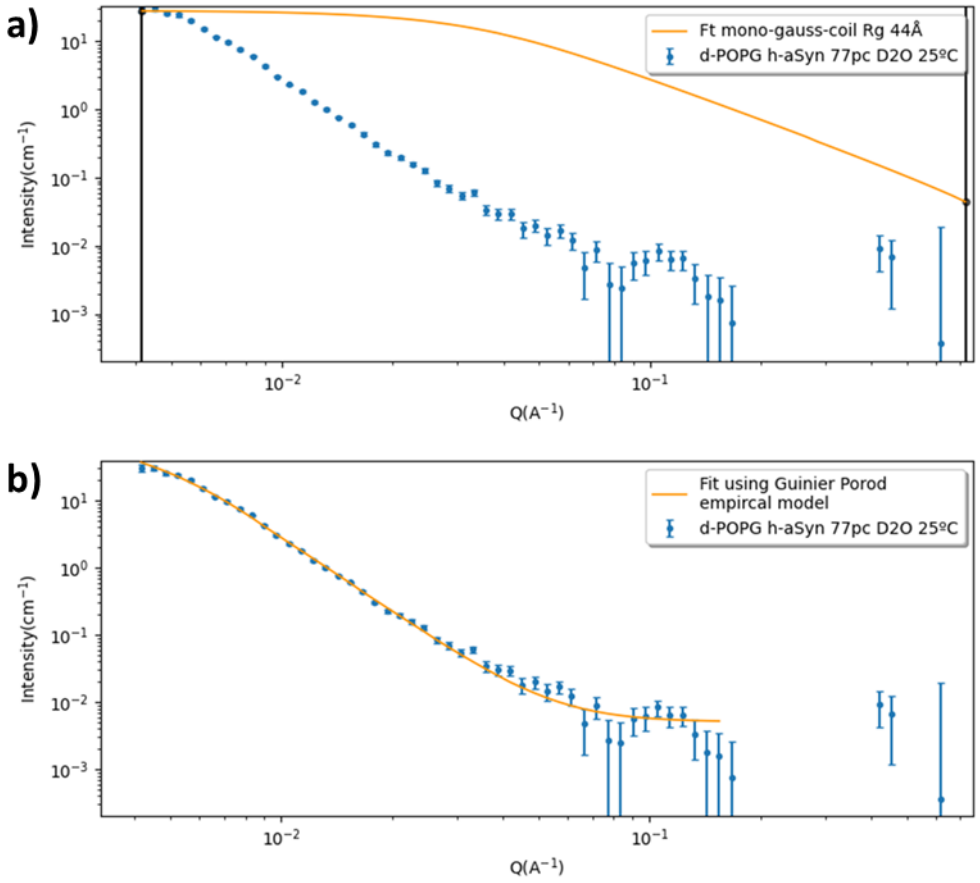

Figure 5.31: α-synuclein neutron scattering in a mixture with POPG.
Neutron scattering of hydrogenous α-synuclein in a mixture with deuterated POPG at a 30:1 POPG:α-synuclein ratio. The solvent contains 77% D_2O to contrast match the POPG signal. The remaining signal from α-synuclein is shown, overlaid are orange fit lines using either a) the monodisperse gaussian coil model or b) the Guinier-Porod model (Section 2.8.11). Figures and data fitting produced by Dr. Andrew Parnell (University of Sheffield).

Measurement	Shape Parameter Fixed at 1	Shape Parameter Unconstrained		
	Rg (Å)	Rg (Å)	Shape Parameter	Porod Exponent
25 °C	230 ± 5.5	262 ± 3.9	0.74	3.59
Initial 45 °C	455 ± 3.8	285 ± 6.6	0.76	3.40
3 hours 45 °C	457 ± 3.9	292 ± 7.2	0.77	3.42
9 hours 45 °C	455 ± 3.8	286 ± 6.2	0.76	3.46
28 hours 45 °C	457 ± 3.9	290 ± 6.7	0.76	3.49
44 hours 45 °C	533 ± 6.5	299 ± 8.7	0.69	3.47

Table 5.5: Guinier-Porod model fitting statistics for α-synuclein in mixed samples.
Time course neutron scattering of hydrogenous α-synuclein in a mixture with deuterated POPG at a 30:1 POPG:α-synuclein ratio in 77% D_2O was fit using the Guinier-Porod model (Section 2.8.11). Measurements at 25 ^oC and time points during incubation at 45 ^oC up to 44 hours are shown. The second column shows the fitted radius of gyration (R_g) when the particle shape is assumed to be fixed rods (shape parameter = 1). The final three columns show an alternative fit where the shape parameter is unconstrained. Data fitting produced by Dr. Andrew Parnell (University of Sheffield).

The primary advantage of this model is that it does not impose any prior assumptions on the shape of the measured particles, instead assigning a shape parameter, which suggests an underlying structure when fit. When the shape parameter was set to a value of '1', which translates to the symmetry required for a rigid cylindrical structure, the radius of gyration (R_g) appears to increase dramatically over time from 230 Å to over 450 Å. However, this increase in R_g is likely artificial due to constraining the shape parameter, as electron microscopy and AFM techniques show highly flexible structures and not rigid rods. Without constraints, the shape parameter appears to prefer a value of around 0.76. A shape parameter of '0' relates to a sphere or highly curved object, and so 0.76 can be interpreted as having rod-like symmetry with a reasonable degree of curvature, which is observed in the microscopy data. Using this shape parameter, the R_g remains largely unchanged over time, with a slight increase upon transitioning from 25 ^oC to 45 ^oC.

An important note is that, based on the microscopy data, these lipoprotein particles are micrometres long and thus their true R_g lies far beyond of the range of SANS, which in this experiment has an upper limit of around 100 nm. Therefore, the model-fit R_g probably tracks smaller, prevalent features, such as individual membrane-bound α-synuclein monomers. Incidentally, using the model proposed by Mizuno et. al. [271], a fully extended α-helical protein of α-synuclein's length (140 residues) would

measure approximately 21 nm in length, assuming the standard 3.6 residues and 5.4 Å per helical turn. This is only slightly below the model-fit R_g of around 29 nm, which could potentially be inflated by instances of close interaction between separate α-synuclein monomers along the membrane surface. Finally, the Porod exponent reports on the nature of surface-solvent interactions, where '3' is considered to be a very rough surface and '4' is very smooth [380]. For α-synuclein this exponent remains between 3.4 and 3.6, which simply indicates some surface roughness, but may also be influenced by membrane interactions in unknown ways.

Meanwhile, the change in scattering of POPG over time can be clearly observed when α-synuclein is contrast matched (Figure 5.32). Assuming the shape of POPG by fitting this series with the flexible cylinder model (Section 2.8.11) allows for the fitting of Kuhn length, a parameter directly proportional to persistence length, which informs on the stiffness of the flexible cylinder. Another parameter for this model is the total length of the cylinder, which as previously mentioned is micrometres long and outside the detectable range of SANS. To work around this, the trend of the data in Figure 5.32 can be compared to the simulated dataset in Figure 5.33, which changes curve shape based upon the ratio of total cylinder length (L) to Kuhn length (b). Given this comparison, it would appear that the POPG data in Figure 5.32 has a decreasing ratio of L/b. If the total cylinder length is assumed to remain an arbitrarily high value, due to it being outside of detectable range, this would translate to an increase in Kuhn length, and stiffness, up until the 29-hour time-point.

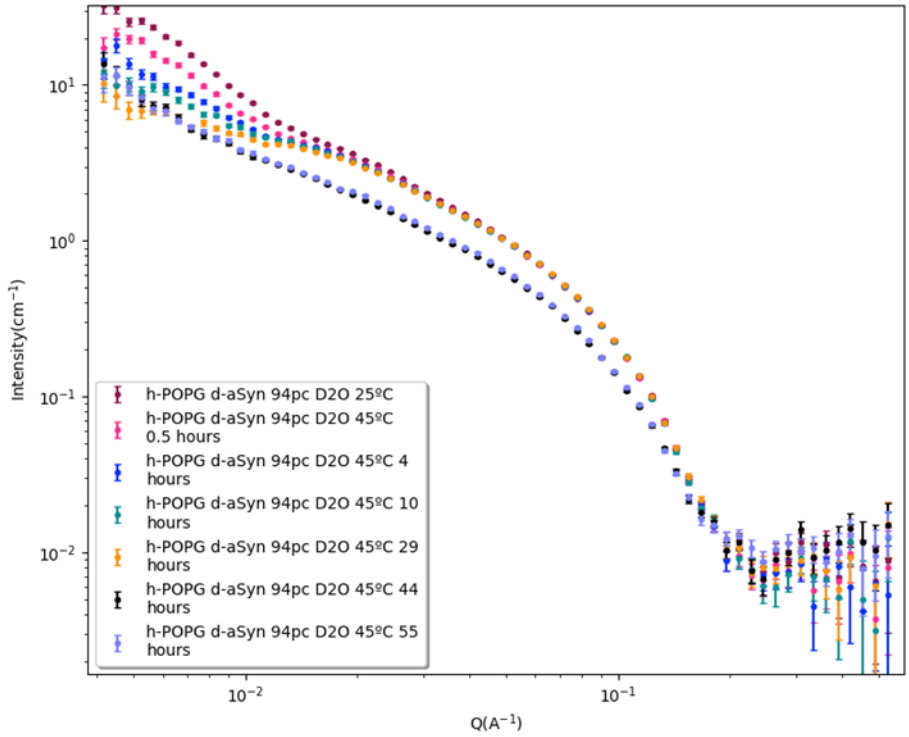

Figure 5.32: SANS time course of POPG in a mixture with α-synuclein.
Neutron scattering of hydrogenous POPG in a mixture with deuterated α-synuclein at a 30:1 POPG:α-synuclein ratio. The solvent contains 94% D2O to contrast match the α-synuclein signal. The remaining signal from POPG is shown at 25 ºC and various 45 ºC incubation time points up to 55 hours. Figure produced by Dr. Andrew Parnell (University of Sheffield).

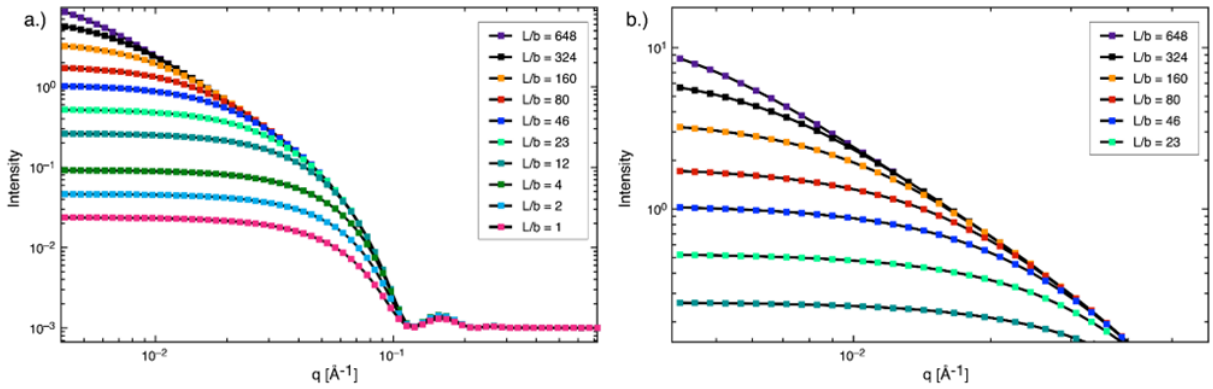

Figure 5.33: Simulated fits for the flexible cylinder model.
Shown are a set of arbitrary curves to display how the shape of the flexible cylinder model fit (Section 2.8.11) changes with the L:b ratio. Where the parameter 'L' is total cylinder length and 'b' is Kuhn length. This is shown to be compared with the SANS time course is Figure 5.32, which follows a similar trend to this simulation at high L:b ratios, between 0 and 29 hours. Figures produced by Dr. Andrew Parnell (University of Sheffield).

The time-dependent increase in rigidity can also be mapped directly from the data, using the same approach, by fixing the total cylinder length to 300 nm and plotting the change in Kuhn length over time (Figure 5.34). Note that Figure 5.34 does not use contrast matched data and instead reports on both α-synuclein and POPG at once. These data appear to show a rapid increase in stiffness over the first 5 hours of incubation, which then plateaus and increases again somewhere between the 10 to 30-hour mark. The final two measurements at 44 and 55 hours have a different scattering curve, similar to those shown in Figure 5.32, but correspond to a point where the cylindrical micelles are now fully rigid and the flexible cylinder model breaks down, hence the high error bars. This can be proven by fitting the 55-hour measurement using a non-flexible cylinder model (Section 2.8.11), which agreed well with the measured data for the late time point (Figure 5.35).

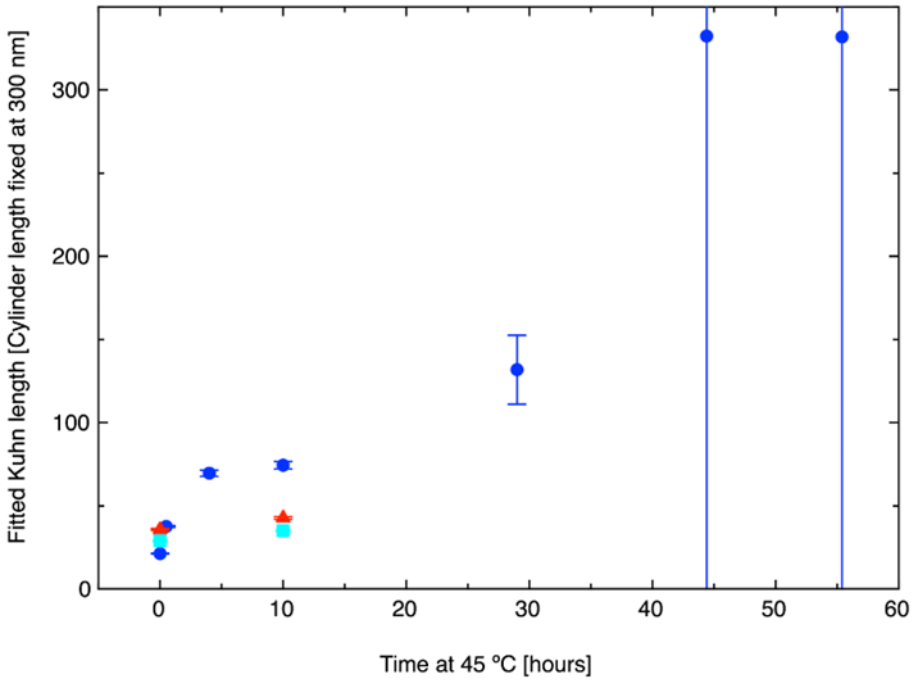

Figure 5.34: Change in fitted Kuhn length over time for a mixture of α-synuclein and POPG.
Time course neutron scattering of hydrogenous α-synuclein and POPG mixed at a 30:1 POPG:α-synuclein ratio in 100% D_2O was fit using the flexible cylinder model (Section 2.8.11) with a fixed total cylinder length of 300 nm. The fitted Kuhn length (in nanometres) is shown against incubation time (blue). Also shown are Kuhn length fits for two similar samples with the addition of minzasolmin at a 1:1 stochiometric ratio with α-synuclein (red and cyan). Figure produced by Dr. Andrew Parnell (University of Sheffield).

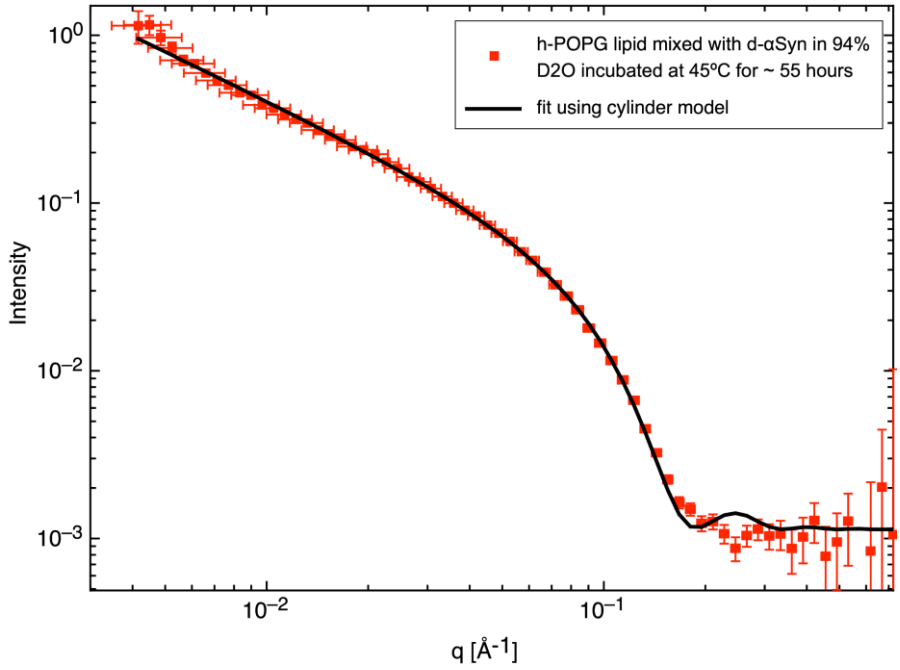

Figure 5.35: Model fitting 55-hour incubation of POPG in a mixture with α-synuclein. Neutron scattering of hydrogenous POPG in a mixture with deuterated α-synuclein at a 30:1 POPG:α-synuclein ratio. The solvent contains 94% D2O to contrast match the α-synuclein signal. The remaining signal from POPG is shown after 55 hours at 45 °C and fit using a non-flexible cylinder model (Section 2.8.11). Figure and data fitting produced by Dr. Andrew Parnell (University of Sheffield).

The time dependence of Kuhn length matches well with the circular dichroism (CD) time course from Section 5.11. Together they support a model of increasing packing and interaction of α-helical α-synuclein monomers on the micelle surface, evidenced by CD, causing a stiffening of the lipoprotein tube over a similar time period, shown by SANS. Both techniques identify a switch after 30-40 hours, which constitutes a structural conversion of α-synuclein from α-helical to β-sheet and a stiffening of the flexible POPG micelles to a non-flexible rod-like structure. It is also worth noting that 10-hour incubations which included minzasolmin, the Parkinson's drug candidate mentioned previously for its ability to disrupt α-synuclein interaction with membranes [109, 110] (Section 1.9), had a much smaller increase in Kuhn length (Figure 5.34). Unfortunately, experimental time constraints prevented a more comprehensive time course of these samples. However, future work could revisit these conditions.

Given the nature of some Parkinson's Disease associated α-synuclein amyloids, which incorporate lipid into their structure [297] (Section 1.9). It seems reasonable to speculate that similar structures may be produced by this system, providing an exciting opportunity for further structural research in this area. Further analysis of the SANS data and downstream structural study of this system after 50+ hours incubation would be required to help validate this hypothesis.

Chapter 6: Summary and Conclusions

6.1 Optimisation of Recombinant Cystatin C Production

The first aim of this project was to expand upon previous attempts to improve production yields for the human cystatin C protein [210, 248, 325], which were significantly reduced in the Staniforth lab when compared with published data using a similar expression system [316]. This involved designing and testing a variety of new expression systems, based on approaches found in the literature and colleague suggestions, whist also adjusting the purification technique, induction temperatures, growth media and culture volume.

There appeared to be a high level of variance in production, even from the same expression vector, over the duration of the project. This remains difficult to explain, but does not appear random, as replicate expressions performed around the same time period were often much more similar than those performed months or years apart. The application of new systems including temperature sensitive induction, thioredoxin fusion and signal peptidase I co-expression did not improve upon prior yields simply using either signal peptide (pelB or ompA).

The most promising factor that seemed to correlate with protein yield was culture volume. Single 500 mL cultures, grown separately, appeared to have dramatically increased yield per unit volume compared with multiple 500 mL cultures grown in tandem. This behaviour may be caused by slower adjustment to temperature change when switching from 37 ^{o}C to an induction temperature (18 ^{o}C or 42 ^{o}C) for larger batches, or due to the extra delay in manipulating larger batches during optical density measurements or induction steps that increase idle wait times. This diminishing return from increasing batch volumes made it challenging to produce large quantities of cystatin C. However, it does provide a solid starting point for future research to attempt to overcome.

6.2 Cytoplasmic Cystatin C Aggregation in ALS

Originally, the project aimed to develop large-scale assays to probe physiological conditions of cystatin C for aggregation and liquid-liquid phase-separation to extrapolate its behaviour that may lead to Bunina bodies in ALS motor neurons. Purification yields were an unfortunate limiting factor on the scale of these assays and liquid-liquid phase-separation was not directly observed, although this may simply require assays using higher concentrations of protein to achieve. Despite this, a several intriguing observations were able to be made through analysing aggregation of cystatin C under various conditions.

In humans, cystatin C is normally localised to oxidising environments, such as within lysosomes or extracellularly [160]. Meanwhile, Bunina bodies form within the cell cytoplasm, which is comparatively more reducing, with a higher density of surrounding macromolecules. In vitro these effects were simulated by addition of the reducing agent dithiothreitol (DTT) and crowding agent polyethylene glycol (PEG). DTT alone was shown to be capable of aggregating cystatin C, though it remains unclear whether the disulphide bonds are broken during this process. Meanwhile, increasing PEG concentration helped to speed up aggregate through molecular crowding. Aggregation under these relatively mild conditions is fairly unique to cystatin C, compared to its homologue chicken cystatin, which remains fairly stable even after its disulphides are reduced at considerably higher DTT concentrations [200]. The observation of an apparent minimum aggregation time of roughly 5 hours suggests a trans- to cis- proline isomerisation step is involved during the aggregation pathway. This unusual isomerisation event has been recognised in other cystatin family proteins [209, 210], involved in tetramerisation and subsequent aggregation, but has not yet been identified in cystatin C. Future structural and kinetic studies on larger screens with higher concentrations would help confirm this finding and may even link this mechanism to Bunina body-like aggregation.

Cystatin C was also screened against RNA, due to unusual co-precipitation of nucleic acids during purification attempts and a literature trend of RNA-induced liquid-liquid phase-separation in other ALS-associated inclusions [115-117]. While the aggregation of cystatin C was not affected by addition of RNA, preliminary NMR results hinted at a potential binding pocket within the dimer form. The quality of the NMR experiment and the source of RNA were both relatively poor, such that these results would require a more robust attempt before any serious conclusions be drawn from them.

Finally, an in vivo approach used two different fluorescent tags to track cystatin C localisation in human cells. GFP appeared to mislocalise cystatin C to mitochondria, while the much smaller HA-tag displayed peri-nuclear localisation more similar to Bunina bodies [213, 227]. Incubation with nocodazole, which destroys the microtubule network, showed HA-cystatin C puncta form throughout the cytoplasm. This indicates that cytosolic cystatin C may be actively transported towards the nuclear membrane through an unknown process, which may help to explain the peri-nuclear localisation of Bunina bodies in ALS motor neurons [213, 227].

6.3 Membrane Aggregation of α-Synuclein in Parkinson's Disease

The existence of a phase II drug trial using minzasolmin to treat Parkinson's disease [109] sheds a spotlight on the model system that helped screen for it. NMR and cross-linking mass-spectrometry has shown α-synuclein oligomers form upon the surface of membranes, and that prevention of α-synuclein membrane binding, by interaction with minzasolmin, is the proposed mechanism of action for the drug against Parkinson's disease [110]. Chapter 5 of this thesis aimed to replicate this model system and further probe the structural and kinetic characteristics of this α-synuclein aggregation pathway, which are potentially relevant in the disease context.

Following prior work optimising the production and separation of these species, 30:1 molar ratio mixtures of POPG and α-synuclein, were separated using AF4 into two distinct fractions "Peak 2" and "Peak 3". Although the elution time and light scattering measurements of each peak were quite different, mass-spectrometry and FTIR showed qualitative evidence that both peaks contained a similar ratio of α-synuclein and POPG. Furthermore, α-synuclein in both peaks and the unfractionated mixture appeared to be in a highly α-helical structure, based on circular dichroism measurements.

Microscopy techniques were able to strongly differentiate Peak 2 and 3. Negative-stain electron microscopy of Peak 2 found it was fairly heterogenous, with large ribbon-like species, intact POPG liposome and potentially lipid nanodiscs, which are a known feature of similar α-synuclein:lipid systems [271, 306, 307], as well as a background signal that implies some unbound α-synuclein. Dry AFM of this peak created a flat "honeycomb" of pore-like structures. Computational analysis of these pores showed a radius of around 12 nm, which could easily be interpreted as dried liposomes that have reduced in size and sagged in the centre, appearing as pores. Both electron microscopy and AFM images for Peak 2 showed a high degree of liposome clustering, which is likely an effect of α-synuclein's ability to anchor between two membranes at once [305]. These vesicles may also be decorated with oligomers of α-synuclein, as previously seen using cross-linking [110]. However, attempts to disrupt the liposomes with phospholipase or methanol were unsuccessful at recovering oligomer-like species. The phospholipase used could not lyse the membrane and methanol clearly altered the structure of α-synuclein at the concentrations necessary to disrupt the liposomes.

Peak 3 was much more homogenous than Peak 2, containing only long, flexible tube-like structures. These bared a striking similarity to α-synuclein-induced lipid tubes identified elsewhere, using different lipids or lipid:protein ratios of POPG [270, 271, 307, 308]. The small 6 nm diameter of these tubes points to them being cylindrical micelles and not bilayer tubes. So far, investigation into the underlying arrangement of these structures has been confined to SAXS and SANS measurements,

computer modelling and fluorescent and spin-labelling of α-synuclein [271, 272, 273, 307]. In particular, a model proposed by Mizuno et. al. 2012 [271] places α-synuclein in a fully extended α-helical structure, embedding lengthways along the micelle surface and maintaining the lipid structure.

This thesis presents work that separates these micelles from other lipoprotein features and confirms that α-synuclein is highly helical in the micelle structure. 3D reconstruction of cryo-electron micrographs was unable to yield a definitive structure; however, this supports an irregular distribution of α-synuclein along the micelle surface, as implied by Mizuno's model. Furthermore, the regularity and defined separation distance of roughly 10-20 nm between micelles during both cryo-electron microscopy and AFM perfectly fits with the bridging distance of α-synuclein between liposomes surfaces (~15 nm) [305]. For the inter-micelle distance to be maintained, a rigid linker region should be required. The amphipathic helical nature of α-synuclein might lend itself to forming coiled-coil dimers, which provides the hypothesis that such dimers bridge the gaps between micelles in solution. The apparent disorder shown in negatively-stained images likely results from the acidity of the stain disrupting these bridging interactions. As a whole, these data support Mizuno's micelle model, with the addition of these bridging interactions between nearby micelles.

Somewhat surprisingly, the literature seems to focus on immediate interactions between α-synuclein and lipids, without often considering how this system might evolve over time. This is especially important for a Parkinson's disease model, where α-synuclein would be expected to aggregate over time and form the amyloids observed in Lewy bodies. The final sections of chapter 5 briefly investigate structural changes in this system over a much longer timescale than the 2.5-hour incubation used for the above preparations.

Scattering techniques (MALS, SAXS and SANS) showed the conversion from liposomes to micelles occurs rapidly upon mixing, at 25 °C or 45 °C, and that the average particle size and relative stiffness of the tubes increases, but plateaus after around 2-4 hours. Throughout this period and the following plateau region, α-synuclein remains in an α-helical state, reported by circular dichroism. This helicity gradually increases over time until a point at around 40-45 hours, at which point there is a rapid conformational change to β-sheet, accompanied by considerable stiffening, forming an inflexible rod structure.

Based on the model proposed thus far, one interpretation of the data is that during the plateau period the randomly distributed α-synuclein forms intermolecular interactions with other nearby helical monomers. The gradual increase in helicity over time supports the idea of an increasing number of helix-helix interactions and would lead to an increase in the packing and regularity of α-synuclein across the surface of the micelles. This, in turn, explains why there is some stiffening over

time, evidenced by an increasing Kuhn length in the SANS analysis. Around the 40-hour mark, the rapid shift to β-sheet structure indicates a cooperative structural change, which may even propagate along the micelles themselves. This shift could indicate the formation of a β-amyloid structure, with incorporated lipids, observed in the structures of some patient-derived α-synuclein amyloids [297], and might well be a disease relevant form. Future work, using structural techniques like cryo-electron microscopy and AFM, would be required to further investigate the β-sheet structure, while 3D reconstruction of micelles shortly prior to the structural conversion at 40 hours may find success due to the potentially more regular distribution of α-synuclein helices.

References

[1] Farrar, C. (2024). “Economic & healthcare impact of dementia”. Alzheimer’s Society UK. https://www.alzheimers.org.uk/sites/default/files/2024-05/the-annual-costs-of-dementia.pdf

[2] Parkinson’s UK. (2017). “The prevalence and incidence of Parkinson’s in the UK”. Published at parkinsons.org.uk. https://www.parkinsons.org.uk/sites/default/files/2018-01/Prevalence%20%20Incidence%20Report%20Latest_Public_2.pdf

[3] Burchardt, J.M. et. al. (2022). “Analysis of incidence of motor neuron disease in England 1998-2019: use of three linked datasets”. Amyotroph Lateral Scler Frontotemporal Degener. *23*(5-6), 363-371. https://doi.org/10.1080/21678421.2021.2016837

[4] Alzheimer’s Society, UK. (2023). “Risk Factors for Alzheimer’s disease”. Published at alzheimers.org.uk. Accessed February 2025. https://www.alzheimers.org.uk/about-dementia/types-dementia/who-gets-alzheimers-disease

[5] National Institute of Neurological Disorders and Stroke, USA. “Parkinson’s Disease”. Published at ninds.nih.gov. Accessed February 2025. https://www.ninds.nih.gov/health-information/disorders/parkinsons-disease

[6] ALS Association, USA. “ALS Risk Factors”. Published at als.org. Accessed February 2025. https://www.als.org/research/als-research-topics/als-risk-factors

[7] Sampson, T.R. et. al. (2016). “Gut Microbiota Regulate Motor Deficits and Neuroinflammation in a Model of Parkinsons’s Disease”. Cell *167*(6), 1469-1480.e12. https://www-sciencedirect-com.sheffield.idm.oclc.org/science/article/pii/S0092867416315902?via%3Dihub

[8] Morimoto, R.I. and Cuervo, A.M. (2014). “Proteostasis and the Aging Proteome in Health and Disease”. J. Gerontol. A. *69*(S1), S33-S38. https://doi.org/10.1093/gerona/glu049

[9] Johanson, C.E. et. al. (2008). “Multiplicity of cerebrospinal fluid functions: New challenges in health and disease”. Cerebrospinal Fluid Res. *5*, 10. https://doi.org/10.1186/1743-8454-5-10

[10] Singh, A. et. al. (2019). “Oxidative Stress: A Key Modulator in Neurodegenerative Disease”. Molecules *24*(8), 1583. https://doi.org/10.3390/molecules24081583

[11] Korovesis, D., Rubio-Tomás, T. and Tavernarakis, N. (2023). “Oxidative Stress in Age-Related Neurodegenerative Diseases: An Overview of Recent Tools and Findings”. Antioxidants (Basel) *12*(1), 131. https://doi.org/10.3390/antiox12010131

[12] Li, X. et. al. (2023). “Inflammation and aging: signaling pathways and intervention therapies”. Signal Transduct Target Ther. *8*, 239. https://doi.org/10.1038/s41392-023-01502-8

[13] Xie, J., Hoecke, L.V. and Vandenbroucke, R.E. (2022). “The Impact of Systemic Inflammation on Alzheimer’s Disease Pathology”. Front Immunol. *12*, 796867. https://doi.org/10.3389/fimmu.2021.796867

[14] Zhang, W. et. al. (2023). “Role of neuroinflammation in neurodegeneration development”. Signal Transduct Target Ther. *8*, 267. https://doi.org/10.1038/s41392-023-01486-5

[15] Trojanowski, J.Q. and Lee, V.M.-Y. (2001). “Brain degeneration linked to “fatal attractions” of proteins in Alzheimer’s disease and related disorders”. J. Alzheimers Dis. *3*(1), 117-119. https://doi.org/10.3233/jad-2001-3116

[16] Alzheimer, A. (1907). “Über eine eigenartige Erkrankung derHirnrinde”. Allgemeine Zeitschrift für Psychiatrie und Psychisch-Gerichtliche Medizin *64*, 146-148. https://doi.org/10.1002/ca.980080612

[17] Alzheimer, A. (1911). “Über eigenartige Krankheitsfälle des späteren Alters”. Zeitschrift für die gesamte Neurologie und Psychiatrie *4*, 356-385. https://doi.org/10.1177/0957154X9100200506

[18] Lewy, F.H. (1912). “Paralysis agitans. I. Pathologische Anatomie”. Lewandowsky’s Handbuch der Neurologie. Dritter Band. Spezielle Neurologie II. Springer, Berlin. 920-933. https://api.semanticscholar.org/CorpusID:204038232

[19] Holdorff, B., Rodrigues e Silva, A.M., Dodel, R. (2013). “Centenary of Lewy bodies (1912 – 2012)”. Journal of Neural Transmission *120*, 509-516. https://doi.org/10.1007/s00702-013-0984-2

[20] Graeber, M.B. and Mehraein, P. (1999). “Reanalysis of the first case of Alzheimer’s disease”. European Archives of Psychiatry and Clinical Neuroscience *249*, S10-S13. https://doi.org/10.1007/pl00014167

[21] Bunina, T.L. (1962). “On intracellular inclusions in familial amyotrophic lateral sclerosis”. Korsakov J. Neuropathol. Psychiat. *62*, 1293-1299.

[22] Leigh, P.N. et. al. (1988). “Ubiquitin deposits in anterior horn cells in motor neurone disease”. Neurosci. Lett. *93*(2-3), 197-203. https://doi.org/10.1016/0304-3940(88)90081-x

[23] Mizusawa, H. et. al. (1991). “Skein-like inclusions in the anterior horn cells in motor neuron disease” Journal of the Neurological Sciences *105*(1), 14-21. https://doi.org/10.1016/0022-510x(91)90112-k

[24] Kato, T. et. al. (1989). “Lewy body-like hyaline inclusions in sporadic motor neuron disease are ubiquitinated”. Acta Neuropathol. *77*, 391-396. https://doi.org/10.1007/bf00687373

[25] Leigh, P. N. et. al. (1991). “Ubiquitin-immunoreactive intraneuronal inclusions in amyotrophic lateral sclerosis: morphology, distribution, and specificity”. Brain *114*(2), 775-788. https://doi.org/10.1093/brain/114.2.775

[26] Hirano, A., Kurland, L.T. and Sayre, G.P. (1967). “Familial Amyotrophic Lateral Sclerosis A Subgroup Characterized by Posterior and Spinocerebellar Tract Involvement and Hyaline Inclusions in the Anterior Horn Cells”. Arch Neurol. *16*(3), 232-243. https://doi.org/10.1001/archneur.1967.00470210008002

[27] Hirano, A. et. al. (1984). “Fine Structural Observations of Neurofilamentous Changes in Amyotrophic Lateral Sclerosis”. J. Neuropathol. Exp. Neurol. *43*(5), 461-470. https://doi.org/10.1097/00005072-198409000-00001

[28] Carpenter, S. (1968). “Proximal axonal enlargement in motor neuron disease”. Neurology *18*(9), 841-851. https://doi.org/10.1212/wnl.18.9.841

[29] Castellanos-Montiel, M.J., Chaineau, M., Durcan, T.M. (2020). “The Neglected Genes of ALS: Cytoskeletal Dynamics Impact Synaptic Degeneration in ALS”. Front. Cell. Neurosci. *14*. https://doi.org/10.3389/fncel.2020.594975

[30] Glanner, G.G. and Wong, C.W. (1984). “Alzheimer’s disease: Initial report of the purification and characterization of a novel cerebrovascular amyloid protein”. Biochem. Biophys. Res. Commun. *120*(3), 885-890. https://doi.org/10.1016/s0006-291x(84)80190-4

[31] Liao, L. et. al. (2004). “Proteomic characterization of postmortem amyloid plaques isolated by laser capture microdissection”. J. Biol. Chem. *279*(35), 37061-8. https://doi.org/10.1074/jbc.m403672200

[32] Brion, J. et. al. (1985). “Mise en évidence immunologique de la protéine tau au niveau des lésions de dégénérescence neurofibrillaire de la maladie d'Alzheimer”. Arch. Biol. *95*, 229-235. https://api.semanticscholar.org/CorpusID:83623289

[33] Drummond, E. (2020). “Phosphorylated tau interactome in the human Alzheimer’s disease brain”. Brain *143*(9), 2803-2817. https://doi.org/10.1093/brain/awaa223

[34] Kosik, K.S., Joachim, C.L. and Selkoe, D.J. (1986). “Microtubule-associated protein tau (tau) is a major antigenic component of paired helical filaments in Alzheimer’s disease”. Proc. Natl. Acad. Sci. U.S.A. *83*(11), 4044-4048. https://doi.org/10.1073/pnas.83.11.4044

[35] Grundke-Iqbal, I. et. al. (1986). “Abnormal phosphorylation of the microtubule-associated protein tau (tau) in Alzheimer cytoskeletal pathology”. Proc. Natl. Acad. Sci. U.S.A. *83*(13), 4913-4917. https://doi.org/10.1073/pnas.83.13.4913

[36] Jakes, R., Spillantini, M.G. and Goedert, M. (1994). “Identification of two distinct synucleins from human brain”. FEBS Letters *345*, 1873-3468. https://doi.org/10.1016/0014-5793(94)00395-5

[37] Uéda, K. et. al. (1993). “Molecular cloning of cDNA encoding an unrecognized component of amyloid in Alzheimer disease”. Proc. Natl. Acad. Sci. U.S.A. *90*, 11282-11286. https://doi.org/10.1073/pnas.90.23.11282

[38] Spillantini, M.G. et. al. (1997). “α-Synuclein in Lewy bodies”. Nature *388*, 839-840. https://doi.org/10.1038/42166

[39] Xia, Q. et. al. (2008). “Proteomic identification of novel proteins associated with Lewy bodies”. Front Biosci. *13*, 3850-3856. https://doi.org/10.2741/2973

[40] Neumann, M. et. al. (2006). “Ubiquitinated TDP-43 in Frontotemporal Lobar Degeneration and Amyotrophic Lateral Sclerosis”. Science *314*(5796), 130-133. https://doi.org/10.1126/science.1134108

[41] Deng, H. et. al. (2010). “FUS-immunoreactive inclusions are a common feature in sporadic and non-SOD1 familial amyotrophic lateral sclerosis”. Ann. Neurol. *67*(6), 739-748. https://doi.org/10.1002/ana.22051

[42] Keller, B.A. et. al. (2012). “Co-aggregation of RNA binding proteins in ALS spinal motor neurons: evidence of a common pathogenic mechanism”. Acta Neuropathol. *124*, 733-747. https://doi.org/10.1007/s00401-012-1035-z

[43] Shibata, N. et. al. (1996). “Intense Superoxide Dismutase-1 Immunoreactivity in Intracytoplasmic Hyaline Inclusions of Familial Amyotrophic Lateral Sclerosis with Posterior Column Involvement”. J. Neuropathol. Exp. Neurol. *55*(4), 481-490. https://doi.org/10.1097/00005072-199604000-00011

[44] Okamoto, K. et. al. (1993). “Bunina bodies in amyotrophic lateral sclerosis immunostained with rabbit anti-cystatin C serum”. Neurosci. Lett. *162*, 125-128. https://doi.org/10.1016/0304-3940(93)90576-7

[45] Ciryam, P. et. al. (2013). “Widespread Aggregation and Neurodegenerative Diseases Are Associated with Supersaturated Proteins”. Cell Reports *5*(3), 781-790. https://doi.org/10.1016/j.celrep.2013.09.043

[46] Ciryam, P. et. al. (2017). “Spinal motor neuron protein supersaturation patterns are associated with inclusion body formation in ALS”. Proc. Natl. Acad. Sci. USA. *114*(20), E3935-E3943. https://doi.org/10.1073/pnas.1613854114

[47] Mathys, H. et. al. (2019). “Single-cell transcriptomics analysis of Alzheimer’s disease”. Nature *570*, 332-337. https://doi.org/10.1038/s41586-019-1195-2

[48] Highley, J.R. et. al. (2014). “Loss of nuclear TDP-43 in amyotrophic lateral sclerosis (ALS) causes altered expression of splicing machinery and widespread dysregulation of RNA splicing in motor neurones”. Neuropathol. Appl. Neurobiol. *40*(6), 670-685. https://doi.org/10.1111/nan.12148

[49] Rapoport, M. et. al. (2002). “Tau is essential to β-amyloid-induced neurotoxicity”. Proc. Natl. Acad. Sci. U.S.A. *99*(9), 6364-6369. https://doi-org.sheffield.idm.oclc.org/10.1073/pnas.092136199

[50] Takashima, A. et. al. (1993). “Tau protein kinase I is essential for amyloid beta-protein-induced neurotoxicity”. Proc. Natl. Acad. Sci. U.S.A. *90*(16), 7789-7793. https://doi.org/10.1073/pnas.90.16.7789

[51] Lewis, J. et. al. (2001). “Enhanced Neurofibrillary Degeneration in Transgenic Mice Expressing Mutant Tau and APP”. Science *293*(5534), 1487-1491. https://doi-org.sheffield.idm.oclc.org/10.1126/science.1058189

[52] Feany, M.B. and Bender, W.W. (2000). “A *Drosophila* model of Parkinson’s disease”. Nature *404*, 394-398. https://doi-org.sheffield.idm.oclc.org/10.1038/35006074

[53] Kirik, D. et. al. (2002). “Parkinson-Like Neurodegeneration Induced by Targeted Overexpression of α-Synuclein in the Nigrostriatal System”. J. Neurosci. *22*(7), 2780-2791. https://doi-org.sheffield.idm.oclc.org/10.1523/JNEUROSCI.22-07-02780.2002

[54] Periquet, M. et. al. (2007). “Aggregated α-Synuclein Mediates Dopaminergic Neurotoxicity *In Vivo*”. J. Neurosci. *27*(12), 3338-3346. https://doi-org.sheffield.idm.oclc.org/10.1523/JNEUROSCI.0285-07.2007

[55] Huang, S.L. et. al. (2020). “A robust TDP-43 knock-in mouse model of ALS”. Acta Neuropathol. Commun. *8*, 3. https://doi.org/10.1186/s40478-020-0881-5

[56] Walker, A.K. et. al. (2015). “Functional recovery in new mouse models of ALS/FTLD after clearance of pathological cytoplasmic TDP-43”. Acta Neuropathol. *130*, 643-660. https://doi.org/10.1007/s00401-015-1460-x

[57] Chew, J. et. al. (2015). “C9ORF72 repeat expansions in mice cause TDP-43 pathology, neuronal loss, and behavioural deficits”. Science *348*(6239), 1151-1154. https://doi.org/10.1126/science.aaa9344

[58] Tran, H. et. al. (2015). “Differential Toxicity of Nuclear RNA Foci versus Dipeptide Repeat Proteins in a *Drosophila* Model of C9ORF72 FTD/ALS”. Neuron *87*(6), 1207-1214. https://doi.org/10.1016/j.neuron.2015.09.015

[59] Gurney, M.E. et. al. (1994). “Motor neuron degeneration in mice that express a human Cu,Zn superoxide dismutase mutation”. Science *264*(5166), 1772-1775. https://doi.org/10.1126/science.8209258

[60] Nagi, M. et. al. (2001). “Rats expressing human cytosolic copper-zinc superoxide dismutase transgenes with amyotrophic lateral sclerosis associated mutations develop motor neuron disease”. J. Neurosci. *21*(23), 9246-9254. https://doi.org/10.1523/jneurosci.21-23-09246.2001

[61] Goate, A. et. al. (1991). “Segregation of a missense mutation in the amyloid precursor protein gene with familial Alzheimer's disease”. Nature *349*, 704-706. https://doi-org.sheffield.idm.oclc.org/10.1038/349704a0

[62] Hardy, J. (1992). “Framing β–amyloid”. Nat. Genet. *1*, 233-234. https://doi-org.sheffield.idm.oclc.org/10.1038/ng0792-233

[63] Hendriks, L. et. al. (1992). “Presenile dementia and cerebral haemorrhage linked to a mutation at codon 692 of the β–amyloid precursor protein gene”. Nat. Genet. *1*, 218-221. https://doi-org.sheffield.idm.oclc.org/10.1038/ng0692-218

[64] Mullan, M. et. al. “A pathogenic mutation for probable Alzheimer's disease in the APP gene at the N–terminus of β–amyloid”. Nat. Genet., *1*, 345-347. https://doi-org.sheffield.idm.oclc.org/10.1038/ng0892-345

[65] Roses, A.D. (2006). “On the discovery of the genetic association of Apolipoprotein E genotypes and common late-onset Alzheimer disease”. JAD *9*(S3), 361-366. https://doi.org/10.3233/JAD-2006-9S340

[66] Strittmatter, W.J. et. al. (1993). “Apolipoprotein E: High-avidity binding to β-amyloid and increased frequency of type 4 allele in late-onset familial Alzheimer disease”. Proc. Natl. Acad. Sci. U.S.A. *90*, 1977-1981. https://doi.org/10.1073/pnas.90.5.1977

[67] Shi, Y. et. al. (2017). “ApoE4 markedly exacerbates tau-mediated neurodegeneration in a mouse model of tauopathy”. Nature *549*, 523-527. https://doi.org/10.1038/nature24016

[68] Polymeropoulos, M.H. et. al. (1997). “Mutation in the α-Synuclein Gene Identified in Families with Parkinson’s Disease”. Science *276* (**5321**), 2045-2047. https://doi.org/10.1126/science.276.5321.2045

[69] Krüger, R. et. al. (1998). “Ala30Pro mutation in the gene encoding α-synuclein in Parkinson's disease”. Nat. Genet. *18*, 106-108. https://doi.org/10.1038/ng0298-106

[70] Zarranz, J.J. et. al. (2004). “The new mutation, E46K, of alpha-synuclein causes Parkinson and Lewy body dementia”. Ann. Neurol. *55*(2), 164-173. https://doi.org/10.1002/ana.10795

[71] Narhi, L. et. al. (1999). “Both Familial Parkinson's Disease Mutations Accelerate α-Synuclein Aggregation”. JBC *274*(14), 9843-9846. https://doi.org/10.1074/jbc.274.14.9843

[72] Taylor, J.P., Brown Jr. R.H. and Cleveland, D.W. (2017). “Decoding ALS: From Genes to Mechanism” Nature *439*(7628), 197-206. https://doi.org/10.1038/nature20413

[73] Kunkle, B.W. et. al. (2019). “Genetic meta-analysis of diagnosed Alzheimer’s disease identifies new risk loci and implicates Aβ, tau, immunity and lipid processing”. Nat. Genet. *51*, 414-430. https://doi.org/10.1038/s41588-019-0358-2

[74] Nalls, M.A. et. al. (2014). “Large-scale meta-analysis of genome-wide association data identifies six new risk loci for Parkinson’s disease”. Nat. Genet. *46*(9), 989-993. https://doi-org.sheffield.idm.oclc.org/10.1038/ng.3043

[75] Chang, et. al. (2017). “A meta-analysis of genome-wide association studies identifies 17 new Parkinson's disease risk loci”. Nat. Genet. *49*, 1511-1516. https://doi-org.sheffield.idm.oclc.org/10.1038/ng.3955

[76] Nalls, M.A. et. al. (2021). “Identification of novel risk loci, causal insights, and heritable risk for Parkinson’s disease: a meta-genome wide association study”. Lancet Neurol. *18*(12), 1091-1102. https://doi.org/10.1016/S1474-4422(19)30320-5

[77] Ryan, M. et. al. (2019). “Lifetime Risk and Heritability of Amyotrophic Lateral Sclerosis”. JAMA Neurol. *76*(11), 1367-1374. https://doi.org/10.1001/jamaneurol.2019.2044

[78] Cronin, S. et. al. (2007). “A genome-wide association study of sporadic ALS in a homogenous Irish population”. Human Molecular Genetics *17*(5), 768-774. https://doi.org/10.1093/hmg/ddm361

[79] van Rheenen, W. et. al. (2016). “Genome-wide association analyses identify new risk variants and the genetic architecture of amyotrophic lateral sclerosis”. Nat. Genet. *48*(9), 1043-1048. https://doi.org/10.1038/ng.3622

[80] van Rheenen, W. et. al. (2021). “Common and rare variant association analyses in amyotrophic lateral sclerosis identify 15 risk loci with distinct genetic architectures and neuron-specific biology”. Nat. Genet. *53*, 1636-1648. https://doi.org/10.1038/s41588-021-00973-1

[81] Zhang, S. et. al. (2022). “Genome-wide Identification of the Genetic Basis of Amyotrophic Lateral Sclerosis”. Neuron *110*(6), 992-1008. https://doi.org/10.1016/j.neuron.2021.12.019

[82] Mitraki, A. and King. J. (1989). “Protein Folding Intermediates and Inculsion Body Formation”. Nat. Biotechnol. *7*, 690-697. https://doi.org/10.1038/nbt0789-690

[83] Wetzel, R. (1994). “Mutations and off-pathway aggregation of proteins”. Trends Biotechnol. *12*(5), 193-198. https://doi.org/10.1016/0167-7799(94)90082-5

[84] Chiti, F. et. al. (2003). “Rationalization of the effects of mutations on peptide and protein aggregation rates”. Nature *424*(6950), 805-808. https://doi.org/10.1038/nature01891

[85] Ohnishi, S. and Takano, K. (2004). “Amyloid fibrils from the viewpoint of protein folding”. Cell Mol. Life Sci. *61*(5), 511-524. https://doi.org/10.1007/s00018-003-3264-8

[86] Benilova, I., Karran, E. and Strooper, B.D. (2012). “The toxic Aβ oligomer and Alzheimer's disease: an emperor in need of clothes”. Nat. Neurosci. *15*(3), 349-357. https://doi.org/10.1038/nn.3028

[87] Corderio Y. et. al. (2014). “Pathological implications of nucleic acid interactions with proteins associated with neurodegenerative diseases”. Biophys. Rev. *6*, 97-110. https://doi.org/10.1007/s12551-013-0132-0

[88] Oberg, K. et. al. (1994). “Nativelike secondary structure in interleukin-1 beta inclusion bodies by attenuated total reflectance FTIR”. Biochemistry *33*(9), 2628-2634. https://doi.org/10.1021/bi00175a035

[89] Fink, A.L. (1998). “Protein aggregation: folding aggregates, inclusion bodies and amyloid”. Fold Des. *3*(1), R9-23. https://doi.org/10.1016/s1359-0278(98)00002-9

[90] Sunde, M. et. al. (1997). “Common Core Structure of Amyloid Fibrils by Synchrotron X-ray Diffraction”. J. Mol. Biol. *273*(3), 729-739. https://doi.org/10.1006/jmbi.1997.1348

[91] Eisenberg, D.S. and Sawaya, M.R. (2017). “Structural Studies of Amyloid Proteins at the Molecular Level”. Annu. Rev. Biochem. *20*(86), 69-95. https://doi.org/10.1146/annurev-biochem-061516-045104

[92] Taylor, A.I.P. and Staniforth, R.A. (2022). “General Principles Underpinning Amyloid Structure”. Front. Neurosci. *16*, 878869. https://doi.org/10.3389/fnins.2022.878869

[93] Scheres, S.H.W., Ryskeldi-Falcon, B. and Goedert, M. (2023). “Molecular pathology of neurodegenerative diseases by cryo-EM of amyloids”. Nature *621*(7980), 701-710. https://doi.org/10.1038/s41586-023-06437-2

[94] Tayeb-Fligelman, E. et. al. (2017). “The cytotoxic Staphylococcus aureus PSMα3 reveals a cross-α amyloid-like fibril”. Science *355*(6327), 831-833. https://doi.org/10.1126/science.aaf4901

[95] Knowles, T.P.J., Vendruscolo, M. and Dobson, C.M. (2014). “The amyloid state and its association with protein misfolding diseases”. Nat. Rev. Mol. Cell. Biol. *15*(6), 384-396. https://doi.org/10.1038/nrm3810

[96] Serio, T.R. et. al. (2000). “Nucleated Conformational Conversion and the Replication of Conformational Information by a Prion Determinant”. Science *289*(5483), 1317-1321. https://doi-org.sheffield.idm.oclc.org/10.1126/science.289.5483.1317

[97] Harper, J.D. and Lansbury Jr., P.T. (1997). “Models of amyloid seeding in Alzheimer’s disease and scrapie: Mechanistic Truths and Physiological Consequences of the Time-Dependent Solubility of Amyloid Proteins”. Anuu. Rev. Biochem. *66*, 385-407. https://doi.org/10.1146/annurev.biochem.66.1.385

[98] Cohen, S.I.A. et. al. (2013). “Proliferation of amyloid-β42 aggregates occurs through a secondary nucleation mechanism”. Proc. Natl. Acad. Sci. USA *110*(24), 9758-9763. https://doi.org/10.1073/pnas.1218402110

[99] Törnquist, M. et. al. (2018). “Secondary nucleation in amyloid formation”. Chem. Commun. *54*(68), 8667-8684. https://doi.org/10.1039/C8CC02204F

[100] Xue, W., Homans, S.W. and Radford, S.E. (2008). “Systematic analysis of nucleation-dependent polymerization reveals new insights into the mechanism of amyloid self-assembly”. Proc. Natl. Acad. Sci. USA *105*(26), 8926-8931. https://doi.org/10.1073/pnas.0711664105

[101] Sawner, A.S. et. al. (2021). “Modulating α-Synuclein Liquid-Liquid Phase Separation”. Biochemistry *60*(48), 3676-3696. https://doi.org/10.1021/acs.biochem.1c00434

[102] Lin, Y. et. al. (2021). “Liquid-Liquid Phase Separation of Tau Driven by Hydrophobic Interaction Facilitates Fibrillization of Tau”. J. Mol. Biol. *433*(2), 166731. https://doi.org/10.1016/j.jmb.2020.166731

[103] Linse, S. (2020). “Kinetic fingerprints differentiate the mechanisms of action of anti-Aβ antibodies”. Nat. Struct. Mol. Biol. *27*(12), 1125-1133. https://doi.org/10.1038/s41594-020-0505-6

[104] Hardy, J. and Selkoe, D.J. (2002). “The amyloid hypothesis of Alzheimer's disease: progress and problems on the road to therapeutics”. Science *297*(5580), 353-356. https://doi.org/10.1126/science.1072994

[105] Selkoe, D.J. (2019). “Alzheimer disease and aducanumab: adjusting our approach”. Nat. Rev. Neurol. *15*(7), 365-366. https://doi.org/10.1038/s41582-019-0205-1

[106] Pike, C.J. et. al. (1991). “In vitro aging of beta-amyloid protein causes peptide aggregation and neurotoxicity”. Brain Res. *563*(1-2), 311-314. https://doi.org/10.1016/0006-8993(91)91553-d

[107] Alam, P. et. al. (2019). “α-synuclein oligomers and fibrils: a spectrum of species, a spectrum of toxicities”. J. Neurochem. *150*(5), 522-534. https://doi.org/10.1111/jnc.14808

[108] Killinger, B.A. et. al. (2019). “Endogenous alpha-synuclein monomers, oligomers and resulting pathology: let's talk about the lipids in the room”. NPJ Parkinsons Dis. *12*(5), 23. https://doi.org/10.1038/s41531-019-0095-3

[109] UCB Pharma (2022). “An Extension Study to Evaluate the Long-Term Efficacy, Safety and Tolerability of Minzasolmin (UCB0599) in Study Participants With Parkinson's Disease”. ClinicalTrials.gov ID: NCT05543252. https://clinicaltrials.gov/study/NCT05543252

[110] Schwarz, T.C. et. al. (2023). “High-resolution structural information of membrane-bound α-synuclein provides insight into the MoA of the anti-Parkinson drug UCB0599”. Proc. Natl. Acad. Sci. USA *120*(15), e2201910120. https://doi.org/10.1073/pnas.2201910120

[111] Braak, H. et. al. (2003). “Staging of brain pathology related to sporadic Parkinson’s disease”. Neurobiol. Aging *24*(2), 197-211. https://doi.org/10.1016/S0197-4580(02)00065-9

[112] Dickson, D.W. et. al. (2010). “Evidence in favor of Braak staging of Parkinson’s disease”. Mov. Disord. *25*(Suppl 1), S78-S82. https://doi.org/10.1002/mds.22637

[113] Mizuno, Y. et. al. (2006). “Transferrin localizes in Bunina bodies in amyotrophic lateral sclerosis”. Acta Neuropathol. *112*, 597-603. https://doi.org/10.1007/s00401-006-0122-4

[114] Webster, C.P. et. al. (2017). “Protein Homeostasis in Amyotrophic Lateral Sclerosis: Therapeutic Opportunities?”. Front. Mol. Neurosci. *10*. https://doi.org/10.3389/fnmol.2017.00123

[115] Strong, M.J. et. al. (2007). “TDP43 is a human low molecular weight neurofilament (hNFL) mRNA-binding protein”. Mol Cell Neurosci. *35*(2), 320-327. https://doi.org/10.1016/j.mcn.2007.03.007

[116] Lagier-Tourenne, C. (2010). “TDP-43 and FUS/TLS: emerging roles in RNA processing and neurodegeneration”. Hum. Mol. Genet. *19*(R1), R46-R64. https://doi.org/10.1093/hmg/ddq137

[117] Ge, W. et. al. (2005). “Mutant copper-zinc superoxide dismutase binds to and destabilizes human low molecular weight neurofilament mRNA”. J. Biol. Chem. *280*(1), 118-124. https://doi.org/10.1074/jbc.m405065200

[118] Daigle, J.G. et. al. (2012). “RNA-binding ability of FUS regulates neurodegeneration, cytoplasmic mislocalization and incorporation into stress granules associated with FUS carrying ALS-linked mutations”. Hum. Mol. Genet. *22*(6), 1193-1205. https://doi.org/10.1093/hmg/dds526

[119] Vance, C. et. al. (2009). “Mutations in FUS, an RNA Processing Protein, Cause Familial Amyotrophic Lateral Sclerosis Type 6”. Science *323*(5918), 1208-1211. https://doi.org/10.1126/science.1165942

[120] Strong, M.J. (2010). “The evidence for altered RNA metabolism in amyotrophic lateral sclerosis (ALS)”. J. Neurol. Sci. *288*(1-2), 1-12. https://doi.org/10.1016/j.jns.2009.09.029

[121] Feng, Y. et. al. (2013). “The machinery of macroautophagy”. Cell Res. *24*, 24-41. https://doi.org/10.1038/cr.2013.168

[122] Kulkarni, A., Chen, J. and Maday, S. (2018). “Neuronal autophagy and intercellular regulation of homeostasis in the brain”. Curr. Opin. Neurobiol. *51*, 29-36. https://doi.org/10.1016/j.conb.2018.02.008

[123] Kumsta, C. et. al. (2019). “The autophagy receptor p62/SQST-1 promotes proteostasis and longevity in C. elegans by inducing autophagy”. Nat. Commun. *10*, 5648. https://doi.org/10.1038/s41467-019-13540-4

[124] Shaid, S. et. al. (2012). “Ubiquitination and selective autophagy”. Cell Death Differ. *20*, 21-30. https://doi.org/10.1038/cdd.2012.72

[125] Liu, C. et. al. (2010). “Autophagy and protein aggregation after brain ischemia”. J. Neurochem *115*(1), 68-78. https://doi.org/10.1111/j.1471-4159.2010.06905.x

[126] Son, J.H. et. al. (2012). “Neuronal autophagy and neurodegenerative diseases”. Exp. Mol. Med. *44*, 89-98. https://doi.org/10.3858/emm.2012.44.2.031

[127] Tannous, P. et. al. (2009). “Intracellular protein aggregation is a proximal trigger of cardiomyocyte autophagy”. Circulation *117*(24), 3070-3078. https://doi.org/10.1161/circulationaha.107.763870

[128] Mori, F. et. al. (2019a). “Phosphorylated TDP-43 aggregates in skeletal and cardiac muscle are a marker of myogenic degeneration in amyotrophic lateral sclerosis and various conditions”. Acta Neuropathol. Commun. *7*, 165. https://doi.org/10.1186/s40478-019-0824-1

[129] Mori, F. et. al. (2019b). “Autophagy Is a Common Degradation Pathway for Bunina Bodies and TDP-43 Inclusions in Amyotrophic Lateral Sclerosis”. J. Neuropathol. Exp. Neurol. *78*(10), 910-921. https://doi.org/10.1093/jnen/nlz072

[130] Rudnick, N.D. et. al. (2017). “Distinct roles for motor neuron autophagy early and late in the SOD1G93A mouse model of ALS”. Proc. Natl. Acad. Sci. USA. *114*(39), E8294-E8303. https://doi.org/10.1073/pnas.1704294114

[131] Babinchak, W.M. et. al. (2019). “The role of liquid–liquid phase separation in aggregation of the TDP-43 low-complexity domain”. J. Biol. Chem. *294*(16), 6306-6317. https://doi.org/10.1074/jbc.RA118.007222

[132] Conicella, A.E. et. al. (2020). “TDP-43 α-helical structure tunes liquid–liquid phase separation and function”. Proc. Natl. Acad. Sci. USA. *117*(11), 5883-5894. https://doi.org/10.1073/pnas.1912055117

[133] Gu, S. et. al. (2022). “A liquid-to-solid phase transition of Cu/Zn superoxide dismutase 1 initiated by oxidation and disease mutation”. J. Biol. Chem. *299*(2), 102857. https://doi.org/10.1016/j.jbc.2022.102857

[134] Das, B. et. al. (2022). “A Zn-dependent structural transition of SOD1 modulates its ability to undergo phase separation”. EMBO J. *42*, e111185. https://doi.org/10.15252/embj.2022111185

[135] Patel, A. et. al. (2015). “A Liquid-to-Solid Phase Transition of the ALS Protein FUS Accelerated by Disease Mutation”. Cell *162*(5), 1066-1077. https://doi.org/10.1016/j.cell.2015.07.047

[136] Renaud, L. et. al. (2019). “Key role of UBQLN2 in pathogenesis of amyotrophic lateral sclerosis and frontotemporal dementia”. Acta Neuropathol. Commun. *7*, 103. https://doi.org/10.1186/s40478-019-0758-7

[137] Jafarinia, H., van der Giessen, E. and Onck, P.R. (2020). “Phase Separation of Toxic Dipeptide Repeat Proteins Related to C9orf72 ALS/FTD”. Biophys. J. *119*(4), 843-851. https://doi.org/10.1016/j.bpj.2020.07.005

[138] Solomon, D.A. et. al. (2021). “Altered Phase Separation and Cellular Impact in C9orf72-Linked ALS/FTD”. Front. Cell. Neurosci. *15*. https://doi.org/10.3389/fncel.2021.664151

[139] Boeynaems, S. et. al. (2017). “Phase Separation of C9orf72 Dipeptide Repeats Perturbs Stress Granule Dynamics”. Mol. Cell *65*(6), 1044-1055. https://doi.org/10.1016/j.molcel.2017.02.013

[140] Pakravan, D. et. al. (2020). “Role and therapeutic potential of liquid–liquid phase separation in amyotrophic lateral sclerosis”. J. Mol. Cell. Biol. *13*(1), 15-28. https://doi.org/10.1093/jmcb/mjaa049

[141] Hyman, A.A., Weber, C.A. and Jülicher, F. (2014). “Liquid-liquid phase separation in biology”. Annu. Rev. Cell Dev. Biol. *30*, 39-58. https://doi.org/10.1146/annurev-cellbio-100913-013325

[142] Jones, R.A.L. (2002). Chapter 3: “Phase Transitions” in “Soft Condensed Matter”. Oxford University Press, volume 49, 25-48. https://doi.org/10.1093/oso/9780198505907.003.0003

[143] Brangwynne, C.P. (2013). “Phase transitions and size scaling of membrane-less organelles”. J. Cell Biol. *203*(6), 875-881. https://doi.org/10.1083/jcb.201308087

[144] Lin, Y. et. al. (2015). “Formation and Maturation of Phase-Separated Liquid Droplets by RNA-Binding Proteins”. Mol. Cell *60*(2), 208-19. https://doi.org/10.1016/j.molcel.2015.08.018

[145] Mathieu, C., Pappu, R.V. and Taylor, J.P. (2020). “Beyond aggregation: Pathological phase transitions in neurodegenerative disease”. Science *370*(6512), 56-60. https://doi.org/10.1126/science.abb8032

[146] Wang, J. et. al. (2018). “A Molecular Grammar Governing the Driving Forces for Phase Separation of Prion-like RNA Binding Proteins”. Cell *174*(3), 688-699. https://doi.org/10.1016/j.cell.2018.06.006

[147] Gomes, E. and Shorter, J. (2018). “The molecular language of membraneless organelles”. J. Biol. Chem. *294*(18), 7115-7127. https://doi.org/10.1074/jbc.TM118.001192

[148] Boeynaems, S. et. al. (2018). “Protein Phase Separation: A New Phase in Cell Biology”. Trends Cell Biol. *28*(6), 420-435. https://doi.org/10.1016/j.tcb.2018.02.004

[149] Holehouse, A.S. and Pappu, R.V. (2018). “Functional Implications of Intracellular Phase Transitions”. Biochemistry *57*(17), 2415-2423. https://doi.org/10.1021/acs.biochem.7b01136

[150] Li, P. et. al. (2012). “Phase transitions in the assembly of multivalent signalling proteins”. Nature *483*(7389), 336-340. https://doi.org/10.1038/nature10879

[151] King, O.D. (2012). “The tip of the iceberg: RNA-binding proteins with prion-like domains in neurodegenerative disease”. Brain Res. *1462*, 61-80. https://doi.org/10.1016/j.brainres.2012.01.016

[152] March, Z.M., King, O.D. and Shorter, J. (2016). “Prion-like domains as epigenetic regulators, scaffolds for subcellular organization, and drivers of neurodegenerative disease”. Brain Res. https://doi.org/10.1016/j.brainres.2016.02.037

[153] Alberti, S. et. al. (2009). “A systematic survey identifies prions and illuminates sequence features of prionogenic proteins”. Cell *137*(1), 146-158. https://doi.org/10.1016/j.cell.2009.02.044

[154] Qamar, S. et. al. (2018). “FUS Phase Separation Is Modulated by a Molecular Chaperone and Methylation of Arginine Cation-π Interactions”. Cell *173*(3), 720-734. https://doi.org/10.1016/j.cell.2018.03.056

[155] Wang, A. et. al. (2018). “A single N-terminal phosphomimic disrupts TDP-43 polymerization, phase separation, and RNA splicing”. EMBO J. *37*(5), e97452. https://doi.org/10.15252/embj.201797452

[156] Piao, Y. et. al. (2006). “Neuropathology with Clinical Correlations of Sporadic Amyotrophic Lateral Sclerosis: 102 Autopsy Cases Examined Between 1962 and 2000”. Brain Pathol. *13*(1), 10-22. https://doi.org/10.1111/j.1750-3639.2003.tb00002.x

[157] Mizuno, Y. et. al. (2011). “Peripherin partially localizes in Bunina bodies in amyotrophic lateral sclerosis”. J. Neurol. Sci. *302*(1-2), 14-18. https://doi.org/10.1016/j.jns.2010.12.023

[158] Saberi, S. et. al. (2015). “Neuropathology of amyotrophic lateral sclerosis and its variants”. Neurol. Clin. *33*(4), 855-876. https://doi.org/10.1016/j.ncl.2015.07.012

[159] Mori, F. et. al. (2014). “Co-localization of Bunina bodies and TDP-43 inclusions in lower motor neurons in amyotrophic lateral sclerosis”. Neuropathology *34*(1), 71-76. https://doi.org/10.1111/neup.12044

[160] Bobek, L.A. and Levine, M.J. (1992). “Cystatins - inhibitors of cysteine proteinases”. Crit. Rev. Oral Biol. Med. *3*(4), 307-332. https://doi.org/10.1177/10454411920030040101

[161] Palsdottir, A. et. al. (1998). “Mutation in cystatin C gene causes hereditary brain haemorrhage”. Lancet. *2*(8611), 603-604. https://doi.org/10.1016/s0140-6736(88)90641-1

[162] Palsdottir, A., Snorradottir, A.O. and Thorsteinsson, L. (2006). “Hereditary Cystatin C Amyloid Angiopathy: Genetic, Clinical and Pathological Aspects”. Brain Pathol. *16*, 55-59. https://doi.org/10.1111/j.1750-3639.2006.tb00561.x

[163] Levy, E., Jaskolski, M. and Grubb, A. (2006). “The Role of Cystatin C in Cerebral Amyloid Angiopathy and Stroke: Cell Biology and Animal Models”. Brain Pathol. *16*, 60-70. https://doi.org/10.1111/j.1750-3639.2006.tb00562.x

[164] Gerhartz, B., Ekiel, I and Abrahamson, M. (1998). “Two stable unfolding intermediates of the disease-causing L68Q variant of human cystatin C”. Biochemistry *37*(49), 17309-17317. https://doi.org/10.1021/bi980873u

[165] Wei, L. et. al. (1998). “Instability of the amyloidogenic cystatin C variant of hereditary cerebral hemorrhage with amyloidosis, Icelandic type”. J. Biol. Chem. *273*(19), 11806-11814. https://doi.org/10.1074/jbc.273.19.11806

[166] Abrahamson, M. and Grubb, A. (1994). “Increased body temperature accelerates aggregation of the Leu-68-->Gln mutant cystatin C, the amyloid-forming protein in hereditary cystatin C amyloid angiopathy” Proc. Natl. Acad. Sci. USA. *91*(4), 1416-1420. https://doi.org/10.1073/pnas.91.4.1416

[167] Zurdel, J. et. al. (2002). “CST3 genotype associated with exudative age related macular degeneration”. Br. J. Ophthalmol. *86*(2), 214-219. https://doi.org/10.1136/bjo.86.2.214

[168] Butler, J.M. et. al. (2015). “A missense variant in CST3 exerts a recessive effect on susceptibility to age-related macular degeneration resembling its association with Alzheimer's disease”. Hum. Genet. *134*(7), 705-715. https://doi.org/10.1007/s00439-015-1552-7

[169] Nguyen, A. and Hulleman, J.D. (2016). “Evidence of Alternative Cystatin C Signal Sequence Cleavage Which Is Influenced by the A25T Polymorphism”. PLoS One *11*(2), e0147684. https://doi.org/10.1371/journal.pone.0147684

[170] Benussi, L. et. al. (2003). “Alzheimer disease-associated cystatin C variant undergoes impaired secretion”. Neurobiol. Dis. *13*(1), 15-21. https://doi.org/10.1016/S0969-9961(03)00012-3

[171] Grubb, A.O. (2006). “Cystatin C-Properties and use as a diagnostic marker”. Adv. Clin. Chem. *35*, 63-99. https://doi.org/10.1016/S0065-2423(01)35015-1

[172] Turk, V. and Bode, W. (1991). “The cystatins: Protein inhibitors of cysteine proteinases”. FEBS Lett. *285*, 213-219. https://doi.org/10.1016/0014-5793(91)80804-c

[173] Löfberg, H. and Grubb, A.O. (1979). “Quantitation of γ-trace in human biological fluids: Indications for production in the central nervous system”. Scand. J. Clin. Lab. *39*(7), 619-626. https://doi.org/10.3109/00365517909108866

[174] Abrahamson, M. et. al. (1986) “Isolation of six cysteine proteinase inhibitors from human urine. Their physicochemical and enzyme kinetic properties and concentrations in biological fluids”. J. Biol. Chem. *261*(24), 11282-11289. PMID: 3488317

[175] Zhang, Z. and Zhan, F. (2023). “Type 2 Cystatins and Their Roles in the Regulation of Human Immune Response and Cancer Progression”. Cancers (Basel), *15*(22), 5363. https://doi.org/10.3390/cancers15225363

[176] Ochieng, J. and Chaudhuri, G. (2010). “Cystatin Superfamily”. J. Health Care Poor Underserved. *21*(1 suppl), 51-70. https://doi.org/10.1353/hpu.0.0257

[177] Kolodziejczyk, R. et. al. (2010). “Crystal structure of human cystatin C stabilized against amyloid formation”. FEBS J. *277*(7), 1726-1737. https://doi.org/10.1111/j.1742-4658.2010.07596.x

[178] Sevier, C.S. and Kaiser, C.A. (2002). “Formation and transfer of disulphide bonds in living cells”. Nat. Rev. Mol. Cell Biol. *3*, 836-847. https://doi.org/10.1038/nrm954

[179] Paraoan, L. et. al. (2001). “Precursor cystatin C in cultured retinal pigment epithelium cells: evidence for processing through the secretory pathway”. Mol. Membr. Biol. *18*(3), 229-36. https://doi.org/10.1080/09687680110075101

[180] Paraoan, L. and Grierson, I. (2007). “Focus on molecules: cystatin C”. Exp. Eye Res. *84*(6), 1019-1020. https://doi.org/10.1016/j.exer.2006.01.024

[181] Mueller-Steiner, S. et. al. (2006). “Antiamyloidogenic and Neuroprotective Functions of Cathepsin B: Implications for Alzheimer's Disease”. Neuron *51*(6), 703-714. https://doi.org/10.1016/j.neuron.2006.07.027

[182] Turk, V. et. al. (2012). “Cysteine cathepsins: From structure, function and regulation to new frontiers”. Biochim. Biophys. Acta, Proteins Proteomics *1824*(1), 68-88. https://doi.org/10.1016/j.bbapap.2011.10.002

[183] Sokol, J.P. and Schiemann, W.P. (2004). “Cystatin C antagonizes transforming growth factor beta signaling in normal and cancer cells”. Mol. Cancer Res. *2*(3), 183-195. PMID: 15037657.

[184] Tian, M. and Schiemann, W.P. (2009). “Preclinical Efficacy of Cystatin C to Target the Oncogenic Activity of Transforming Growth Factor β in Breast Cancer”. Transl. Oncol. *2*(3), 174-183. https://doi.org/10.1593/tlo.09145

[185] Taupin, P. et. al. (2000). “FGF-2-responsive neural stem cell proliferation requires CCg, a novel autocrine/paracrine cofactor”. Neuron *28*(2), 385-397. https://doi.org/10.1016/s0896-6273(00)00119-7

[186] Zou, J. et. al. (2017). “Cystatin C as a potential therapeutic mediator against Parkinson’s disease via VEGF-induced angiogenesis and enhanced neuronal autophagy in neurovascular units”. Cell Death Dis. *8*, e2854. https://doi.org/10.1038/cddis.2017.240

[187] Warfel, A.H. et. al. (1987). “Constitutive secretion of cystatin C (gamma-trace) by monocytes and macrophages and its downregulation after stimulation”. J. Exp. Med. *166*(6), 1912-1917. https://doi.org/10.1084/jem.166.6.1912

[188] Babnik, J. et. al. (1988). “Cysteine proteinase inhibitors in inflamed human gingiva”. Biol. Chem. Hoppe. Seyler. *369*, Suppl: 271-276. PMID: 3144295.

[189] Leung-Tack, J. et. al. (1990). “Neutrophil chemotactic activity is modulated by human cystatin C, an inhibitor of cysteine proteases”. Inflammation *14*(3), 247-258. https://doi.org/10.1007/bf00915809

[190] Li, W. et. al. (2016). “Autophagy dysfunction and regulatory cystatin C in macrophage death of atherosclerosis”. J. Cell. Mol. Med. *20*(9), 1664-1672. https://doi.org/10.1111/jcmm.12859

[191] Hunaiti, S. et. al. (2020). “Secreted cystatins decrease proliferation and enhance apoptosis of human leukemic cells”. FEBS Open Bio *10*(10), 2166-2181. https://doi.org/10.1002/2211-5463.12958

[192] Zi, M. and Xu, Y. (2018). “Involvement of cystatin C in immunity and apoptosis”. Immunol. Lett. *196*, 80-90. https://doi.org/10.1016/j.imlet.2018.01.006

[193] Verdot, L. et. al. (1996). “Cystatins up-regulate nitric oxide release from interferon-gamma-activated mouse peritoneal macrophages”. J. Biol. Chem. *271*(45), 28077-28081. https://doi.org/10.1074/jbc.271.45.28077

[194] Wallin, H., Abrahamson, M. and Ekström, U. (2013). “Cystatin C properties crucial for uptake and inhibition of intracellular target enzymes”. J. Biol. Chem. *288*(23), 17019-17029. https://doi.org/10.1074/jbc.m113.453449

[195] Ekström, U. et. al. (2008). “Internalization of cystatin C in human cell lines”. FEBS J. *275*(18), 4571-4582. https://doi.org/10.1111/j.1742-4658.2008.06600.x

[196] Jurczak, P. et. al. (2024). “Monomer-Dimer Equilibrium of Human Cystatin C During Internalization Into Cancer Cells”. ChemBioChem *25*(16), e202400226. https://doi.org/10.1002/cbic.202400226

[197] Björck, L., Grubb, A. and Kjellén, L. (1990). “Cystatin C, a human proteinase inhibitor, blocks replication of herpes simplex virus”. J. Virol. *64*(2), 941-943. https://doi.org/10.1128/jvi.64.2.941-943.1990

[198] Hayn, M. et. al. (2021). “Natural cystatin C fragments inhibit GPR15-mediated HIV and SIV infection without interfering with GPR15L signaling”. Proc. Natl. Acad. Sci. USA *118*(3), e2023776118. https://doi.org/10.1073/pnas.2023776118

[199] Sun, B. et. al. (2008). “Cystatin C-cathepsin B axis regulates amyloid beta levels and associated neuronal deficits in an animal model of Alzheimer's disease”. Neuron, *60*(2), 247-257. https://doi.org/10.1016/j.neuron.2008.10.001

[200] Staniforth, R.A. et. al. (2001). “Three-dimensional domain swapping in the folded and molten-globule states of cystatins, an amyloid-forming structural superfamily”. EMBO J. *20*(17), 4774-4781. https://doi.org/10.1093/emboj/20.17.4774

[201] Janowski, R. et. al. (2001). “Human cystatin C, an amyloidogenic protein, dimerizes through three-dimensional domain swapping”. Nat. Struct. Mol. Biol. *8*, 316-320. https://doi.org/10.1038/86188

[202] Janowski, R. et. al. (2004). “Domain Swapping in N-truncated Human Cystatin C”. J. Mol. Biol. *341*(1), 151-160. https://doi.org/10.1016/j.jmb.2004.06.013

[203] Merz, G.S. et. al. (1997). “Human cystatin C forms an inactive dimer during intracellular trafficking in transfected CHO cells”. J. Cell. Physiol. *173*(3), 423-432. https://doi.org/10.1002/(sici)1097-4652(199712)173:3%3C423::aid-jcp15%3E3.0.co;2-c

[204] Abrahamson, M. (1996). “Molecular basis for amyloidosis related to hereditary brain hemorrhage”. Scand. J. Clin. Lab. Invest. Suppl. *226*, 47-56. PMID: 8981667.

[205] Taube, M. et. al. (2019). “The domain swapping of human cystatin C induced by synchrotron radiation”. Sci. Rep. *9*(1), 8548. https://doi.org/10.1038/s41598-019-44811-1

[206] Wojciechowska, D. et. al. (2022). “Oligomerization of Human Cystatin C-An Amyloidogenic Protein: An Analysis of Small Oligomeric Subspecies”. Int. J. Mol. Sci. *23*(21), 13441. https://doi.org/10.3390/ijms232113441

[207] Sanders, A. et. al. (2004). “Cystatin forms a tetramer through structural rearrangement of domain-swapped dimers prior to amyloidogenesis”. J. Mol. Biol. *366*(1), 165-178. https://doi.org/10.1016/j.jmb.2003.12.011

[208] Kokalj, S.J. et. al. (2007). “Essential role of proline isomerization in stefin B tetramer formation”. J. Mol. Biol. *366*(5), 1569-1579. https://doi.org/10.1016/j.jmb.2006.12.025

[209] Sharma, C.A. (2009). “Elucidating the Topology of Cystatin B Amyloid Fibrils”. PhD Thesis, University of Sheffield.

[210] Williams, A.J. (2014). “Cystatin C and Alzheimer’s Disease”. PhD Thesis, University of Sheffield. https://etheses.whiterose.ac.uk/id/eprint/8547/

[211] Wilson, M.E. et. al. (2010). “Cystatin C: a candidate biomarker for amyotrophic lateral sclerosis”. PLoS One *5*(12), e15133. https://doi.org/10.1371/journal.pone.0015133

[212] Zhu, Y. et. al. (2018). “Aberrant Levels of Cystatin C in Amyotrophic Lateral Sclerosis: a Systematic Review and Meta Analysis”. Int. J. Biol. Sci. *14*(9), 1041-1053. https://doi.org/10.7150/ijbs.25711

[213] Granger, S.M. and Highley, J.R. (2000). “Pathological Correlates of TDP-43 Proteinopathy: The Role of Bunina Bodies and Cystatin C in Amyotrophic Lateral Sclerosis”. University of Sheffield, Master’s Dissertation.

[214] Zhang, Y. et. al. (2009). “Aberrant cleavage of TDP-43 enhances aggregation and cellular toxicity”. Proc. Natl. Acad. Sci. USA *106*(18), 1607-1612. https://doi.org/10.1073/pnas.0900688106

[215] Nonaka, T. et. al. (2009). “Truncation and pathogenic mutations facilitate the formation of intracellular aggregates of TDP-43”. Hum. Mol. Genet. *18*(18), 3353-3364. https://doi.org/10.1093/hmg/ddp275

[216] Igaz, L.M. et. al. (2009). “Expression of TDP-43 C-terminal Fragments in Vitro Recapitulates Pathological Features of TDP-43 Proteinopathies”. J. Biol. Chem. *284*(13), 8516-8524. https://doi.org/10.1074/jbc.m809462200

[217] Hart, M.P. and Gitler, A.D. (2012). “ALS-associated ataxin 2 polyQ expansions enhance stress-induced caspase 3 activation and increase TDP-43 pathological modifications”. J. Neurosci. *32*(27), 9133-9142. https://doi.org/10.1523/jneurosci.0996-12.2012

[218] Dormann, D. et. al. (2009). “Proteolytic processing of TAR DNA binding protein-43 by caspases produces C-terminal fragments with disease defining properties independent of progranulin”. J. Neurochem. *110*(3), 1082-1094. https://doi.org/10.1111/j.1471-4159.2009.06211.x

[219] Suzuki, Y., Jin, C. and Yazawa, I. (2014). “Cystatin C Triggers Neuronal Degeneration in a Model of Multiple System Atrophy”. Am. J. Pathol. *184*(3), 790-799. https://doi.org/10.1016/j.ajpath.2013.11.018

[220] Stoka, V. et. al. (2001). “Lysosomal Protease Pathways to Apoptosis”. JBC 276(5), 3149-3157. https://doi.org/10.1074/jbc.M008944200

[221] Mori, F. et. al. (2010). “Relationship between Bunina bodies and TDP-43 inclusions in spinal anterior horn in amyotrophic lateral sclerosis”. Neuropathol. Appl. Neurobiol. *36*(4), 345-352. https://doi.org/10.1111/j.1365-2990.2010.01081.x

[222] Lowe, J. (1994). “New pathological findings in amyotrophic lateral sclerosis”. J. Neurol. Sci. *124*(Suppl.), 38-51. https://doi.org/10.1016/0022-510x(94)90175-9

[223] Piao, Y. et. al. (2003). “Neuropathology with clinical correlations of sporadic amyotrophic lateral sclerosis: 102 autopsy cases examined between 1962 and 2000”. Brain Pathol. *13*(1), 10-22. https://doi.org/10.1111/j.1750-3639.2003.tb00002.x

[224] Sasaki, S., Komori, T. and Iwata, M. (2006). “Neuronal inclusions in sporadic motor neuron disease are negative for alpha-synuclein”. Neurosci. Lett. *397*(1-2). https://doi.org/10.1016/j.neulet.2005.11.056

[225] Mizuno, Y. et. al. (2006). “Immunoreactivities of p62, an ubiqutin-binding protein, in the spinal anterior horn cells of patients with amyotrophic lateral sclerosis”. J. Neurol. Sci. *249*(1), 13-18. https://doi.org/10.1016/j.jns.2006.05.060

[226] Sasaki, S. and Iwata, M. (1999). “Immunoreactivity of beta-amyloid precursor protein in amyotrophic lateral sclerosis”. Acta Neuropathol. *97*(5), 463-468. https://doi.org/10.1007/s004010051015

[227] Okamoto, K., Mizuno, Y. and Fujita, Y. (2008). “Bunina bodies in amyotrophic lateral sclerosis”. Neuropathology *28*(2), 109-115. https://doi.org/10.1111/j.1440-1789.2007.00873.x

[228] Murray, M.E. et. al. (2012). “Clinical and neuropathologic heterogeneity of c9FTD/ALS associated with hexanucleotide repeat expansion in C9ORF72”. Acta Neuropathol. *122*(6), 673-690. https://doi.org/10.1007/s00401-011-0907-y

[229] Cooper-Knock, J. et. al. (2012). “Clinico-pathological features in amyotrophic lateral sclerosis with expansions in C9ORF72”. Brain, *135*(pt 3), 751-764. https://doi.org/10.1093/brain/awr365

[230] Fujita, Y. et. al. (2011). “Numerous FUS-positive inclusions in an elderly woman with motor neuron disease”. Neuropathology *31*(2), 170-176. https://doi.org/10.1111/j.1440-1789.2010.01146.x

[231] Rademakers, R. et. al. (2010). “Fus gene mutations in familial and sporadic amyotrophic lateral sclerosis”. Muscle Nerve *42*(2), 170-176. https://doi.org/10.1002/mus.21665

[232] Tan, C. et. al. (2007). “TDP-43 immunoreactivity in neuronal inclusions in familial amyotrophic lateral sclerosis with or without SOD1 gene mutation”. Acta Neuropathol. *113*(5), 535-542. https://doi.org/10.1007/s00401-007-0206-9

[233] van Welsem, M.E. et. al. (2002). “The relationship between Bunina bodies, skein-like inclusions and neuronal loss in amyotrophic lateral sclerosis”. Acta Neuropathol. *103*, 583-589. https://doi.org/10.1007/s00401-001-0507-3

[234] Tomonaga, M. et. al. (1978). “Ultrastructure of the Bunina bodies in anterior horn cells of amyotrophic lateral sclerosis”. Acta Neuropathol. *42*, 81-86. https://doi.org/10.1007/BF00690971

[235] Sasaki, S. and Maruyama, S. (1993). “Ultrastructural study of Bunina bodies in the anterior horn neurons of patients with amyotrophic lateral sclerosis”. Neurosci. Lett. *154*(1-2), 117-120. https://doi.org/10.1016/0304-3940(93)90185-N

[236] Yoshida, S. et. al. (1995). “Bunina body formation in amyotrophic lateral sclerosis: a morphometric-statistical and trace element study featuring aluminum”. J. Neurol. Sci. *130*(1), 88-94. https://doi.org/10.1016/0022-510X(95)00011-P

[237] Clarke, C.E. (2007). “Parkinson’s disease”. BMJ *335*, 441. https://doi.org/10.1136/bmj.39289.437454.AD

[238] Ni, A. and Ernst, C. (2022). “Evidence That Substantia Nigra Pars Compacta Dopaminergic Neurons Are Selectively Vulnerable to Oxidative Stress Because They Are Highly Metabolically Active”. Front. Cell. Neurosci. *16*. https://doi.org/10.3389/fncel.2022.826193

[239] Dauer, W. and Przedborski, S. (2003). “Parkinson's Disease: Mechanisms and Models”. Neuron *39*(6), 889-909. https://doi.org/10.1016/S0896-6273(03)00568-3

[240] Spillantini, M.G. et. al. (1998). “alpha-Synuclein in filamentous inclusions of Lewy bodies from Parkinson's disease and dementia with lewy bodies”. Proc. Natl. Acad. Sci. USA *95*(11), 6469-6473. https://doi.org/10.1073/pnas.95.11.6469

[241] Baba, M. et. al. (1998). “Aggregation of alpha-synuclein in Lewy bodies of sporadic Parkinson's disease and dementia with Lewy bodies”. Am. J. Pathol. *152*(4), 879-884. PMID: 9546347

[242] Shahmoradian, S.H. et. al. (2019). “Lewy pathology in Parkinson’s disease consists of crowded organelles and lipid membranes”. Nat Neurosci. *22*, 1099-1109. https://doi.org/10.1038/s41593-019-0423-2

[243] Galloway, P.G., Mulvihill, P. and Perry, G. (1992). “Filaments of Lewy bodies contain insoluble cytoskeletal elements”. Am. J. Pathol. *140*(4), 809-822. PMID: 1314025.

[244] Forno, L.S. (1996). “Neuropathology of Parkinson’s Disease”. J. Neuropathol. Exp. Neurol. *55*(3), 259-272. https://doi.org/10.1097/00005072-199603000-00001

[245] Soper, J.H. et. al. (2008). “α-Synuclein–induced Aggregation of Cytoplasmic Vesicles in Saccharomyces cerevisiae”. Mol. Biol. Cell *19*(3), 765-1280. https://doi.org/10.1091/mbc.e07-08-0827

[246] El-Agnaf, O.M.A. et. al. (2003). “α-Synuclein implicated in Parkinson's disease is present in extracellular biological fluids, including human plasma”. FASEB J. *17*(13), 1-16. https://doi.org/10.1096/fj.03-0098fje

[247] Irwin, D.J., Lee, V.M.-Y. and Trojanowski, J.Q. (2013). “Parkinson's disease dementia: convergence of α-synuclein, tau and amyloid-β pathologies”. Nat. Rev. Neurosci. *14*, 626-636. https://doi.org/10.1038/nrn3549

[248] Goldman, J.E. et. al. (1983). “Lewy Bodies of Parkinson’s Disease Contain Neurofilament Antigens”. Science *221*(4615), 1082-1084. https://doi.org/10.1126/science.6308771

[249] Chung, K.K. et. al. (2001). “Parkin ubiquitinates the alpha-synuclein-interacting protein, synphilin-1: implications for Lewy-body formation in Parkinson disease”. Nat. Med. *7*(10), 1144-1150. https://doi.org/10.1038/nm1001-1144

[250] Ito, T. et. al. (2003). “Dorfin localizes to Lewy bodies and ubiquitylates synphilin-1”. J. Biol. Chem. *278*(31), 29106-29114. https://doi.org/10.1074/jbc.m302763200

[251] Nagano, Y. et. al. (2003). “Siah-1 facilitates ubiquitination and degradation of synphilin-1”. J. Biol. Chem. *278*(51), 51504-51514. https://doi.org/10.1074/jbc.m306347200

[252] Lowe, J. et. al. (1990). “Ubiquitin carboxyl-terminal hydrolase (PGP 9.5) is selectively present in ubiquitinated inclusion bodies characteristic of human neurodegenerative diseases”. J. Pathol. *161*(2), 153-160. https://doi.org/10.1002/path.1711610210

[253] Engelender, S. et. al. (1999). “Synphilin-1 associates with α-synuclein and promotes the formation of cytosolic inclusions”. Nat. Genet. *22*, 110-114. https://doi.org/10.1038/8820

[254] Wakabayashi, K. et. al. (2000). “Synphilin-1 is present in Lewy bodies in Parkinson's disease”. Ann. Neurol. *47*(4), 521-523. PMID: 10762166.

[255] Szargel, R. et. al. (2009). “Synphilin-1A Inhibits Seven in Absentia Homolog (SIAH) and Modulates α-Synuclein Monoubiquitylation and Inclusion Formation”. J. Biol. Chem. *284*(17), 11706-11716. https://doi.org/10.1074/jbc.M805990200

[256] Liani, E. et. al. (2004). “Ubiquitylation of synphilin-1 and α-synuclein by SIAH and its presence in cellular inclusions and Lewy bodies imply a role in Parkinson's disease”. Proc. Natl. Acad. Sci. USA *101*(15), 5500-5505. https://doi.org/10.1073/pnas.0401081101

[257] Singleton, A.B. et. al. (2003). “alpha-Synuclein locus triplication causes Parkinson's disease” Science *302*(5646), 841. https://doi.org/10.1126/science.1090278

[258] Miller, D.W. et. al. (2004). “Alpha-synuclein in blood and brain from familial Parkinson disease with SNCA locus triplication”. Neurology *62*(10), 1835-1838. https://doi.org/10.1212/01.wnl.0000127517.33208.f4

[259] Chartier-Harlin, M. et. al. (2004). “Alpha-synuclein locus duplication as a cause of familial Parkinson's disease”. Lancet. *364*(9440), 1167-1169. https://doi.org/10.1016/s0140-6736(04)17103-1

[260] Iwai, A. et. al. (1995). “The Precursor Protein of Non-Aβ Component of Alzheimer’s Disease Amyloid Is a Presynaptic Protein of the Central Nervous System”. Neuron *14*, 467-475. https://doi.org/10.1016/0896-6273(95)90302-x

[261] Weinreb, P.H. et. al. (1996). “NACP, A Protein Implicated in Alzheimer’s Disease and Learning, Is Natively Unfolded”. Biochemistry *35* (**43**), 13709-13715. https://doi.org/10.1021/bi961799n

[262] Binolfi, A., Theillet, F. and Selenko, P. (2012). “Bacterial in-cell NMR of human α-synuclein: a disordered monomer by nature?”. Biochem. Soc. Trans. *40*(5), 950-954. https://doi.org/10.1042/BST20120096

[263] Burré, J. et. al. (2010). “α-Synuclein Promotes SNARE-Complex Assembly in Vivo and in Vitro”. Science *329*(5999), 1663-1667. https://doi.org/10.1126/science.1195227

[264] Sulzer, D. and Edwards, R.H. (2019). “The physiological role of α-synuclein and its relationship to Parkinson’s Disease”. J. Neurochem. *150*(5), 475-486. https://doi.org/10.1111/jnc.14810

[265] Davidson, W.S. et. al. (1998). “Stabilization of α-Synuclein Secondary Structure upon Binding to Synthetic Membranes”. J. Biol. Chem. *273*(16), 9443-9449. https://doi.org/10.1074/jbc.273.16.9443

[266] Whittaker, H.T. et. al. (2017). “Multiple system atrophy: genetic risks and alpha-synuclein mutations”. F1000Res. *6*, 2072. https://doi.org/10.12688/f1000research.12193.1

[267] Middleton, E.R. and Rhoades, E. (2010). “Effects of curvature and composition on α-synuclein binding to lipid vesicles”. Biophys. J. *99*(7), 2279-2288. https://doi.org/10.1016/j.bpj.2010.07.056

[268] Braun, A.R. et. al. (2012). “α-Synuclein induces both positive mean curvature and negative Gaussian curvature in membranes”. J. Am. Chem. Soc. *134*(5), 2613-2620. https://doi.org/10.1021/ja208316h

[269] Wang, L. et. al. (2014) “α-synuclein multimers cluster synaptic-vesicles and attenuate recycling”. Curr. Biol. *24*(19), 2319-2326. https://doi.org/10.1016/j.cub.2014.08.027

[270] Jiang, Z., de Messieres, M. and Lee, J.C. (2014). “Membrane Remodeling by α-Synuclein and Effects on Amyloid Formation”. J. Am. Chem. Soc. *135*(43), 15970-15973. https://doi.org/10.1021/ja405993r

[271] Mizuno, N. et. al. (2012). “Remodeling of Lipid Vesicles into Cylindrical Micelles by α-Synuclein in an Extended α-Helical Conformation”. J. Biol. Chem. *287*(35), 29301-29311. https://doi.org/10.1074/jbc.M112.365817

[272] Braun, A.R. et. al. (2014). “α-Synuclein-Induced Membrane Remodeling Is Driven by Binding Affinity, Partition Depth, and Interleaflet Order Asymmetry”. J. Am. Chem. Soc. *136*(28), 9962-9972. https://doi.org/10.1021/ja5016958

[273] Shi, Z. et. al. (2015). “Biophysics of α-synuclein induced membrane remodelling”. Phys. Chem. Chem. Phys. *17*(24), 15561-15568. https://doi.org/10.1039/C4CP05883F

[274] Butler, B. et. al. (2015). “Dopamine Transporter Activity Is Modulated by α-Synuclein”. J. Biol. Chem. *290*(49), 29542-29554. https://doi.org/10.1074/jbc.M115.691592

[275] Wersinger, C., Rusnak, M. and Sidhu, A. (2006). “Modulation of the trafficking of the human serotonin transporter by human alpha-synuclein”. Eur. J. Neurosci. *24*(1), 55-64. https://doi.org/10.1111/j.1460-9568.2006.04900.x

[276] Chandra, S. et. al. (2005). “α-Synuclein Cooperates with CSPα in Preventing Neurodegeneration”. Cell *123* (**3**), 383-396. https://doi.org/10.1016/j.cell.2005.09.028

[277] Bonini, N.M. and Giasson, B.I. (2005). “Snaring the Function of α-Synuclein” Cell *123* (**3**), 359-361. https://doi.org/10.1016/j.cell.2005.10.017

[278] Roberts, H.L. and Brown, D.R. “Seeking a Mechanism for the Toxicity of Oligomeric -Synuclein”. Biomolecules *5*(2), 282-305. https://doi.org/10.3390/biom5020282

[279] Conway, K.A. et. al. (2000). “Acceleration of oligomerization, not fibrillization, is a shared property of both alpha-synuclein mutations linked to early-onset Parkinson's disease: implications for pathogenesis and therapy”. Proc. Natl. Acad. Sci. USA *97*(2), 571-576. https://doi.org/10.1073/pnas.97.2.571

[280] Cremades, N. et. al. (2012). “Direct observation of the interconversion of normal and toxic forms of α-synuclein”. Cell, *149*(5), 1048-1059. https://doi.org/10.1016/j.cell.2012.03.037

[281] Nakamura, K. et. al. (2011). “Direct membrane association drives mitochondrial fission by the Parkinson disease-associated protein alpha-synuclein”. J. Biol. Chem. *286*(23), 20710-20726. https://doi.org/10.1074/jbc.m110.213538

[282] Emmanouilidou, E., Stefanis, L. and Vekrellis, K. (2010). “Cell-produced alpha-synuclein oligomers are targeted to, and impair, the 26S proteasome”. Neurobol. Aging *31*(6), 953-968. https://doi.org/10.1016/j.neurobiolaging.2008.07.008

[283] Kayed, R. et. al. (2003). “Common structure of soluble amyloid oligomers implies common mechanism of pathogenesis”. Science *300*(5618), 486-489. https://doi.org/10.1126/science.1079469

[284] Volpicelli-Daley, L.A. et. al. (2011). “Exogenous α-Synuclein Fibrils Induce Lewy Body Pathology Leading to Synaptic Dysfunction and Neuron Death”. Neuron *72*(1), 57-71. https://doi.org/10.1016/j.neuron.2011.08.033

[285] Lorenzen, N. et. al. (2014). “The Role of Stable α-Synuclein Oligomers in the Molecular Events Underlying Amyloid Formation”. J. Am. Chem. Soc. *136*(10), 3859-3868. https://doi.org/10.1021/ja411577t

[286] van Rooijen, B.D., Claessens, M.M.A.E. and Subramaniam, V. (2009). “Lipid bilayer disruption by oligomeric α-synuclein depends on bilayer charge and accessibility of the hydrophobic core”. Biochim. Biophys. Acta – Biomembr. *1788*(6), 1271-1278. https://doi.org/10.1016/j.bbamem.2009.03.010

[287] Danzer, K.M. et. al. (2007). “Different Species of α-Synuclein Oligomers Induce Calcium Influx and Seeding”. J. Neurosci. *27*(34), 9220-9232. https://doi.org/10.1523/JNEUROSCI.2617-07.2007

[288] Kostka, M. et. al. (2008). “Single Particle Characterization of Iron-induced Pore-forming α-Synuclein Oligomers”. J. Biol. Chem. *283*(16), 10992-11003. https://doi.org/10.1074/jbc.M709634200

[289] Chen, S.W. et. al. (2015). “Structural characterization of toxic oligomers that are kinetically trapped during α-synuclein fibril formation”. Proc. Natl. Acad. Sci. USA *112*(16), e1994-e2003. https://doi.org/10.1073/pnas.1421204112

[290] Lashuel, H.A. et. al. (2002). “α-Synuclein, Especially the Parkinson's Disease-associated Mutants, Forms Pore-like Annular and Tubular Protofibrils”. J. Mol. Biol. *322*(5), 1089-1102. https://doi.org/10.1016/S0022-2836(02)00735-0

[291] Tsigelny, I.F. et. al. (2012). “Role of α-synuclein penetration into the membrane in the mechanisms of oligomer pore formation”. FEBS J. *279*(6), 1000-1013. https://doi.org/10.1111/j.1742-4658.2012.08489.x

[292] Fusco, G. et. al. (2017). “Structural basis of membrane disruption and cellular toxicity by a-synuclein oligomers” Science *358*(6369), 1440-1443. https://doi.org/10.1126/science.aan6160

[293] Nakamura, K. (2013). “α-Synuclein and Mitochondria: Partners in Crime?”. Neurother. *10*(3), 391-399. https://doi.org/10.1007/s13311-013-0182-9

[294] Burré, J., Sharma, M. and Südhof, T.C. (2014). “α-Synuclein assembles into higher-order multimers upon membrane binding to promote SNARE complex formation”. Proc. Natl. Acad. Sci. USA *111*(40), e4274-4283. https://doi.org/10.1073/pnas.1416598111

[295] Kasten, M. and Klein, C. (2013). “The many faces of alpha-synuclein mutations”. Mov. Disord. *28*(6), 697-701. https://doi.org/10.1002/mds.25499

[296] Fredenburg, R.A. et. al. (2007). “The impact of the E46K mutation on the properties of alpha-synuclein in its monomeric and oligomeric states”. Biochemistry *46*(24), 7107-7118. https://doi.org/10.1021/bi7000246

[297] Frieg, B. et. al. (2022). “The 3D structure of lipidic fibrils of α-synuclein”. Nat. Commun. *13*, Article number: 6810. https://doi.org/10.1038/s41467-022-34552-7

[298] Hähl, H. et. al. (2015). “α-Synuclein Insertion into Supported Lipid Bilayers As Seen by in Situ X-ray Reflectivity”. ACS Chem. Neurosci. *6*(3), 374-379. https://doi.org/10.1021/cn5002683

[299] Kayed, R. et. al. (2004). “Permeabilization of Lipid Bilayers Is a Common Conformation-dependent Activity of Soluble Amyloid Oligomers in Protein Misfolding Diseases”. J. Biol. Chem. *279*(45), 46363-46366. https://doi.org/10.1074/jbc.c400260200

[300] Stöckl, M.T., Zijlstra, N and Subramaniam, V. (2013). “α-Synuclein Oligomers: an Amyloid Pore?”. Mol. Neurobiol. *47*, 613-621. https://doi.org/10.1007/s12035-012-8331-4

[301] Volles, M.J. and Lansbury, P.T. (2002). “Vesicle Permeabilization by Protofibrillar α-Synuclein Is Sensitive to Parkinson's Disease-Linked Mutations and Occurs by a Pore-like Mechanism”. Biochemistry *41*(14), 4595-4602. https://doi.org/10.1021/bi0121353

[302] Stöckl, M.T., Claessens, M.M.A.E. and Subramaniam, V. (2012). “Kinetic measurements give new insights into lipid membrane permeabilization by α-synuclein oligomers”. Mol. BioSyst. *8*(1), 338-345. https://doi.org/10.1039/C1MB05293D

[303] Diao, J. et. al. (2013). “Native α-synuclein induces clustering of synaptic-vesicle mimics via binding to phospholipids and synaptobrevin-2/VAMP2”. eLife *2*, e00592. https://doi.org/10.7554/eLife.00592

[304] Cai, B. et. al. (2020). “Single-vesicle imaging quantifies calcium’s regulation of nanoscale vesicle clustering mediated by α-synuclein”. Microsyst. Nanoeng. *6*, 38. https://doi.org/10.1038/s41378-020-0147-1

[305] Fusco, G. et. al. (2016). “Structural basis of synaptic vesicle assembly promoted by α-synuclein”. Nat. Comm. *7*, 12563. https://doi.org/10.1038/ncomms12563

[306] Eichmann, C. et. al. (2016). “Preparation and characterization of stable α-synuclein lipoprotein particles”. J. Biol. Chem. *291*(16), 8516-8527. https://doi.org/10.1074/jbc.M115.707968

[307] Galvagnion et. al. (2024). “Structural characterisation of α-synuclein-membrane interactions and the resulting aggregation using small angle scattering”. Phys. Chem. Chem. Phys. *26*(14), 10998-11013. https://doi.org/10.1039/D3CP05928F

[308] Varkey, J. et. al. (2010). “Membrane Curvature Induction and Tubulation Are Common Features of Synucleins and Apolipoproteins”. J. Biol. Chem. *285*(42), 32486-32493. https://doi.org/10.1074/jbc.M110.139576

[309] Marlet, F.R. et. al. (2024). “Lipid levels correlate with neuronal and dopaminergic markers during the differentiation of SH-SY5Y cells”. Biochim. Biophys. Acta *1870*(6), 167212. https://doi.org/10.1016/j.bbadis.2024.167212

[310] Reynolds, N.P. et. al. (2011). “Mechanism of Membrane Interaction and Disruption by α-Synuclein”. J. Am. Chem. Soc. *133*(48). 19366-19375. https://doi.org/10.1021/ja2029848

[311] Galvagnion, C. et. al. (2015). “Lipid vesicles trigger α-synuclein aggregation by stimulating primary nucleation”. Nat. Chem. Biol. *11*, 229-234. https://doi.org/10.1038/nchembio.1750

[312] Studier, F.W. (2005). “Protein production by auto-induction in high density shaking cultures”. Protein Expr. Purif. *41*(1), 207-234. https://doi.org/10.1016/j.pep.2005.01.016

[313] Keeley, E. (2007). “Folding, dimerisation and the interaction with Aβ1-40 of human cystatin C”. PhD thesis. University of Sheffield. https://www.proquest.com/docview/2559008044

[314] Williamson, M.P. (2013). “Using chemical shift perturbation to characterise ligand binding”. Prog. Nucl. Magn. Reson. Spectrosc. *73*, 1-16. https://doi.org/10.1016/j.pnmrs.2013.02.001

[315] Abrahamson, M. et. al. (1988). “Efficient production of native, biologically active human cystatin C by Escherichia coli”. FEBS Lett. *236*(1), 14-18. https://doi.org/10.1016/0014-5793(88)80276-X

[316] Dalbøge, H. et. al. (1989). “High-level expression of active human cystatin C in Escherichia coli”. https://doi.org/10.1016/0378-1119(89)90214-X

[317] Wang, Q. et. al. (2012). “Codon Preference Optimization Increases Prokaryotic Cystatin C Expression”. Biomed Res. Int., 732017. https://doi.org/10.1155/2012/732017

[318] Li, Y.M. et. al. (2014). “Effect of codon optimization on expression levels of human cystatin C in Pichia pastoris”. Genet. Mol. Res. *13*(3), 4990-5000. http://dx.doi.org/10.4238/2014.July.4.14

[319] Hayashi, M. (2013). “Efficient production of recombinant cystatin C using a peptide-tag, 4AaCter, that facilitates formation of insoluble protein inclusion bodies in Escherichia coli”. Protein Expr. Purif. *88*(2), https://doi.org/10.1016/j.pep.2013.01.011

[320] Zhang, Q. (2014). “Expression and purification of soluble human cystatin C in Escherichia coli with maltose-binding protein as a soluble partner”. Protein Expr. Purif. *104*, 14-19. https://doi.org/10.1016/j.pep.2014.09.010

[321] Zhou, Y. et. al. (2015). “Efficient expression, purification and characterization of native human cystatin C in Escherichia coli periplasm”. Protein Expr. Purif. *111*, 18-22. https://doi.org/10.1016/j.pep.2015.03.006

[322] Perlenfein, T.J. and Murphy, R.M. (2015). “Expression, Purification, and Characterization of Human Cystatin C Monomers and Oligomers”. Protein Expr. Purif. *117*, 35-43. https://doi.org/10.1016/j.pep.2015.09.023

[323] Auerswald, E.A. et. al. (1991). "Purification and characterization of a chicken egg white cystatin variant expressed in an Escherichia coli pIN-III-ompA system". Eur. J. Biochem. *200*(1), 131-138. https://doi.org/10.1111/j.1432-1033.1991.tb21059.x

[324] Ghrayeb, J. et. al. (1984). "Secretion cloning vectors in Escherichia coli". EMBO J. *3*(10), 2437-2442. https://doi.org/10.1002/j.1460-2075.1984.tb02151.x

[325] El Shawaihde, A. (2012). "Role of human cystatin C in Alzheimer's disease". PhD Thesis, University of Sheffield.

[326] Aubrey, L. (2018). "The impact of surfaces on the self-assembly and other molecular interactions of the amyloid β peptide". PhD Thesis, University of Sheffield. https://etheses.whiterose.ac.uk/id/eprint/23016/

[327] Mussap, M. and Plebani, M. (2004). "Biochemistry and clinical role of human cystatin C". Crit. Rev. Clin. Lab. Sci. *41*(5-6), 467-550. https://doi.org/10.1080/10408360490504934

[328] Wilfinger, W.W., Mackey, K. and Chomczynski, P. (1997). "Effect of pH and ionic strength on the spectrophotometric assessment of nucleic acid purity". Biotechniques *22*(3), 474-476, 478-481. https://doi.org/10.2144/97223st01

[329] Sayers, J.R. and Eckstein, F. (1991). "A single-strand specific endonuclease activity copurifies with overexpressed T5 D15 exonuclease". Nucleic Acids Res. *19*(15), 4127-4132. https://doi.org/10.1093/nar/19.15.4127

[330] O'Connor, C.D. and Timmis, K.N. (1987). "Highly repressible expression system for cloning genes that specify potentially toxic proteins". J. Bacteriol. *169*(10), 4457-4462. https://doi.org/10.1128/jb.169.10.4457-4462.1987

[331] Sambrook, J. and Russell, D.W. (2001). "Molecular Cloning: A Laboratory Manual". 3rd edition, vol. 1. Cold Spring Harbor Laboratory Press, New York.

[332] Singh, P. et. al. (2013). "Effect of Signal Peptide on Stability and Folding of Escherichia coli Thioredoxin". PLOS ONE *8*(5), e63442. https://doi.org/10.1371/journal.pone.0063442

[333] Gawin, A. et. al. (2020). "Translational regulation of periplasmic folding assistants and proteases as a valuable strategy to improve production of translocated recombinant proteins in Escherichia coli". BMC Biotechnol. *20*, Article number: 24. https://doi.org/10.1186/s12896-020-00615-0

[334] van Dijl, J. M. et. al. (1991). "Non-functional expression of Escherichia coli signal peptidase I in Bacillus subtilis". Microbiology *137*(9), 2073-2083. https://doi.org/10.1099/00221287-137-9-2073

[335] Ritz, D. and Beckwlth, J. (2002). "[34] – Redox State of Cytoplasmic Thioredoxin". Methods Enzymol. *347*, 360-370. https://doi.org/10.1016/S0076-6879(02)47036-X

[336] Rasooli, F. and Hashemi, A. (2019). "Efficient expression of EpEX in the cytoplasm of Escherichia coli using thioredoxin fusion protein". Res. Pharm. Sci. *14*(6), 554-565. https://doi.org/10.4103/1735-5362.272564

[337] LaVallie, E.R. et. al. (1993). "A Thioredoxin Gene Fusion Expression System That Circumvents Inclusion Body Formation in the E. coli Cytoplasm". Nat. Biotechol. *11*, 187-193. https://doi-org.sheffield.idm.oclc.org/10.1038/nbt0293-187

[338] de Marco, A. (2009). "Strategies for successful recombinant expression of disulfide bond-dependent proteins in Escherichia coli". Microb. Cell Fact. *8*, Article number: 26. https://doi.org/10.1186/1475-2859-8-26

[339] Deng, B. and Wan, G. (2024). “Technologies for studying phase-separated biomolecular condensates”. Adv. Biotechol. (Singap.) *2*(1), 10. https://doi.org/10.1007/s44307-024-00020-0

[340] Wang, B. et. al. (2021). “Liquid–liquid phase separation in human health and diseases”. Sig. Transduct. Target. Ther. *6*, 290. https://doi.org/10.1038/s41392-021-00678-1

[341] Zhang, X. et. al. (2023). “Study liquid–liquid phase separation with optical microscopy: A methodology review”. APL Bioeng. *7*(2), 021502. https://doi.org/10.1063/5.0137008

[342] Irving, P.H. (2016). “Physics of the human body” 2nd edition. Springer Cham. Page 464, Table 6.45. https://doi.org/10.1007/978-3-319-23932-3

[343] Llopis, J. et. al. (1998). “Measurement of cytosolic, mitochondrial, and Golgi pH in single living cells with green fluorescent proteins”. Proc. Natl. Acad. Sci. USA *95*(12), 6803-6808. https://doi.org/10.1073/pnas.95.12.6803

[344] Brangwynne, C.P., Tompa, P. and Pappu, R.V. (2015). “Polymer physics of intracellular phase transitions”. Nat. Phys. *11*, 899-904. https://doi.org/10.1038/nphys3532

[345] Barrett, A.J. (1987). “The cystatins: a new class of peptidase inhibitors”. Trends Biochem. Sci. *12*, 193-196. https://doi.org/10.1016/0968-0004(87)90092-2

[346] Carmel-Harel, O. and Storz, G. (2000). “Roles of the Glutathione- and Thioredoxin-Dependent Reduction Systems in the Escherichia Coli and Saccharomyces Cerevisiae Responses to Oxidative Stress”. Annu. Rev. Microbiol. https://doi.org/10.1146/annurev.micro.54.1.439

[347] Brandes, N., Schmitt, S. and Jakob, U. (2009). “Thiol-Based Redox Switches in Eukaryotic Proteins”. Antioxid. Redox Signal. *11*(5), 997-1014. https://doi.org/10.1089/ars.2008.2285

[348] Alberti, S., Gladfelter, A. and Mittag, T. (2019). “Considerations and Challenges in Studying Liquid-Liquid Phase Separation and Biomolecular Condensates”. Cell *176*(3), 419-434. https://doi.org/10.1016/j.cell.2018.12.035

[349] Minton, A.P. and Wilf, J. (1981). “Effect of macromolecular crowding upon the structure and function of an enzyme: glyceraldehyde-3-phosphate dehydrogenase”. Biochemistry *20*(17), 4821-4826. https://doi.org/10.1021/bi00520a003

[350] Puck, T.T., Marcus, P.I. and Cieciura, S.J. (1956). “CLONAL GROWTH OF MAMMALIAN CELLS IN VITRO: GROWTH CHARACTERISTICS OF COLONIES FROM SINGLE HELA CELLS WITH AND WITHOUT A "FEEDER" LAYER”. J. Exp. Med. *103*(2), 273-284. https://doi.org/10.1084/jem.103.2.273

[351] Gossen, M. and Bujard, H. (1992). “Tight control of gene expression in mammalian cells by tetracycline-responsive promoters”. Proc. Natl. Acad. Sci. USA *89*(12), 5547-5551. https://doi.org/10.1073/pnas.89.12.5547

[352] Grubb, A. and Löfberg, H. (1985). “Human gamma-trace. Structure, function and clinical use of concentration measurements”. Scand. J. Clin. Lab. Invest. Suppl. *177*, 7-13. PMID: 3865346

[353] Cleland, W.W. (1964). “Dithiothreitol, a new protective reagent for SH groups”. Biochemistry *3*, 480-482. https://doi.org/10.1021/bi00892a002

[354] Creighton, T.E. and Goldenberg, D.P. (1984). “Kinetic role of a meta-stable native-like two-disulphide species in the folding transition of bovine pancreatic trypsin inhibitor”. J. Mol. Biol. *179*(3), 497-526. https://doi.org/10.1016/0022-2836(84)90077-9

[354] RayBiotech Inc. (2022). “GFP Stably expression HeLa Cell Line”. User Manual. https://doc.raybiotech.com/pdf/Manual/GFP-0002.pdf

[355] Foster, M.P., McElroy, C.A. and Amero, C.D. (2008). “Solution NMR of large molecules and assemblies”. Biochemistry *46*(2), 331-340. https://doi.org/10.1021/bi0621314

[356] Frueh, D.P. et. al. (2014). “NMR methods for structural studies of large monomeric and multimeric proteins”. Curr. Opin. Struct. Biol. *23*(5), 734-739. https://doi.org/10.1016/j.sbi.2013.06.016

[357] Baldwin, R.L. (1996). “How Hofmeister ion interactions affect protein stability”. Biophys. J. *71*(4), 2056-2063. https://doi.org/10.1016/S0006-3495(96)79404-3

[358] Goto, Y., Calciano, L.J. and Fink, A.L. (1990). “Acid-induced folding of proteins”. Proc. Natl. Acad. Sci. USA *87*(2), 573-577. https://doi.org/10.1073/pnas.87.2.573

[359] Staniforth, R.A. et. al. (1998). “Unfolding of apomyoglobin from Aplysia limacina: the effect of salt and ph on the cooperativity of folding”. J. Mol. Biol. *275*(1), 133-148. https://doi.org/10.1006/jmbi.1997.1409

[360] Silver, I.A., Deas, J. and Erecińska, M. (1997). “Ion homeostasis in brain cells: differences in intracellular ion responses to energy limitation between cultured neurons and glial cells”. Neuroscience *78*(2), 589-601. https://doi.org/10.1016/S0306-4522(96)00600-8

[361] Izhikevich, E.M. (2006). “Dynamical Systems in Neuroscience: The Geometry of Excitability and Bursting”. The MIT Press. Page 26. https://doi.org/10.7551/mitpress/2526.001.0001

[362] Mitrea, D.M. et. al. (2022). “Modulating biomolecular condensates: a novel approach to drug discovery”. Nat. Rev. Drug Discov. *21*, 841-862. https://doi.org/10.1038/s41573-022-00505-4

[363] Lesnak, M. et. al. (2021). “The Determination of Cystatin C in Biological Samples via the Surface Plasmon Resonance Method”. BioTechniques *70*(5), 263-270. https://doi.org/10.2144/btn-2020-0151

[364] Lippincott-Schwartz, J., Snapp, E. and Kenworthy, A. (2001). “Studying protein dynamics in living cells”. Nat. Rev. Mol. Cell. Biol. *2*, 444-456. https://doi.org/10.1038/35073068

[365] Field, J. et. al. (1988). “Purification of a RAS-responsive adenylyl cyclase complex from Saccharomyces cerevisiae by use of an epitope addition method”. Mol. Cell Biol. *8*(5), 2159-2165. https://doi.org/10.1128/mcb.8.5.2159

[366] Samson, F. et. al. (1979). “Nocodazole action on tubulin assembly, axonal ultrastructure and fast axoplasmic transport”. J. Pharmacol. Exp. Ther. *208*(3), 411-417. PMID: 85702

[367] Taylor, A.I.P. et. al. (2022). “Simple, Reliable Protocol for High-Yield Solubilization of Seedless Amyloid-β Monomer”. ACS Chem. Neurosci. *14*(1), 53-71. https://doi.org/10.1021/acschemneuro.2c00411

[368] Lee, H. J., Choi, C. and Lee, S. J. (2002). “Membrane-bound alpha-synuclein has a high aggregation propensity and the ability to seed the aggregation of the cytosolic form”. J. Biol. Chem. *277*, 671–678. https://doi.org/10.1074/jbc.m107045200

[369] Chen, Y.H., Yang, J.T. and Martinez, H.M. (1972). “Determination of the secondary structures of proteins by circular dichroism and optical rotatory dispersion”. Biochemistry *11*(22), 4120-4131. https://doi.org/10.1021/bi00772a015

[370] Hirst, J.D. and Brookes 3rd, C.L. (1994). “Helicity, circular dichroism and molecular dynamics of proteins”. J. Mol. Biol. *243*(2), 173-178. https://doi.org/10.1006/jmbi.1994.1644

[371] Greenfield, N. and Fasman, G.D. (1969). “Computed circular dichroism spectra for the evaluation of protein conformation”. Biochemistry *8*(10), 4108-4116. https://doi.org/10.1021/bi00838a031

[372] Mishra, M.K. et. al. (2009). “Lipase activity of Lecitase® Ultra: characterization and applications in enantioselective reactions”. Tetrahedron: Asymmetry *20*(24), 2854-2860. https://doi.org/10.1016/j.tetasy.2009.11.012

[373] López-Amaya, C. and Marangoni, A.G. (1999). “Comparison of dynamic and integrated light-scattering techniques in the study of the interaction of *Candida rugosa* lipase with DPPC liposomes”. Biophys. Chem. *80* (2), 69-83. https://doi.org/10.1016/S0301-4622(99)00062-9

[374] Op Den Kamp, J.A.F., De Gier, J. and van Deenen, L.L.M. (1974). “Hydrolysis of phosphatidylcholine liposomes by pancreatic phospholipase A_2 at the transition temperature”. Biochim. Biophys. Acta – Biomembr. *345*(2), 253-256. https://doi.org/10.1016/0005-2736(74)90263-6

[375] Zettlmeissl, G., Rudolph, R. and Jaenicke, R. (1979). “Reconstitution of lactic dehydrogenase. Noncovalent aggregation vs. reactivation. 1. Physical properties and kinetics of aggregation”. Biochemistry *18*(25), 5567-5571. https://doi.org/10.1021/bi00592a007

[376] Dickey, A. and Faller, R. (2008). “Examining the Contributions of Lipid Shape and Headgroup Charge on Bilayer Behavior”. Biophys. J. *95*(6), 2636-2646. https://doi.org/10.1529/biophysj.107.128074

[377] Punjani, A. et. al. (2017). “cryoSPARC: algorithms for rapid unsupervised cryo-EM structure determination”. Nat. Methods *14*, 290-296. https://doi.org/10.1038/nmeth.4169

[378] Kučerka, N. et. al. (2011). “Scattering Density Profile Model of POPG Bilayers As Determined by Molecular Dynamics Simulations and Small-Angle Neutron and X-ray Scattering Experiments”. J. Phys. Chem. *116*(1), 232-239. https://doi.org/10.1021/jp208920h

[379] Lin, C. et. al. (2011). “Size-Dependent Properties of Small Unilamellar Vesicles Formed by Model Lipids”. Langmuir *28*(1), 689-700. https://doi.org/10.1021/la203755v

[380] Hammouda, B. (2010). “A new Guinier-Porod model”. J. Appl. Crystallogr. *43*, 716-719.

[381] (no given author or date). “mono_gauss_coil”. SasView 6.0.1 web documentation. https://www.sasview.org/docs/user/models/mono_gauss_coil.html

[382] Butler, P. (2016). “vesicle”. SasView 6.0.1 web documentation. https://www.sasview.org/docs/user/models/vesicle.html

[383] (no given author or date). “guinier_porod”. SasView 6.0.1 web documentation. https://www.sasview.org/docs/user/models/guinier_porod.html

[384] (no given author or date). “flexible_cylinder”. SasView 6.0.1 web documentation. https://www.sasview.org/docs/user/models/flexible_cylinder.html

[385] Butler, P. (2022). “cylinder”. SasView 6.0.1 web documentation. https://www.sasview.org/docs/user/models/cylinder.html

[386] Liu, Q. et. al. (2023). “Nascent mitochondrial proteins initiate the localized condensation of cytosolic protein aggregates on the mitochondrial surface”. Proc. Natl. Acad. Sci. U.S.A. *120*(31), e2300475120. https://doi.org/10.1073/pnas.2300475120